UNIVERSITÉ DE GENÈVE
Département de physique nucléaire et corpusculaire

FACULTÉ DES SCIENCES
Professeur Allan Clark

Search for a supersymmetric partner of the top quark in the one-lepton channel with the ATLAS detector

THÈSE

présentée à la Faculté des sciences de l'Université de Genève
pour obtenir le grade de Docteur ès sciences, mention physique

par

Kilian Rosbach

de Allemagne

Thèse N° 4798

GENÈVE
Atelier d'impression ReproMail
2015

UNIVERSITÉ
DE GENÈVE

FACULTÉ DES SCIENCES

Doctorat ès sciences
Mention physique

Thèse de ***Monsieur Kilian ROSBACH***

intitulée :

"Search for a Supersymmetric Partner of the Top Quark in the One-lepton Channel with the ATLAS Detector"

La Faculté des sciences, sur le préavis de Monsieur A. CLARK, professeur honoraire et directeur de thèse (Département de physique nucléaire et corpusculaire), Monsieur X. WU, professeur associé et codirecteur de thèse (Département de physique nucléaire et corpusculaire), Monsieur G. IACOBUCCI, professeur ordinaire (Département de physique nucléaire et corpusculaire) et Madame M. D'ONOFRIO, docteure (Oliver Lodge Laboratory, School of Physical Sciences, University of Liverpool, United Kingdom), autorise l'impression de la présente thèse, sans exprimer d'opinion sur les propositions qui y sont énoncées.

Genève, le 19 juin 2015

Thèse - 4798 -

Le Doyen

N.B. - La thèse doit porter la déclaration précédente et remplir les conditions énumérées dans les "Informations relatives aux thèses de doctorat à l'Université de Genève".

Abstract

This thesis presents a search for evidence of a scalar top quark (top squark, or *stop*), predicted by supersymmetry (SUSY), which is a hypothetical extension of the Standard Model of particle physics (SM). The search is using the full dataset recorded in 2012 using the ATLAS detector, one of the four main detectors at the Large Hadron Collider.

The search is developed using simplified models containing only a small number of SUSY particles. Besides the top squarks, only the lightest neutralinos and charginos are considered, which are spin-1/2 particles predicted by SUSY. The neutralino is electrically neutral and assumed to be stable, leaving the detector without interaction. In each simplified model, top squarks are produced in pairs and are allowed to decay (a) into a top quark and a neutralino; (b) into a bottom quark and a chargino; or (c) into a bottom quark, a W boson, and a neutralino (*three-body decay*).

This work extends earlier searches for pair-produced top squarks: *mixed* scenarios are studied, where decay modes (a) and (b) can occur simultaneously; decay mode (c) is studied for the first time using data recorded with the ATLAS detector.

Using datasets of simulated events, selection criteria for proton-proton collision events are established, defining regions of phase-space enriched in hypothetical supersymmetric events and with few expected Standard Model events. Among other requirements, the selected events need to have exactly one isolated electron or muon, and high missing transverse momentum. Several dedicated variables are presented and their performance is demonstrated. The most important SM background contributions stem from top-antitop pair production events and W boson events with additional jet production. Modified event selection requirements are defined in order to estimate the normalisation of these background contributions from data, significantly reducing the uncertainty of this background estimate.

No significant excess of recorded events over the expected number of SM events is observed, and for certain mass assumptions of the supersymmetric particles, the signal hypothesis can be ruled out at 95% confidence level. Stop pair production followed by three-body decays is ruled out for stop masses below 300 GeV assuming a stop-neutralino mass difference of 150 GeV. Mixed stop decays at an equal branching ratio of the considered decay modes are excluded up to a stop mass of 550 GeV for a neutralino mass of 150 GeV. The search reach is expected to improve significantly when the analysis is updated using the ATLAS data to be recorded in 2015.

Resumé

La supersymétrie est une extension hypothétique du modèle standard de la physique des particules. Cette thèse présente une recherche qui vise à trouver des indications sur des particules nouvelles prédites par des modèles supersymétriques, en particulier sur le partenaire du quark top de spin zéro, appelé squark top ou *stop*. La recherche est réalisée avec l'ensemble des données enregistrées par le détecteur ATLAS en 2012. Le détecteur ATLAS est l'un des quatre détecteurs du grand collisionneur de hadrons (LHC).

Selon les modèles considérés, les squarks top sont produits par paires et chaque squark top peut se désintégrer en (a) un quark top et un neutralino; (b) un quark bottom et un chargino; ou (c) un quark bottom, un boson W et un neutralino (*désintégration à trois corps*). Le travail présenté dans cette thèse enrichit les précédentes recherches de squarks top des scénarios *mixtes* qui sont caracterisés par la présence simultanée des désintégrations (a) et (b); le mode de désintégration (c) est pour la première fois analysé avec des données enregistrées par le détecteur ATLAS.

La présente recherche repose sur des événements avec, dans l'état final, la présence d'un électron ou muon isolé et d'énergie transverse manquante. Les critères de sélection des collisions proton-proton sont définis à l'aide des données simulées. Ils sont optimisés pour accepter plus fréquemment des événements avec des particules supersymétriques, et plus rarement accepter des événements prédits par le modèle standard. Au cours de la thèse, plusieurs variables sont définies et leurs performances sont démontrées. Les processus du modèle standard les plus importants sont dus à des collisions proton-proton produisants des paires top-antitop et à des événements de boson W avec la production de jets additionnels. Pour estimer la normalisation de ces processus dans les données, les critères de sélection sont modifiés. Ainsi, l'incertitude de l'estimation de ce bruit de fond est réduite.

Aucun excès significatif d'événements mesurés sur l'estimation n'a été observé. L'hypothèse supersymétrique peut être rejetée pour certaines suppositions de masses à un niveau de confiance de 95%. La production de stop par paires suivie d'une désintégration à trois corps est rejetée pour des masses de stop sous 300 GeV sous condition d'une difference de masse de stop-neutralino de 150 GeV. Les désintégrations de stop mixtes avec les mêmes rapports de branchement pour les deux modes de désintégration sont rejetées pour des masses de stop sous 550 GeV quand la masse de neutralino est 150 GeV. Les données mesurées avec le détecteur ATLAS en 2015 permettront d'augmenter considérablement la puissance de la recherche.

Contents

Introduction **1**

1 Standard Model **3**
- 1.1 Particles and forces . . . 3
- 1.2 Electroweak symmetry breaking . . . 10
- 1.3 Open questions and theoretical problems . . . 12
- 1.4 Beyond the Standard Model . . . 16

2 Supersymmetry **19**
- 2.1 Basic Concepts . . . 19
  - 2.1.1 SUSY transformations . . . 19
  - 2.1.2 Wess-Zumino model . . . 20
  - 2.1.3 SUSY algebra . . . 23
  - 2.1.4 Supermultiplets . . . 24
  - 2.1.5 Combined SUSY Lagrangian . . . 25
  - 2.1.6 R-parity . . . 26
- 2.2 Minimal Supersymmetric Standard Model . . . 27
- 2.3 SUSY breaking mechanisms . . . 29
- 2.4 Top squark properties and mixing . . . 34
- 2.5 Impact of Higgs boson discovery . . . 35
- 2.6 Pre-LHC limits on SUSY . . . 36

3 The ATLAS Detector **39**
- 3.1 The Large Hadron Collider at CERN . . . 39
- 3.2 Detector overview . . . 41
  - 3.2.1 Magnets . . . 44
  - 3.2.2 Inner detector . . . 44
  - 3.2.3 Calorimetry . . . 46
  - 3.2.4 Muon spectrometer . . . 47
- 3.3 Reconstruction, identification, performance . . . 49

3.3.1 Pile-up . . . 50
3.3.2 Tracks and vertices . . . 50
3.3.3 Electrons and photons . . . 51
3.3.4 Muons . . . 53
3.3.5 Jets . . . 55
3.3.6 Overlap removal . . . 57
3.3.7 Missing transverse momentum . . . 58
3.4 Trigger . . . 59

4 Signal and background processes 63
4.1 Simulation of *pp*-collision events . . . 63
4.1.1 Parton distribution functions . . . 63
4.1.2 Event generation . . . 64
4.1.3 Fragmentation and hadronisation . . . 65
4.1.4 Detector simulation . . . 66
4.2 Signal processes considered in the analysis . . . 67
4.2.1 Stop decay modes . . . 67
4.2.2 Model parameters . . . 68
4.2.3 Mixed stop decays at arbitrary branching ratios . . . 69
4.3 SM background processes . . . 70
4.3.1 Dominant SM backgrounds: top-antitop and W+jets production . 71
4.3.2 Other SM backgrounds . . . 72
4.4 Samples of simulated events . . . 73
4.4.1 Signal grids and generator filters . . . 75
4.4.2 Event weights, scale-factors and sample normalisation . . . 77
4.4.3 Re-weighting of top-antitop events . . . 80

5 Analysis 83
5.1 Analysis Strategy . . . 83
5.2 Event preselection . . . 86
5.3 Discriminating variables . . . 93
5.3.1 Jet kinematics . . . 93
5.3.2 Transverse mass, m_{T2} and variations . . . 94
5.3.3 Topness . . . 98
5.3.4 Hadronic top mass reconstruction . . . 100
5.3.5 Hadronic tau veto . . . 101
5.4 Signal Region definition . . . 102
5.5 Systematic uncertainties . . . 107
5.5.1 Modelling uncertainties . . . 107
5.5.2 Experimental uncertainties . . . 110

5.6 Control regions 114
  5.6.1 Reduced systematic uncertainties 119
  5.6.2 Comparison of measurement and simulation 120
5.7 Shape-fit for three-body decays 124

6 Results **127**
6.1 Statistical method 127
6.2 Mixed and three-body stop decays 128
6.3 LHC run 1 limits on SUSY 137

7 Summary and Outlook **141**

A Long term study of SCT optical units **145**

B Data-driven QCD multi-jet estimate **151**
B.1 Anti-electron selection 152
B.2 QCD multi-jet model evaluation 156
B.3 Triggers for the anti-electron model 157
B.4 Extraction of QCD multi-jet fraction 160

Bibliography **164**

List of Figures **178**

List of Tables **181**

Magicians and scientists are, on the face of it, poles apart. Certainly, a group of people who often dress strangely, live in a world of their own, speak a specialised language and frequently make statements that appear to be in flagrant breach of common sense have nothing in common with a group of people who often dress strangely, speak a specialised language, live in… er…

Terry Pratchett (1948–2015), "The Science of Discworld"

Introduction

The Standard Model of Particle Physics summarises our knowledge of elementary particles and their interactions. Despite its numerous successes it cannot be considered a final theory. For example, it does not contain any particles that might explain the large amount of dark matter in the universe, it fails to explain the observed predominance of matter over antimatter and it does not explain the vast differences in the energy and mass scales present in the theory, from neutrino masses below 1 eV/c^2, over the electroweak bosons near 100 GeV/c^2, up to the Planck mass around 10^{19} GeV/c^2.

After summarising the key features of the Standard Model in chapter 1, we will show that Supersymmetry offers compelling answers to these problems in chapter 2.

In this thesis we search for evidence of the top squark, the scalar supersymmetric partner of the top quark. If it exists, it might be produced in collisions at the Large Hadron Collider and observed in the events recorded by the ATLAS detector described in chapter 3. Accurate simulations of proton-proton collision events (chapter 4) of the relevant signal models and SM background processes are indispensable to design the search and to compare recorded data with models that include the hypothetical particles predicted by Supersymmetry.

Knowing the existing theoretical framework as well as the experimental and theoretical tools we are ready to embark on the search for the top squark (chapter 5). After an outline of the analysis strategy an overview of dedicated variables is given, and the development of signal regions is discussed. Systematic uncertainties are evaluated and the normalisation of the dominant background processes is derived using control regions. Chapter 6 presents the results, using the expected and observed event yields in statistical tests for discovery and exclusion, and places them in context with other recent top squark searches at the Large Hadron Collider; we conclude this work with an outlook on upcoming stop searches in chapter 7.

1 | Standard Model

> Our experience hitherto justifies us in trusting that nature is the realisation of the simplest that is mathematically conceivable.
>
> *Albert Einstein*

The Standard Model of Particle Physics (SM) summarises and structures our knowledge of elementary particles and their interactions through the electromagnetic, weak and strong forces. The structure of the SM is essentially unchanged since its main components, the electroweak theory and quantum chromodynamics (QCD), have been formulated in the 1960s and 1970s. It is based on quantum field theories, which combine special relativity and quantum mechanics to describe fundamental processes at high energies and small length scales.

We introduce briefly the SM particles and interactions, as well as the mechanism of electroweak symmetry breaking. We conclude the overview with a list of open questions hinting at possible physics Beyond the Standard Model (BSM).

1.1 Particles and forces

Only three elementary fermions make up the ordinary matter surrounding us in every-day life: electrons, up quarks, and down quarks. Up and down quarks are the constituents of protons and neutrons. Protons and neutrons can combine to form atomic nuclei of ordinary matter. Nuclei are surrounded by electrons to yield electrically neutral atoms.

While electrons were discovered over a century ago in cathode-ray experiments by Thomson (1897), evidence for the existence of quarks was found only in the 1960s in deep inelastic scattering experiments at SLAC [1]. Besides an electric charge, quarks also carry a strong charge called *colour*, which comes in three types usually labelled red, green and blue. Just as there are positive and negative electric charges, there are colour and anticolour charges. Possibly the most convincing evidence of the quarks' existence was the experimental evidence for three colour charges (see figure 1.1).

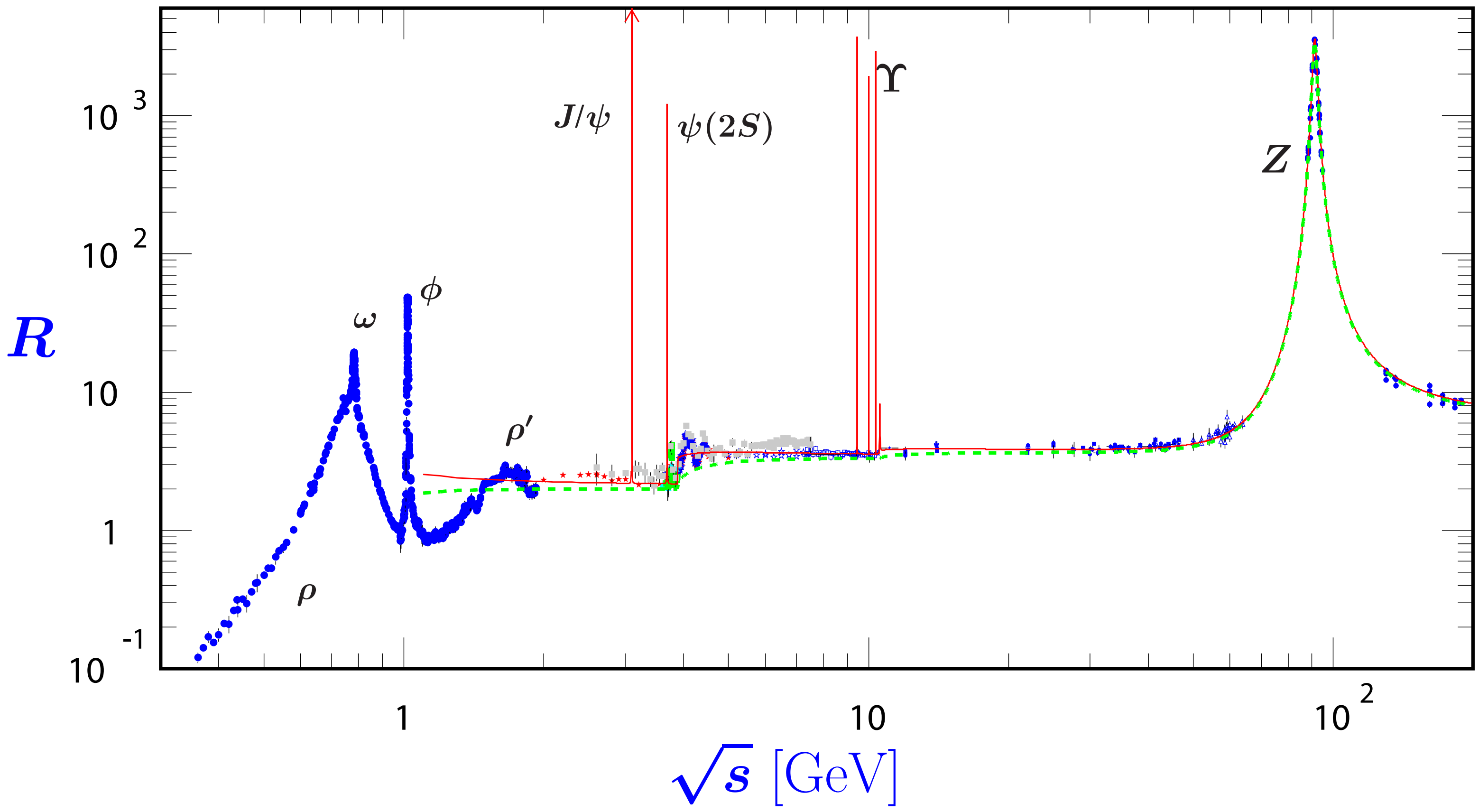

Figure 1.1: The ratio R between the cross-sections for production of hadrons over production of muon pairs in electron-positron scattering experiments. Near the thresholds of meson or Z production the production of hadrons dominates, otherwise R is well approximated by $R(E) = N_C \cdot \sum q_i^2$, where N_C is the number of quark colours and the sum runs over all quarks accessible at energy E. Only for $N_C = 3$ are the data well described (from [2]; see ref. [3] for a full list of contributing experiments and applied corrections).

The interaction between the electron and the nucleus is governed by the *electromagnetic force*, whose exchange or messenger particle is the photon. It couples to the electromagnetic charge of the electron and of the quarks in the nucleus. Particles with colour charge interact with each other by the exchange of gluons, the messenger particles of the *strong force*.

The electron and the quarks are examples of *fermions*, particles with half-integer spin (1/2, 3/2, ...). Particles with integer spin are called *bosons*[1]; photon and gluons are spin-1 bosons. All of the elementary matter particles in the SM have spin 1/2, all exchange particles have spin 1 ("vector" particles). The Higgs boson, described below, is the only spin-0 (or "scalar") particle in the SM.

For every matter particle there is an *antiparticle* of the same mass, but with opposite quantum numbers. The positron e^+ is the antiparticle of the electron e^-, it has theoretically identical mass $m_{e^+} = m_{e^-} = 511$ keV/c^2, but opposite electric charge $q_{e^+} = -q_{e^-} = +e = +1.6 \times 10^{-19}$ C, and negative intrinsic parity. Since the total electric charge is conserved in the SM, electrically charged particles are always annihilated or produced in pairs, for example: an up quark (charge $2/3e$) and anti up quark (charge $-2/3e$) can annihilate into a photon, which then decays into an electron-positron pair. This mechanism is exploited in colliders: if the centre-of-mass energy of the annihilated pair is sufficiently high, particle-antiparticle pairs more massive than the colliding particles may be produced.

Let us further compare the electromagnetic and strong interactions. Both can be understood in terms of charged fermions and the exchange of massless bosons corresponding to the type of charge. While the electromagnetic force determines the size of an atom ($\sim 10^{-10}$ m), the stronger coupling of the strong force results in typical sizes of atomic nuclei of $\sim 10^{-15}$ m. While photons do not carry electric charge, gluons do have colour[2]. With increasing distance r between charged particles, the electromagnetic interaction becomes weaker as r^{-2}. Electrical charges are screened by virtual electron-positron pairs. At short distance or high energy, this screening becomes less effective, leading to an apparent increase in the strength of the electromagnetic force. For the strong force, the screening behaviour is inverted due to the gluon self-coupling, leading to an increased force at large distance or low energy. This results in *confinement*: quarks cannot exist freely, as the strong interaction binds them in colour singlets[3], called hadrons, possibly creating particle-antiparticle pairs from the vacuum in the process. However, at high energy or short distance of the interacting particles, the coupling of the strong force is reduced, resulting in *asymptotic freedom* of particles inside hadrons.

---

[1] Groups of fermions and bosons behave differently: while no two fermions can occupy the same quantum state (Pauli exclusion principle), there is no such restriction for bosons. The spin-statistics theorem proves this connection under very general assumptions.

[2] Both colour and anticolour, actually. While 9 such combinations are possible, only 8 linear combinations of them are realised in nature.

[3] This means the bound state is overall uncoloured, or all colours are present in equal amounts.

Two classes of hadrons are observed in experiments: mesons, which are bosons consisting of a quark-antiquark pair (e.g. a positive pion, $\pi^+ = u\bar{d}$), and baryons, which are fermions consisting of three quarks (e.g. protons and neutrons, uud and udd). The interplay of confinement and asymptotic freedom governs the process of *hadronisation*: quarks or gluons produced in a particle collision are not observed directly in the experiment, but are identified by a cascade of particles created by fragmentation and hadronisation, called a *hadronic jet*.

Neutrinos are electrically neutral, uncoloured particles, interacting only through the *weak force*. As the name suggests, the cross-section for weak interactions is small, making it challenging to detect neutrinos. Their existence was predicted from theoretical considerations on the conservation of energy in β-decays (Pauli, 1930) long before they were observed experimentally in the Savannah River experiment (Cowan and Reines, 1956) [4, 5]. Neutrinos are much lighter than all other massive particles, and are treated as massless in the SM. More than eighty years after their conception, neutrinos are still a very active research topic [6].

The "weak charge" is determined by the third component of the *weak isospin* T^3 of a particle, and the weak force is transmitted through the W^+, W^- and Z^0 bosons. All left-chiral fermions carry weak isospin T and participate in weak interactions, while right-chiral fermions do not, maximally violating parity symmetry.

Since a consistent description of the tensor structure of general relativity in a renormalisable quantum field theory has not yet been found, gravity is not described by the SM; this omission is acceptable from an experimental viewpoint, as the effect of gravity on elementary particles is much weaker even than the weak force, and can safely be neglected in the vast majority of particle physics experiments.

The electron, its associated neutrino (ν_e), and the up and down quarks form the so-called first generation (or family) of elementary particles. Starting with the muon (μ) in 1936 and completed (for now?) with the tau neutrino (ν_τ) in 2000, two more generations of elementary particles were discovered, which can be seen as "heavier copies" of the first one. An important difference is that the heavier particles are unstable and eventually decay into particles from the first generation. For the *charged leptons* (e, μ, τ), such decays always involve the production of neutrinos or antineutrinos (i.e. *uncharged* leptons) in a way that conserves the total number of leptons for each family separately. The total number of any of the six types of quarks may change in interactions involving a W boson and is conserved otherwise. The mixing between quark generations in charged weak interactions is described by the $SU(3)$ Cabibbo-Kobayasha-Maskawa (CKM) matrix.

Measurements of the decay width of the Z^0 made by the experiments at the electron-positron collider LEP provided evidence that there cannot be another light neutrino (up to a mass of $m_Z/2 \approx 45$ GeV/c^2) [7], suggesting that future elementary particles might not have an obvious place in the current scheme. Searches for additional quarks continue [8].

The properties of all matter and exchange particles of the SM are summarised in table 1.1 (based on ref. [2]). The table also includes the recently discovered Higgs boson, whose measured properties so far match those predicted by the SM well.

All SM interactions are characterised by local gauge symmetries, with particles corresponding to group representations. The gauge group of the strong interaction is $SU(3)_\mathrm{C}$, where the subscript indicates that colour is the relevant charge. Before electroweak symmetry breaking (detailed in section 1.2), the remaining gauge groups are $SU(2)_\mathrm{L} \times U(1)_Y$, where L is a reminder that only left-chiral particles are affected by the weak isospin interaction, and Y is the weak hypercharge. After electroweak symmetry breaking, an $U(1)_\mathrm{Q}$ symmetry of the electromagnetic interaction remains, where $Q = Y/2 + T_3$ is the common electric charge.

Demanding local gauge invariance under $SU(3)_\mathrm{C} \times SU(2)_\mathrm{L} \times U(1)_Y$ symmetry transformations was an important guiding principle in finding the SM *Lagrangian density*, which governs all SM kinematics and gauge interactions, describes the Higgs sector, and has Yukawa mass terms for quarks and (charged) leptons. All field equations can be derived from the Lagrangian. Depending on the notation, it can be expressed in different ways[4]. A detailed introduction is given in chapter 10 of ref. [11], a more concise summary is found in ref. [12].

For the purpose of this thesis, it suffices to point out that terms bilinear in a field can be interpreted as mass terms, while trilinear or quadrilinear terms can be interpreted as interactions, and represented by Feynman diagrams. We now illustrate the general idea with the Lagrangian for quantum electrodynamics (QED), capturing the kinematics of electrically charged particles and their interaction with the photon field. Starting from the free Dirac Lagrangian

$$\mathcal{L}_\mathrm{Dirac} = \bar{\Psi}(i\gamma^\mu \partial_\mu - \frac{mc}{\hbar})\Psi, \tag{1.1}$$

where Ψ is a four-component spinor field, γ^μ (μ=$0,1,2,3$) are a representation of the Dirac matrices, and $\partial_\mu \equiv \partial/\partial x^\mu$, we allow a local phase factor for Ψ: $\Psi \rightarrow e^{-iq\theta(x)}\Psi$, $\bar{\Psi} \rightarrow e^{+iq\theta(x)}\bar{\Psi}$. $\mathcal{L}_\mathrm{Dirac}$ is not invariant under this transformation:

$$\mathcal{L}_\mathrm{Dirac} \rightarrow \mathcal{L}_\mathrm{Dirac} + q\bar{\Psi}\gamma^\mu\Psi(\partial_\mu\theta). \tag{1.2}$$

We counter the additional term by including a massless gauge field A^μ, transforming as $A^\mu \rightarrow A^\mu + \partial^\mu\theta$, in the Lagrangian:

$$\mathcal{L}_\mathrm{QED} = i\bar{\Psi}\gamma^\mu\partial_\mu\Psi - \frac{mc}{\hbar}\bar{\Psi}\Psi - q\bar{\Psi}\gamma^\mu\Psi A_\mu - \frac{1}{4}F^{\mu\nu}F_{\mu\nu}, \tag{1.3}$$

---

[4] Some of which are short enough to fit on a t-shirt or a coffee mug.

Fermions (spin 1/2)			
Charged Leptons (uncoloured)			
electron	e^-	$m_e = 511\ \mathrm{keV}/c^2$	
muon	μ^-	$m_\mu = 106\ \mathrm{MeV}/c^2$	
tau	τ^-	$m_\tau = (1776.82 \pm 0.16)\ \mathrm{MeV}/c^2$	
Neutrinos (uncoloured, electrically neutral, only left-chiral)			
ν_e, ν_μ, ν_τ		$m_\nu < 2\ \mathrm{eV}/c^2$; $m_\nu \equiv 0$ in the SM	
Left-chiral leptons belong to weak isospin doublets ($T = \frac{1}{2}$), weak hypercharge $Y = -1$: $(\nu_e, e)_L$, $(\nu_\mu, \mu)_L$, $(\nu_\tau, \tau)_L$. The right-chiral charged leptons are isospin singlets: e_R, μ_R, τ_R.			
Quarks (coloured, $T = \frac{1}{2}$, $Y = \frac{1}{3}$)			
up down	$\begin{pmatrix}u\\d\end{pmatrix}$	$m_u \approx$ 2-3 MeV/c^2 $m_d \approx 5\ \mathrm{MeV}/c^2$	*Up-type quarks carry electric charge $q = +2/3\lvert e\rvert$, down-type quarks have $q = -1/3\lvert e\rvert$.*
charm strange	$\begin{pmatrix}c\\s\end{pmatrix}$	$m_c \approx 1.3\ \mathrm{GeV}/c^2$ $m_s \approx 95\ \mathrm{MeV}/c^2$	
top bottom	$\begin{pmatrix}t\\b\end{pmatrix}$	$m_t \approx 173\ \mathrm{GeV}/c^2$ $m_b \approx 4 - 5\ \mathrm{GeV}/c^2$	
Gauge bosons (spin 1)			
photon	γ	$m_\gamma = 0$, uncoloured, $T = 0$, $q = 0$	
8 gluons	g	$m_g = 0$, colour octet, $T = 0$, $q = 0$	
	$W^\pm$, Z^0	$m_W = (80.385 \pm 0.015)\ \mathrm{GeV}/c^2$ $m_Z = (91.1876 \pm 0.0021)\ \mathrm{GeV}/c^2$ uncoloured, weak isospin triplet ($T = 1$)	
Higgs boson (spin 0)			
H		$m_H^{\mathrm{ATLAS}} = (125.36 \pm 0.41)\ \mathrm{GeV}/c^2$ $m_H^{\mathrm{CMS}} = (125.03^{+0.29}_{-0.31})\ \mathrm{GeV}/c^2$	$T^3 = -1/2$, $Y = 1$

Table 1.1: Summary of the SM particles and properties. Masses are taken from [2], with the exception of the Higgs boson mass, for which recent ATLAS and CMS results are quoted [9, 10]. Electron and muon masses have been measured to a high relative accuracy in atomic mass units (4×10^{-10} and 2.5×10^{-9}, respectively), the accuracy of their mass expressed in eV is limited by the accuracy of the measurement of the elementary charge ($\sim 10^{-8}$). Since quarks are not observed as free particles, their exact masses depend on the employed theoretical framework.

where the field strength tensor $F^{\mu\nu} = \partial^\mu A^\nu - \partial^\nu A^\mu$ is invariant under the transformation of A^μ, as is the final term in (1.3), the kinetic term of the gauge field. The combined transformation of Ψ and A^μ results in an overall invariant Lagrangian. The same effect can be achieved by replacing the derivative ∂_μ by the covariant derivative $\mathcal{D}_\mu = \partial_\mu + iqA_\mu$ in the free Dirac Lagrangian in (1.1) and adding the gauge kinetic term $-\frac{1}{4}F^{\mu\nu}F_{\mu\nu}$.

The first and the last term of (1.3) respectively describe the kinematics of the Dirac particle and the gauge field (say, the electron and the photon). The second term is bilinear in the Dirac field, and represents is mass, while no such term exists for the gauge field, as it would spoil the gauge invariance. The third term is an interaction term, involving two Dirac fields and one gauge field. It can be represented by the *Feynman diagram* in figure 1.2 a). The *Feynman rules* for a given Lagrangian allow to compute a probability amplitude for each diagram.

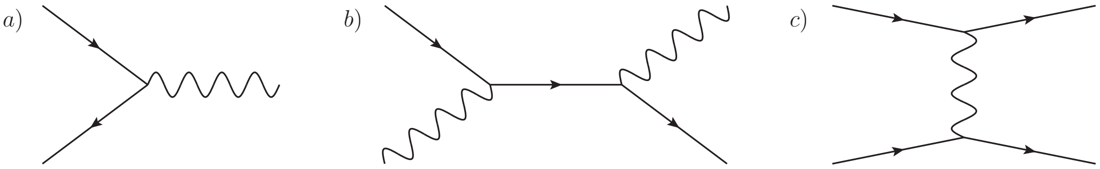

Figure 1.2: **a)** Feynman diagram of the elementary QED process. Interpreting the horizontal direction as the passage of time, it represents the annihilation of an electron (upper solid line, arrow in direction of *particle*) and a positron (lower solid line) into a photon (wiggly line). **b)** and **c)** Combining two elementary diagrams allows to represent contributions to fundamental processes such as the Compton and Møller scattering shown here.

The theory describing the strong interaction is called *quantum chromodynamics* (QCD), from Greek χρόμος (colour). Much like QED, it describes quarks by a Lagrangian of free Dirac particles and introduces the interaction by imposing invariance under local gauge transformations. However, instead of multiplying the quark field by a simple phase factor, it is imbued with an $SU(3)$ structure representing the 3 colour charges:

$$\Psi = \begin{pmatrix} \Psi_r \\ \Psi_g \\ \Psi_b \end{pmatrix}, \tag{1.4}$$

$$\Psi \to e^{-ig_s\theta_a\lambda^a/2}\Psi, \tag{1.5}$$

where g_s is the coupling constant of the strong interaction, λ^a ($a = 1\dots8$) are the 3×3 Gell-Mann matrices and the θ_a are infinitesimal transformation parameters. As before, massless gauge fields are introduced with a transformation that keeps the overall

Lagrangian invariant, and the notation can be made more compact by introducing a suitable covariant derivative. While the free part of the Lagrangian only relates quark field components of identical colour, interactions occur between different colours. The gauge fields are identified with the gluons. The most important difference between QCD and QED is that consecutive transformations of the form (1.5) do not commute, with the consequence that the gluons interact with themselves (related to the antiscreening mentioned earlier). When modelling the interaction between a quark and an antiquark or a system of three quarks by a potential, one finds that only the colour singlet configuration results in a (pairwise) attractive force [11], in line with the claim that only colour singlets occur in nature.

1.2 Electroweak symmetry breaking

Electroweak symmetry breaking (EWSB) via the Higgs mechanism [13–15] gives masses to the weak gauge bosons without spoiling local gauge invariance. Spontaneous symmetry breaking occurs when a symmetry of the physical laws is not reflected in the physically realised ground state, without any influence of an external force.

The Higgs mechanism introduces a complex scalar doublet field. For simplicity, we only consider one complex scalar field here: $\phi \equiv \phi_1 + i\phi_2$ and assume the following Lagrangian density (following the derivation in [11] for the Abelian case):

$$\mathcal{L} = \frac{1}{2}\left(\partial_\mu \phi\right)^\dagger \left(\partial^\mu \phi\right) \underbrace{+\frac{1}{2}\mu^2 \left(\phi^\dagger \phi\right) - \frac{1}{4}\lambda^2 \left(\phi^\dagger \phi\right)^2}_{-\mathrm{V}(\phi)}, \tag{1.6}$$

where λ and μ are positive constants. The potential $V(\phi)$ is visualised in figure 1.3. It is unusual in that its ground state is not located at $\phi = 0$, but there is a continuum of equivalent ground states at $|\phi| = \mu/\lambda = v$, where v is called *vacuum expectation value* (vev). The way forward is to introduce new coordinates $\eta \equiv \phi_1 - v$ and $\xi \equiv \phi_2$ so that $\eta = \xi = 0$ is a ground state, and the terms in $\mathcal{L}$ can be interpreted as possible interactions between the η and ξ fields:

$$\begin{aligned}\mathcal{L} = &\left[\frac{1}{2}\left(\partial_\mu \eta\right)\left(\partial^\mu \eta\right) - \mu^2 \eta^2\right] + \left[\frac{1}{2}\left(\partial_\mu \xi\right)\left(\partial^\mu \xi\right)\right] \\ &- \left[\mu\lambda\left(\eta^3 + \eta\xi^2\right) + \frac{\lambda^2}{4}\left(\eta^4 + \xi^4 + 2\eta^2\xi^2\right)\right] + \frac{\mu^4}{4\lambda^2}.\end{aligned} \tag{1.7}$$

The unusual sign in front of the ϕ mass term in (1.6) has disappeared, instead we find an η mass term, while ξ is the massless Goldstone boson [16]. The third term gives rise to five self-couplings of the ϕ field components.

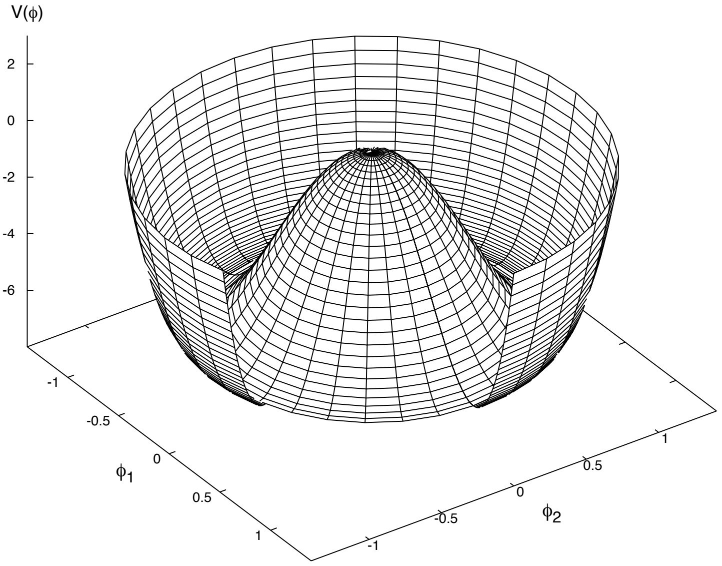

Figure 1.3: Illustration of the Higgs field potential $V(\phi)$ using $\mu = \lambda = 1$. The minima of the potential are located along a circle with $|\phi| = \mu/\lambda$.

As in the QED example above, one can introduce a local gauge symmetry by allowing a $U(1)$ phase, $\phi \rightarrow e^{i\theta(x)}\phi$, accompanied by a massless gauge field A^{μ}. To make the Lagrangian density invariant, the usual derivatives are replaced by covariant derivatives, and (1.6) becomes

$$\begin{aligned} \mathcal{L} = \frac{1}{2} &\left[\left(\partial_{\mu} - \frac{iq}{\hbar c} A_{\mu} \right) \phi^{*} \right] \left[\left(\partial^{\mu} + \frac{iq}{\hbar c} A^{\mu} \right) \phi \right] \\ &+ \frac{1}{2}\mu^{2} \left(\phi^{*}\phi \right) - \frac{1}{4}\lambda^{2} \left(\phi^{*}\phi \right)^{2} - \frac{1}{4} F^{\mu\nu} F_{\mu\nu}, \end{aligned} \tag{1.8}$$

where the last term describes the gauge field kinematics. Changing variables as before yields η and ξ interaction terms, but also gives rise to a mass term for the gauge field ($m_A \propto vq/c^2$), and a bilinear term describing an interaction between the ξ and A fields. This interaction can be eliminated by fixing the gauge $\theta(x) = -\operatorname{atan}(\phi_2/\phi_1)$. We find a Lagrangian with a spontaneously broken symmetry, a massive scalar field η, a massive gauge field A^{μ}, as well as couplings between the two and self-couplings of the scalar field:

$$\begin{aligned} \mathcal{L} = &\left[\frac{1}{2} \left(\partial_{\mu}\eta \right) \left(\partial^{\mu}\eta \right) - \mu^{2}\eta^{2} \right] + \left[-\frac{1}{16\pi} F^{\mu\nu} F_{\mu\nu} + \frac{1}{2} \left(\frac{q}{\hbar c} \frac{\mu}{\lambda} \right)^{2} A_{\mu} A^{\mu} \right] \\ &+ \left[\frac{\mu}{\lambda} \left(\frac{q}{\hbar c} \right)^{2} \eta \left(A_{\mu} A^{\mu} \right) + \frac{1}{2} \left(\frac{q}{\hbar c} \right)^{2} \eta^{2} \left(A_{\mu} A^{\mu} \right) - \lambda\mu\eta^{3} - \frac{1}{4}\lambda^{2}\eta^{4} \right] + \left(\frac{\mu^{2}}{2\lambda} \right)^{2}. \end{aligned} \tag{1.9}$$

The full electroweak theory as established by Glashow, Weinberg and Salam uses a complex weak-isospin doublet Higgs field ϕ with the same potential $V(\phi)$, resulting in one massive scalar (the Higgs boson) and three massless Goldstone bosons. Instead of an $U(1)$ symmetry, the non-Abelian electroweak $SU(2) \times U(1)$ gauge symmetry of the W^a ($a = 1 \ldots 3$) and B fields is used. As an additional feature, electroweak mixing occurs along with electroweak symmetry breaking: instead of massless W^a and B fields, we find the massive $W^\pm$ and Z^0 fields, while the photon field A remains massless. The Goldstone bosons resurface as the longitudinal polarisation degrees of freedom of the massive gauge bosons.

The detailed computation can be found in ref. [17], chapter 20.2. The key observation is that squaring the covariant derivative $\mathcal{D}_\mu = \partial_\mu - igW_\mu^a\tau^a - \frac{i}{2}g'B_\mu$, where g and g' are the $SU(2)$ and $U(1)$ coupling strengths, respectively, together with a coordinate change as before, results in the following term in the Lagrangian:

$$\Delta\mathcal{L} = \frac{1}{2}\frac{v^2}{4}\left[g^2\left(W_\mu^1\right)^2 + g^2\left(W_\mu^2\right)^2 + \left(-gW_\mu^3 + g'B_\mu\right)^2\right]. \tag{1.10}$$

This term allows to identify as physical particles

$$W^\pm = 1/\sqrt{2}(W^1 \mp iW^2) \qquad \text{with } m_W = gv/2, \tag{1.11}$$

$$Z^0 = 1/\sqrt{g^2 + g'^2}\,(gW^3 - g'B) \qquad \text{with } m_Z = \sqrt{g^2 + g'^2}\,v/2, \text{ and} \tag{1.12}$$

$$A = 1/\sqrt{g^2 + g'^2}\,(gW^3 + g'B) \qquad \text{(massless)}. \tag{1.13}$$

It is easy to see that A and Z^0 are related to W^3 and B via a rotation around θ_W, the weak mixing angle. From this we find the useful relations $\cos\theta_\mathrm{W} = g/\sqrt{g^2 + g'^2}$, $m_W = m_Z \cos\theta_\mathrm{W}$ and $e = g\sin\theta_\mathrm{W}$, relating the electromagnetic and electroweak interactions.

While the electroweak theory had been widely accepted already after the observation of neutral currents [18] (1973, Gargamelle) and electroweak bosons [19–22] (1983, UA1 and UA2), the most direct evidence was found only in 2012 by ATLAS and CMS [23, 24]: a spin-0 boson with a mass of about 125 GeV/c^2 [9, 25, 26] (see also figure 1.4), decaying into pairs of massive particles or photons, with branching ratios compatible to the expected ones shown in figure 1.5. The newly discovered particle is still under intense study. To date, all of its properties are compatible with the SM predictions.

1.3 Open questions and theoretical problems

The SM is the combined theory of the electroweak interaction and QCD with the particle content shown in table 1.1.

While the SM is very successful in the description and prediction of experimental observations, it cannot be considered a final theory of elementary particles and their

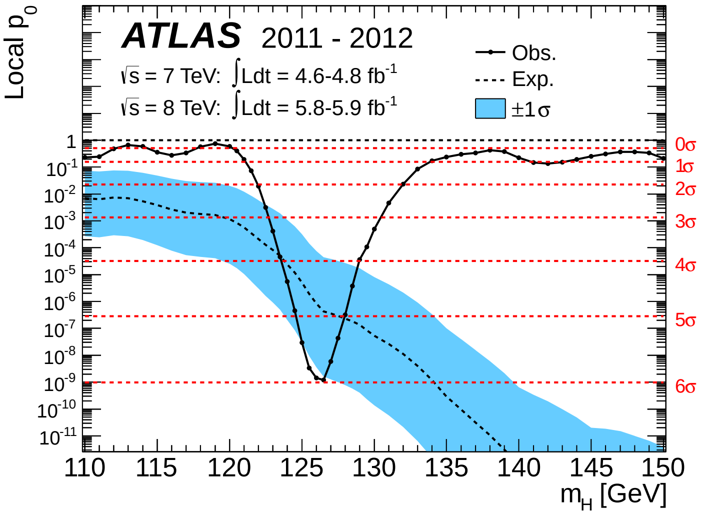

Figure 1.4: This plot, taken from [27], shows as a solid line the local p_0, the probability of a chance observation, as a function of m_{H}, compared to the expected local p_0 assuming a SM Higgs boson at that mass (dashed line) with its 1σ systematic uncertainty band.

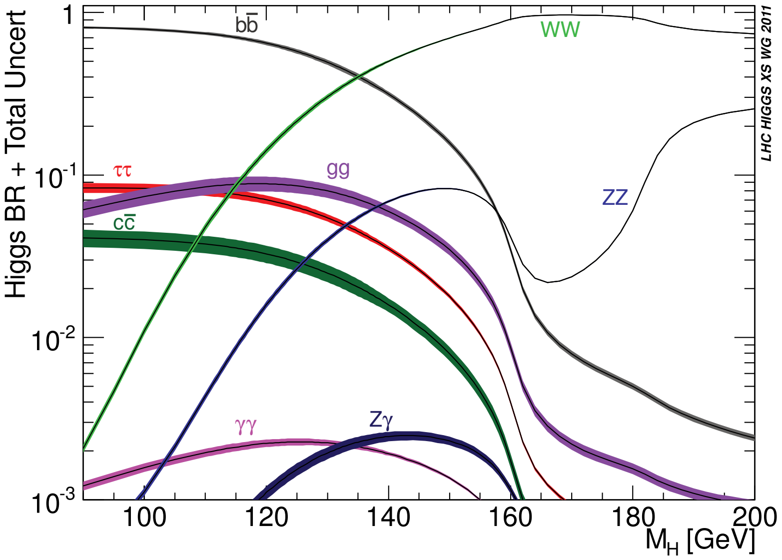

Figure 1.5: Expected branching ratios for different Higgs boson mass assumptions (from [28]). The measured branching ratios of the newly discovered boson are compatible with the expectation for a mass of 125 GeV.

interactions. There are several questions that it does not address. From an experimental viewpoint, possibly the most important missing piece is a *dark matter* candidate, a type of particle without electromagnetic interactions and sufficiently massive or abundant to explain the observed discrepancies between the visible masses of galaxies, their rotational speed in clusters, and their gravitational interaction [29]. It does not explain the observed predominance of matter over antimatter in the universe (*baryogenesis*), as in the SM the two are created and annihilated in identical amounts, and it does not describe neutrino flavour oscillations since it assumes neutrinos to be massless[5]. The SM does not offer an explanation for the particular values of its 18 fundamental parameters: the masses of 3 charged leptons, 6 quarks and 1 Higgs boson, 3 coupling strength parameters of electromagnetic, weak, and strong force, 4 physical parameters of the CKM matrix, and the Higgs field vacuum expectation value [30]. The existence of precisely three generations is not predicted by the SM; it is however the minimum number of generations to allow a physical CP-violating phase in the CKM matrix.

Hierarchy problem

The masses of the known elementary particles span several orders of magnitude, but quantum field theories can be used at much higher energies, as long as one is not near the Planck scale $m_{\mathrm{P}} = \sqrt{G_N/\hbar c} \sim 10^{19}$ GeV, where the gravitational interaction can no longer be neglected. Since the mass range still unexplored by collider experiments spans about 16 orders of magnitude, it seems unlikely that there are no massive elementary particles left to be discovered[6].

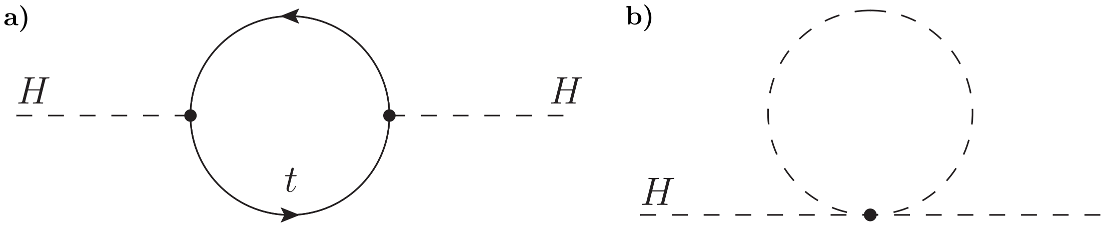

Figure 1.6: In the SM, fermions receive their masses through Yukawa interactions with the Higgs field, with a coupling strength proportional to the fermion's mass. Both diagrams shown here are quadratically divergent and need to be regularised. **a)** Through fermion loop diagrams, the fermion masses also contribute to the Higgs boson mass. **b)** Higgs field self-coupling due to ϕ^4 term in the SM Lagrangian.

---

[5] This is not a principal problem: one can include neutrino oscillations without explicitly introducing mass terms into the SM Lagrangian. Neutrinos interact as flavour eigenstates and propagate as mass eigenstates, the mixing is described by the 3×3 MNS matrix.

[6] A large stretch on the mass scale without any new particle is sometimes referred to as a "desert".

An indication for the scale at which the SM becomes inconsistent results from the problem of quadratic divergences. For each SM fermion, one can draw a loop diagram like the one in figure 1.6 (left), shifting the bare Higgs boson mass up by (see for example ref. [31]):

$$\Delta\left(m_H^2\right) = -\frac{|\lambda_f|^2}{8\pi^2}\Lambda^2, \tag{1.14}$$

where λ_f is the Yukawa coupling and Λ is a loop momentum ultra-violet cut-off. From the SM fermions, the largest Yukawa coupling occurs for the top quark, with $\lambda_t \approx 1$. Then, to find a physical Higgs boson mass near 125 GeV, Λ should be $\sim$1 TeV to avoid an unnaturally large value of Δm_H^2. This points to the existence of non-SM particles with masses on the TeV scale. If we assume additional fermions, with Yukawa couplings > 1, the problem obviously gets worse, and it persists even if there is no Yukawa interaction term directly relating the new fermions and the Higgs field, since such contributions will still arise from higher order loop diagrams (see e.g. ref. [32]). Even without any Yukawa couplings at all, the Higgs self-coupling (figure 1.6, right) leads to similar quadratic divergences in the Higgs boson mass. Additional spin-0 particles would also contribute to the physical Higgs boson mass, but with a relative minus sign to their contribution, so that a cancellation is in principle possible. Taking $\Lambda \to m_\mathrm{P}$, it is easy to see that an implausible amount of fine-tuning of such contributions is necessary to keep the Higgs boson mass at its observed value.

Besides upper limits derived from consistency arguments (partial wave unitary in WW-scattering and Higgs self-coupling triviality bounds) indicating the Higgs boson mass should be $\lesssim$800 GeV, the SM doesn't have an explanation for the electroweak scale and the Higgs mass to be 17 orders of magnitude below the Planck scale (nor a mechanism to stabilise the small mass scales). This is known as (the technical aspect of) the gauge hierarchy problem or *naturalness* problem[7].

Gauge coupling evolution

The history of particle physics shows several examples in which finding a common description for apparently distinct phenomena resulted in an improved, more predictive theory: Newton's discovery of a unified law of gravity describing terrestrial and celestial motion, Maxwell's unification of the electric and magnetic forces in his famous equations, and the electroweak unification based on work by Glashow, Weinberg and Salam. One famous unsuccessful attempt was Einstein's idea to unify the two well understood forces of his era, electromagnetism and gravity.

---

[7] "A system is natural if its observable properties are stable against small variations of the fundamental parameters." [33]

Grand unified theories (GUTs) aim to unify the electroweak and the strong force in the sense that the resulting unified force describes both coloured and uncoloured particles. To this end, one embeds quarks and leptons in a common representation of a new gauge group, for example SU(5), that contains $SU(3)$ and $SU(2) \times SU(1)$ as subgroups. Immediate consequences are the non-conservation of baryon and lepton numbers, and the possibility of proton decay, opening possibilities for experimental study.

Although there is no generally agreed-upon GUT at this time, the underlying idea is supported by the experimental fact that the running of the strong, weak, and electromagnetic coupling "constants", extrapolated to higher energies, lead to almost identical coupling strengths at high interaction energies, as shown in figure 1.7. However, the SM renormalisation group equations (RGEs) result in a near-miss, and modifications to the RGEs used in the extrapolation are necessary to make the unification exact.

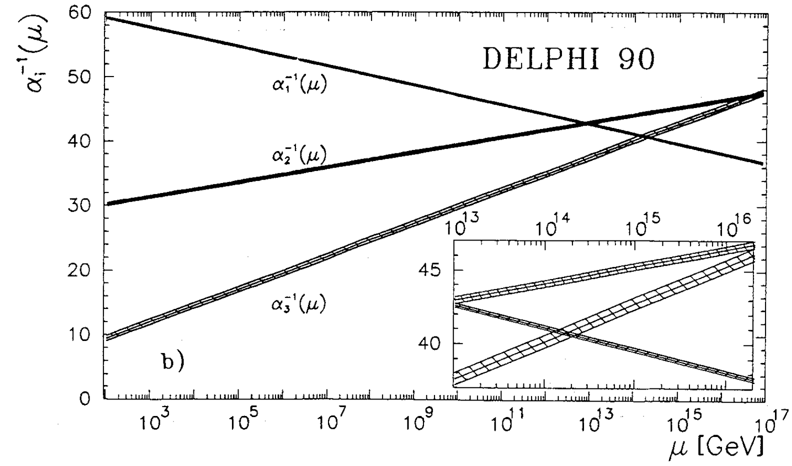

Figure 1.7: Extrapolating the coupling constants of the electroweak and strong interactions ($\alpha_1 = \frac{5}{3}\alpha_{\mathrm{em}}/\cos^2\theta_{\mathrm{W}}$, $\alpha_2 = \alpha_{\mathrm{em}}/\sin^2\theta_{\mathrm{W}}$, and $\alpha_3 = \alpha_{\mathrm{S}}$) to higher momentum transfer μ based on the SM renormalisation group equations, they approach each other for $\mu \sim 10^{13}$–10^{17} GeV, but do not meet in a single point (from [34]).

1.4 Beyond the Standard Model

Various models of new physics have been proposed. Some extensions of the SM simply predict one or a small number of additional particles similar to the known ones, such as a heavier copy of the top quark [8], the W boson or the Z boson [35–38], without necessarily embedding them in a larger theoretical framework. Current mass limits are [2]: $m_{t'} > 685$ GeV/c^2, $m_{W'} > 2.63$ TeV/c^2, $m_{Z'} > 2.33$ TeV/c^2. Other extensions foresee neutrino masses, which amounts to including right-chiral neutrinos that are weak isospin singlets into the theory. As their only "interaction" is with left-handed neutrinos, they are sometimes also referred to as sterile neutrinos [39], some recent possible experimental hints of which are reported in refs. [40, 41].

To avoid the quadratic divergences from fundamental scalars, *technicolor* introduces composite scalars instead, fermion-antifermion bound states held together by a new force acting at an energy scale not yet explored by experiments [42]. A variety of new composite pseudo-Goldstone bosons is predicted with masses on the order of tens of GeV, which should have been observed in experiments by now.

Supersymmetry (SUSY) answers many of the open questions: contributions from supersymmetry stabilise the Higgs mass in the presence of new massive fermions, may explain the observed matter-antimatter asymmetry, and add the necessary degrees of freedom to the RGEs to allow an exact gauge coupling unification. Many SUSY models have a dark matter candidate. SUSY will be discussed in more detail in chapter 2.

String theories describe all physics processes in terms of 1-dimensional strings or higher-dimensional manifolds ("branes") in a (typically) 11-dimensional space-time, with the additional spatial dimensions compactified. Particles are identified with different vibrational modes of the manifolds, with one of them corresponding to the spin-2 graviton. By assuming gravitons as closed strings rather than point-like objects, a consistent treatment of quantum mechanics and general relativity becomes possible. For string theory to describe fermions, it needs to be made supersymmetric. The relative weakness of the gravitational interaction can qualitatively be understood if the gravitational interaction spreads into all spatial dimensions (this idea is also pursued in models that do not explicitly rely on string theory, such as the Randall-Sundrum model of the graviton [43]).

String theory predictions that can be experimentally tested are not computationally tractable at this time. Nonetheless, the inclusion of gravity and its unification with the other forces makes string theory a promising framework for an eventual Theory of Everything (ToE).

2 | Supersymmetry

> There is a theory, which states that if ever anyone discovered exactly what the universe is for, and why it is here, it will instantly disappear and be replaced by something even more bizarrely inexplicable.
>
> There is *another* theory, which states that this has already happened.
>
> *Douglas Adams (1952–2001), "Hitchhiker's Guide to the Galaxy"*

In this chapter we illustrate the basic Supersymmetry (SUSY) concepts using the Minimal Supersymmetric Standard Model (MSSM), as an example. The MSSM has more than a hundred free parameters, necessitating further assumptions to allow a systematic experimental study. We also discuss the special role of the top squark (or *stop*).

As in the previous chapter, we only sketch the most important concepts here. Many good fundamental texts about SUSY are available, for example refs. [31–33, 44–46], where the material presented in this chapter is explained in more depth.

2.1 Basic Concepts

2.1.1 SUSY transformations

Supersymmetry relates bosonic and fermionic states. Using Q to denote the generator of SUSY transformations, we can write:

$$Q\,|\text{fermion}\rangle = |\text{boson}\rangle \quad \text{and} \quad Q\,|\text{boson}\rangle = |\text{fermion}\rangle\,. \tag{2.1}$$

The application of Q changes the state's spin by 1/2, which implies that Q itself has a fermionic character. All other quantum numbers remain unchanged. Q commutes with the energy-momentum operator P^μ, and hence with P^2. From this it follows that the corresponding boson and fermion must have identical mass, $m_b = m_f$:

$$P^2 Q \left|b\right\rangle = P^2 \left|f\right\rangle = m_f^2 \left|f\right\rangle \tag{2.2}$$

$$= Q P^2 \left|b\right\rangle = m_b^2 Q \left|b\right\rangle = m_b^2 \left|f\right\rangle . \tag{2.3}$$

As we will see in the following, SUSY also predicts that the couplings of the boson and the fermion are directly related. The practical result is that for each fermion loop contributing to the Higgs boson mass, there is now also a boson loop of equal magnitude but opposite sign (figure 2.1). In this way, unbroken SUSY solves the technical aspect of the hierarchy problem.

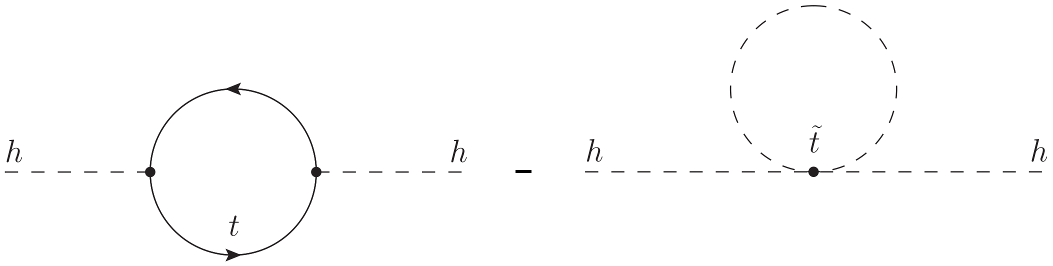

Figure 2.1: In supersymmetric theories, quadratic divergences in scalar masses resulting from loop contributions to the 2-point function are cancelled by the corresponding diagrams involving the newly introduced partner particles, marked with a $\sim$ symbol.

Boson-fermion pairs of identical mass are not observed in experiments, and SUSY must be a broken symmetry. The cancellation of diagrams then is not complete any longer; the divergent term is proportional to the difference of the squared masses of the boson and the fermion.

2.1.2 Wess-Zumino model

Wess and Zumino [47] were the first to construct a specific example of a Lagrangian with a symmetry transformation that transforms bosons and fermions into another. The model contains two real scalar fields A, B and one 4-component Majorana spinor ψ (following the notation of [32]). A Majorana spinor describes a particle that is its own charge conjugate $\psi = \mathcal{C}\bar{\psi}^T$, leaving only two independent components. As we will see, it proves useful to include two more real scalar fields F and G. The non-interacting Wess-Zumino

Lagrangian is then

$$\begin{aligned} \mathcal{L}_{WZ} &= \mathcal{L}_{\text{kin}} + \mathcal{L}_{\text{mass}}, \quad \text{where} && (2.4) \\ \mathcal{L}_{\text{kin}} &= \frac{1}{2}(\partial_\mu A)^2 + \frac{1}{2}(\partial_\mu B)^2 + \frac{i}{2}\bar{\psi}\not{\partial}\,\psi + \frac{1}{2}(F^2 + G^2) \quad \text{and} && (2.5) \\ \mathcal{L}_{\text{mass}} &= -\,m\left[\frac{1}{2}\bar{\psi}\psi - GA - FB\right]. && (2.6) \end{aligned}$$

Note in particular the absence of kinetic terms for F and G, meaning they do not propagate. Such fields are referred to as auxiliary fields. From their Euler-Lagrange equations one finds (substituting $\phi = F, G$):

$$\frac{\partial \mathcal{L}}{\partial \phi} = \partial_\mu \frac{\partial \mathcal{L}}{\partial(\partial_\mu \phi)} \Rightarrow F = -mB \quad \text{and} \quad G = -mA. \tag{2.7}$$

This allows to eliminate the auxiliary fields from the Lagrangian to describe the case where the equations of motions are fulfilled exactly[1]. To describe virtual particles (internal lines in Feynman diagrams), the auxiliary fields are needed. There is another advantage to them: one can express SUSY transformations through linear changes of the fields. The infinitesimal Wess-Zumino transformations are given by:

$$\begin{aligned} &A \to A + i\bar{\alpha}\gamma_5\psi, \\ &B \to B - \alpha\bar{\psi}, \\ &F \to F + i\bar{\alpha}\not{\partial}\,\psi, \\ &G \to G + \alpha\gamma_5\not{\partial}\,\psi, \\ &\psi \to \psi - F\alpha + iG\gamma_5\alpha + \not{\partial}\,\gamma_5 A\alpha + i\not{\partial}\,B\alpha. \end{aligned} \tag{2.8}$$

The transformations are parametrised by α, which is itself an anticommuting Majorana spinor. Applying these transformations to $\mathcal{L}_{\text{WZ}}$ and simplifying, one finds that it changes only by a total derivative, leaving the action invariant as required. This remains true also if one adds to equation (2.6) an interaction term of the form

$$\mathcal{L}_{\text{int}} = -\frac{g}{\sqrt{2}}A\bar{\psi}\psi + \frac{ig}{\sqrt{2}}B\bar{\psi}\gamma_5\psi + \frac{g}{\sqrt{2}}(A^2 - B^2)G + g\sqrt{2}ABF. \tag{2.9}$$

This completes the Wess-Zumino model [47]. The two real scalars, the Majorana spinor, and their interaction are described with just one mass parameter m and one coupling g.

There is a more modern way of expressing $\mathcal{L}_{WZ}$ that is useful to introduce here as it will help to interpret other Lagrangians later. Firstly, it is common to combine the scalars into complex fields: $\phi = (A + iB)/\sqrt{2}$ and $\mathcal{F} = (F + iG)/\sqrt{2}$. In general, there can be several related sets of bosons and fermions (corresponding to internal degrees

---

[1] Called "on-shell" case, because particles are on their mass-shell, where $p^\mu p_\mu = m^2$.

of freedom, for example flavour), so scalars and Dirac spinors receive a corresponding subscript: ϕ_i, ψ_i. We rewrite the kinetic part as [45]

$$\mathcal{L}_{\text{kin}} \;=\; \partial_\mu \phi_i^* \partial^\mu \phi_i + \bar{\psi}_i i \not{\partial}\, \psi_i + F_i^* F_i, \tag{2.10}$$

and introduce the superpotential

$$W = \frac{1}{2} M_{ij} \phi_i \phi_j + \frac{1}{6} y_{ijk} \phi_i \phi_j \phi_k, \tag{2.11}$$

where M will play the role of a mass matrix, and y consists of coupling constants. Both are totally symmetric in their indices. In principle one could also add a term $A_i \phi_i$ in equation (2.11) which yields the most general expression resulting in a renormalisable Lagrangian[2]. The superpotential must be analytic in ϕ_i; in particular, it must not depend on ϕ_i^*. Lastly, we state the prescription to obtain from the superpotential the mass and interaction part of a supersymmetric Lagrangian:

$$\mathcal{L}_{\text{int}} = \frac{\partial W}{\partial \phi_i} F_i - \frac{1}{2} \frac{\partial W}{\partial \phi_i \partial \phi_j}\; \bar{\psi}_i \psi_j + \text{h.c.} \tag{2.12}$$

As before, one can eliminate the auxiliary field with its Euler-Lagrange equations, $F_i = -\partial W^* / \partial \phi_i^* \equiv W_i^*$ and $F_i^* = -\partial W / \partial \phi_i \equiv W_i$, to find the total Wess-Zumino Lagrangian

$$\begin{aligned}
\mathcal{L}_{\text{WZ}} &= \partial_\mu \phi_i^* \partial^\mu \phi_i + \bar{\psi}_i i \not{\partial}\, \psi_i \underbrace{+ F_i^* F_i + W_i F_i + W_i^* F_i^*}_{= -|F_i|^2 = -|W_i|^2} - \left(\frac{1}{2} \frac{\partial W}{\partial \phi_i \partial \phi_j} \bar{\psi}_i \psi_j + \text{h.c.} \right) \\
&= \partial_\mu \phi_i^* \partial^\mu \phi_i + \bar{\psi}_i i \not{\partial}\, \psi_i \\
&\quad + \left| M^2 \right|_{ij} \phi_i^* \phi_j + \frac{1}{2} \left(M_{i\ell}^* y_{ijk} \phi_i \phi_j \phi_k^* + \frac{1}{2} y_{ijk}^* y_{i\ell m} \phi_j^* \phi_k^* \phi_\ell \phi_m + \text{h.c.} \right) \\
&\quad + \frac{1}{2} \left(M_{ij} \bar{\psi}_i \psi_j + y_{ijk} \bar{\psi}_i \psi_j \phi_k + \text{h.c.} \right) .
\end{aligned} \tag{2.13}$$

One can clearly identify kinetic parts of the scalar and fermion fields, a scalar mass term, cubic and quartic scalar interactions, a fermion mass term and a Yukawa term connecting scalar and fermion fields. The mass and coupling parameters are identical for all fields within each of the sets i.

There is one important theoretical concept we cannot properly present within the scope of this introductory chapter: it is common to combine the component fields of a set into one superfield that is a function of superspace, $\Phi(\underline{x}, \theta, \bar{\theta})$. Besides a more concise

---

[2] The Lagrangian itself has mass dimension four, $[\mathcal{L}] = 4$, which one can confirm for equation (2.10) knowing that $[\phi] = [\partial] = 1$, $[\psi] = 3/2$ and $[F] = 2$. Combinations of fields that do not have mass dimension four are imbued with a coupling constant. A coupling constant with a negative mass dimension results in a non-renormalisable theory.

notation, this allows to more easily identify rules for constructing general Lagrangians, and to express the SUSY operators as differential operators. In particular, the superpotential (2.11) can be directly generalised to contain superfields instead of component fields, resulting in a wealth of new interaction terms when writing Lagrangians as above. An introduction to superfields is given for example in chapter 6 of ref. [45].

2.1.3 SUSY algebra

The set of transformations (2.8) demonstrates that it is possible to connect bosons and fermions in the way foreseen in (2.1). However, there is no explicit mention of the SUSY generator, which is needed to systematically study Lagrangians that are invariant under SUSY transformations. The spin of a state affects its behaviour under spacetime transformations; in order to change the spin, SUSY transformations need to act on spacetime. This means SUSY needs to add another layer of structure onto the Poincaré group describing rotations, boosts, and translations in spacetime. It has been shown [48] that this is not possible with a Lie algebra, instead an algebra based on anticommutators is needed [49]. One can derive:

$$[Q_a, Q_b^\dagger]_+ = 2\,(\sigma^\mu)_{ab}\,P_\mu. \tag{2.14}$$

The SUSY generator Q is itself a 2-component spinor ($a = 1, 2$). The presence of P^μ in (2.14) makes explicit that SUSY is indeed a spacetime symmetry. While it is mathematically possible to have more than one SUSY generator, $N > 1$ SUSY algebras have both left- and right-chiral states in their supermultiplets, which is difficult to reconcile with the fact that the electroweak interaction only acts on left-handed isospin doublets.

The Hamilton operator can directly be expressed through the SUSY generator:

$$H = P^0 = \frac{1}{4}\left(Q_1 Q_1^\dagger + Q_1^\dagger Q_1 + Q_2 Q_2^\dagger + Q_2^\dagger Q_2\right) = \frac{1}{4}\left(QQ^\dagger + Q^\dagger Q\right), \tag{2.15}$$

with an implicit sum over the spinor components in the last expression. For a complete set of states $|i\rangle$ with the same 4-momentum eigenvalue p^μ, and using the fact that $(-1)^{2S}$ anticommutes with a fermionic operator, one finds that

$$\begin{aligned} 0 &= \sum_i \langle i|\,(-1)^{2S} Q Q^\dagger\,|i\rangle - \sum_{i,j} \langle j|\,(-1)^{2S} Q\,|i\rangle\,\langle i|\,Q^\dagger\,|j\rangle && (2.16)\\ &= \sum_i \langle i|\,(-1)^{2S} [Q, Q^\dagger]_+\,|i\rangle && (2.17)\\ &\propto p^0 \sum_i \langle i|\,(-1)^{2S}\,|i\rangle && (2.18)\\ &= p^0\,(n_b - n_f)\,, && (2.19)\end{aligned}$$

meaning that the corresponding numbers of bosonic and fermionic degrees of freedom must be identical, $n_b = n_f$.

For the SUSY vacuum $|\Omega\rangle$, one may have $\langle\Omega| H |\Omega\rangle = 0$, in which case the conclusion does not hold. One can show that $\langle\Omega| H |\Omega\rangle > 0$ is equivalent to a spontaneously broken supersymmetry (e.g. ref. [50], chapter 2.3).

2.1.4 Supermultiplets

One can group the particles related by SUSY transformations into supermultiplets, with Q and $Q^\dagger$ acting as ladder operators of the spin. Besides spin, all particles within a supermultiplet have identical masses and quantum numbers. One can differentiate several types of massless supermultiplets based on the largest occurring spin:

- **Chiral supermultiplet:** two real scalars + spin 1/2 fermion,
- **Vector supermultiplet:** spin 1/2 gaugino + spin 1 gauge boson,
- **Supergravity multiplet:** spin 3/2 Majorana gravitino + spin 2 graviton.

In each supermultiplet, we have $n_b = n_f = 2$ on-shell degrees of freedom, not counting the auxiliary fields. The Wess-Zumino model is an example describing chiral supermultiplets, with each supermultiplet containing the set of fields with a common index i. However, instead of assuming a Majorana fermion, it is more practical here and in the other multiplets to use left-chiral Weyl fermions to also allow charged particles. The Lagrangian of vector supermultiplets –also called gauge multiplets, since in the SM the only vector bosons are gauge bosons– is introduced below. Since the graviton is not included in the SM, the simplest supersymmetric extensions do not require supergravity multiplets.

For spontaneously broken SUSY, one can show the **supertrace mass sum rule**, holding separately for each supermultiplet [51]:

$$\sum_{J,\text{bosons}} (2J+1)m_J^2 = \sum_{J,\text{fermions}} (2J+1)m_J^2. \tag{2.20}$$

For the chiral supermultiplet containing the electron, for example, this predicts that one of the two scalar bosons is lighter than the electron while carrying electric charge! To reconcile this with observation, one needs to break SUSY explicitly, by adding scalar mass terms.

Gauge supermultiplets

The Lagrangian density of a gauge supermultiplet is

$$\mathcal{L}_\text{gauge} = -\frac{1}{4}F^a_{\mu\nu}F^{\mu\nu a} + \frac{i}{2}\bar{\lambda}^a\gamma^\mu D_\mu\lambda^a + \frac{1}{2}D^aD^a. \tag{2.21}$$

Here, λ^a are Majorana spinors describing the gaugino fields, one for each generator of the gauge symmetry we want to model ($a = 1\dots 8$ for $SU(3)_C$, or $1\dots 3$ for $SU(2)_L$, or just one for $U(1)_Y$), and $F^{\mu\nu a}$ is the field strength tensor

$$F^a_{\mu\nu} = \partial_\mu A^a_\nu - \partial_\nu A^a_\mu + g f^{abc} A^b_\mu A^c_\nu, \tag{2.22}$$

where f^{abc} are the structure constants of the symmetry group (vanishing for the Abelian $U(1)$). $A^{\mu a}$ are the massless gauge fields, and lastly D^a is a real scalar auxiliary field, required to have four bosonic and four fermionic degrees of freedom off-shell. The covariant derivative D_μ acts on the gaugino field as

$$D_\mu \lambda^a = \partial_\mu \lambda^a + g f^{abc} A^b_\mu \lambda^c. \tag{2.23}$$

The Lagrangian is invariant under the following SUSY transformation (see for example [50], section 3.2.1) parametrised by an infinitesimal spinor ϵ:

$$\begin{aligned}
A^a_\mu &\to A^a_\mu + \bar{\epsilon}^a \gamma_\mu \gamma_5 \lambda^a, \\
\lambda^a_r &\to \lambda^a - D^a \epsilon_r + \frac{1}{8}\left([\gamma^\mu, \gamma^\nu]\gamma_5 \epsilon\right)_r \ F_{\mu\nu}, \\
D^a &\to D^a - i\bar{\epsilon}\gamma^\mu \gamma_5 \partial_\mu \lambda.
\end{aligned} \tag{2.24}$$

2.1.5 Combined SUSY Lagrangian

Since the SM has vector bosons and a scalar Higgs boson, we require chiral and vector supermultiplets to describe it. To combine the Lagrangians (2.13) and (2.21), we need to introduce the covariant derivative D^μ also for the chiral supermultiplet, consider possible new interaction terms between the chiral and vector fields, and extend the SUSY transformations (2.8) and (2.24). We only present the resulting Lagrangian here:

$$\begin{aligned}
\mathcal{L}_{SUSY} = &\underbrace{-\frac{1}{4} F^a_{\mu\nu} F^{\mu\nu a} + \frac{i}{2}\bar{\lambda}^a \gamma^\mu D_\mu \lambda^a + \frac{1}{2} D^a D^a}_{\mathcal{L}_{\text{Gauge}}} \\
&+ \underbrace{D_\mu \phi^*_i D^\mu \phi_i + \bar{\psi}_i i \not{D} \psi_i + F^*_i F_i + \left(\frac{\partial W}{\partial \phi_i} F_i - \frac{1}{2}\frac{\partial W}{\partial \phi_i \partial \phi_j} \bar{\psi}_i \psi_j + \text{h.c.}\right)}_{\mathcal{L}_{\text{Chiral}}} \\
&\underbrace{-\sqrt{2} g \left[(\phi^*_i (t^a \psi)_i) \cdot \lambda^a + \text{h.c.}\right]}_{\text{scalar}-\text{fermion}-\text{gaugino}} - g(\phi^* (t^a \phi)_i) D^a,
\end{aligned} \tag{2.25}$$

where the covariant derivative acts on the component fields of the chiral supermultiplet as

$$\partial_\mu \phi_i \to D_\mu \phi_i = \partial_\mu \phi_i + i g A^a_\mu \left(t^a \phi\right)_i, \tag{2.26}$$

$$\partial_\mu \psi_i \to D_\mu \psi_i = \partial_\mu \psi_i + i g A^a_\mu \left(t^a \psi\right)_i. \tag{2.27}$$

The t^a are the hermitian matrices representing the generators of the relevant gauge group (proportional to the Pauli matrices for $SU(2)$, or the Gell-Mann matrices for $SU(3)$). If a matter field has more than one gauge interaction, its covariant derivative contains several gauge coupling terms. As before, the index i runs over all internal degrees of freedom, and all fields of a given i are exposed to the same couplings in their covariant derivatives. For the on-shell case, the equations of motion yield $F_i = -W_i^*$ as before, and $D^a = g(\phi^*(t^a\phi)_i)$, resulting in another scalar self-coupling term ($\propto\phi^4$). This is usually absorbed into the definition of the scalar potential, which groups several terms from (2.25) that only depend on the scalar fields:

$$V(\phi, \phi^*) = -\left(F_i^* F_i + (W_i F_i + \text{h.c.}) + \frac{1}{2} D^a D^a - g(\phi_i^*(t^a\phi)_i)D^a\right) \tag{2.28}$$

$$= F_i^* F_i + \frac{1}{2} g^2 (\phi_i^* T \phi_i)^2. \tag{2.29}$$

Equation (2.25) is an exactly supersymmetric Lagrangian containing supermultiplets of fields with spin 0 and spin 1/2, or spin 1/2 and spin 1, with identical masses and couplings within each supermultiplet.

2.1.6 *R*-parity

It is possible to introduce another $U(1)$ symmetry, denoted by R, that commutes with the generators of the Poincaré group (P^μ, $M^{\mu\nu}$), but not with the SUSY generators by making R act on the superspace coordinates: $\theta \to e^{i\varphi}\theta$, $\bar{\theta} \to e^{-i\varphi}\bar{\theta}$. Consequently, also the SUSY generators, the superfields and their component fields receive phase factors of the form $e^{i\varphi R}$, where R is the conserved charge of the R-symmetry. It turns out that this approach is problematic, as quantum anomalies occur that violate charge conservation [52].

It is possible to retain the $\mathbb{Z}_2$ subgroup of the R-symmetry by fixing $\varphi = \pi$. The value of $e^{i\pi R} = (-1)^R = \pm 1$ of each component field is called its R-parity R_p. It can be assigned consistently such that SM particles have $R_p = +1$, while $R_p = -1$ for their supersymmetric partners. While the R-charges defined above are additive in nature, R-parity is a multiplicative property: R_p of a many-particle state is found by multiplying R_p of the individual fields.

Two important consequences arise if one assumes R-parity conservation. Firstly, SUSY particles are produced in pairs, so that the system's R_p is not changed. Secondly, the lightest SUSY particle (LSP) cannot decay, as this would violate R_p conservation or energy conservation. This means an R-parity conserving SUSY model automatically has a dark matter candidate.

2.2 Minimal Supersymmetric Standard Model

We now assign all SM particles into supermultiplets, adding the minimum number of SUSY particles (or *sparticles*) to obtain the minimal supersymmetric extension of the Standard Model, the MSSM. All of the supermultiplets contain at least one sparticle – there is no boson-fermion pairing that would allow to assign two SM particles into the same supermultiplet based on their quantum numbers. For example, neutrinos and the Higgs boson are electrically neutral and uncoloured, differ in spin by 1/2 as required, and are components of a weak isodoublet. But only the neutrino carries lepton number, hence they cannot be superpartners.

The SM fermions and their superpartners (*sfermions*, or $\tilde{f}$) are assigned to chiral supermultiplets, as assigning them to gauge multiplets would result in new gauge interactions. The sfermion names are also prefixed with the letter "s": for each charged SM lepton, there are scalar SUSY sleptons (selectron $\tilde{e}$, smuon $\tilde{\mu}$, stau $\tilde{\tau}$), the partners of the neutrinos are the sneutrinos ($\tilde{\nu}$), and for each quark, there are scalar squarks (e.g. scharm $\tilde{c}$, sbottom $\tilde{b}$, stop $\tilde{t}$). Since these are part of chiral supermultiplets, each sfermion field has two real degrees of freedom.

The SM partners of the gauge bosons are the gluinos $\tilde{g}$, the winos and the bino, collectively called gauginos. For technical reasons[3], another Higgs doublet needs to be introduced in SUSY theories:

$$H_1 = \begin{pmatrix} H_1^0 \\ H_1^- \end{pmatrix} \quad \text{and} \quad H_2 = \begin{pmatrix} H_2^+ \\ H_2^0 \end{pmatrix}. \tag{2.30}$$

Because each doublet has two complex degrees of freedom, and only three real degrees of freedom are required to give masses to the electroweak gauge bosons, five physical Higgs particles remain. In addition to the SM Higgs boson h^0, one now expects a heavy scalar H^0 and a pseudoscalar Higgs boson A^0, as well as two charged Higgs bosons $H^\pm$, with five corresponding higgsinos as their partners.

Wino, bino and higgsinos are colourless spin 1/2 particles with charges between -1 and +1. As in electroweak symmetry breaking, gauge bosons with the same quantum numbers can mix (due to the Higgs-higgsino-gaugino term in (2.25)), yielding two charginos $\chi^\pm_{1,2}$ and four neutralinos $\chi^0_{1,2,3,4}$. Their actual mixing matrices depend on the way in which the SUSY breaking is realised.

Table 2.1 summarises the MSSM particle content and introduces the names of the containing superfields. With those, we can adapt the superpotential from eq. (2.11) to

---

[3] For example, the sum of the third components of the higgsino hypercharges has to vanish, $Y^3_{\tilde{H}_1^0} + Y^3_{\tilde{H}_2^0} = 0$, to avoid anomalies [53].

Left chiral matter superfields			representation
Lepton doublets			
$L_1 = \begin{pmatrix} L_{\nu_e} \\ L_e \end{pmatrix}$	$L_2 = \begin{pmatrix} L_{\nu_\mu} \\ L_\mu \end{pmatrix}$	$L_3 = \begin{pmatrix} L_{\nu_\tau} \\ L_\tau \end{pmatrix}$	$\left(1, +\frac{1}{2}, -1\right)$ $\left(1, -\frac{1}{2}, -\frac{1}{2}\right)$
Antilepton singlets			
$\bar{E}_e$	$\bar{E}_\mu$	$\bar{E}_\tau$	$(1, 0, 2)$
Quark doublets			
$Q_1 = \begin{pmatrix} Q_u \\ Q_d \end{pmatrix}$	$Q_2 = \begin{pmatrix} Q_c \\ Q_s \end{pmatrix}$	$Q_3 = \begin{pmatrix} Q_t \\ Q_b \end{pmatrix}$	$\left(3, \frac{1}{2}, \frac{1}{3}\right)$
Antiquark singlets			
$\bar{U}_1$	$\bar{U}_2$	$\bar{U}_3$	$\left(\bar{3}, 0, -\frac{4}{3}\right)$
$\bar{D}_1$	$\bar{D}_2$	$\bar{D}_3$	$\left(\bar{3}, 0, \frac{2}{3}\right)$
Higgs and gauge superfields			
$H_1 = \begin{pmatrix} H_1^0 \\ H_1^- \end{pmatrix}$	$(Y = -1)$	$H_2 = \begin{pmatrix} H_2^+ \\ H_2^0 \end{pmatrix}$	$(Y = +1)$
V^Y (hypercharge)	$\vec{V}^W$ (weak isospin)	V_g^a (colour)	

Table 2.1: The MSSM particle content (adapted from [33]). Each superfield contains all particles of its supermultiplet, e.g. L_e comprises electron and selectron component fields. The numbers in parentheses indicate the corresponding $SU(3)_C \times SU(2)_L \times SU(1)_Y$ gauge group representations. Only left-chiral superfields may appear in the superpotential. For this reason, the right-chiral singlets are represented through the left-chiral superfields of their antiparticles.

the MSSM case:

$$\mathcal{W}_{\text{MSSM}} = y_{u,ij}\bar{U}_i Q_j \cdot H_2 + y_{d,ij}\bar{D}_i Q_j \cdot H_1 + y_{e,ij}\bar{E}_i L_j \cdot H_1 + \mu H_1 \cdot H_2 \tag{2.31}$$

The 3×3 Yukawa matrices y_u, y_d, y_e give rise to the masses and CKM mixing of the SM up-type quarks, down-type quarks, and charged leptons, respectively, and also determine related SUSY couplings (for example squark-quark-higgsino). Internal degrees of freedom are summed implicitly. Only bilinear and trilinear terms of left-chiral superfields are allowed in the superpotential. This excludes Higgs mass terms $H_1^* H_1$ or $H_2^* H_2$ (as the conjugates transform as right-chiral fields), and is another reason for the second Higgs doublet. The same requirement dictates the form of the trilinear Yukawa terms, always combining a fermion doublet with an antifermion singlet and the Higgs doublet which results in a hypercharge $Y = 0$. Several other terms, trilinear in the superfields, are possible in principle but violate R-parity [46]:

$$\varepsilon_{ijk}\bar{U}_i\bar{D}_j\bar{D}_k, \quad \bar{D}L \cdot Q, \quad \bar{E}LL, \quad LH_1, \tag{2.32}$$

where family indices have been suppressed for readability (any mixing is possible), and i, j, k are colour indices required to make the first expression a colour singlet. Each term changes either baryon number or lepton number, and needs to be suppressed with a sufficiently small coefficient even in R-parity violating models [54].

The MSSM assumes R-parity conservation as introduced above. For the MSSM, the prescription of $R_p = +1$ for particles and $R_p = -1$ for sparticles is equivalent to defining

$$R_p = (-1)^{3(B-L)+2S}, \tag{2.33}$$

where B, L, and S denote baryon number, lepton number, and spin, respectively.

The additional particle content of the MSSM leads to different coefficients in the RGEs (figure 2.2). Above the SUSY scale of about 1 TeV, the $U(1)_Y$ coupling is running faster, the $SU(3)_C$ coupling slower, and the $SU(2)_L$ running has changed sign [34], resulting in the unification of couplings at a scale of $\sim 10^{16}$ GeV.

2.3 SUSY breaking mechanisms

As discussed above, if SUSY is broken spontaneously, unacceptably light sparticles appear in the theory, which are experimentally ruled out. In the MSSM, an explicit, soft breaking is used instead (see [33], section 9.1). "Explicit" here refers to the addition of new terms to the Lagrangian density, and "soft" means that the new terms leave the cancellation of quadratic divergences to all orders of perturbation theory intact. $\mathcal{L}_{\text{soft}}$ includes explicit mass terms for all sparticles (sfermions, gauginos, and higgsinos), an independent set of Yukawa matrices (A_u, A_d, A_e) similar to y_u, y_d and y_e introduced in equation (2.31),

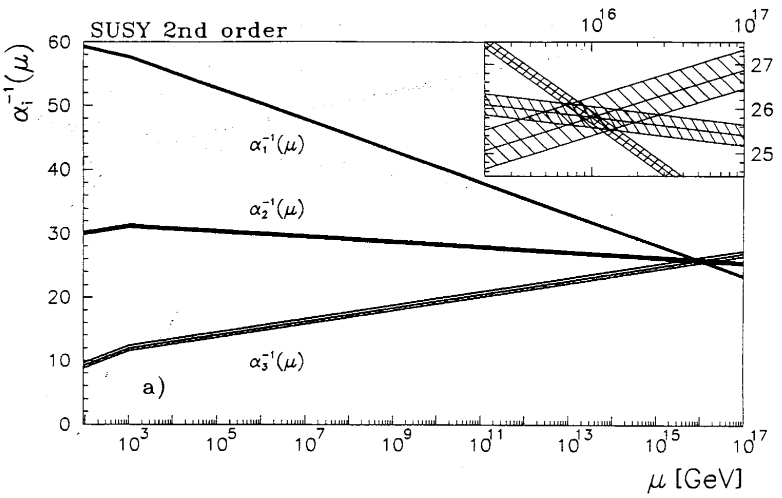

Figure 2.2: The additional particles in the MSSM affect the gauge coupling evolution. Using a χ^2-fit for a single unification point, the scale at which SUSY particles become relevant and the slopes change was determined to be around 1 TeV, resulting in a GUT scale of about $\sim 10^{16}$ GeV (from [34]).

but affecting sfermions only, as well as a contribution to the Higgs mass term, $bH_1 \cdot H_2$. The MSSM introduces 105 new physical parameters [55].

A theory with this number of free parameters has limited predictive power, and it is clear that the soft parameters' values eventually need to be derived from a common underlying principle. The problem of additional light particles appearing in the theory can be avoided if the spontaneous symmetry breakdown takes places in a "hidden sector" of particles without SM gauge interactions. The effects of the spontaneous breakdown are then transmitted to the visible sector by messenger particles that are significantly more massive than the MSSM fields.

One can also choose gravity to play the messenger role, in which case the resulting theory is called minimal supergravity (mSUGRA). One introduces universal SUSY breaking parameters: a common tree-level mass and a common Yukawa coupling for the sfermions (m_0 and A_0, respectively), a common gaugino mass $M_{1/2}$ and two constraints for the Higgs fields: the ratio of the their vev's $\tan\beta = \langle H_2^0 \rangle / \langle H_1^0 \rangle$, and the sign of the mixed term coefficient, $\mathrm{sgn}(\mu)$. These masses and couplings are defined at some high mass scale and are evolved down to the weak scale using renormalisation group equations (see [33], chapter 11). Other important approaches of this kind are anomaly mediated SUSY breaking (AMSB) and gauge mediated SUSY breaking (GMSB), discussed in chapters 12 and 13 of the same reference.

Many of the MSSM parameters are already severely restricted by experiments, for example several off-diagonal elements in the slepton and squark mass matrices that can result in CP violation and flavour changing neutral currents (FCNC) beyond experimental limits. We now illustrate this using the flavour changing transition between neutral kaons K^0 and antikaons $\bar{K}^0$, that in the SM occurs through loop contributions from the weak interaction (figure 2.3).

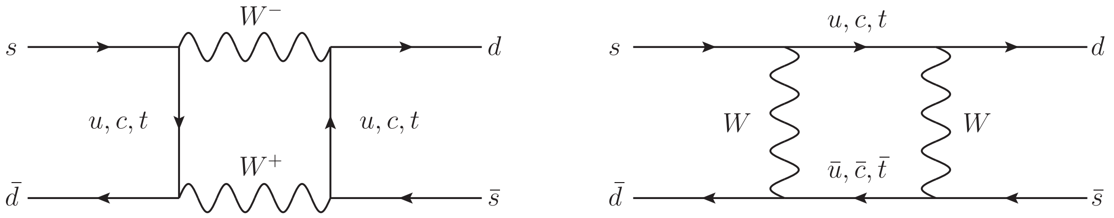

Figure 2.3: SM diagrams contributing to neutral kaon mixing and the K_L-K_S mass difference.

The CP eigenstates are $K_1 = (K_0 + \bar{K}_0)/\sqrt{2}$ and $K_2 = (K_0 - \bar{K}_0)/\sqrt{2}$. These two are distinguished by their decays: K_1 predominantly decays into two pions, while K_2 exclusively decays into three pions. However, K_1 and K_2 are not mass eigenstates, but mix slightly into $K_S \propto K_1 + \epsilon K_2$ and $K_L \propto K_2 + \epsilon K_1$ ($|\epsilon| \approx 2.2 \times 10^{-3}$), which are distinguished by their lifetime. Experimentally one finds that K_S has a short lifetime of $c\tau = 2.7$ cm and K_L has a longer lifetime of $c\tau \approx 15$ m. The diagrams in figure 2.3 contribute to the mass difference $\Delta m_K = m(K_L) - m(K_S)$, measured to be about 3.5 μeV (tiny compared to the kaon mass of 497.6 MeV; all results in this paragraph are taken from [2]).

The MSSM allows several new FCNC loop diagrams contributing to the neutral kaon mixing (figure 2.4), and hence also to Δm_K. The contribution from squark-gluino loops has the form (see section 9.1.1 in [32])

$$\Delta m_{K,\mathrm{MSSM}} = \sum_{\tilde{d}_L, \tilde{s}_L}^{\alpha,\beta=} \left(U\tilde{U}^\dagger\right)_{i\alpha} \left(U\tilde{U}^\dagger\right)^*_{j\alpha} \left(U\tilde{U}^\dagger\right)_{i\beta} \left(U\tilde{U}^\dagger\right)^*_{j\beta} f\left(m_\alpha^2, m_\beta^2\right), \qquad (2.34)$$

where U and $\tilde{U}$ are unitary matrices diagonalising the quark and squark mass-squared matrices, f is some function of the squark mass eigenvalues and i and j label the two flavours of external squarks (s and d in this case, so $i \neq j$). There are several ways in which $\Delta m_{K,\mathrm{MSSM}}$ can vanish or remain small:

- *mass degeneracy:* if all squarks have identical mass, f will be a constant, and (2.34) will be proportional to δ_{ij},
- *alignment:* if the mass matrices of quarks and squarks can be diagonalised by the same unitary transformation, then $U\tilde{U}^\dagger = \mathbb{1}$, again making the off-diagonal term contributing to neutral kaon mixing vanish,

- *decoupling:* if the sparticles in the loop are heavier than 40 TeV, their contributions are sufficiently suppressed.

All of these assumptions lead to a simplified phenomenology and have to be clearly stated for the interpretation of an experimental result. Excluded parameter regions may become significantly smaller when the assumptions are relaxed [56].

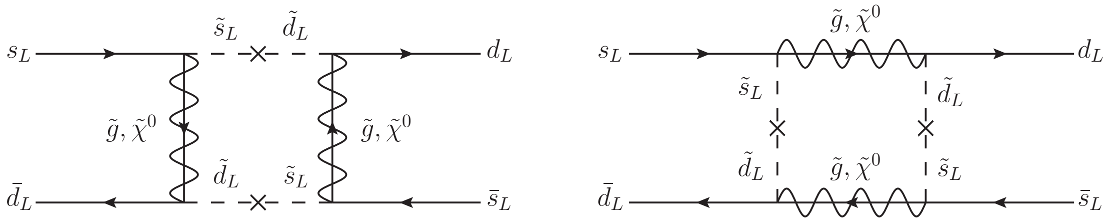

Figure 2.4: Some of the MSSM diagrams contributing to neutral kaon mixing and the K_L-K_S mass difference. Another type of diagram has charginos and up-type squarks running in the loop.

It is possible to remain agnostic about the details of the SUSY breaking mechanism, and use other inputs to reduce the parameter space. *Natural* SUSY models put particular emphasis on naturalness requirements and the constraints derived from those [57, 58]. As an example, the following MSSM relation holds at lowest order in perturbation theory:

$$-m_Z^2/2 = |\mu|^2 + m_{H_2}^2. \tag{2.35}$$

It directly relates a known SM mass to the μ parameter affecting Higgs and higgsino masses and to the soft mass term of the up-type Higgs doublet, $m_{H_2}^2$, which is <0 as required for EWSB. For this relation to be fulfilled, the terms on the right-hand side need to be balanced against each other. If the superpartners are too heavy, this balance requires *fine-tuning* of the SUSY breaking parameters; it becomes more delicate and theoretically less well motivated. This directly affects higgsino masses (controlled by μ) as well as the masses of sparticles with a strong Higgs coupling, most notably top and bottom squarks, but also gluinos through second-order loops.

Naturalness constraints allow to build models with a light Higgs boson mass compatible to the experimentally observed value and in accordance with the experimental sparticle mass limits, without relying too much on particular values for the remaining model parameters. Natural SUSY predicts the top squarks, the left-chiral bottom squark, the higgsinos, and the gluinos to be the lightest sparticles (figure 2.5).

The phenomenological MSSM (pMSSM) [59, 60] assumes CP-conservation and minimal flavour violation [61] and uses a variety of existing theoretical and experimental constraints to reduce the number of independent, real model parameters to 19 (or 22, ref. [59]): 10 sfermion masses (assuming the first and second generation to be mass de-

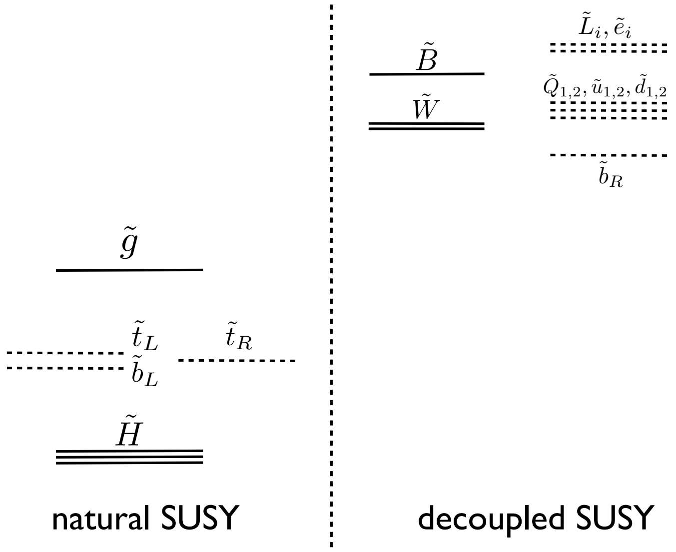

Figure 2.5: Generic mass spectrum of a natural SUSY model (from [58]). Only some of the sparticles are light and may contribute to processes observable at the LHC. The remaining sparticles contribute at a negligible level due to their high masses, they are effectively *decoupled.* The natural sparticles are predicted to have masses of at most a few TeV, while the decoupled particles can be much heavier.

generate and all soft mass matrices to be diagonal), 3 gaugino masses, 3 soft Yukawa couplings only affecting the third generation sfermions[4], the pseudoscalar Higgs mass m_A, as well as μ, and $\tan\beta$. The experimental constraints used in the pMSSM (and elsewhere) are [60]: the thermal relic density, which limits allowed cross-sections for WIMP pair-annihilation; rates of rare flavour changing decays ($b \to s + \gamma$, $B_s \to \mu^+\mu^-$); and the anomalous magnetic moment of the muon $(g-2)_\mu$.

For the analysis presented in this thesis, simplified models with a reduced sparticle content are used: only top squarks, charginos, and neutralinos are included, while all other sparticles are assumed to be decoupled. This means certain decay modes which are possible in principle (for example involving $\tilde{t}_1 \to \tilde{\tau}$ decays) are not studied. The simulated sparticle masses are chosen within the experimentally accessible range, which is similar to the natural SUSY range.

---

[4] This means that the A matrices introduced for soft SUSY breaking only have one non-zero element. One can define $A_t = (A_u)_{33}$, $A_b = (A_d)_{33}$, and $A_\tau = (A_e)_{33}$. Compare this to the mSUGRA case, where all of these are derived from A_0 defined at the high energy scale.

2.4 Top squark properties and mixing

We summarise here from the previous sections the most relevant aspects for the stop ($\tilde{t}$). The stop is of particular interest because of its role in the cancellation of the top-Higgs loop contributions discussed earlier; due to the large top Yukawa coupling, this loop correction (and the cancellation) are particularly important. Further, as we've seen in the discussion of neutral kaon mixing in the MSSM, only the third generation squarks can safely be made light without potentially creating large FCNC contributions. Within the framework of natural SUSY, a stop mass below 700 GeV is preferred to keep fine-tuning small [58]. This limit is based on the arbitrary but common choice $\Delta < 10\%$, where Δ is the relative size of corrections to the Higgs boson mass squared due to higher order diagrams, $(\delta m_h^2)/m_h^2$.

Except for their spin, stops carry the same quantum numbers as top quarks. This means in particular that they have colour charge and carry an electric charge of $\pm 2/3$ ($-2/3$ for antistops, $\tilde{t}_1^*$). This remains true also in broken supersymmetry, while other stop properties such as the mass or the effective Yukawa coupling might change.

To have the same number of degrees of freedom across the chiral supermultiplet, two spin-0 stops are required as partners of the spin-1/2 top, coupling to the left-chiral and right-chiral components of the top quark. Whenever the distinction is relevant, we refer to them as $\tilde{t}_L$ and $\tilde{t}_R$, respectively.

However, the mass eigenstates are mixtures of $\tilde{t}_L$ and $\tilde{t}_R$, labelled $\tilde{t}_1$ and $\tilde{t}_2$, with $\tilde{t}_1$ being the lighter one. Their masses are determined by the top mass (entering via the top Yukawa coupling in the superpotential, eq. (2.31)), by the explicit soft mass terms $M_{Q_3}^2$ and $M_{U_3}^2$, by the Higgs-sfermion cross-terms Δ_f (part of the final term in eq. (2.29)), and by the soft Yukawa-like coupling term, proportional to A_t.

The stop mixing angle and the masses of $\tilde{t}_1$ and $\tilde{t}_2$ are determined by diagonalising the stop mass-squared matrix

$$m_{\tilde{t}}^2 = \begin{pmatrix} m_t^2 + M_{Q_3}^2 + \Delta_{u,L} & m_t X_t \\ m_t X_t & m_t^2 + M_{U_3}^2 + \Delta_{u,R} \end{pmatrix}, \tag{2.36}$$

where[5]

$$X_t = A_t/y_t - \mu/\tan\beta, \tag{2.37}$$

$$\Delta_f = (T^3 - Q\sin^2\theta_W) m_Z^2 \cos 2\beta \tag{2.38}$$

---

[5] It is also common to factor out the SM Yukawa couplings in the definition of the A terms, which results in $X_t = A_t - \mu/\tan\beta$.

$$\Rightarrow \begin{cases} \Delta_{u,L} = \left(\frac{1}{2} - \frac{2}{3}\sin^2\theta_W\right) m_Z^2 \cos 2\beta, & \text{(LH doublet)} \\ \Delta_{u,R} = +\frac{2}{3}\sin^2\theta_W m_Z^2 \cos 2\beta. & \text{(RH singlet)} \end{cases} \tag{2.39}$$

The mixing parameters also have an impact on the stop decay branching ratios. For natural SUSY, only $\tilde{b}_L$ (but not $\tilde{b}_R$) is required to be light, possibly opening the $\tilde{t}_L \to \tilde{b}_L$ decay channel. Thus, when one studies models without this decay, it is more plausible to assume $\tilde{t}_1$ as predominantly $\tilde{t}_R$. In SUSY models that derive weak-scale phenomenology from a unified high energy theory (such as mSUGRA discussed above), one often finds that M_{U_3} is running faster than M_{Q3}, so that $M_{U_3}^2 < M_{Q_3}^2$ at the weak-scale, again making $\tilde{t}_1$ predominantly $\tilde{t}_R$ [46]. For $\tilde{t}_1 \to t + \tilde{\chi}_1^0$ decays with an on-shell top, the polarisation affects the angular distributions of the stop decay products [62] and other kinematic distributions.

2.5 Impact of Higgs boson discovery

At tree-level, the lightest Higgs boson cannot be heavier than the Z boson ($m_h < m_Z \cos 2\beta$); however, this limit can be raised by several tens of GeV when radiative corrections are included [63]. An approximation of this limit as a function of the stop mass is given by [64]:

$$m_h^2 \lesssim m_Z^2 + \frac{3 G_F m_t^4}{\sqrt{2}\pi^2} \ln \frac{m_{\tilde{t}_1} m_{\tilde{t}_2}}{m_t^2}. \tag{2.40}$$

Now that m_h has been measured to be near 125 GeV, this approximation predicts a relatively large average stop mass, $\sqrt{m_{\tilde{t}_1} m_{\tilde{t}_2}} \gtrsim 880$ GeV.

Similarly, ref. [65] states an upper limit of $m_h^{max} \approx 135$ GeV for the case of maximal stop mixing (122 GeV for minimal mixing), assuming sfermion masses on the order of 2 TeV. The observed value of m_h thus suggests a fairly heavy stop with large mixing. These theoretical upper bounds were found long before the Higgs boson discovery, and can thus be seen as indirect evidence for SUSY or other BSM physics, even more so since the SM prefers a heavy Higgs boson (through top loop corrections).

Figure 2.6 shows numerically obtained estimates of m_h^{max} for various models of SUSY breaking; GMSB and AMSB are clearly disfavoured by the observed value. Also many natural SUSY models are being severely challenged, as the observed Higgs mass necessitates a significant amount of electroweak fine-tuning; a possible way out are radiatively generated natural SUSY models [66].

The Higgs production cross-section and branching ratios can be modified by stop loop contributions, possibly increasing $\sigma_{gg\to h} \times \mathrm{BR}(h \to \gamma\gamma)$, which means Higgs coupling

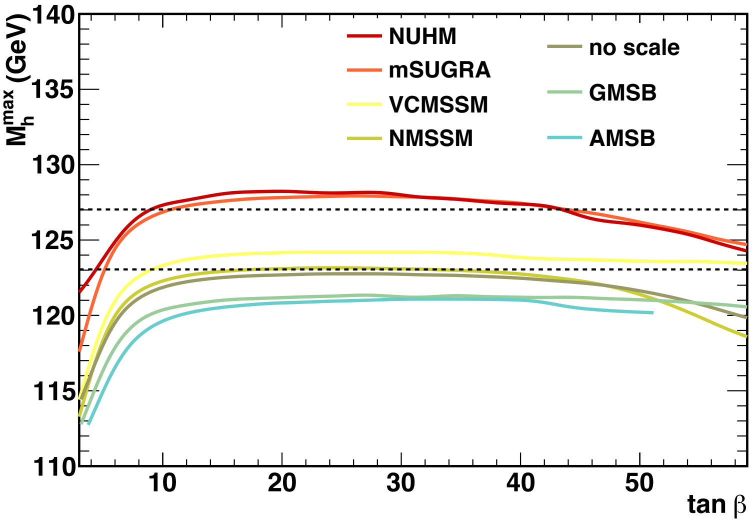

Figure 2.6: Upper limits for the light Higgs boson mass for different SUSY models (from [67]; see there also for the parameter ranges that were scanned). The dashed horizontal lines mark the range 125 ± 2 GeV; meanwhile, the Higgs boson mass has been measured with a 1σ uncertainty of ±0.4 GeV (cf. table 1.1).

measurements may provide indirect limits on light stops [58]. Conversely, it is also possible to constrain invisible Higgs decays from stop search results [68].

2.6 Pre-LHC limits on SUSY

In this section, we state important exclusion results prior to the analysis reported in this thesis, and that helped to define the scope of the analysis. Once the ATLAS stop search using one-lepton final states has been discussed in detail (chapter 5), we will compare our results to other recent searches (section 6.3).

Several direct limits on sparticle masses were obtained by the LEP II experiments. Charginos have been excluded up to masses of around 100 GeV in two combined analyses [69].

The Tevatron experiments CDF and D0 have searched for SUSY in proton-antiproton ($p\bar{p}$) collision events at $\sqrt{s} = 1.96$ TeV [70]. In a stop search assuming a sneutrino LSP or NLSP, light stops have been excluded up to ~230 GeV (see figure 2.7). Another interesting possibility is for the stop to be lighter than a top quark and to undergo the flavour changing decay $\tilde{t}_1 \to c\tilde{\chi}_1^0$. OPAL and D0 have excluded this stop decay mode for $m(\tilde{t}_1) \lesssim 100$ GeV [71–73], this limit was later extended up to $m(\tilde{t}_1) > 180$ GeV by CDF (Run II) [74] using a neural network analysis. The decay mode $\tilde{t}_1 \to b\,W\,\tilde{\chi}_1^0$, which becomes accessible at $m(\tilde{t}_1) > m_W + m_b$ has not been studied by the LEP and Tevatron collaborations. Long-lived stops, moving slowly and not decaying inside the detector have been excluded by CDF up to $m(\tilde{t}_1) = 250$ GeV [75].

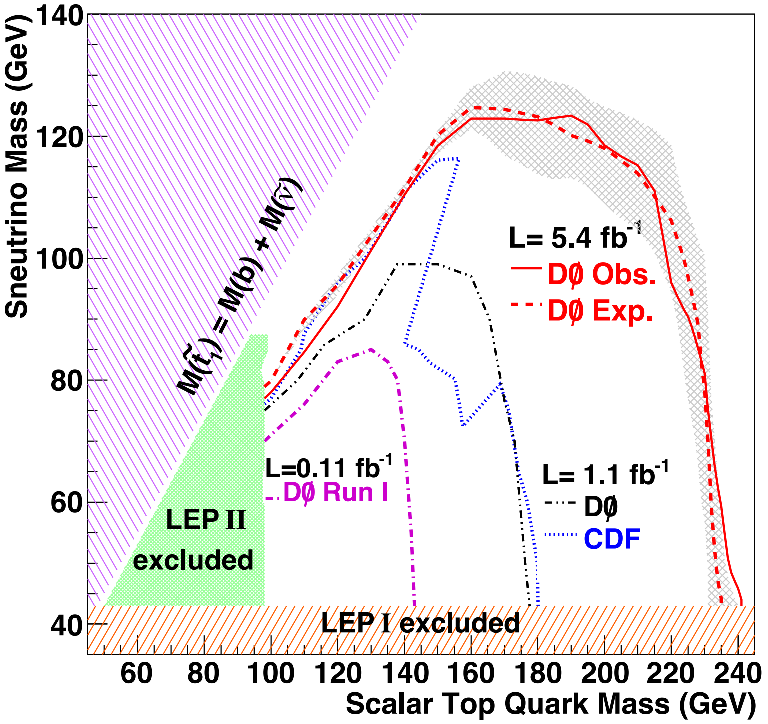

Figure 2.7: Excluded parts of the $m(\tilde{t}_1)$-$m(\tilde{\nu})$ plane obtained in a search using events with an electron and a muon in their final state recorded with the D0 detector (from [76]).

Due to the large SUSY breaking parameter space, all SUSY limits make some assumptions about the breaking mechanism, the relevant sparticles, their masses, and allowed decays. Care has to be taken when comparing results. It is common to recast search results into different interpretations.

3 | The ATLAS Detector

> A detector that ran perfectly at all times would be considered either obsolete or not daring enough in conception.
>
> *Sharon Traweek, "Beamtimes and Lifetimes", p. 49*

3.1 The Large Hadron Collider at CERN

The Large Hadron Collider (LHC) [77] is a two-ring accelerator and collider primarily used for proton-proton (pp) collisions at high centre-of-mass energy, $\sqrt{s}$. It is located in the former LEP tunnel, in and around the European Centre for Nuclear Research (Centre Européene pour la Recherche Nucléaire, CERN) in Geneva, Switzerland, between 45 m and 170 m underground and with a circumference of 26.7 km. Its design luminosity is $\mathcal{L} = 10^{34}$ cm^{-2}s^{-1} at a bunch crossing rate of $f = 40$ MHz and $\sqrt{s} = 14$ TeV. In 2012, the design luminosity was almost reached at $\sqrt{s} = 8$ TeV and at reduced $f = 20$ MHz by allowing a higher number of collisions per bunch crossing than originally foreseen.

The ring consists of eight straight sections and eight arcs. The beams are accelerated using a 400 MHz superconducting cavity system, concentrated in and around the cavern in one of the straight sections (point 4). Coming from CERN's Super Proton Synchroton (SPS), they are inserted into the LHC rings at a proton energy of 450 GeV and accelerated to their collision energy of 4 TeV (in 2012) or 7 TeV (design value, foreseen to be reached in 2016). The beams are kept on their orbit by 1232 superconducting 8 T dipole magnets using the "twin-bore" or "two-in-one" design, which uses a common cold mass and cryostat for both beam channels. A variety of quadrupole, sextupole and octupole magnets are used to focus and correct the beam.

There are four large detectors located along the collider, ATLAS, CMS, LHCb and ALICE. Two of them, ATLAS and CMS, are general purpose, high luminosity experiments, suitable both for discovery and precision physics, as was illustrated by the Higgs discovery (cf. figure 1.4) and measurements of numerous SM properties, including the cross-sections shown in figure 3.1. LHCb is a forward detector designed for B flavour

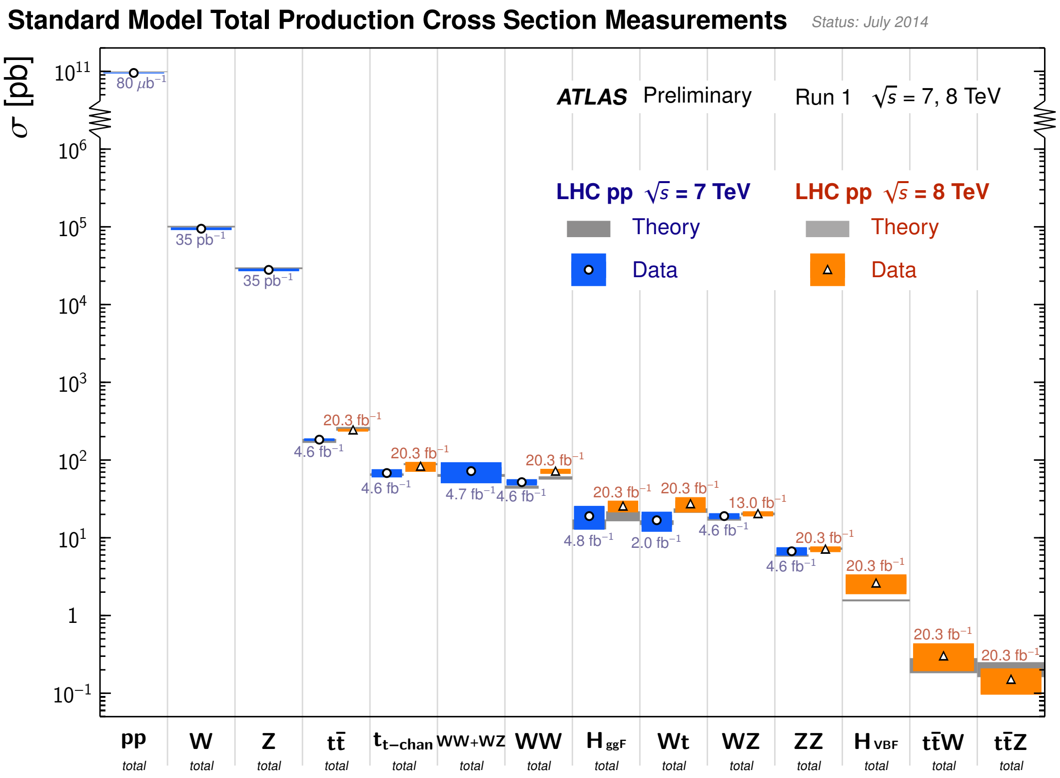

Figure 3.1: This plot summarises the SM cross-section measurements published by the ATLAS collaboration using 7 and 8 TeV pp collisions (from [78]).

physics [79]. Its design enables it to distinguish hadron types much more accurately than the larger LHC experiments, as was demonstrated in measurements of rare decays, including for example the observation of new B_s^0 decay modes [80] and the heavy baryons $\Xi_b^{-\prime}$ and Ξ_b^{-*} [81]. The LHCb detector is one of the low luminosity experiments at the LHC, aimed at only $\mathcal{L} = 10^{32}$ cm^{-2}s^{-1}. The ALICE detector is used for the study of quark-gluon plasma states created in lead-lead collisions [82] at $\mathcal{L} = 10^{29}$ cm^{-2}s^{-1}.

This thesis uses data from pp collisions recorded with the ATLAS detector in 2012, corresponding to an integrated luminosity of 20.3 fb^{-1} at $\sqrt{s} = 8$ TeV (figure 3.2).

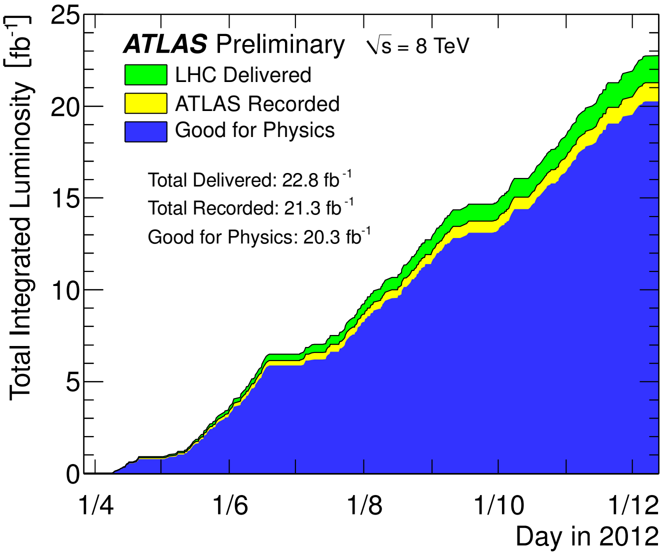

Figure 3.2: Integrated luminosity recorded with the ATLAS detector in 2012 (from [83]). Almost 90% of the $\sqrt{s} = 8$ TeV pp collisions delivered by the LHC were recorded and classified as suitable for physics analysis, based on the conditions of the sub-detectors.

3.2 Detector overview

This section uses ref. [84] as its primary source, describing the as-built detector. Results of recent performance measurements are summarised in section 3.3.

The ATLAS detector is our tool to study the processes described by the SM and to look for hints of SUSY or other BSM physics. Pairs of protons accelerated by the LHC are brought to collision in the centre of the ATLAS detector. The particles created in the collision and their decay products are reconstructed from the signals they create in the various sub-detectors.

The detector comprises a central barrel part and two end-caps, and most sub-detectors also come in barrel and end-cap components (figure 3.3). The design is cylindrically symmetric around the incoming proton beams. Moving outward from the centre of the detector orthogonal to the incoming proton beams, the produced particles first traverse the inner detector (ID), which records hits from charged particles, that can then be used to reconstruct tracks. A solenoid magnet surrounds the ID and bends the charged particles' trajectories, allowing a measurement of their $\vec{p}/m$ (momentum to mass ratio). The solenoid is surrounded by the electromagnetic (EM) and hadronic (HAD) calorimeters, in which the majority of particles will be stopped and the deposited energy is recorded. Apart from particle showers with an extremely high momentum and particles passing through gaps in the calorimeters, muons and neutrinos are the only SM particles that reach the outermost component of the ATLAS detector: the muon spectrometer (MS). While the presence of neutrinos is inferred indirectly from an apparent transverse momentum imbalance (section 3.3.7), muons interact with three layers of the MS, allowing the reconstruction of curved tracks similar to the ID. The necessary magnetic field of the MS is generated by 3 toroidal magnets, each arranged with an 8-fold coil symmetry around the calorimeters. This gives ATLAS its characteristic appearance, and in fact its name: A Toroidal LHC ApparatuS.

Besides the components of the ATLAS detector described in this chapter, there are three auxiliary detectors located relatively far from the interaction point (two of them outside the ATLAS cavern): LUCID is a set of online luminosity monitors located at ±17 m from the interaction point. It mainly detects Cherenkov radiation from the forward protons of inelastic pp collisions. The Zero Degree Calorimeter (ZDC) is located at ±140 m from the interaction point, where the straight-section of the beam-pipe is divided into two independent beam-pipes. Its primary purpose is the detection of very forward ($|\eta| > 8.3$) neutrons, and it can also provide a minimum-bias trigger. About ±240 m from the interaction point, the Absolute Luminosity For ATLAS (ALFA) detectors measure the elastic-scattering amplitude in the forward direction, which is related to the total cross-section via the optical theorem.

The ATLAS detector uses a right-handed coordinate system with its origin at the nominal interaction point in the centre of the detector. The x-axis points to the centre of the LHC ring, the y-axis points upward, and the z-axis is aligned with the beam direction. The particles from collision events are frequently described using spherical coordinates: radial position r, azimuthal angle φ and polar angle θ, such that the x-axis is located at $\varphi = 0$, while the z-axis coincides with $\theta = 0$. The pseudo-rapidity is defined as $\eta = -\ln \tan(\theta/2)$. For massless objects it is identical to the rapidity $y = 1/2 \ln \left[(E + p_z)/(E - p_z)\right]$.

Not all of the recorded event information can be stored permanently: with more than a 100 million read-out channels, and many millions of events per second, this is not possible using existing technology. This challenge is overcome by the ATLAS trigger system (see section 3.4), which selects only a few hundred "interesting" events per second. The trigger decision is taken in three stages: the first stage is realised in the detector

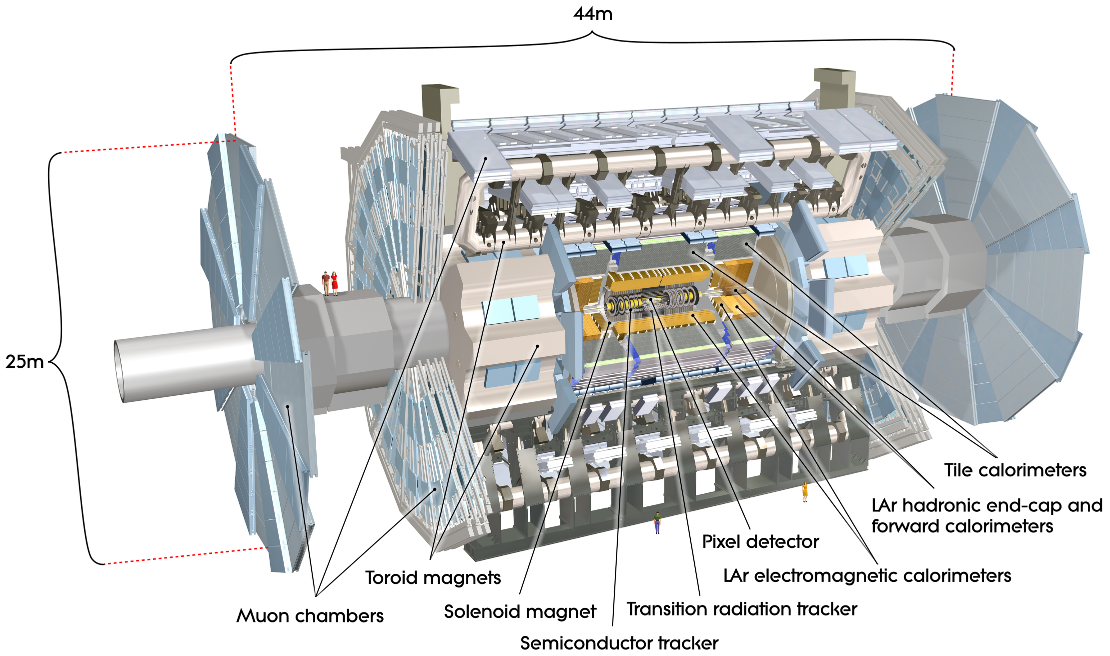

Figure 3.3: The overall layout of the ATLAS detector and its main sub-detectors (from [84]).

hardware, two software stages then refine the decision. This flexible setup allows to profit from the large luminosity while keeping the storage requirements at an acceptable level.

3.2.1 Magnets

The ID and the MS require strong magnetic fields to allow a momentum measurement of charged particles from the curvature of reconstructed tracks. The inner detector is surrounded by a superconducting solenoid magnet with a field strength of 2 T near its centre. The steel of the hadronic tile calorimeter and its girder structure return the magnetic flux. To reduce the amount of material in front of the calorimeters, the solenoid is contained in the same cryostat as the electromagnetic barrel calorimeter, where it is cooled to 4.5 K using liquid helium. Its single-layer coil is constructed from high-strength Al-stabilised Nb/Ti conductor and is located inside an Al support cylinder. Charging or discharging the solenoid takes about 30 minutes. In case of a quench, the stored energy of 40 MJ is absorbed by the magnet's 5.4 t cold mass, raising its temperature to 120 K. No damage is caused to the solenoid at this temperature, and cooling down to 4.5 K requires approximately one day.

Most of the MS is located inside a toroidal magnetic field. This field geometry is special in that its magnetic flux is contained entirely inside the magnet. The barrel and the two end-cap toroids each consist of eight coils arranged in an 8-fold symmetry around the beam axis. The toroid field is inhomogeneous and varies between 0.15 T and 2.5 T in the barrel region and between 0.2 T and 3.5 T in the end-cap region. The toroid windings are made from Al-stabilised Nb/Ti/Cu conductor. A normal magnet ramp or dump takes less than 2 hours. The magnets are protected by a quench detection system, which can heat up the magnets at four places per coil to distribute the stored energy of 1.1 GJ across more material by forcing the entire magnet into a normal conducting state in less than 2 seconds. After such an event, the magnet needs to be re-cooled from approximately 58 K to 4.6 K, which takes 50 hours.

3.2.2 Inner detector

The ID consists of three sub-systems: the pixel detector, the semi-conductor tracker (SCT), and the transition radiation tracker (TRT). Their layout and coverage is shown in figure 3.4. In the transverse plane, the pixel, SCT and TRT detectors have nominal position resolutions of 10 µm, 17 µm, and 130 µm, respectively. The TRT complements the precise measurements of the silicon detectors (pixel and SCT) by a high number of recorded hits: all charged tracks with a transverse momentum $p_{\mathrm{T}} > 500$ MeV and $|\eta| < 2.0$ will traverse at least 22 straws (at least 36 outside the barrel-end-cap transition region $0.8 < |\eta| < 1.0$).

The silicon detector consists of several thousand individual modules: there are 1744 identical pixel modules, 2112 SCT barrel modules and 1976 SCT end-cap modules. The

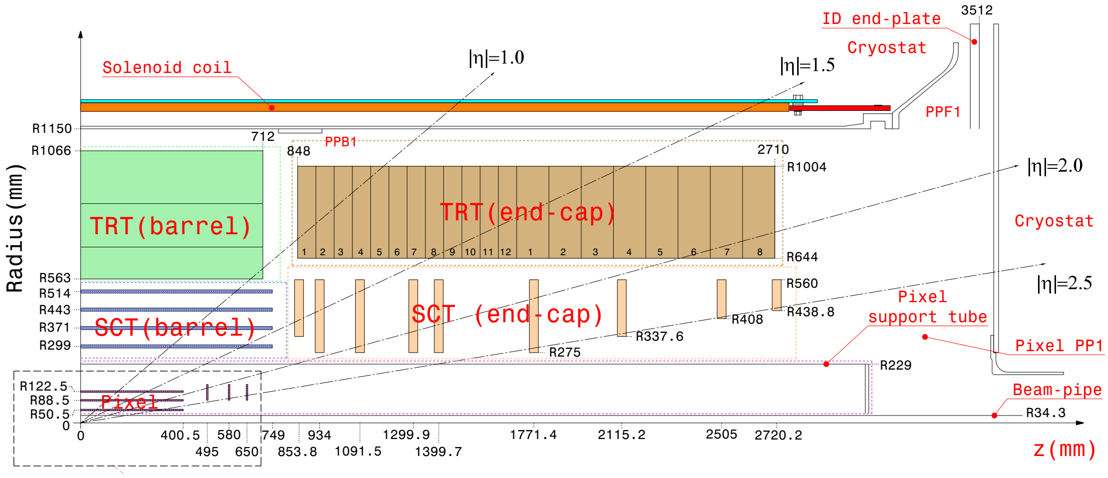

Figure 3.4: The inner detector comprises the silicon detectors and the transition radiation tracker (TRT). The silicon detector modules are arranged in multiple cylindrical structures (barrel) and several discs (end-caps), recording tracks up to $|\eta| < 2.5$, while the TRT end-cap modules extend to $|\eta| < 2$. As indicated on the z-axis, the entire inner detector is less than 6 m long (from [84]).

pixel sensors are 19×63 mm^2 large, and have 47232 pixels with a nominal size of 50×400 µm^2. They are operated at a bias voltage of initially 150 V. For the SCT, silicon strips are used instead of pixels. Each SCT module contains two layers of sensors that are rotated by 40 mrad against each other. In this way, it is possible to reconstruct a space-point from the hits on both sides of a module. The sensor sizes are different between barrel and end-cap modules, with typical sizes on the order of 60×60 mm^2. While the strips in the rectangular barrel sensors are parallel to each other, they are slightly rotated in the trapezoidal end-cap sensors. To keep electronic noise at an acceptable level over an extended period of high radiation exposure, the silicon detectors are operated at -5 to -10°C.

During 2010 operation, an unexpectedly large number of SCT module failures was observed. The problem was identified and corrected; a study related to this topic is described in appendix A.

In the long shutdown in 2013 and 2014 (LS1), an additional layer of pixel modules was inserted inside the existing pixel detector (insertible b-layer, IBL).

The TRT modules consist of polyimide drift tubes and gold-plated tungsten anode wires with a diameter of ~30 µm. The anode wires are kept at ground potential and the cathodes are operated at a voltage of -1530 V. In the barrel modules, the straws are oriented along the z-direction, while the end-cap straws are oriented radially. The straws are filled with a Xenon-based gas mixture and interleaved with fibres and foils, where transition-radiation photons are created by traversing electrons, adding electron identification capabilities to the TRT.

3.2.3 Calorimetry

The ATLAS calorimeters are divided into several components and use different technologies. The barrel contains both an EM and a HAD calorimeter, covering the pseudo-rapidity range $|\eta| \lesssim 1.5$ and $|\eta| < 1.0$, respectively. The EM barrel calorimeter uses alternating layers of lead and liquid argon (LAr), which was chosen for its linear behaviour and its radiation hardness. Absorbers and electrodes use an accordion shape geometry, allowing to have several active layers in depth (see figure 3.5). It shares a cryostat with the solenoid magnet (see section 3.2.1), thereby eliminating the need for two vacuum walls. The HAD calorimeter surrounds the EM calorimeter cryostat. It uses steel absorbers and scintillator tiles as the active material. The scintillation light from traversing hadronic showers is read out by wavelength shifting fibres. The HAD tile calorimeter is divided into 64 modules azimuthally. Readout cells are defined by grouping the fibres into photo-multipliers, with up to three layers in depth. The cells are

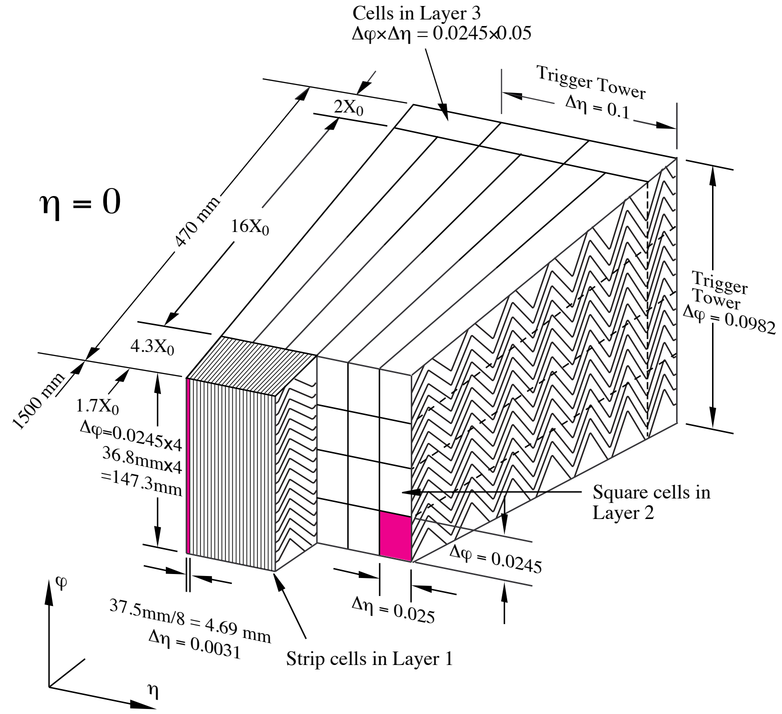

Figure 3.5: Schematic view of an electromagnetic barrel module, showing the accordion structure, the three radial layers of different cell granularity, and the size of the groups of cells that are used for triggering ("towers") (from [84]).

shaped such that consecutive layers approximately project back towards the interaction region.

The EM barrel calorimeter is extended up to $|\eta| = 3.2$ on both sides by end-cap discs, contained in cryostats that also house HAD end-cap discs ($1.5 < |\eta| < 3.2$) and LAr forward detectors ($3.1 < |\eta| < 4.9$). The HAD end-caps also use LAr as active medium, interleaved with $25 - 50$ mm parallel copper plates, while the LAr forward calorimeter uses copper and tungsten plates. The HAD tile calorimeter has no end-cap discs, instead the end-cap cryostats are surrounded by additional modules of the same type used in the HAD tile barrel, extending its coverage to $|\eta| < 1.7$.

The thickness of the EM calorimeter corresponds to > 22 radiation lengths over its full coverage. The HAD calorimeter provides > 10 interaction lengths (see figure 3.6).

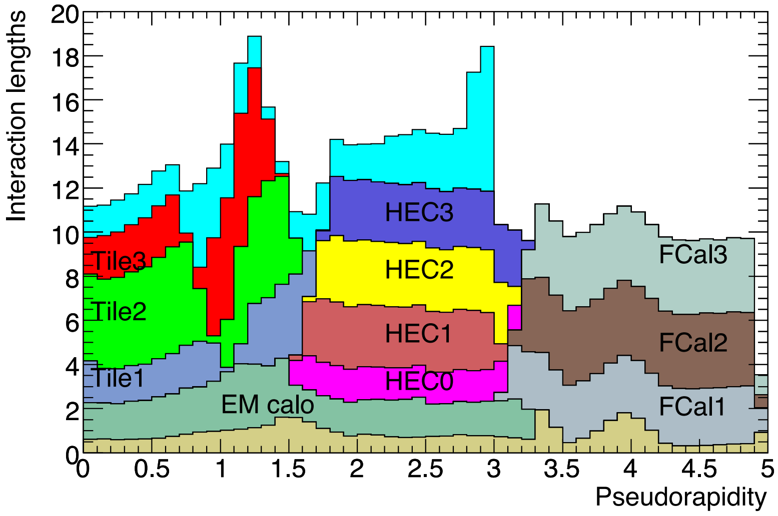

Figure 3.6: Overview of the material, in units of interaction lengths, and pseudo-rapidity coverage of the various calorimeter components (from [84]). The two unlabelled layers represent the material inside and outside the calorimeters. In between are the EM calo(rimeter) and the layers of the HAD calorimeters: the Tile calorimeter, the Hadronic End-Cap (HEC), and the Forward Calorimeter (FCal).

3.2.4 Muon spectrometer

The muon spectrometer consists of four sub-detectors and is contained within a toroidal magnetic field. Monitored drift-tubes (MDTs) are used for muon position and energy measurements in three concentric barrel layers and three end-cap discs, each providing up to 8 η measurements per layer. Each layer consists of “large” and “small” elements, that slightly overlap each other to achieve full ϕ coverage and to facilitate alignment (figure 3.7).

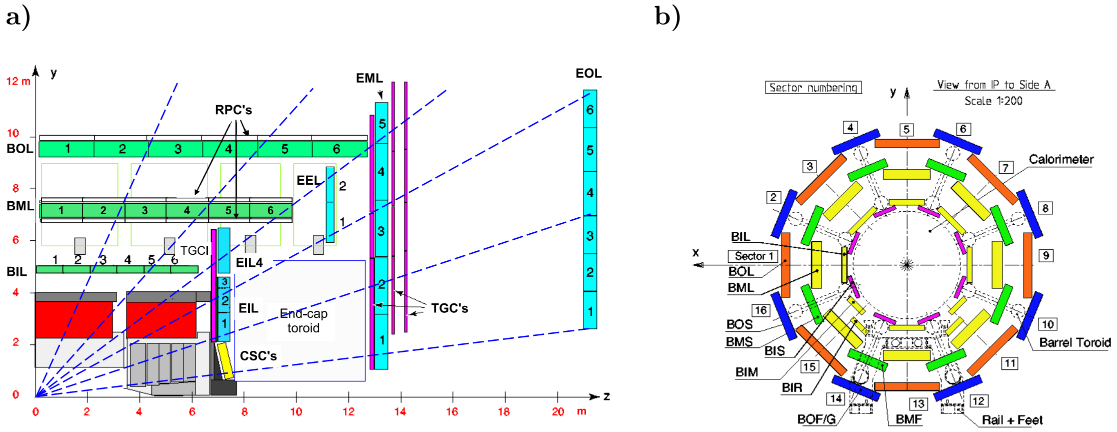

Figure 3.7: **a)** Positions of the various muon sub-systems, further described in the text. The monitored drift tube detectors are labelled according to their position: barrel or end-cap (B or E); inner, middle, or outer layer (I, M, or O). **b)** Cross-section view (r-ϕ plane), showing Long (L) and Short (S) MDT barrel chambers. The layout has a few irregularities around sectors 12 and 14 because of the detector support structure (from [84]).

The MDTs are contained in chambers arranged in three stations in the barrel and in three end-cap discs. Their basic elements are Al drift tubes with a diameter of 3 cm and filled with Ar/CO$_2$ gas at 3 bar. Each tube has a central tungsten-rhenium wire at a potential of 3 kV. The wire is centred in the tube to an rms accuracy better than 10 µm. The average spatial resolution per tube is 80 µm, which is improved by combining several measurements. For a track crossing three stations, an rms sagitta resolution of $\sigma = 45$ µm is expected, corresponding to a relative track momentum resolution of better than 10% at 1 TeV.

At the innermost end-cap segment, at $|\eta| > 2$, the counting rates will exceed the safe limit for MDT operation of 150 Hz/cm^2. At this location, cathode strip chambers (CSCs) are used instead. These are multi-wire proportional chambers, with a layer of wires oriented radially, enclosed by a layer of cathode strips on each side of the chamber, one of them orthogonal to the wires, the other parallel. The CSCs are filled with an Ar/CO$_2$ mixture and operated at 1.9 kV. Using a strip pitch of ~5.5 mm, the CSCs achieve a resolution of 60 µm, slightly better than the MDTs.

An optical alignment system is used to determine the relative MDT chamber and CSC positions to an accuracy better than 40 µm. This is further improved with track-based alignment strategies.

The resistive plate chamber (RPC) and thin gap chamber (TGC) detectors provide fast muon track triggers. As shown in figure 3.7, the three RPC layers are located in the barrel, one on each side of the middle muon station and one outside the outer muon station. The RPC consists of two parallel resistive plates with a separation of 2 mm with a gas mixture[1] between them. A voltage of ∼10 kV is applied between the two plates. The signal is read out through metallic strips that are capacitively coupled to the outsides of the plates. Hits in the middle RPC layer are extrapolated back to the innermost layer to trigger on low p_T muons, and forward to the outermost layer to trigger on high p_T muons. A spatial resolution of ∼1 cm, and a time resolution of ∼1 ns is achieved for rates of up to 1 kHz/cm^2.

The TGCs are multi-wire proportional chamber detectors. They are located in four discs between 7 m and 14 m away from the interaction point. They are capable of processing the higher rates of muons occurring in the forward direction, up to and exceeding 20 kHz/cm^2, with a similar spatial resolution as the RPCs, but a temporal resolution of ∼25 ns.

3.3 Reconstruction, identification, performance

Table 3.1 lists the energy and momentum resolution goals for the tracking system, the calorimeters and the muon spectrometers, defined with the Higgs discovery and the search for physics beyond the Standard Model in mind.

After discussing one of the main challenges in the reconstruction of physics events recorded with ATLAS, the occurrence of several simultaneous *pp* collisions (also called *pile-up*), we give an overview of the techniques used to reconstruct and identify the physics objects used in the top squark search discussed in this thesis: electrons, muons, jets and missing transverse momentum.

Detector Component	**Required resolution**	**η coverage**	
		Measurement	Trigger
Tracking	$\sigma_{p_\mathrm{T}}/p_\mathrm{T} = (0.05\,p_\mathrm{T}[\mathrm{GeV}] \oplus 1)\%$	± 2.5	–
EM calorimeter	$\sigma_E/E = (10/\sqrt{E[\mathrm{GeV}]} \oplus 0.7)\%$	± 3.2	± 2.5
Hadronic cal., central	$\sigma_E/E = (50/\sqrt{E[\mathrm{GeV}]} \oplus 3)\%$	± 3.2	± 3.2
forward	$\sigma_E/E = (100/\sqrt{E[\mathrm{GeV}]} \oplus 10)\%$	$3.1 < \lvert\eta\rvert < 4.9$	
Muon spectrometer	$\sigma_{p_\mathrm{T}}/p_\mathrm{T} =$ 10% at $p_\mathrm{T} = 1$ TeV	± 2.7	± 2.4

Table 3.1: Goal specification for relative momentum and energy resolutions and pseudorapidity coverage for the ATLAS detector (from [84]). The required resolutions are expressed by a term depending on the track momentum or particle energy, and a constant term. The two are summed in quadrature, as indicated by the $\oplus$ symbol.

---

[1] 94.7% tetrafluoroethane $C_2H_2F_4$, 5% isobutene C_4H_{10}, 0.3% sulphur-hexaflouride SF_6.

3.3.1 Pile-up

Figure 3.8 shows the distribution of μ, the average number of inelastic pp collisions per bunch crossing, during the 2012 ATLAS data-taking at $\sqrt{s} = 8$ TeV. This is recorded for each luminosity block (typically 2 minutes of data-taking). The actual number of pp collisions for each bunch crossing is Poisson-distributed with an expectation value of μ. Besides pile-up within one bunch crossing ("in-time pile-up"), there can also be overlap between signals resulting from adjacent bunch crossings ("out-of-time pile-up"), in particular for the calorimeters. Each part of the detector, each reconstruction technique, and each efficiency or fake rate estimate must be characterised as a function of the pile-up.

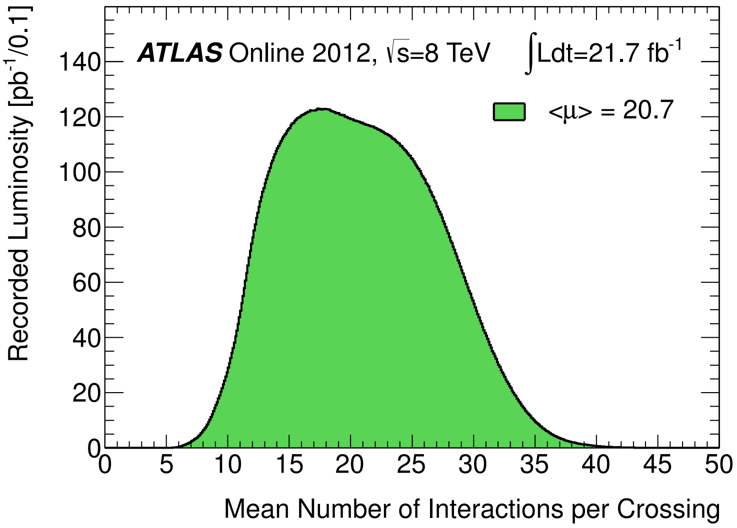

Figure 3.8: Luminosity-weighted distribution of the number of interactions per bunch crossing in pp events recorded with ATLAS in 2012 (from [83]). For the x-axis, the average value per luminosity block is used, not the actual bunch-by-bunch value (see [85]).

3.3.2 Tracks and vertices

The baseline algorithm for the reconstruction of tracks from charged particles uses 3 pixel clusters or SCT space-points in the 4 innermost silicon detector layers as track seeds. It iteratively adds hits using a Gaussian sum filter [86] or a global χ^2 fitter, extending the track through the SCT and into the TRT [87].

Fake tracks due to hits from additional in-time pp collisions or from instrumental effects are minimised by requiring at least 9 hits in the silicon detectors, and no "holes" in the track (non-existing but expected measurement points).

There are several variations of the tracking algorithm that are also capable of handling TRT-only tracks, muon tracks, or tracks of lower p_{T}.

The z-position of each reconstructed track is then extrapolated back to the beamline and tested as a vertex candidate. Tracks within 7σ from a vertex candidate are tested for their compatibility using an iterative χ^2 fit, and weights are assigned to each track based on the χ^2. The three-dimensional beam spot position is used as a fit constraint. The procedure is repeated until no further vertices can be found.

Figure 3.9 shows the vertex reconstruction efficiency on a simulated sample of minimum bias events. For most physics processes of interest, the hard scattering process has a larger number of high momentum tracks, resulting in a vertex reconstruction efficiency significantly higher than that of minimum bias events: for example, 96% for $H \to \gamma\gamma$ events, and close to 100% for $t\bar{t}$ events (section 10.2.4 in [84]). The vertex with the largest $\sum p_{\mathrm{T}}^2$ of all constituent tracks is selected as *primary vertex*; this prescription selects the correct vertex for 99% of $t\bar{t}$ events [84].

In a post-processing stage, secondary vertices and photon conversion vertices are reconstructed by dedicated algorithms.

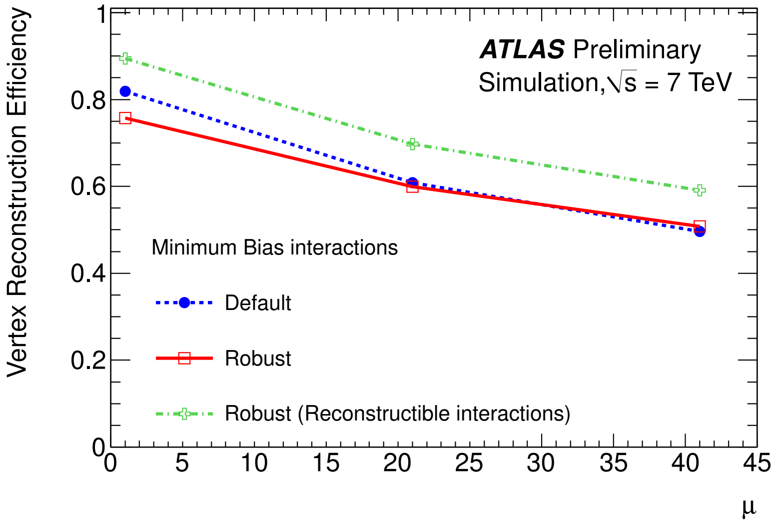

Figure 3.9: Vertex reconstruction efficiency determined on a minimum bias sample at different levels of pile-up, taken from [87]. The “robust” algorithm requires three or more tracks to be assigned to a vertex, while the default algorithm also accepts vertices with only two assigned tracks. Events with at least two charged particles with $|\eta| < 2.5$ and $p_{\mathrm{T}} > 400$ MeV are considered to be ’reconstructible’; ignoring non-reconstructible events naturally results in a higher efficiency. For most physics processes of interest, the vertex reconstruction efficiency is significantly higher than for minimum bias events.

3.3.3 Electrons and photons

Electrons are reconstructed by loosely matching clusters in the EM calorimeter to inner detector tracks. The clusters are seeded from energy deposits with $E_T > 2.5$ GeV, found using a sliding-window algorithm with a window size of 0.075 × 0.125 in η–ϕ space. Once a matching track has been found, the cluster size is adjusted depending on its position in the calorimeter, resulting in an improved energy resolution [88]. The electron direction is always taken from the associated track, while its energy is obtained from the calorimeter for $E > 20$ GeV, and from the track energy otherwise, as tracks have a superior resolution at low momentum (cf. table 3.1). Several sets of electron identification requirements are evaluated, differing in their selection efficiency and the fraction of fake reconstructed electrons. Some of the variables taken into consideration are (see [89]): the shower shape in the calorimeter; the track impact parameter and track quality; the energy-momentum ratio; the presence of a hit in the innermost silicon layer; the fraction of high-threshold hits in the TRT. Figure 3.10 shows the combined electron reconstruction and identification efficiency for various electron definitions used for the reconstruction of data recorded in the 2012 run period. Figure 3.11 shows the electron track momentum resolution achieved in the inner detector and the electron energy resolution achieved in the electromagnetic calorimeter. With increasing electron momentum, the track curvature decreases, resulting in a deteriorated track resolution; the relative energy resolution improves, however.

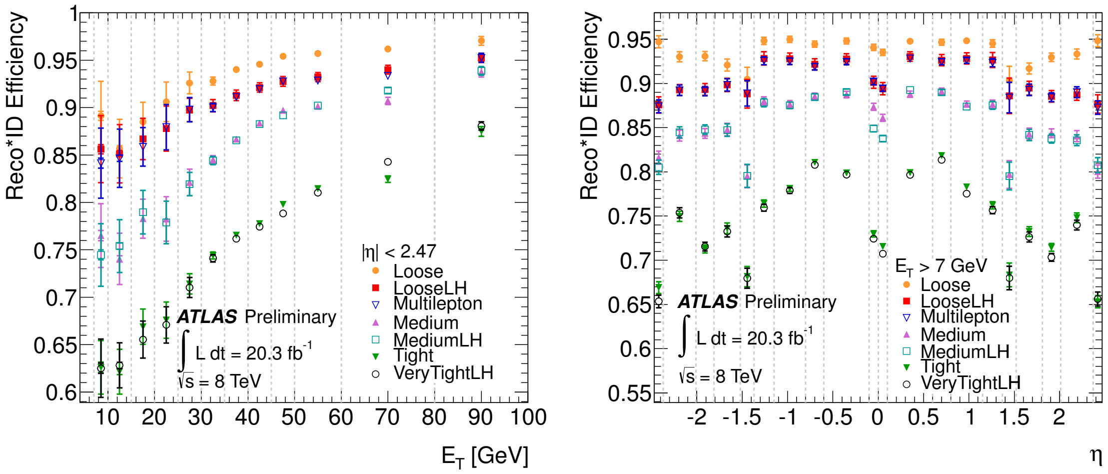

a) **b)**

Figure 3.10: Measured combined electron reconstruction and identification efficiency for different electron definitions as functions of **a)** electron energy and **b)** pseudorapidity (from [89]). Both *loose* and *tight* electron definitions are used in the stop search.

The stop search uses two electron definitions: a *baseline electron* must pass the loose identification criteria, have a reconstructed transverse momentum $p_{\mathrm{T}} > 10$ GeV and be within the inner detector acceptance, $|\eta| < 2.47$. The EM fraction of the electron energy deposited in the calorimeters is required to be at least 80%. In addition, a *signal electron* has to fulfil the tight identification criteria, and must have $p_{\mathrm{T}} > 25$ GeV. Its trajectory

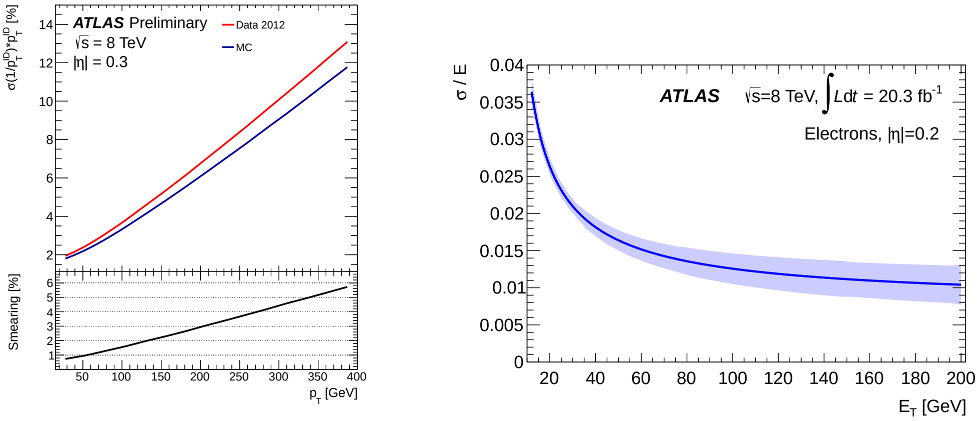

a) **b)**

Figure 3.11: Electron performance in 2012: **a)** electron track momentum resolution (from [90]), **b)** electron energy resolution (from [91]). The resolutions for these electrons with small $|\eta|$ are well within the goal specifications (table 3.1).

must be compatible with having originated from the primary vertex, i.e. the smallest distance between track and primary vertex in the x–y plane is $d_0 < 1$ mm (transverse impact parameter), and less than $z_0 < 2$ mm along the beam-axis (longitudinal impact parameter). Further, the electron's track has to be isolated, using a track-based isolation criterion: the p_T sum of nearby tracks ($\Delta R = \sqrt{(\Delta\phi)^2 + (\Delta\eta)^2} \leqslant 0.2$) with $p_\mathrm{T} >$ 400 MeV and associated to the primary vertex does not exceed 10% of the electron p_T.

Having two electron definitions avoids threshold effects in the definition of an event selection with exactly one lepton: one signal lepton is required, and events with any additional baseline lepton are not used in the analysis (*second lepton veto*).

Photons are reconstructed with a technique similar to that used for electrons, with the main difference that no inner detector track matching the calorimeter cluster must be found, or that it is flagged as a photon conversion. Also for photons several sets of identification criteria have been defined. Photon reconstruction has no direct relevance for the presented analysis. However, the kinematics of $t\bar{t}+\gamma$ events are similar to those of $t\bar{t}+Z$ events; the latter are an important SM background especially at high stop masses, and $t\bar{t}+\gamma$ events are used to verify their modelling in simulation.

3.3.4 Muons

Muon tracks are reconstructed starting from the MS and extrapolated backward to the origin accounting for the energy loss in the calorimeter. First the hits within each muon station are used to form track segments, these are then combined. The muon spectrometer reconstructs standalone tracks with $|\eta| < 2.7$. For muon tracks that are within the inner detector acceptance ($|\eta| < 2.5$), it is possible to obtain combined tracks. For the analysis presented here, this is done using a statistical combination of the MS and ID track parameters.

Besides the successful combined track reconstruction with certain ID hit requirements (at least 1 pixel layer hit, 5 SCT hits, 9 TRT hits, not more than 2 holes in the silicon detectors), no further conditions need to be fulfilled to identify the track as a muon object.

A momentum resolution of $\sim$3% over a wide $p_{\rm T}$ range, increasing to 10% at $p_{\rm T} =$ 1 TeV with a reconstruction efficiency above 96% is achieved [92]. There are two pseudorapidity regions with lower efficiencies: $|\eta| \approx 0$, where the MS is not fully equipped as the space was needed for the ID and calorimeter services, and $1.1 < |\eta| < 1.3$ where not all chambers were installed yet (in 2012). These inefficiencies are largely compensated by calorimeter-tagged tracks (see figure 3.12).

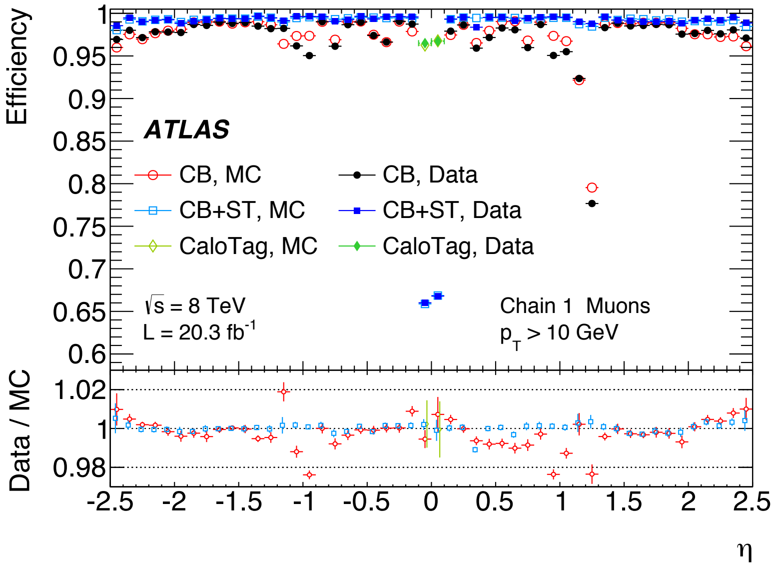

Figure 3.12: Measured muon reconstruction efficiency for combined (CB), segment-tagged (ST, ID track + one MS segment) and calorimeter-tagged muons (from [92]).

Stand-alone muon tracks with muon $p_{\rm T} > 5$ GeV contain a few percent of fakes, partly due to electromagnetic showers created by the muon itself that may result in additional charged tracks in the muon spectrometer from electrons and positrons, and partly due to the cavern background from thermal neutrons and low-energy γ rays. By using combined tracks, fakes are reduced to a negligible level [84].

As for the electrons, the stop analysis uses a *baseline muon* and a *signal muon* definition. Muons that are identified as detailed above and satisfying $p_{\rm T} > 10$ GeV and $|\eta| < 2.4$, are called baseline muons. Signal muons must satisfy $p_{\rm T} > 25$ GeV and fulfil a track-based isolation criterion with an absolute threshold such that the p_{T} sum of all tracks within $\Delta R < 0.2$ satisfying $p_{\mathrm{T}} > 400$ MeV must not exceed 1.8 GeV.

Any muons not fulfilling transverse and longitudinal impact parameter requirements of $d_0 < 0.2$ mm, $z_0 < 1$ mm might be the result of cosmic rays. Events with such muons are not used in the analysis.

3.3.5 Jets

The fragmentation and hadronisation of quarks and gluons lead to the production of hadronic jets that can be detected as showers in the combined EM and HAD calorimeters. As a first step, calorimeter cells are grouped into topological clusters: cells with a signal-to-noise[2] ratio S/N>4 are used as seeds, adjacent cells with S/N>2 are joined iteratively, and finally one set of neighbouring cells is joined. Clusters are split if there are local maxima inside. The cluster energies are corrected to the hadronic scale using a local cell signal weighting (LCW) method. Cluster four-momenta are determined from the total energy of the contained cells, the energy-weighted average position, and setting their mass to zero [93].

Clusters are the input for the anti-k_t jet building algorithm [94]. This algorithm also allows the use of tracks or truth-level partons as inputs; this can be used in performance studies. The algorithm iteratively selects the two closest input objects and merges them (by adding their four-momenta), using the following distance metric:

$$d_{ij} = \frac{1}{\max\left(k_{t,i}^2, k_{t,j}^2\right)} \frac{\Delta \bar{R}_{ij}^2}{R}, \tag{3.1}$$

where the i, j are indices numbering the input objects, k_t, i are their transverse momenta, and $\Delta \bar{R}$ is the angular separation of i and j in rapidity y and azimuth ϕ: $\Delta \bar{R} = \sqrt{\Delta y^2 + \Delta \phi^2}$. The dimensionless size parameter R determines when then algorithm stops: jet i is completed when it is closer to the beam than to any other input, $d_{iB} < d_{ij}$ (for all $j \neq i$), where

$$d_{iB} = \frac{1}{k_{t,i}^2}. \tag{3.2}$$

The anti-k_t algorithm is infrared and collinear safe [94]: additional soft emissions have no impact on the clustering sequence, as inputs with large k_t^2 are merged first, and collinear-split objects are merged early due to their small ΔR.

Once the jets in an event have been reconstructed, several corrections are applied [95]: an energy offset is applied to compensate for the expected pile-up; the jet is corrected to point at the selected primary vertex instead of the ATLAS detector centre; an additional p_{T}- and η-dependent calibration is applied to further improve agreement between the

---

[2] Noise stems from electronics and from pile-up.

recorded data and simulated events. To remove jets not coming from the primary interaction (beam-induced backgrounds, cosmic ray muons, and calorimeter noise), highly effective identification requirements exist [96].

The systematic uncertainties affecting the jet energy have been modelled in fine detail: the recommendation for 2012 data foresees 17 sources contributing to the jet energy scale (JES) systematic uncertainty. Figure 3.13 gives an impression of typical JES uncertainty contributions. The typical per-jet JES uncertainty is about 2%, increasing for jets with $p_{\mathrm{T}} \lesssim 50$ GeV or above 1 TeV. The average JES uncertainty for central jets is better ($\sim$1%) than for forward jets ($\sim 3 - 4\%$ at $|\eta| = 2.5$).

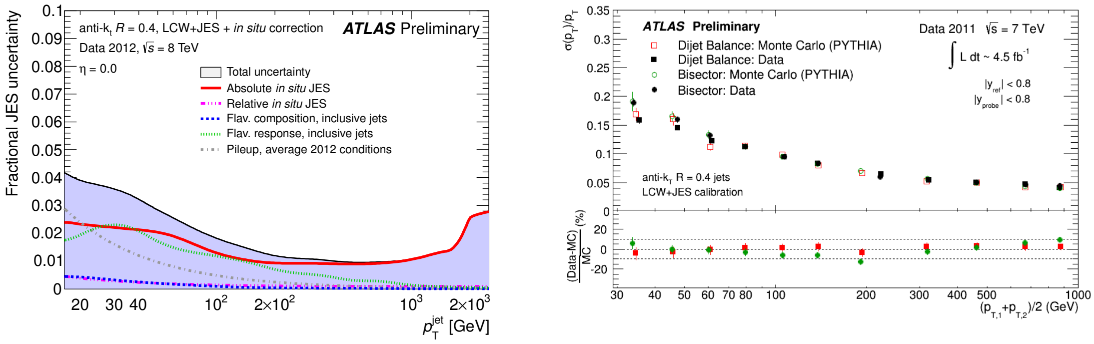

a) **b)**

Figure 3.13: **a)** The overall 2011 JES uncertainty for hadronic jets (LCW calibration) at $|\eta| = 0.5$ built with the anti-k_t algorithm with size parameter $R = 0.4$. The main components of this uncertainty are also shown (from [95, 97]). **b)** The jet energy resolution, shown for the same jet reconstruction and calibration techniques (from [98, 99]; not updated for 2012).

Jets are the observable objects from free quarks or gluons produced in the pp collision. To identify the flavour of the originating quark, one can use properties of the jet such as for example its impact parameter or its associated secondary vertices [100]. For measurements with ATLAS, the MV1 algorithm [101] is used for the tagging of b-quark jets, named after the multi-variate method that was used to combine several jet properties in order to optimise the discriminating power. The MV1 algorithm returns a value between 0 and 1; depending on the desired selection efficiency or rejection power, a suitable *tagging* threshold needs to be chosen. While 70% of all b-quark jets in a simulated sample of $t\bar{t}$ events fulfil MV1$>$ 0.7892, fewer than 1 in 100 light jets pass this MV1 threshold (figure 3.14a). Jets originating from a c-quark are b-tagged with a probability of $\sim$20% in a simulated $t\bar{t}$ sample. This fraction depends on the source of the c-jet: it increases to about $\sim$40% for a sample of D^{*+} mesons with at least three charged tracks [101]. The b-tagging efficiency has some dependency on the jet p_{T} (figure 3.14b), and is practically flat in η. The b-tagging efficiency found in data agrees well with its description in simulated events (sometimes referred to as Monte Carlo, MC), see figure 3.15.

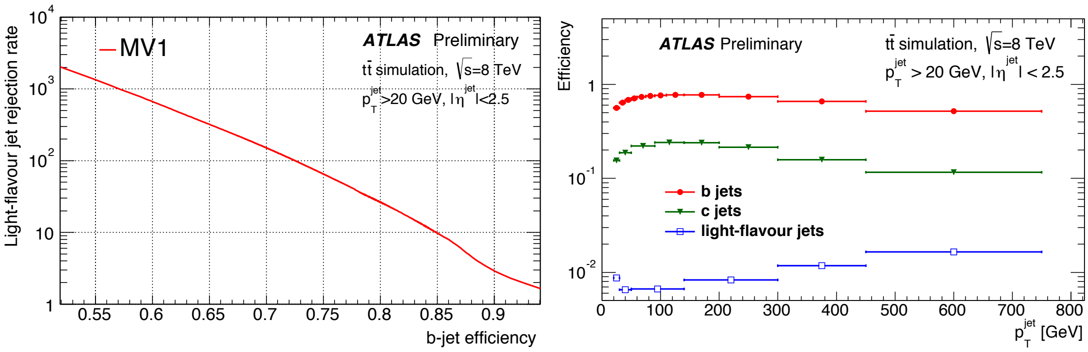

a) **b)**

Figure 3.14: Expected performance of the MV1 b-tagging algorithm **a)** shown as a ROC curve: the efficiency of tagging a b-quark jet is compared to the rate of not tagging a light-quark jet (u,d,s). **b)** b-tagging efficiency as a function of the jet p_{T}, using the 70% working point (WP) [101]. Also shown is the probability of tagging a c-quark jet. The efficiencies were evaluated on a simulated sample of top-antitop events. Both figures taken from [101].

The analysis presented in this thesis primarily uses anti-k_t jets with a size parameter of $R = 0.4$ satisfying $p_{\mathrm{T}} > 25$ GeV, $|\eta| < 2.5$, and the 70% working point of the MV1 b-tagging algorithm. For the overlap removal described below, the kinematic requirements are loosened to $p_{\mathrm{T}} > 20$ GeV and $|\eta| < 2.8$. The stop decays of interest (described in detail in section 4.2) have at least four jets in their final state, two of which originate from b-quarks. Whenever a requirement on the number of b-tagged jets is mentioned, only the four jets with the highest p_{T} are taken into account to avoid reliance on additional jets from initial or final state radiation.

3.3.6 Overlap removal

Once the different types of objects have been identified, a check for overlaps between them is performed. An electron always is accompanied by an electromagnetic jet. Thus, untagged jets near electrons ($\Delta R < 0.2$) are removed. Conversely, if an electron is found near a b-tagged jet ($\Delta R < 0.2$), the electron is removed. Jets originating from b-quarks may contain muons, so muons near a jet ($\Delta R < 0.4$) are removed. Lastly, poorly isolated electrons near a jet ($\Delta R < 0.4$) are removed.

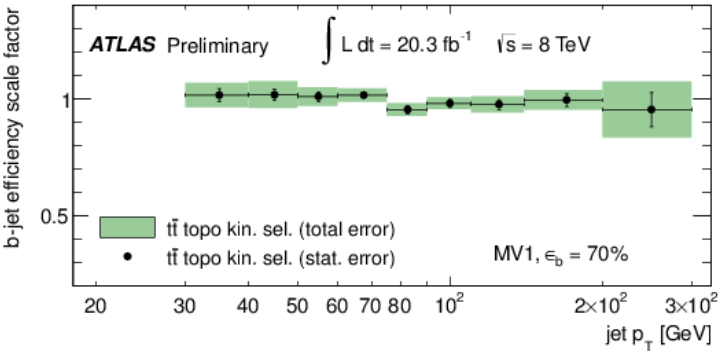

Figure 3.15: *b*-tagging efficiency scale factor and its uncertainties. The scale factor is used to improve the agreement between data and simulation: its value near 1 over the full considered jet p_{T} range indicates that the *b*-tagging performance is well described by the simulation.

3.3.7 Missing transverse momentum

Neutrinos escape the detector without interacting with its material, making it impossible to detect their presence directly. Indirect detection is possible by invoking momentum conservation: the sum of all particle momenta produced in the collision equals the sum of the momenta of the colliding partons. Any violation of this balance is evidence for at least one particle escaping the detector without interaction:

$$\sum_{\text{in}} \vec{p}_i - \sum_{\text{out}} \vec{p}_i = \sum_{\substack{\text{out}\\ \text{invisible}}} \vec{p}_i \equiv \vec{p}^{\,\text{miss}} \tag{3.3}$$

At the LHC this approach works well only for the transverse component of the missing momentum, as the longitudinal components of the partons in the hard interaction are much less constrained. Early ATLAS algorithms computed an event's missing transverse momentum by summing calorimeter energy deposits in a vectorial way, using the cell's location as direction, and the size of the energy deposit as magnitude[3].

Current algorithms improve the $E_{\mathrm{T}}^{\mathrm{miss}}$ computation by using reconstructed objects as inputs, and adding calorimeter cell energies only for cells not associated to any object (referred to as *soft term*). This has the advantage that tracking information can also be used in the $E_{\mathrm{T}}^{\mathrm{miss}}$ computation, and that any improvement in the object reconstruction will also benefit the $E_{\mathrm{T}}^{\mathrm{miss}}$ computation.

An important step is the suppression of possible contributions from additional *pp*-collisions that affect the jet term and soft term. This is done by subtracting $A_{\text{jet}} \times \rho$,

---

[3] This may explain why the missing transverse momentum is normally referred to as missing transverse energy ($E_{\mathrm{T}}^{\mathrm{miss}}$), although energy as a scalar quantity doesn't have a transverse component.

where A_{jet} is the jet area, and ρ is the average transverse momentum density $p_{T,\text{jet}}/A_{\text{jet}}$ in the event [102].

While the missing transverse momentum is needed for the detection of neutrinos, it can equally well be used to search for invisible BSM particles. Additionally, it can be of use in partially reconstructed events, where for example a lepton is outside the inner detector acceptance (rendering it invisible to the detector).

Table 3.2 summarises the most important requirements for the physics objects used in the stop search presented in this thesis.

Object	**Baseline / looser definition**	**Signal / tighter definition**
Electron	loose ID	tight ID
	$p_{\mathrm{T}} > 10$ GeV	$p_{\mathrm{T}} > 25$ GeV
	$\lvert\eta\rvert < 2.47$	$\lvert\eta\rvert < 2.47$
	EM fraction >0.8	EM fraction >0.8
	–	$d_0 < 1$ mm, $z_0 < 1$ mm
	–	$\sum p_{\mathrm{T}}^{\text{tracks}}$ in 0.2 cone $< 0.1 p_{\mathrm{T}}^{\text{electron}}$
Muon	$p_{\mathrm{T}} > 10$ GeV	$p_{\mathrm{T}} > 25$ GeV
	$\lvert\eta\rvert < 2.4$	$\lvert\eta\rvert < 2.4$
	–	$\sum p_{\mathrm{T}}^{\text{tracks}}$ in 0.2 cone < 1.8 GeV
	cosmic muon if $d_0 > 0.2$ mm or $z_0 > 1$ mm	
Jet	anti-k_t $R = 0.4$	anti-k_t $R = 0.4$
	$p_{\mathrm{T}} > 20$ GeV	$p_{\mathrm{T}} > 25$ GeV
	$\lvert\eta\rvert < 2.8$	$\lvert\eta\rvert < 2.5$
	–	b-tagging: MV1 at 70% WP
$E_{\mathrm{T}}^{\text{miss}}$	Computed from calibrated objects and unassociated cells, corrected for pile-up using jet area suppression.	

Table 3.2: Summary of object definitions used in the stop analysis.

3.4 Trigger

The ATLAS trigger system [103] decides whether to record or ignore a *pp* collision event. This occurs in three stages: at level-1 (L1), a fast decision based on the presence of calorimeter energy deposits and muons is taken. The sub-detectors retain the data of up to 100 events in read-out buffers to allow a latency of 2.5 µs at a bunch-crossing rate of 40 MHz. The L1 decision is based on information from the calorimeters or the MS, the ID does not contribute. L1 accepts events with a rate of up to 100 kHz, identifying regions of interest (RoIs) in the process.

Level-2 (L2) is realised in software, running on several hundred conventional CPUs on the ATLAS trigger farm. The events accepted by L1 are reconstructed using partial event information for the RoIs (about 2-6% of the total data volume) and fast custom algorithms. The L2 decision needs to be taken within 40 milliseconds on average, and reduces the event rate to approximately 3 kHz. The third trigger stage (called event-filter, EF) uses the full event information and the offline algorithms for reconstruction to make a final acceptance decision within 4 seconds on average, reducing the event rate to a few hundred Hz. All raw detector signals of the accepted events are stored to disk to allow later reprocessing with the most accurate detector geometry and most recent algorithms.

The sequence of reconstruction and selection steps for each trigger are defined via the trigger menu. Several hundred sequences have been defined, in some cases with a "prescale" (suppression factor) to stay within rate constraints. Each sequence is linked to a L1 acceptance decision. Figure 3.16 shows the example of a generic electron trigger.

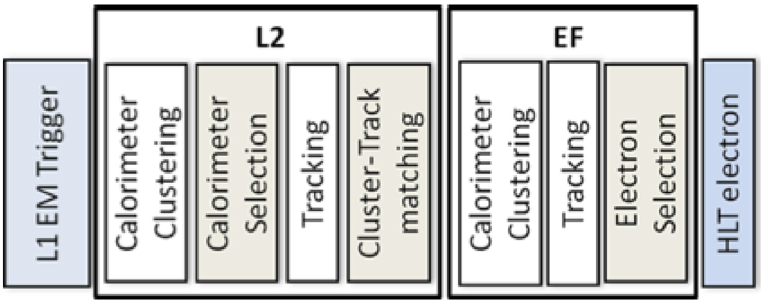

Figure 3.16: Different reconstruction and selection steps used in an electron trigger decision (adapted from [103]). The trigger chain is initiated by a L1 acceptance decision based on EM calorimeter information. In L2, calorimeter clusters and tracks in the RoIs are reconstructed and matched using partial event information; if satisfactory objects are found, the full event information is retrieved and the event reconstruction is repeated in the EF stage. If the electron candidate fulfils the trigger specific requirements on object quality and energy, the trigger chain terminates with a positive acceptance decision.

The majority of triggers are based on the presence of one or several physics objects of a certain type and exceeding some energy or momentum thresholds (for example the requirement of one electron with $E_{\mathrm{T}} > 22$ GeV in the case of an inclusive electron trigger, or 3 jets with $p_{\mathrm{T}} > 20$ GeV in the case of a multi-jet trigger). Other triggers react to $E_{\mathrm{T}}^{\mathrm{miss}}$ or to calorimeter energy sums. There can be several variants of a trigger: electron triggers for example may include an isolation criterion, or a veto on hadronic calorimeter activity near the electron candidate.

Based on the triggers that accept an event, it is assigned to one or more trigger streams (for example: Egamma or Muon streams, for events for which an electron/photon or muon trigger condition was met, respectively), reducing the amount of data to be processed by analyses relying only on a specific type of trigger. Events for which the L2 or EF reconstruction took unusually long (>5 s or >180 s, respectively) are recorded in the debug stream.

To understand the efficiency of a trigger, its behaviour near threshold, and any possible selection bias, one can compare its decision to that of another trigger with looser requirements. The loosest trigger available randomly selects events at a very low rate (zero bias trigger), other triggers use for example dedicated scintillators installed near the beam-pipe just outside the calorimeter end-caps (minimum-bias trigger scintillators, see [104]) to assure that a pp interaction occurred[4]. The process of iteratively evaluating trigger efficiencies in this way is referred to as "boot-strapping". For many triggers, one can find additional methods to estimate their efficiency. For example, the "tag-and-probe" method uses $Z \rightarrow ee$ events triggered by the electron to find the trigger efficiency of the positron as a function of its momentum, pseudo-rapidity or other properties that may be used in its identification.

The stop search in final states with one isolated lepton uses single lepton triggers and augments them with missing energy triggers. For electrons the `EF_e24vhi_medium1` and `EF_e60_medium1` are used, optimised for medium electron identification criteria and with nominal p_{T} thresholds of 24 GeV and 60 GeV. The lower threshold trigger has a veto on energy deposits in the hadronic calorimeter near the electron candidate ("vh"), as well as an isolation requirement. Events with muons are selected using the `EF_mu24i_tight` and `EF_mu36_tight` triggers, also with nominal p_{T} thresholds of 24 GeV and 60 GeV, and optimised to be used with tight muon identification criteria. Again, the lower threshold has an added isolation requirement. The higher threshold triggers help to recover inefficiencies resulting from differences between trigger and offline isolation requirements. Additional efficiency is gained by including events selected by the missing momentum triggers `EF_xe80T_tclcw_loose` and `EF_xe80_tclcw_loose`. The efficiency of this combined trigger setup is $\sim 98-99\%$ for typical signal events with a signal lepton and $E_{\mathrm{T}}^{\mathrm{miss}} > 150$ GeV.

---

[4] This method works best at low instantaneous luminosities and is not suitable for the design luminosity of 10^{34} cm^{-2}s^{-1}. The minimum-bias trigger scintillators have been removed from ATLAS during the 2013/2014 shutdown.

4 | Signal and background processes

> This illustrates an important point about searching for new physics: until you know what you are looking for, you have little chance of finding it.
>
> *Barger, Philips – Collider Physics, Updated Ed., p. 3*

A *pp* collision in which sparticles are produced will typically not be clearly distinguishable from a non-SUSY event. Instead, one expects SUSY to leave its mark through an enhanced rate of events with certain characteristics.

To identify those characteristics, it is crucial to have accurate models of possible SUSY event signatures as well as an accurate simulation of SM events, verified by the data, that constitute the background to our search. The simulation of collision events also allows the study of systematic uncertainties, related for example to the description of the detector or the reconstruction process, by varying the relevant parameters and observing the effect on the simulated kinematic distributions.

We outline the general concepts behind the simulation of *pp* collisions (section 4.1), describe the stop decay modes considered in the following analysis (section 4.2), the relevant SM background processes (section 4.3), and the software that was used to generate these samples (section 4.4); this section also describes the sampled SUSY parameter space as well as the prescriptions used to improve the agreement between simulation and measurement.

In order to illustrate the limitations of simulations, a data-driven estimate of QCD multi-jet background events is shown in appendix B.

4.1 Simulation of *pp*-collision events

4.1.1 Parton distribution functions

Protons have significant inner structure, and their description as a system of three valence quarks is insufficient for the highly energetic *pp* collisions occurring at the LHC. The quarks inside a proton constantly exchange gluons, and virtual quark-antiquark pairs (*sea quarks*) are created and annihilated. It might well be a gluon or a sea quark that participates in a collision, and not one of the valence quarks. The momentum transferred in the collision determines how finely the proton's inner structure is resolved (*De Broglie wavelength*). For the theoretical description of the collisions, we are interested in how often the different types of *partons* (collective term for the proton's constituents) participate in the hard process, and which fraction of the proton's momentum they carry (described by the Bjørken scaling variable x); this information is expressed in the *parton distribution functions* (PDFs). Extracting PDFs from data recorded at different collider experiments was and is a major effort: several groups regularly refine and publish their best estimates, based on data coming (for example) from the H1 and ZEUS experiments at the HERA *ep*-collider. In this analysis, we primarily use the CT10 NLO [105] (see figure 4.1) and CTEQ6L1 [106] PDF sets, both prepared by the same group.

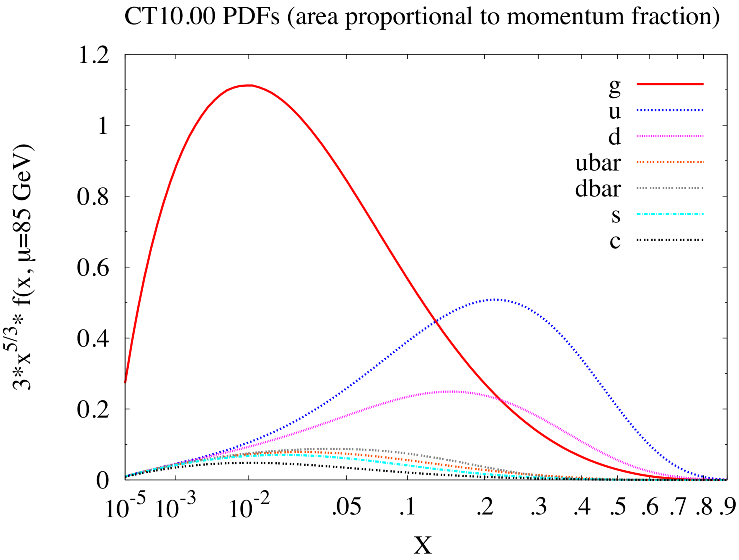

Figure 4.1: CT10 NLO parton distribution functions at $\mu = 85$ GeV (auxiliary figure for [105]). The plot shows the momentum fraction x carried by the constituent partons. About half of the proton's momentum is carried by gluons (see e.g. [107]). It is common to plot $x \cdot f(x)$, in which case the area under the curve is simply the expectation value of x. To visually emphasise the low x part of the PDFs, the abscissa is presented as $x^{1/3}$; the ordinate has been scaled accordingly.

4.1.2 Event generation

The cross-section σ for producing a final state of interest is given by the distribution of initial states, the transition amplitude relating initial and final state, and a phase-space factor that quantifies in how many ways the final state can be kinematically realised. The distribution of initial states is obtained from PDFs, the other two parts are *factorised* into the function $\hat{\sigma}$ describing only the hard process:

$$\sigma = \int \mathrm{d}x_1 f_{q1}(x_1, \mu_F^2) \int \mathrm{d}x_2 f_{q2}(x_2, \mu_F^2) \hat{\sigma} \left(x_1 p_1, x_2 p_2, \mu_F^2, \mu_R^2 \right) , \tag{4.1}$$

where f_{q1} and f_{q2} are the PDFs of the two interacting partons, x_1 and x_2 are their momentum fractions, and p_1 and p_2 are the momenta of the colliding protons. At energies below the *factorisation scale* μ_F, soft and collinear QCD corrections to the initial state are not treated perturbatively, but are instead absorbed into the PDFs. QCD corrections to the final state below the *renormalisation scale* μ_R are not absorbed into the PDFs, but are described as part of the fragmentation and hadronisation modelling described below. Both scales are unphysical and their impact on the computation is reduced with each order of perturbation theory that is considered. Variations of μ_F and μ_R around the energy scale of the hard process can be used to obtain a rough estimate of the contribution from missing higher order diagrams.

The transition amplitude is computed by applying the Feynman rules for the considered interaction to all Feynman diagrams connecting the relevant initial and final states. In practice, only the lower orders of these diagrams are computed, as the perturbation expansion often converges sufficiently fast; one refers to such computations as leading-order (LO), next-to-leading order (NLO), or even NNLO. Several event generators (for example Alpgen [108] and Sherpa [109]) compute the exact LO matrix element for the hard process with N additional parton legs (typically $0 \leqslant N \leqslant 5$). This improves the description of the large jet multiplicity in *pp* collision events, but does not describe all observables well; angular distributions in particular are described better by NLO generators.

4.1.3 Fragmentation and hadronisation

The quarks and gluons generated in the previous step do not exist as free particles, and additional techniques are required to describe how (meta-)stable particles are formed from partons.

Fragmentation, often also called *parton showering*, refers to the emission of additional soft-gluon radiation by the final state partons. The two most common approaches are *virtuality ordered emission* (hardest interactions first), and *angular ordering*, which means that successive emissions occur at increasingly small angles with respect to the emitting parton. This leads to the formation of one or more distinct *jets*, and continues until any further emission would result in a particle momentum below a cut-off of typically 1 GeV. At this point, colour confinement through the strong force results in *hadronisation*, meaning the formation of hadrons from nearby partons of similar energy. While the fragmentation of each final state parton can be treated separately, this is not possible

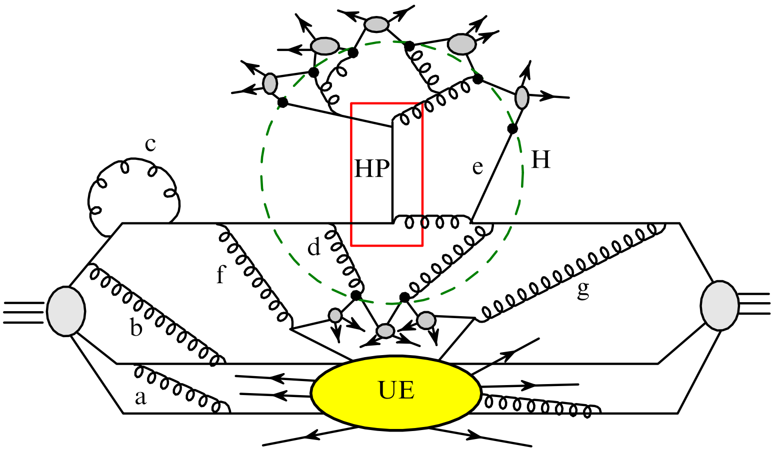

Figure 4.2: The general structure of a *pp* collision, separated into internal proton structure, hard process (HP) and underlying event (UE). The dashed line labelled "H" surrounds the additional partons that are radiated as the interacting partons find their way back onto the mass shell. From [110].

for hadronisation, where in principle all possible colour singlet combinations of partons must be considered. Several models with good agreement to observation exist [111].

Connecting the event generator and the parton shower is not trivial, as the delineation between the two regimes is not always clear: a gluon emitted from a final state quark (*final state radiation*, FSR) can equally well be viewed as an NLO contribution from the event generation or as part of the fragmentation process described in the parton shower software. A *matching* scheme is used to prevent double counting by vetoing events where additional jets have been created by the parton shower [112].

In an actual *pp* collision, there are two additional sources of particles besides the hard process: the *underlying event* and *pile-up*. The underlying event results from the remnants of the two protons from which the interacting partons originated, typically leading to additional jet activity in the forward regions of the detector (figure 4.2). These are also described by the parton shower programs, using phenomenological models tuned to the data in dedicated studies [113]. Pile-up is the collective term for decay products from additional *pp* collisions within a bunch crossing (in-time pile-up) or resulting from an earlier bunch crossing (out-of-time pile-up), it is accounted for during the detector simulation step (see section 3.3.1).

4.1.4 Detector simulation

Further steps are needed to connect the event description at the particle level to events in recorded data. The interaction of the produced particles with the material of various sub-detectors and support structures is usually simulated using Geant4 [114]. This results in a set of energy deposits in the detector (also called *hits*). To model the pile-up of the event, additional hits from simulated minimum bias events are overlaid at this stage, using a Poisson distribution around the expected amount of pile-up events [115]. An estimated distribution of the number of simultaneous *pp* collisions is used initially, and event weights are used later to accurately reproduce the measured distribution. Digitisation software specific to each sub-detector simulates the response of the electronics. The reconstruction of tracks, calorimeter clusters and other objects is then performed with the same algorithms that are used for recorded *pp* collision events (described in section 3.3).

The detector simulation uses a detailed geometrical model of the as-built detector [116] and takes several minutes on a modern CPU for a typical collision event. Most of the time is spent in the Geant4 stage related to interactions inside the calorimeter. A significant speed-up is achieved by replacing this detailed simulation with parametrised longitudinal and lateral energy profiles to describe the calorimeter cell responses (FastCaloSim). This simulation setup is referred to as AtlFast-II, or simply *fast-sim*, and gives a sufficiently accurate description for most purposes [117].

As the detector simulation is computationally expensive, it is common to apply a filter on the generated events and run the detector simulation only for events that are relevant for the analysis, for example by requiring the presence of a lepton or sufficiently high $E_{\mathrm{T}}^{\mathrm{miss}}$.

4.2 Signal processes considered in the analysis

The analysis described in chapter 5 is restricted to R-parity conserving models, where stops are produced in pairs and the LSP is stable. We only consider the direct production of stop pairs through the strong force, in contrast to models where gluinos are produced and decay to stops, for example. We assume the lightest neutralino, $\tilde{\chi}_1^0$, to be the LSP, in order to have an electrically neutral, spin-1/2 dark matter candidate.

4.2.1 Stop decay modes

The analysis is developed around two major decay modes, where the stop either decays into a top quark and the LSP (figure 4.3a) or into a bottom quark and a light chargino $\tilde{\chi}_1^{\pm}$, which subsequently decays into a W boson and the LSP (figure 4.3b). All sparticles not appearing in the Feynman diagrams of figure 4.3 are assumed to be sufficiently massive to be of no relevance. In both decay modes, two W bosons are generated, which can then decay leptonically or hadronically. As illustrated, we are interested in the *semi-leptonic* case with exactly one electron or muon in the final state.

There are a few special cases to be aware of, for example when the stop mass is very near the top quark mass (*stealth stop*), or when some of the mass differences are

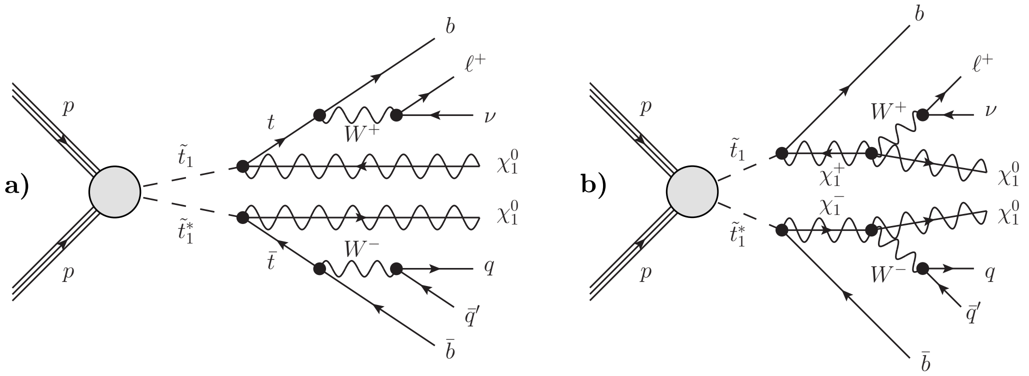

Figure 4.3: Tree-level Feynman diagrams of direct stop pair production with subsequent decays to **a)** $t + \tilde{\chi}_1^0$ or **b)** $b + \tilde{\chi}_1^\pm$ followed by $\tilde{\chi}_1^\pm \rightarrow W + \tilde{\chi}_1^0$. Both diagrams show the semi-leptonic case, where one W decays leptonically and the other hadronically. The big circle represents various strong production modes; at the LHC, the largest contributions are from gluon-gluon processes.

insufficient to produce on-shell particles. The first case can be searched for in precision measurements of the $t\bar{t}$ production cross-section [118] or the $t\bar{t}$ spin correlation [119].

Figure 4.4a shows an example of the second case: if the mass difference Δm between $\tilde{t}_1$ and $\tilde{\chi}_1^0$ is less than the top mass, and no other stop decay mode is available, the top quark will necessarily be produced off-shell. In the Feynman diagram, this is represented by collapsing the top propagator line and having the stop decay directly into a b-quark, a W boson and a $\tilde{\chi}_1^0$. For this reason, this decay mode is also referred to as a *three-body* decay. If the mass difference is reduced further, $\Delta m < m_W + m_b$, also the W boson cannot be produced on-shell, further collapsing the diagram to yield a *four-body* stop decay. In both cases, the same final state objects as for larger Δm are present, but with different kinematic properties. In particular, it is no longer possible to identify a top quark using the invariant mass of its decay products in a three-body stop decay.

While the decay modes shown in figure 4.3 can be studied separately, assuming a 100% branching ratio for one or the other, it is also possible to study both decay modes together, resulting in the additional type of diagram shown in figure 4.4b, referred to as an *asymmetric* stop decay. We refer to signal models where both $\tilde{t}_1 \rightarrow t + \tilde{\chi}_1^0$ and $\tilde{t}_1 \rightarrow b + \tilde{\chi}_1^\pm$ decays are allowed and consequently all three diagrams (4.3a, 4.3b, 4.4b) can occur as *mixed* stop models.

4.2.2 Model parameters

The masses of $\tilde{t}_1$, $\tilde{\chi}_1^\pm$, and $\tilde{\chi}_1^0$ are free parameters. To reduce the number of parameters, we always assume $m(\tilde{\chi}_1^\pm) = 2 \times m(\tilde{\chi}_1^0)$. While other choices are possible, this is justified from SUSY GUT models with *gaugino universality* [120] (or *gaugino unification*; see for

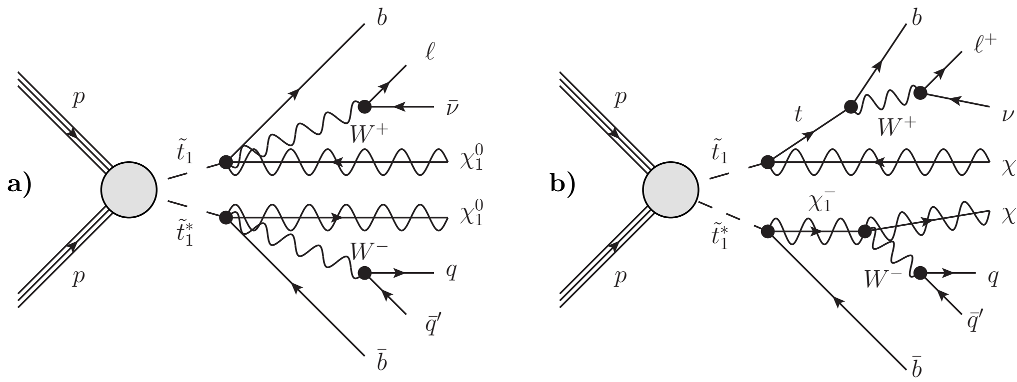

Figure 4.4: Tree-level Feynman diagrams of stop pair production with the particular decay patterns that are the focus of this thesis: **a)** three-body decay (off-shell top) and **b)** asymmetric decays (the opposite assignment of leptonic and hadronic W decays is also possible).

example ref. [46], sec. 4.3), and it assures that the $\tilde{\chi}_1^\pm \to W + \tilde{\chi}_1^0$ decay products are produced on-shell and with significant transverse momentum, except near the edge of the experimental constraint $m(\tilde{\chi}_1^\pm) \gtrsim 100$ GeV established by the LEP experiments [69].

The lightest neutralino, $\tilde{\chi}_1^0$, which is in general a mixture of the uncharged gauginos and higgsinos ($\tilde{B}$, $\tilde{W}^3$, $\tilde{H}_1^0$, $\tilde{H}_2^0$), is assumed to be mostly bino. This means the effects of EWSB are assumed to result only in a small perturbation on the neutralino mass matrix.

In the $\tilde{t}_1 \to t + \tilde{\chi}_1^0$ models, $\tilde{t}_1$ is mostly $\tilde{t}_R$, while the $\tilde{t}_1 \to b + \tilde{\chi}_1^\pm$ models assume $\tilde{t}_1$ to be fully $\tilde{t}_L$. For the asymmetric decays, equal contributions of $\tilde{t}_L$ and $\tilde{t}_R$ are assumed. As outlined in section 2.4, an increasing contribution from $\tilde{t}_R$ is expected as the branching ratio for the $\tilde{t}_1 \to t + \tilde{\chi}_1^0$ decay mode increases. Models with $\tilde{t}_1 = \tilde{t}_L$ have been evaluated for comparison, and have been found to have lower lepton transverse momentum, reducing the exclusion limits on the stop mass by typically 50–100 GeV (figure 4.5).

4.2.3 Mixed stop decays at arbitrary branching ratios

Since the asymmetric events on their own do not represent a physical sample, one needs to mix them with t+$\tilde{\chi}_1^0$ and b+$\tilde{\chi}_1^\pm$ samples according to the assumed branching ratio. Since we do not consider other stop decay modes beyond these, we always have $\mathcal{BR}\left(\tilde{t}_1 \to t + \tilde{\chi}_1^0\right) + \mathcal{BR}\left(\tilde{t}_1 \to b + \tilde{\chi}_1^\pm\right) = 1$. Using x as a shorthand for $\mathcal{BR}\left(\tilde{t}_1 \to t + \tilde{\chi}_1^0\right)$, we can express mixed quantities in the following way, using the expected yield as an example:

$$N_{\text{mixed}}(x) = x^2 \cdot N_{t\tilde{\chi}_1^0, t\tilde{\chi}_1^0} + (1-x)^2 \cdot N_{b\tilde{\chi}_1^\pm, b\tilde{\chi}_1^\pm} + 2x(1-x) \cdot N_{t\tilde{\chi}_1^0, b\tilde{\chi}_1^\pm}. \qquad (4.2)$$

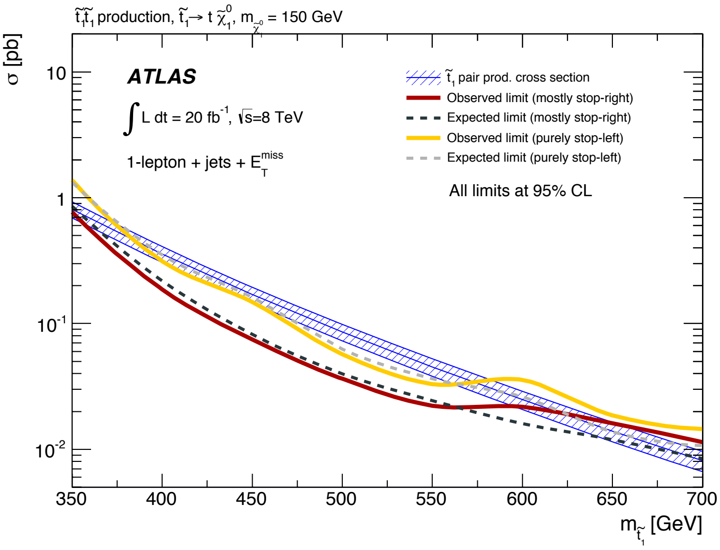

Figure 4.5: Impact of different stop mixing assumptions on the exclusion reach for $\tilde{t}_1 \rightarrow t + \tilde{\chi}^0_1$ models with a $\tilde{\chi}^0_1$ mass of 50 GeV from [121]. The $\tilde{t}_1$ is either pure $\tilde{t}_L$ (yellow lines) or mostly $\tilde{t}_R$ (red lines). The upper and lower blue lines correspond to the nominal signal cross-section scaled up and down by the theoretical uncertainty.

The expressions on the right-hand-side should be normalised separately according to the theoretical stop production cross-section, and should use the same SUSY masses and mixing assumptions. The mixed decays use the same $\tilde{\chi}^\pm_1$ mass assumption $m(\tilde{\chi}^\pm_1) = 2 \times m(\tilde{\chi}^0_1)$ as the pure $\tilde{t}_1 \rightarrow b + \tilde{\chi}^\pm_1$ decays. For most of the thesis, we use an equal mixing between the two stop decay modes (i.e. $x = 0.5$), as this results in the highest contribution of asymmetric decays, but the results for mixing with $x = 0.25$ or $x = 0.75$ are evaluated as well.

4.3 SM background processes

We briefly mention the SM backgrounds relevant for the stop search and some corresponding experimental results. Since the theoretical stop production cross-section is on the order of a few *pb* or lower (depending on the assumed stop mass), also SM processes with a low cross-section need to be considered.

However, these measurements are not used directly for the stop search, with the exception of the $t\bar{t}$ differential cross-section measurement (see section 4.4.3). Instead, all SM background processes are modelled using simulation and normalised using the theoretical cross-sections shown in table 4.3.

4.3.1 Dominant SM backgrounds: top-antitop and W+jets production

W+jets and $t\bar{t}$ events are the most relevant background processes for the stop search, as they have relatively high production cross-sections and because they share some of the event characteristics of stop pair production events, for example the final state objects (one lepton, four or more jets, and high missing transverse momentum), or traces of the (intermediate) presence of top quarks and W bosons, which can also be found in events with stop decays.

The cross-section for the production of a W boson and additional jets is on the order of 100 nb for pp collisions at $\sqrt{s}$ = 7–8 TeV, sufficiently high to allow a measurement already using $L_{\text{int}} = 33\ \text{pb}^{-1}$ of collision data recorded with ATLAS in 2010 [122]. About one third of the W bosons decay leptonically (32.4% ± 0.3% [2]), possibly resulting in significant missing transverse momentum due to the neutrino. Due to the additional jets, the event may satisfy event selection criteria used in a stop search. These jets originate from extra partons that were radiated either before or after the hard process (initial or final state radiation, respectively) or from the underlying event. The majority of additional jets come from gluons or light quarks (u,d,s), but c- and b-quark initiated jets (*heavy flavour jets*) do occur (approximately 5% and 1% of the W+jets events, cf. table 4.3). The fiducial cross-section for $W \to \ell\nu\ + \geqslant 4$ jets ($\ell = e$ or μ; $p_{\text{T}}^{\ell} > 20$ GeV, $p_{\text{T}}^{\nu} > 25$ GeV, $p_{\text{T}}^{\text{jet}} > 30$ GeV; $|\eta^{\ell}| < 2.5$, $|\eta^{\text{jet}}| < 4.4$), has been measured to be 20 pb at $\sqrt{s} = 7$ TeV [123].

Top quarks are assumed to always decay into a bottom quark and a W boson, and $t\bar{t}$ events are then classified by the decay modes of the two W bosons. From the leptonic W branching fraction one finds that fully leptonic $t\bar{t}$ decays[1] occur least often (10.5%±0.1%), and fully hadronic $t\bar{t}$ decays most often (45.7% ± 0.3%). The remaining $t\bar{t}$ decays are referred to as *semi-leptonic* (43.8% ± 0.4%) .

The production cross-section of $t\bar{t}$ events in pp-collisions at $\sqrt{s} = 7$ TeV was also measured using the 2010 ATLAS dataset [124], with about 3000 selected semi-leptonic events. The reason this *channel* was used initially, is that it is almost as frequent as the fully hadronic channel, while the requirement of one lepton rejects the majority of multi-jet events. Meanwhile, the production cross-section $\sigma_{t\bar{t}}$ has been measured by ATLAS in all decay channels [125, 126]. It is a function of the centre-of-mass energy of the pp collisions: $\sigma_{t\bar{t}}^{7\,\text{TeV}} = (173 \pm 10)$ pb (LHC combined result), and $\sigma_{t\bar{t}}^{8\,\text{TeV}} = (242 \pm 10)$ pb (ATLAS, [118]). Other important results include differential cross-section measurements ($\sigma_{t\bar{t}}$ as a function of jet multiplicity or jet momentum [127] or the momentum of the $t\bar{t}$ system [128]), or measurements of the top mass $m_t = (174.5 \pm 2.4)$ GeV [129]; for the latter,

---

[1] Because of their short life-time, $c\tau = 87.11\ \mu\text{m}$, decays involving τ leptons sometimes need special attention when classifying events; only 35% of the time, a τ decays into an electron or muon (plus the corresponding neutrino and antineutrino required to conserve lepton family numbers). For computing the branching ratios, we do not make this distinction.

the precision has been improved through a combination of LHC and Tevatron results to $m_t = (173.34 \pm 0.76)$ GeV [130]; the simulated $t\bar{t}$ samples used in this thesis have been produced assuming $m_t = 172.5$ GeV, a common choice in the existing literature.

For the stop analysis with one lepton final states, the dominant background initially stems from semi-leptonic $t\bar{t}$ events, since their final state objects differ from a stop pair event only through the absence of two neutralinos. Fully hadronic $t\bar{t}$ decays are a negligible background process: besides the absence of a lepton (which will occasionally be imitated by a jet), these events have no invisible particles and therefore no genuine $E_{\mathrm{T}}^{\mathrm{miss}}$. Dileptonic $t\bar{t}$ events will be selected if additional jets are present and one of the leptons is not identified or out of acceptance (geometrically or kinematically). This case is referred to as an *incomplete dileptonic $t\bar{t}$ event*, and it is difficult to identify. Top-pair production events where one top quark decays leptonically, and the other decays to a τ which then decays hadronically, may have an enhanced $E_{\mathrm{T}}^{\mathrm{miss}}$ due to additional neutrinos, and therefore also present an important category of $t\bar{t}$ decays.

4.3.2 Other SM backgrounds

There are several additional processes that may satisfy typical stop event selection criteria. Pairs of electroweak bosons (WW, WZ, ZZ) [131] can be radiated from a quark-antiquark pair or through anomalous triple gauge coupling (figure 4.6). An event with two W bosons can be mistaken for a $t\bar{t}$ or stop pair-production event if additional jets are present.

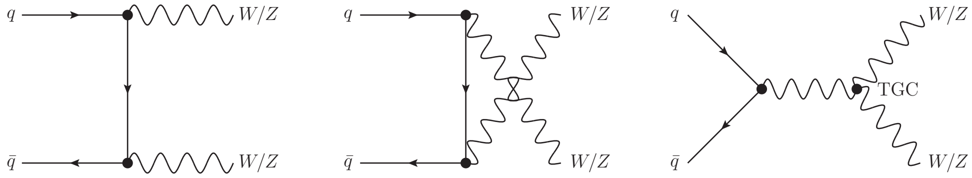

Figure 4.6: Feynman diagrams contributing to diboson production. The rightmost plot involves a triple gauge coupling (TGC) vertex.

Single top quarks [132] can be produced through the three channels shown in figure 4.7. For pp-collisions at the LHC, t-channel production (exchange of a W boson in the t-channel) is dominant (28.4 pb at $\sqrt{s} = 8$ TeV), while s-channel production is suppressed (1.82 pb) due to the small antiquark contribution to proton PDFs. At leading order, Wt-channel production proceeds through a single top-quark being produced from a b-quark radiating a W^- boson. There is an interference between $t\bar{t}$ and Wt diagrams: the production of a top-antitop pair and the decay of one of the top quarks also results in a single-top final state (at NLO). This is treated by removing Wt diagrams that also represent top-antitop production at amplitude level (diagram removal scheme). Events with a top quark and an additional jet (t- or s-channel) or an additional W boson (Wt

production) may occasionally also pass $t\bar{t}$ requirements, especially when only one b-tag is required; hence they also constitute a relevant background in a stop search.

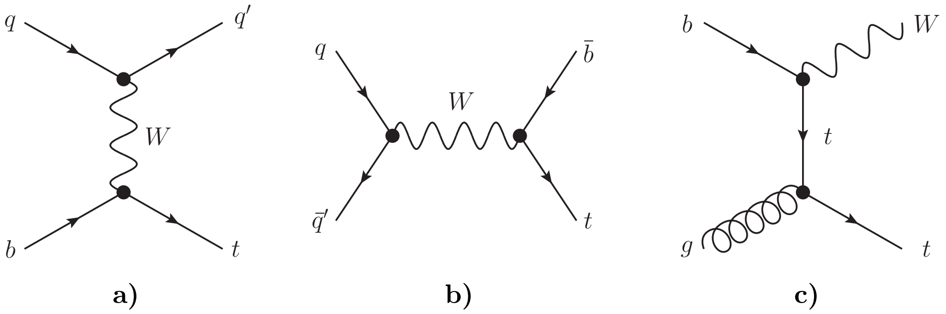

Figure 4.7: Feynman diagrams contributing to single-top production: **a)** the t-channel production is dominant in pp-collisions at the LHC; **b)** due to its low cross-section, single-top s-channel production has not yet been observed by the LHC experiments; **c)** tree-level diagram of Wt production; at NLO, the interference with $t\bar{t}$ production needs to be taken into account.

Events with Z boson production [133] are not an important background to a search requiring exactly one lepton in the final state, as Z bosons decay either into two leptons, into two quarks, or invisibly. QCD multi-jet production events are negligible, as they will not satisfy $E_{\mathrm{T}}^{\mathrm{miss}}$ requirements and do not have a lepton.

The associated production of a top-antitop pair and an electroweak boson [134] is a relevant background, especially $t\bar{t} + Z$ followed by an invisible Z decay ($Z \to \nu\bar{\nu}$), since this final state is identical to the considered stop decays. Measurements at $\sqrt{s} = 7$ TeV constrain the cross-section for $t\bar{t}$+Z production to below 0.71 pb [135, 136], the theoretical production cross-section is 115 fb at 8 TeV, and the branching ratio for invisible Z decays is $(20.00 \pm 0.06)\%$ [2], making this process a relevant background at high stop masses ($\sigma_{\tilde{t}_1\tilde{t}_1^*} = 7$ fb for $m(\tilde{t}_1) = 700$ GeV).

The theoretical cross-section of $t\bar{t}$ with associated Higgs-boson production in pp collisions at $\sqrt{s} = 7$ TeV is on the order of 100 fb [137]. Invisible Higgs decay modes can safely be neglected for a SM Higgs boson, but might pose a sizeable background otherwise.

4.4 Samples of simulated events

The samples have been produced with the following event generator versions: Herwig++ 2.5.2 [138], MadGraph 5.1.4.8 [139], PowHeg r2129 [140], AcerMC 3.8 [141] and Sherpa 1.4.1 [109]. Table 4.1 summarises the software and settings used for the production of signal and background samples used in the top squark search.

The CT10 NLO PDF set [105] has been used for PowHeg and Sherpa samples, and the CTEQ6L1 PDF set [106] has been used otherwise. The underlying event has been modelled either using the ATLAS Underlying Event Tune AUET2B [142] (MadGraph samples), the Perugia 2011C tune [143] (PowHeg, AcerMC), or UEEE3 [144] (Herwig++); Sherpa comes with its own underlying event tune. The parton shower has been simulated in Pythia 6.426 [145], except for Sherpa and Herwig++ samples, for which the event generators' built-in models have been used.

The choice of event generators and parton shower programs is motivated by comparison studies, but also by experience and practical considerations.

The detector simulation is made with the AtlFast-II setup for all signal and the majority of background samples. For the $t\bar{t}$ background, comparisons between kinematic distributions obtained with AtlFast-II and the full Geant4 simulation have been made to confirm the validity of the fast-sim approach. The overlaid minimum-bias events for pile-up modelling have been generated with Pythia 8.160 [146].

Background samples

process	**generator / remarks**	**PDF**	**UE**
$t\bar{t}$	PowHeg+Pythia6, $m_t = 172.5$ GeV lepton filter (>1 MeV, $\varepsilon = 54.3\%$)	CT10 NLO	P2011C
W/Z+jets	Sherpa, up to four additional jets, massive c and b quarks only leptonic W/Z decays	CT10 NLO	internal
dibosons (WW, WZ, ZZ)	Sherpa, massive c and b quarks	CT10 NLO	internal
single-top			
t-channel	AcerMC+Pythia6	CTEQ6L1	P2011C
Wt and s-channel	PowHeg+Pythia6	CT10 NLO	P2011C
single-top+Z	MadGraph+Pythia6	CTEQ6L1	AUET2B
$t\bar{t}$ + vector boson(s) (W, Z, WW)	MadGraph+Pythia6	CTEQ6L1	AUET2B

Table 4.1: The generators and settings, PDF sets and underlying event tunes used for the production of the nominal background samples.

The dominant background from $t\bar{t}$ events is well described by the NLO generator PowHeg, as was confirmed in comparisons with other generators and with data. The agreement is improved further by the event re-weighting described in section 4.4.3.

The sub-dominant W+jets background is found to be well modelled by Alpgen [108] (using the MLM matching scheme [147]) and Sherpa (using CKKW matching [148]). While Alpgen allows to separate samples by the number of additional hard partons N, Sherpa allows to easily generate samples restricted to a certain W p_{T} range. The latter is more practical in our case, as it allows to better sample the high p_{T} tail.

Signal samples (direct stop pair production)

decay modes	**generator / remarks**	**PDF set**	**UE tune**
$\tilde{t}_1 \rightarrow t^{(*)} + \tilde{\chi}_1^0$	Herwig++	CTEQ6L1	UEEE3
$\tilde{t}_1 \rightarrow b + \tilde{\chi}_1^{\pm}$ $\hookrightarrow W^{(*)} + \tilde{\chi}_1^0$	MadGraph, parton shower in Pythia6, $\tilde{t}_1$ decay in Pythia6 for off-shell W	CTEQ6L1	AUET2B
$\tilde{t}_1, \tilde{t}_1 \rightarrow t + \tilde{\chi}_1^0, b + \tilde{\chi}_1^{\pm}$	MadGraph+Pythia6	CTEQ6L1	AUET2B

Table 4.2: Generators, PDF sets and underlying event (UE) tunes used for the production of the signal samples. Depending on the assumed sparticle masses, the decays may involve off-shell top quarks or W bosons, indicated by a * symbol.

As shown in table 4.2, the stop signal samples have been produced with Herwig++ for the $\tilde{t}_1 \rightarrow t + \tilde{\chi}_1^0$ samples (including the three-body decay mode), while MadGraph+Pythia6 has been used for the $\tilde{t}_1 \rightarrow b + \tilde{\chi}_1^{\pm}$ and asymmetric decay samples. The main advantage of MadGraph is the more accurate modelling of additional jets from initial state radiation (ISR). However, the polarisation information is lost in the transition from MadGraph to Pythia, so decays should be simulated in MadGraph whenever polarisation effects cannot be neglected (most notably for *compressed* models having small sparticle mass differences and therefore decay products with lower momenta). For the scenarios studied in this thesis, the two generators are largely equivalent, as the selections developed in the following do not rely on ISR. The most important remaining differences are in the lepton p_{T} distribution, which is harder in the Herwig++ samples, and the b-jet p_{T} distribution, which is harder in the samples produced using MadGraph+Pythia6 (see figure 4.8).

4.4.1 Signal grids and generator filters

The three-body events were simulated for stop masses between 110 GeV and 400 GeV, and with a stop-neutralino mass difference 90 GeV<Δm<170 GeV, roughly corresponding to the kinematic limits of the three-body decay model. Step sizes of $20 - 30$ GeV in the sparticle masses were used. The number of events to be simulated for each signal model shown in figure 4.9a follows the theoretical stop pair production cross-section, which falls steeply with increasing stop mass. A filter is applied that only accepts events with a lepton ($p_{\mathrm{T}} > 20$ GeV, $|\eta| < 2.8$) and satisfying $E_{\mathrm{T}}^{\mathrm{miss}} > 60$ GeV. The filter is applied at generator level (before running the full reconstruction), where the event kinematics is only approximately known. For this reason, the filter requirements are less stringent than the object identification requirements and region definitions used in the following. The usage of the filter reduces the required storage and CPU time: at $m(\tilde{t}_1) = 110$ GeV, only

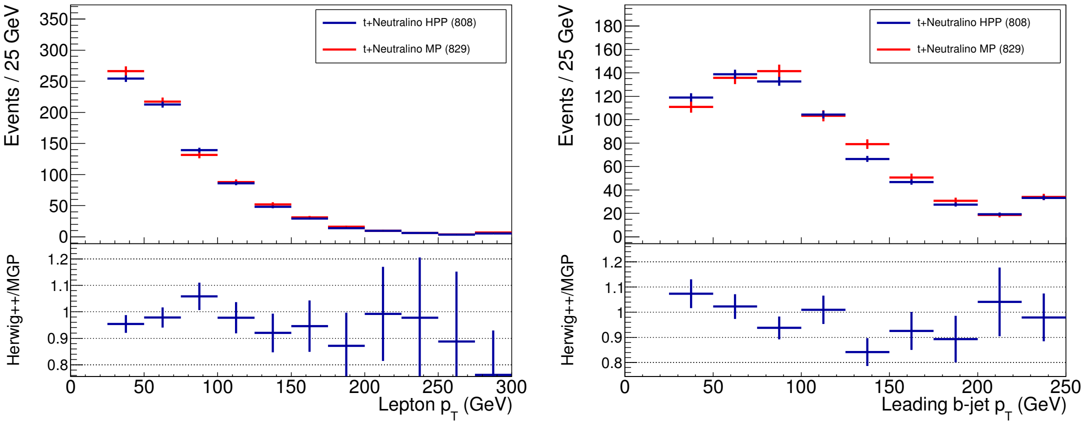

a) **b)**

Figure 4.8: Comparison of signal benchmark samples with $m_{\tilde{t}_1} = 400$ GeV and $m_{\tilde{\chi}_1^0} = 100$ GeV produced with Herwig++ (blue) and MadGraph+Pythia6 (MGP, red). **a)** The leptons in the Herwig++ sample have a higher p_T on average, **b)** while the leading b-jet p_T tends to be lower in comparison. The distributions are obtained using events with exactly one lepton, 3 or more jets and $E_\mathrm{T}^\mathrm{miss} > 100$ GeV.

$\sim$8% of the events pass the filter, due to the relatively soft event kinematics, increasing to $\sim$25% at $m(\tilde{t}_1) = 400$ GeV.

Also the pure $\tilde{t}_1 \to b + \tilde{\chi}_1^\pm$ events are filtered at generator level: about 1/3 of the events are removed because they do not have a lepton ($p_\mathrm{T} > 10$ GeV, $|\eta| < 2.8$) in the final state. This should be kept in mind when looking at selection efficiencies, but is irrelevant once typical selection requirements have been applied.

For each mixed mass point, three samples corresponding to the different decay modes were produced with a typical mass spacing of 50 GeV. The grid is shown in figure 4.9b, with the amount of simulated events mixed according to (4.2). Neutralino masses below 50 GeV are not considered due to the LEP limit on the chargino mass ($\gtrsim$100 GeV) [69]. The three decay modes considered in the mixed models use the same SUSY mixing assumptions as detailed above. While it would have been preferable to use identical mixing assumptions for the three processes, this minor inconsistency was accepted as it allowed to reuse many existing samples. Its impact is expected to be small: the possibly optimistic assumption of a mostly right-handed stop results in a stop mass exclusion limit about 50–100 GeV compared to a model with a fully left-handed stop. However, this assumption is used only for the decays where both stops decay as $\tilde{t}_1 \to t + \tilde{\chi}_1^0$, which contribute 25% of the events at $x = 0.5$, while the pure $\tilde{t}_1 \to b + \tilde{\chi}_1^\pm$ events assume a fully left-handed stop.

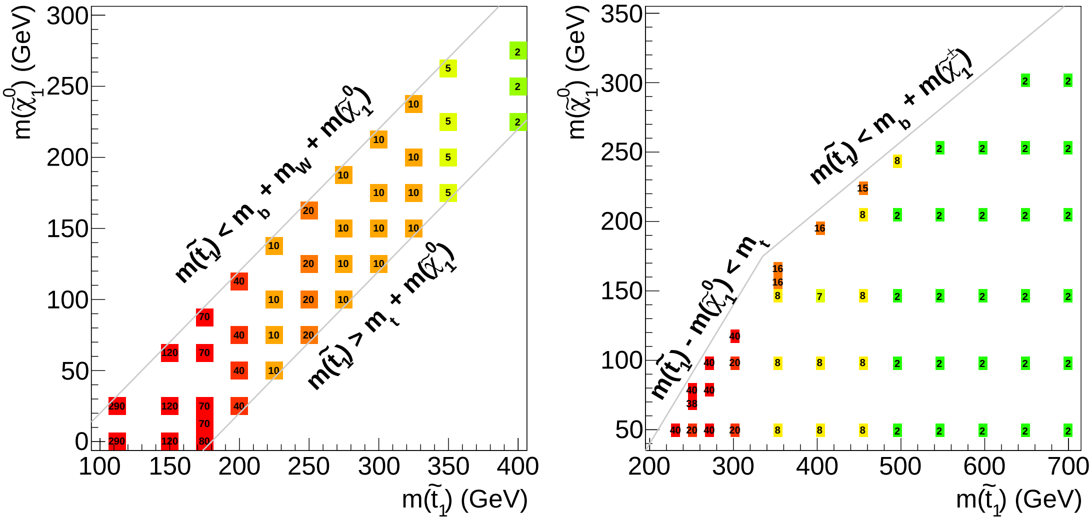

a) **b)**

Figure 4.9: Number of simulated events in multiples of 10,000 for different **a)** three-body stop and **b)** mixed stop ($\mathcal{BR}$ = 50%) models. In the context of these grids, the individual models are also referred to as *mass points*. For the three-body events and for the $\tilde{t}_1 \rightarrow b + \tilde{\chi}_1^\pm$ component of the mixed models, generator filters were applied, and only events passing the filter were reconstructed and processed further. For example, roughly 35 million events were generated at $m(\tilde{t}_1)$ = 110 GeV, $m(\tilde{\chi}_1^0)$ = 1 GeV to obtain 2.9 million events after the filter.

4.4.2 Event weights, scale-factors and sample normalisation

To describe the kinematic distributions observed in data as precisely as possible, it is common to assign a *weight* to each simulated event, increasing or reducing its contribution to yields or in histograms. Several sources contribute to this weight: a generator event weight; pile-up re-weighting (section 4.1.4); and *scale-factors* (SFs) for the trigger and selected objects.

The SFs have been derived by the ATLAS performance groups to improve the agreement of data and simulation, and are evaluated following their current recommendations, including p_{T}- and η-dependent SFs for selected electrons and muons [89, 92], SFs for the single lepton triggers [149, 150], and SFs for b-tagging of jets [101] (accounting also for the possibility of mistakenly b-tagging a light jet). Each SF has an uncertainty that needs to be propagated to the systematic uncertainty of the expected event yields.

Each simulated sample is normalised to match the number of simulated events, N_{MC}, to the expected number of events, N_{exp}. The latter is the product of the process cross-section σ, the generator filter efficiency ε (determined during the sample generation) and the recorded integrated luminosity $\mathcal{L}_{\text{int}} = 20.3\ \text{fb}^{-1}$. The normalisation factor is therefore $N_{\text{exp}}/N_{\text{MC}} = \sigma\varepsilon\mathcal{L}_{\text{int}}/N_{\text{MC}}$.

Table 4.3 lists the amount of simulated events produced for each SM process, the theoretical cross-section, and the resulting *equivalent luminosity*, defined as the number of simulated events divided by the theoretical cross-section. For all major backgrounds, the equivalent luminosity is larger than the recorded integrated luminosity, as otherwise a needlessly large statistical uncertainty would arise. For the evaluation of some of the systematic uncertainties on the $t\bar{t}$ and W+jets backgrounds, additional variants of the samples have been used, see section 5.5.1 for details.

Backgrounds from $t\bar{t}$ and W+jets events are only initially normalised using theoretical cross-sections ([151–156] and [157]), this is later refined with a data-driven method (see section 5.6). For the remaining SM processes, the theoretical cross-sections are used throughout the analysis (Z+jets [157], diboson [158, 159], single-top [160–162], single-top+Z [163] and $t\bar{t}+W/Z$ production [164, 165]). The W+jets sample can be subdivided into samples where all of the additional jets are of light flavour (originating from a gluon or u, d, s quark), or heavy flavour (originating from c or b quark), abbreviated as WLF or WHF. When this is not mentioned explicitly, we refer to the entire W+jets sample. Events with hadronic W decays or fully hadronic $t\bar{t}$ decays are not simulated, as their contributions are negligible compared to the other decay modes in a single lepton event selection.

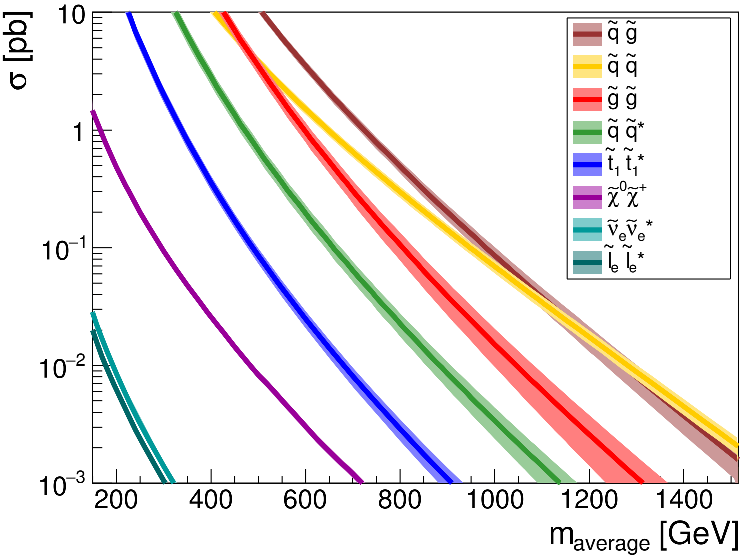

Figure 4.10: Sparticle production cross-sections computed using the SUSY generator Prospino [166] and corrected for soft-gluon emissions at NLL accuracy [167].

process	N_{MC}	$\sigma \times \mathcal{BR}$	**equivalent luminosity**
$t\bar{t}$, semi- and di-leptonic	75M	137.4 pb	546 fb^{-1}
W+jets, $W \to \ell\nu$	125M	36.6 nb	3.17 fb^{-1}
b-jet	16M	468 pb	26.8 fb^{-1}
c-jet	13M	1.68 nb	5.85 fb^{-1}
light quark or gluon jets	97M	34.4 nb	2.63 fb^{-1}
Z+jets, $Z \to \ell\ell$	55M	10.4 nb	5.00 fb^{-1}
b-jet	13M	301 pb	37.8 fb^{-1}
c-jet	17M	2.94 nb	5.28 fb^{-1}
light quark or gluon jets	25M	7.20 nb	3.39 fb^{-1}
WW, WZ, ZZ, semi- and di-leptonic	19M	61.1 pb	315 fb^{-1}
WW	10M	28.8 pb	357 fb^{-1}
WZ	4.2M	22.3 pb	208 fb^{-1}
ZZ	4.8M	9.99 pb	479 fb^{-1}
single-top	34M	52.6 pb	1072 fb^{-1}
t-channel	7.7M	28.4 pb	271 fb^{-1}
Wt-channel	20M	22.4 pb	891 fb^{-1}
s-channel	6.0M	1.82 pb	3300 fb^{-1}
single-top + Z	200k	35.3 fb	5670 fb^{-1}
$t\bar{t}$ + vector boson	1.6M	227 fb	5480 fb^{-1}
$t\bar{t} + W$	0.8M	111 fb	5150 fb^{-1}
$t\bar{t} + Z$	0.8M	115 fb	5820 fb^{-1}
$t\bar{t} + WW$	10k	0.92 fb	10900 fb^{-1}

Table 4.3: Summary of SM sample sizes produced with the software and settings described in section 4.4, and the theoretical cross-sections they were normalised to. Most samples are subdivided, for example the W+jets sample is composed of 54 sub-samples, separated by W p_{T} (6 slices), 3 W decay modes, and the presence of c or b quarks (3 slices). This allows to represent the more relevant processes with a higher equivalent luminosity.

The signal samples are normalised using the theoretical stop pair production cross-section computed at NLO+NLL [166, 167], shown in figure 4.10 in a comparison with other SUSY production processes. For a given mass, the production cross-section of stop pairs is smaller than for other squarks (simply denoted as $\tilde{q}$). This is due to the absence of top sea quarks in the protons, and hence the absence of the corresponding t-channel production diagram.

4.4.3 Re-weighting of top-antitop events

The overall agreement between data and simulated events in many kinematic distributions is further improved when the simulated $t\bar{t}$ events receive an event-weight which is based on the momentum of the $t\bar{t}$ system at truth-level as shown in table 4.4. The weights were derived using a recent ATLAS measurement of differential $t\bar{t}$ production cross-sections [128], including a measurement of $\mathrm{d}\sigma_{t\bar{t}}/\mathrm{d}p_{\mathrm{T}}(t\bar{t})$. Since a measurement of the $p_{\mathrm{T}}(t\bar{t})$ distribution in data is beyond the scope of this work, we observe the positive effect of the re-weighting procedure on the agreement between data and simulation in other kinematic distributions: as an example, figure 4.11 shows a comparison of the $E_{\mathrm{T}}^{\mathrm{miss}}$ spectrum in data and simulation before and after $t\bar{t}$ re-weighting. Both the overall normalisation and the shape of the distribution improve notably, although discrepancies in the tail remain.

$\mathbf{p_T(t\bar{t})}$ **in GeV**	**event-weight**
< 40	0.9971
$40 \ldots 170$	0.9396
$170 \ldots 340$	0.7343
> 340	0.5701

Table 4.4: Weights applied to simulated $t\bar{t}$ events.

This re-weighting procedure for the PowHeg+Pythia6 $t\bar{t}$ events was chosen from several options. This particular re-weighting will not be necessary in the future, as recent studies show that the agreement between data and simulated events generated with PowHeg is much improved when the model parameter `hdamp` is set to m_{top} [168].

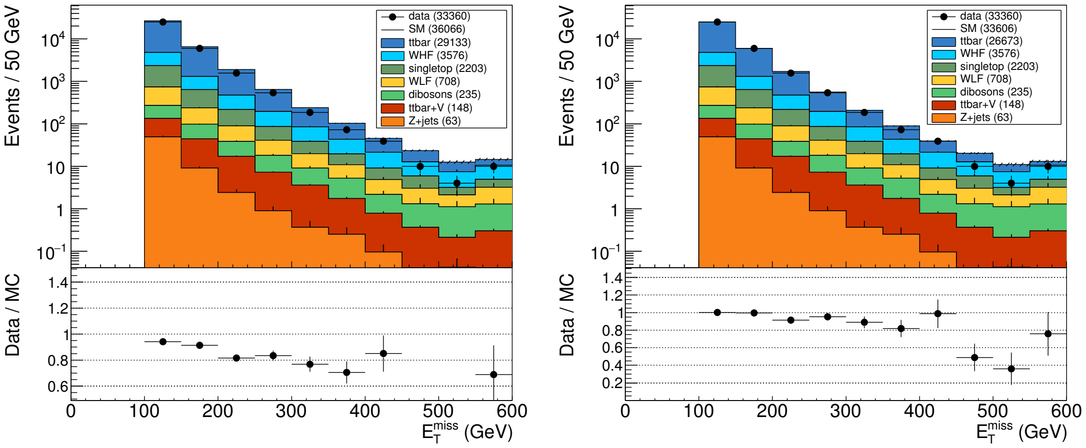

a) **b)**

Figure 4.11: Distribution of missing transverse momentum $E_{\mathrm{T}}^{\mathrm{miss}}$ **a)** before and **b)** after $t\bar{t}$ re-weighting; other SM processes and data are unchanged between the two plots. A basic preselection with a b-tag requirement (see section 5.2) has been applied to enhance the fraction of $t\bar{t}$ events. Here and in the following plots, the numbers in the legend are event yields (observed yield for data; expected yield for simulation). The *SM* legend entry shows the sum of all SM processes. The rightmost bin also contains all events with higher $E_{\mathrm{T}}^{\mathrm{miss}}$.

5 | Analysis

> If you wish to become an optimist and understand life, stop believing what people say and write; observe and discover for yourself.
>
> *Anton Chekhov*

The stop search presented in this chapter has been developed by a team of ATLAS physicists over a period of approximately two years, improving on the $\sqrt{s} = 7$ TeV results published in ref. [169]. Intermediate progress reports for the $\sqrt{s} = 8$ TeV analysis were presented at several conferences [170, 171] and the final results were published in JHEP [121]. This chapter puts emphasis on my personal contributions to this analysis; in particular, out of the fifteen signal regions presented in the publication, only the two established by my effort are discussed in detail.

5.1 Analysis Strategy

There are two principal strategies to search for new particles: one can tailor the analysis to the properties of a specific hypothetical particle, or instead study a variable or a region of phase space looking for deviations from SM predictions without necessarily having a specific model of new physics in mind. The present analysis uses the first approach, and restrictions have been placed on the considered production and decay modes of the hypothetical particle: the selections target stop pairs directly produced by the strong interaction that decay into final states with exactly one electron or muon.

The core principle of this search can be summarised as follows: a set of selection criteria is defined which has a significantly higher selection efficiency for the targeted stop events (*signal*) than for SM events (*background*). The resulting region of phase space is referred to as a *signal region* (SR); the full analysis has several SRs, defined and evaluated independently. The number of SR events is evaluated from the data and is also estimated using simulated events. Depending on how well measurement and simulation agree, statistical statements about discovery or non-observation of the top squark can be made.

The power of this approach depends on the achieved signal-to-background ratio (S/B) in the SR and the size of the uncertainties of the predicted signal and background yields. Statistical uncertainties may become the limiting factor for very tight selections; what is feasible mostly depends on the integrated luminosity of the recorded data, as it is usually possible to generate additional simulated events. If the exclusion is limited by the size of the systematic uncertainties (for example related to the detector modelling or the understanding of the simulated process), adding more events will be of little use. One important way of reducing the systematic uncertainties on the dominant background yields is through the use of *control regions* (CRs); this is explained in detail in section 5.6.

A good SR definition needs to address various requirements and is thus usually found in an iterative procedure. Once a preliminary SR has been defined, a statistical analysis based on simulated yields is used to evaluate the *expected* potential for a possible discovery or exclusion. The latter is usually presented in so-called contour plots; figure 5.1 shows the situation in summer 2012 as an example. The figure shows the expected exclusion contour as well as the actually *observed* exclusion contour, using the full recorded dataset available at that time; this curve is only evaluated once the SR definition is final, to avoid a possible bias. The key difference between the estimated and observed exclusion contour is that the estimate does not take into account the actual number of data events observed in the SR. This statistical technique is referred to as *blinding*.

The results in figure 5.1 have been derived using SUSY models with a reduced sparticle content and different stop and neutralino masses, assuming a mostly right-handed $\tilde{t}_1$ and 100% branching ratio for $\tilde{t}_1 \rightarrow t + \tilde{\chi}_1^0$. The numbers overlaid on the figure show the signal cross-section excluded at 95% confidence level (CL) for each simulated mass hypothesis. Whenever this value is larger than the stop pair production cross-section predicted from theory, the corresponding point on the mass-plane is excluded. Signal models for which the mass difference between $\tilde{t}_1$ and $\tilde{\chi}_1^0$ is below the top mass have not been studied.

Most of the systematic uncertainties are included in the yellow band: event generation (including among others the choice of generator, PDF set, renormalisation and factorisation scale); detector modelling and its effects on reconstructed objects and trigger decisions; as well as the uncertainty on the recorded integrated luminosity – everything that can influence the estimated maximal number of signal events compatible with observation. The expected number of signal events has an additional uncertainty coming from the theoretical uncertainty on the signal cross-section, indicated by dotted lines surrounding the observed contour. By convention, any mass hypothesis inside the -1σ theory line is considered as excluded.

Once all data yields have been evaluated, and the observed exclusion contour has been computed, an interesting situation may arise: a signal model that is expected to be excluded based on simulated events is not in fact excluded by the data. This is a possible hint of new physics.

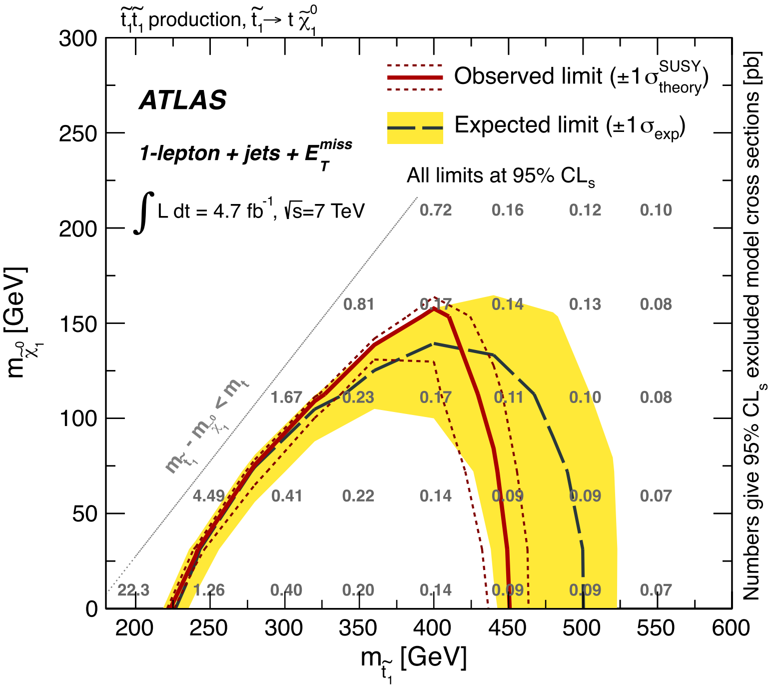

Figure 5.1: Expected (black dashed line) and observed (red solid line) exclusion contours in the plane spanned by $m(\tilde{t}_1)$ and $m(\tilde{\chi}_1^0)$, found in an ATLAS search for $\tilde{t}_1 \to t + \tilde{\chi}_1^0$ decays at $\sqrt{s} = 7$ TeV [169]. The yellow band describes the uncertainty due to experimental and theoretical uncertainties affecting the background estimates, while the red dotted line accounts for the uncertainty of the theoretical signal cross-section. For a massless $\tilde{\chi}_1^0$, one excludes $m(\tilde{t}_1)$ in the range from 225 to 435 GeV at 95% CL.

An important recent example of such a development was the inability to exclude (at 95% CL) a Higgs boson at the LHC in the mass ranges between 122 GeV and 127 GeV [172, 173], followed by its discovery at 5σ with a mass of $m_H \approx 125$ GeV with more data several months later [24, 27]; see also sections 1.2 and 2.5. For supersymmetric particles this has not yet occurred.

Over the past two years, the overall strategy of the 7 TeV stop analysis was maintained, but improved in several important aspects that are discussed in the remainder of this chapter:

- The full $\sqrt{s} = 8$ TeV dataset recorded by ATLAS in 2012 has been used ($L_{\text{int}} = 20.3$ fb^{-1}, compared to 4.7 fb^{-1} in the 7 TeV analysis [169]).
- The original analysis only considered $\tilde{t}_1 \to t + \tilde{\chi}_1^0$ decays. Additional $\tilde{t}_1$ decay modes have been added (see section 4.2).
- The SR definitions have been updated and new SRs have been introduced, reaching a total of 15 SRs (compared to 5 SRs [169]), optimised for different decay modes and sparticle mass assumptions, and carefully validated.
- Powerful discriminating variables have been added and employed in the SR construction.
- The method used to normalise the dominant backgrounds has been refined by updating the CR definitions and employing shape-fits.

As before, the analysis is built on event selections with exactly one lepton in the final state. The two SRs which are my main personal contribution target the so-called three-body and mixed stop scenarios described in the next section.

5.2 Event preselection

The signal models presented in section 4.2 all contain the same final state objects: exactly one lepton, four or more jets (two of which originate from b-quarks, and the other two from a hadronic W decay) and typically large missing transverse momentum $E_{\text{T}}^{\text{miss}}$ from the neutrino and the two neutralinos. With this in mind, the following preselection is defined as a starting point for further investigation:

- Typical ATLAS *event and data quality* cuts are applied: at least one primary vertex, reconstructed from at least four tracks ($p_{\text{T}} > 400$ MeV) is required to reject non-collision backgrounds (beam-halo, beam-gas interactions, and cavern backgrounds). Events with muons not passing near the primary vertex may be the result of cosmic ray background and are rejected, as are events with badly reconstructed muons or jets.

- A *trigger* from a sufficiently energetic electron or muon, or from sufficiently large $E_{\mathrm{T}}^{\mathrm{miss}}$ is required. Any of the triggers listed in section 3.4 is accepted (logical OR). For the lepton triggers, the type of trigger is required to correspond to the type of the selected signal lepton.

- Exactly *one signal electron or muon* ($p_{\mathrm{T}} > 25$ GeV, within ID acceptance, see sections 3.3.3 and 3.3.4 for details) is required. Events with another electron or muon fulfilling at least the baseline definition ($p_{\mathrm{T}} > 10$ GeV) are vetoed.

- *Four or more jets* reconstructed with the anti-k_t algorithm using a size parameter of $R = 0.4$ (cf. section 3.3.5). The jets are ordered by descending transverse momentum p_{T}. The leading jet is required to exceed a p_{T} threshold of 80 GeV, while for the other three jets the threshold used in the jet object definition is used ($p_{\mathrm{T}} > 25$ GeV). The jets must be in the ID acceptance ($|\eta| < 2.5$).

- The leading two jets must not be aligned with the missing momentum $\Delta\phi(\mathrm{jet}_{1,2}, \vec{E}_{\mathrm{T}}^{\mathrm{miss}}) > 0.8$. This is a precaution against events with fake $E_{\mathrm{T}}^{\mathrm{miss}}$ resulting from a poorly measured jet energy.

- Optionally, at least *one b-tagged jet* among the leading four jets may be required, using the MV1 algorithm at its 70% WP. This significantly reduces the contribution from W+jets events.

- Significant *missing transverse momentum*, $E_{\mathrm{T}}^{\mathrm{miss}} > 100$ GeV, strongly reducing several backgrounds, and bringing multi-jet events to a negligible level.

For some of the distributions shown in the following, we deviate slightly from this preselection for illustration purposes; this is mentioned explicitly in the figure captions. Detailed descriptions of object reconstruction and identification are given in section 3.3.

Although two jets from b-quark decays are present in signal events, there is a significant inefficiency in the b-tagging procedure, so a looser preselection requirement is used. The published analysis occasionally deviates from this preselection, for example a b-tag veto is used to study models with $\tilde{t}_1 \to b + \tilde{\chi}_1^{\pm}$ decays where the mass difference between $\tilde{t}_1$ and $\tilde{\chi}_1^{\pm}$ is small and the b-jet may be too "soft" to be tagged; other mass assumptions are best studied using a two b-tag requirement at a more efficient working point. For the three-body and asymmetric stop decay scenarios these possibilities were explored, but not found to be useful.

Requiring exactly one lepton in the final state means that the analysis is designed around stop pair production events in which one W decays hadronically and the other leptonically (semi-leptonic events). This requirement, together with the high $E_{\mathrm{T}}^{\mathrm{miss}}$ cut, helps to reduce the impact of multi-jet backgrounds to a negligible level, while still profiting from a high branching ratio. Searches in the fully hadronic and dileptonic stop decay channels have also been performed [174, 175].

requirements	**$t\bar{t}$ yields and efficiencies**				**W+jets yields and efficiencies**			
	e channel		μ channel		e channel		μ channel	
Generated events	5135.9×10^3	100.0%	5135.9×10^3	100.0%	2415.9×10^6	100.0%	2415.9×10^6	100.0%
Generator filter	2788.8×10^3	54.3%	2788.8×10^3	54.3%	805.3×10^6	33.3%	805.3×10^6	33.3%
Skimming	2754.9×10^3	98.8%	2754.9×10^3	98.8%	304.3×10^6	37.8%	304.3×10^6	37.8%
Generator weight	–		–		305.8×10^6	100.5%	305.8×10^6	100.5%
Custom reweighting	2623.8×10^3	95.2%	2623.8×10^3	95.2%	–		–	
Pile-up re-weighting	2619.1×10^3	99.8%	2619.1×10^3	99.8%	273.9×10^6	89.6%	273.9×10^6	89.6%
Event/data quality	2590.5×10^3	98.9%	2590.5×10^3	98.9%	260.0×10^6	94.9%	260.0×10^6	94.9%
Trigger (any)	1617.1×10^3	62.4%	1617.1×10^3	62.4%	199.3×10^6	76.7%	199.3×10^6	76.7%
Lepton ($\geqslant$1 baseline)	732.8×10^3	45.3%	668.2×10^3	41.3%	95.3×10^6	47.8%	92.5×10^6	46.4%
Lepton ($\geqslant$1 signal)	558.9×10^3	76.3%	562.6×10^3	84.2%	77.6×10^6	81.4%	85.7×10^6	92.6%
Lepton (= 1 signal)	497.9×10^3	89.1%	497.7×10^3	88.5%	77.6×10^6	100.0%	85.7×10^6	100.0%
Lepton (= 1 baseline)	447.1×10^3	89.8%	445.1×10^3	89.4%	77.3×10^6	99.6%	85.3×10^6	99.5%
Trigger (corresponding)	446.8×10^3	99.9%	444.8×10^3	99.9%	77.3×10^6	100.0%	85.3×10^6	100.0%
$\geqslant$3 jets > 25 GeV	372.7×10^3	83.4%	371.7×10^3	83.6%	1742.6×10^3	2.3%	1892.4×10^3	2.2%
$\geqslant$3 jets $> 60, 25, 25$ GeV	336.7×10^3	90.3%	337.2×10^3	90.7%	894.6×10^3	51.3%	963.0×10^3	50.9%
$\geqslant$4 jets $> 80, 25, 25, 25$ GeV	181.4×10^3	53.9%	182.6×10^3	54.2%	217.4×10^3	24.3%	235.7×10^3	24.5%
$E_{\mathrm{T}}^{\mathrm{miss}} > 50$ GeV	103.5×10^3	57.0%	109.1×10^3	59.8%	109.1×10^3	50.2%	124.0×10^3	52.6%
$E_{\mathrm{T}}^{\mathrm{miss}} > 100$ GeV	31.9×10^3	30.9%	34.0×10^3	31.2%	32.1×10^3	29.4%	36.3×10^3	29.3%
$\geqslant$1 b-tag (70% WP)	25.7×10^3	80.6%	27.5×10^3	80.8%	4.5×10^3	14.1%	5.1×10^3	14.0%
$\geqslant$2 b-tags (70% WP)	10.4×10^3	40.4%	11.2×10^3	40.6%	470.7	10.4%	552.3	10.8%

Table 5.1: Expected event yields and relative selection efficiencies for $t\bar{t}$ and W+jets at each step of the preselection. Fully hadronic $t\bar{t}$ events have been removed at generator level. Similarly, all W+jets events have been produced with a leptonic W decay. Electron and muon channel selections are common up to the lepton requirements. The single b-tag requirement is an optional part of the preselection, and the double b-tag requirement is shown only for illustration.

requirements	**three-body stop yields & eff.**				**mixed stop yields & eff.**			
	e channel		μ channel		e channel		μ channel	
Generated events	376398	100.0%	376398	100.0%	1737	100.0%	1737	100.0%
Generator filter	70164	18.6%	70164	18.6%	1595	91.8%	1595	91.8%
Skimming	69328	98.8%	69328	98.8%	1595	100.0%	1595	100.0%
Pile-up weight	69201	99.8%	69201	99.8%	1595	100.0%	1595	100.0%
Event/data quality	68283	98.7%	68283	98.7%	1580	99.1%	1580	99.1%
Trigger (any)	57356	84.0%	57356	84.0%	1425	90.2%	1425	90.2%
Lepton ($\geqslant$1 baseline)	28790	50.2%	25209	44.0%	373	26.2%	319	22.4%
Lepton ($\geqslant$1 signal)	22106	76.8%	21428	85.0%	257	68.9%	264	82.8%
Lepton (= 1 signal)	19322	87.4%	18554	86.6%	224	87.3%	231	87.5%
Lepton (= 1 baseline)	16944	87.7%	16291	87.8%	205	91.4%	213	92.1%
Trigger (corresponding)	16936	100.0%	16281	99.9%	205	100.0%	213	100.0%
$\geqslant$3 jets >25 GeV	12798	75.6%	12505	76.8%	193	94.0%	199	93.8%
$\geqslant$3 jets $>60, 25, 25$ GeV	10062	78.6%	10001	80.0%	189	98.1%	197	98.9%
$\geqslant$4 jets $>80, 25, 25, 25$ GeV	4978	49.5%	5071	50.7%	149	78.9%	156	79.4%
$E_{\mathrm{T}}^{\mathrm{miss}} > 50$ GeV	4681	94.0%	4797	94.6%	142	94.9%	149	95.1%
$E_{\mathrm{T}}^{\mathrm{miss}} > 100$ GeV	2406	51.4%	2541	53.0%	121	85.2%	128	86.2%
$\geqslant$1 b-tag (70% WP)	1695	70.5%	1789	70.4%	100	83.0%	108	84.4%
$\geqslant$2 b-tags (70% WP)	527	31.1%	532	29.7%	46	45.5%	48	44.6%

Table 5.2: Expected event yields and relative selection efficiencies for two benchmark signal models at each step of the preselection. The single b-tag requirement is an optional part of the preselection, and the double b-tag requirement is shown only for illustration. The three-body model assumes $m(\tilde{t}_1) = 200$ GeV and $m(\tilde{\chi}_1^0) = 50$ GeV, resulting in $\tilde{t}_1 \rightarrow t + \tilde{\chi}_1^0$ decays with an off-shell top quark. The mixed decays assume $m(\tilde{t}_1) = 500$ GeV, $m(\tilde{\chi}_1^{\pm}) = 300$ GeV and $m(\tilde{\chi}_1^0) = 150$ GeV and a 50% branching ratio each for $\tilde{t}_1 \rightarrow t + \tilde{\chi}_1^0$ and $\tilde{t}_1 \rightarrow b + \tilde{\chi}_1^{\pm}$.

Tables 5.1 and 5.2 show the effect of the preselection on the dominant SM backgrounds and on benchmark signal models one requirement at a time (*cutflow*), separated into *electron channel* and *muon channel* based on the flavour of the selected lepton. The statistical uncertainties on the yields are $\lesssim$1% for all entries.

Since we are designing a one lepton event selection, we use $t\bar{t}$ and W+jets samples that do not contain (fully) hadronic events. Similarly, events without leptons are removed from part of the signal samples by a generator filter (to allow sharing of samples between analyses, not all samples are filtered in the same way). The pure $\tilde{t}_1 \to b + \tilde{\chi}_1^{\pm}$ samples are subjected to a lepton filter ($p_{\mathrm{T}} > 10$ GeV, $|\eta| < 2.8$), mostly removing fully hadronic decays. The three-body signal events also need to pass a lepton filter ($p_{\mathrm{T}} > 20$ GeV, $|\eta| < 2.8$) and are further required to satisfy $E_{\mathrm{T}}^{\mathrm{miss}} > 60$ GeV at generator level. The pure $\tilde{t}_1 \to t + \tilde{\chi}_1^0$ and the asymmetric stop decay samples are not filtered at generator level. It is important to remember these differences when comparing the background and signal tables. Since the filters are applied before detector simulation, their requirements are applied to truth-level variables, which can differ significantly from reconstructed variables. This can be seen clearly at the (reconstructed) $E_{\mathrm{T}}^{\mathrm{miss}} > 50$ GeV requirement for the three-body sample, which still rejects ∼6% of the events, although the generator filter rejected all events with a (truth) $E_{\mathrm{T}}^{\mathrm{miss}} < 60$ GeV. The full preselection requires a reconstructed $E_{\mathrm{T}}^{\mathrm{miss}} > 100$ GeV, and the signal region requirements discussed in section 5.4 are even more stringent, creating a large safety margin that prevents the generator filter from removing signal events that would pass the selection.

The next step for each process is *skimming*, another preprocessing step that removes events that are not of interest for our analysis. Only events that satisfy at least one of a list of trigger conditions are kept (longer than the list used in the analysis itself: various single lepton triggers, missing energy triggers, or a $\geqslant$3 jets with $p_{\mathrm{T}} > 25$ GeV trigger). Skimming hardly affects signal and $t\bar{t}$ events, but significantly reduces storage and CPU consumption for W+jets events.

The event generator and pile-up weights are applied early in the cutflow. Scale-factors (section 4.4.2) are applied together with the object requirements they relate to: the trigger SF is applied together with the check for any of the accepted triggers. The lepton SF is applied together with the signal lepton requirement, and the b-tagging SF is applied with the first b-tagging requirement. Only the b-tagging SF can have a sizeable impact (figure 5.2), while the trigger and lepton SFs are always close to 1 and rarely deviate by more than a few percent.

The trigger efficiency for signal appears to be lower than claimed earlier. This is a consequence of applying this requirement early on; if it is evaluated after the lepton and $E_{\mathrm{T}}^{\mathrm{miss}}$ requirements, efficiencies between 98% and 100% are found. This illustrates a more fundamental difficulty: since all kinematic variables are correlated to some extent, the apparent impact of each requirement depends on its position in the cutflow.

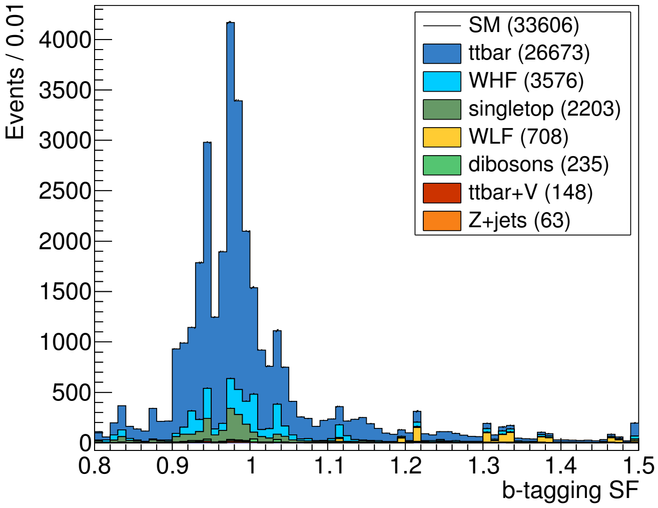

Figure 5.2: Distribution of b-tagging SFs computed for the events passing the preselection with b-tagging requirement. The SF is the product of correction factors for each jet, these factors depend on the p_{T}, η and source of the jet (b-quark, c-quark, light quark or gluon).

To compare the requirements on an equal footing while staying close to the full preselection, one can evaluate the effect of removing one requirement at a time; this *"$n-1$" comparison* is shown in table 5.3. As well as the trigger, the lepton and jet requirements also have a different impact when estimated this way. The following discussion is based on the cutflow tables (5.1 and 5.2), but remarks are made on the $n-1$ comparison where relevant.

There are no striking differences between corresponding electron and muon channel lepton selection efficiencies; the muon baseline definition appears to be relatively tighter, but the signal lepton selection efficiencies are similar. The second lepton veto, rejecting events with an additional signal or baseline lepton (shown as two separated lines in the tables) has nearly no impact for W+jets events, and removes about 20% of the $t\bar{t}$ and signal events, approximately corresponding to the expected fraction of dileptonic events. This fraction is reduced to about 10% in the $n-1$ comparison, as the jet requirements also reduce the fraction of dileptonic events. After the lepton selection, the trigger requirement is repeated, with the additional condition that an electron trigger is not accepted if the signal lepton is a muon, and vice versa, which occurs very rarely.

In the cutflows, only ~2% of W+jets events have three or more jets ($p_{\mathrm{T}} > 25$ GeV), while 75% or more of the other processes fulfil this requirement. Tightening the selection to events with four or more jets (leading jet $p_{\mathrm{T}} > 80$ GeV), about 50% of $t\bar{t}$ and about 12% of W+jets events remain (while in absolute numbers, W+jets is still the dominant background), as do about 80% of the mixed events and 25% of the three-body events, indicating very different jet characteristics between the two signal models. The $n-1$

$n{-}1$ selection efficiency	**$t\bar{t}$**		**W+jets**	
	e channel	μ channel	e channel	μ channel
Pile-up re-weighting	1.45%	1.02%	4.85%	4.29%
Event quality	0.83%	1.09%	0.77%	1.02%
Trigger	0.72%	1.67%	1.16%	0.70%
Trigger correspondence	0.03%	0.02%	0.01%	0.00%
Exactly one signal e/μ	77.18%	76.12%	85.90%	84.40%
Second lepton veto	10.67%	10.50%	1.54%	1.82%
Fourth jet presence	37.65%	37.92%	75.71%	75.57%
Leading jet $p_{\mathrm{T}} > 80$ GeV	10.90%	11.20%	10.06%	11.16%
$E_{\mathrm{T}}^{\mathrm{miss}} > 100$ GeV	83.05%	82.00%	85.07%	84.36%
$\geqslant$1 b-tag	19.44%	19.20%	85.88%	85.97%

$n{-}1$ selection efficiency	**three-body stop**		**mixed stop**	
	e channel	μ channel	e channel	μ channel
Pile-up re-weighting	0.9%	0.4%	0.1%	-1.8%
Event quality	1.0%	1.1%	0.9%	0.6%
Trigger	0.4%	2.9%	0.4%	1.2%
Trigger correspondence	0.0%	0.0%	0.0%	0.0%
Exactly one signal e/μ	51.7%	51.2%	84.2%	83.3%
Second lepton veto	9.6%	9.4%	7.8%	8.1%
Fourth jet presence	35.5%	35.1%	22.1%	22.0%
Leading jet $p_{\mathrm{T}} > 80$ GeV	22.8%	22.7%	3.4%	2.6%
$E_{\mathrm{T}}^{\mathrm{miss}} > 100$ GeV	52.3%	50.9%	19.2%	18.1%
$\geqslant$1 b-tag	29.5%	29.6%	17.0%	15.6%

Table 5.3: Fraction of expected background and signal event yields removed by various requirements ($n{-}1$ comparison), using the same stop models as in tables 5.1 and 5.2. For example, if all preselection requirements except the fourth jet presence have been applied, 37.65% of the selected e-channel $t\bar{t}$ events have at most three reconstructed jets and therefore will not satisfy the full preselection; in the same way, 83.05% have an $E_{\mathrm{T}}^{\mathrm{miss}}$ between 0 and 100 GeV. For the mixed stop benchmark point, the expected yield increases when pile-up re-weighting is applied, indicated by a minus sign. The efficiencies, especially for the lepton and $E_{\mathrm{T}}^{\mathrm{miss}}$ requirements, are distorted by the generator filters discussed above.

comparison shows a similar effect of the jet requirements, except that their impact on W+jets is significantly reduced when also $E_{\mathrm{T}}^{\mathrm{miss}} > 100$ GeV is required. The $E_{\mathrm{T}}^{\mathrm{miss}}$ requirements (shown in two steps, $E_{\mathrm{T}}^{\mathrm{miss}} > 50$ GeV and $E_{\mathrm{T}}^{\mathrm{miss}} > 100$ GeV, in the tables) reduce the SM backgrounds to about 15%, the three-body signal to about 50% (not accounting for events already removed by the generator filter), and the mixed signal to about 80%, meaning that also the $E_{\mathrm{T}}^{\mathrm{miss}}$ spectrum is harder for the mixed signal events. In the same way, the b-tagging efficiencies are higher for the latter (38% vs. 21% for double b-tagging). The selection efficiency of the b-tag requirement for $t\bar{t}$ events (32%) is in between that of the two signal models, while W+jets are reduced to about 1.5% by a b-tagging requirement.

Looking at the combined effect of the jet, $E_{\mathrm{T}}^{\mathrm{miss}}$ and b-tagging selection, the W+jets background is strongly suppressed, the $t\bar{t}$ background is suppressed by a factor ∼10 in comparison to the mixed signal model, but only by a factor ∼2 in comparison to the three-body signal model (comparing S/B before the jet requirements and after the 1 b-tag requirement). This already indicates that a search for three-body stop decays is at least as challenging as a search for mixed decays, despite the higher theoretical production cross-section.

While strongly enhancing the fraction of signal events in all selected events, the preselection by itself is not a suitable SR definition: it has expected yields of more than 20000 SM events (sum of both channels), but only ∼1000 three-body and ∼100 mixed stop events. Statistical uncertainties would clearly prevent us from making a meaningful statement about the mixed scenario, and systematic uncertainties on the yields also prevent this for the three-body scenario.

5.3 Discriminating variables

We now consider several kinematic distributions at preselection level, starting with commonly used variables before introducing more specialised ones. The comparison plots use the same reference signal models as used in the cutflows above: three-body decays with $m(\tilde{t}_1) = 200$ GeV and $m(\tilde{\chi}_1^0) = 50$ GeV and mixed decays with $m(\tilde{t}_1) = 500$ GeV, $m(\tilde{\chi}_1^\pm) = 300$ GeV and $m(\tilde{\chi}_1^0) = 150$ GeV at 50% branching ratio for both stop decay modes.

5.3.1 Jet kinematics

Signal events have four jets at tree-level, while most SM backgrounds have fewer; the exceptions are semi-leptonic and fully hadronic $t\bar{t}$ events, and diboson events (WW, WZ or ZZ) with fully hadronic decays. The actual number of jets will often differ: it can be smaller because jets are outside the detector acceptance (too forward or too soft) or not reconstructed due to an inefficiency, and it can be larger due to additional radiation in the hard process or the underlying event.

Figure 5.3 shows the distribution of the number of jets for a loosened preselection, requiring at least 3 jets ($p_{\mathrm{T}} > 60, 25, 25$ GeV) and optionally a b-tag requirement. Both signal models mostly have four or more jets, both in absolute numbers and relative to the SM background. A minimum requirement of four jets is therefore reasonable, while requiring five or more jets would result in a dependence on jets not originating from the hard process. The b-tag requirement further enhances S/B, and $t\bar{t}$ events become the dominant background, while W+light flavour jets events are strongly suppressed.

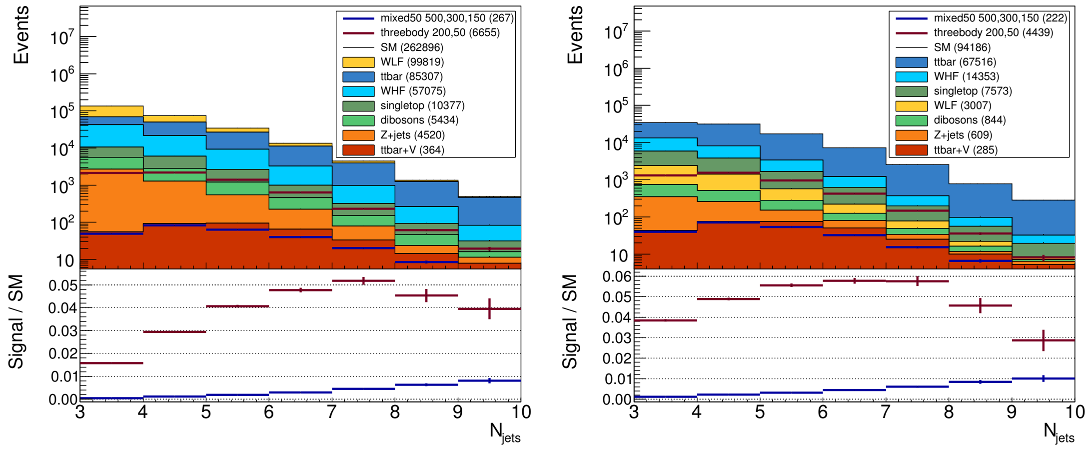

a) **b)**

Figure 5.3: Number of jets in simulated SM background and stop signal events using the $\geqslant$3 jet preselection. **a)** no b-tag requirement, **b)** one or more b-tags required. The signal benchmark models mentioned earlier in the text are included and labelled as “mixed50” and “threebody”. The normalisation corresponds to $\mathcal{L}_{\mathrm{int}} = 20.3\ \mathrm{fb}^{-1}$.

The p_T^{jet} distributions of the leading or sub-leading jet are shown in figure 5.4 for the $\geqslant$4 jet preselection with b-tagging requirement and the leading jet requirement kept at $p_{\mathrm{T}} > 60$ GeV. As seen in the cutflows, the three-body events have softer jets than the SM backgrounds, while the opposite is true for the mixed decays. In the tail of the signal distributions, some statistical fluctuations can be seen; it is important not to rely on such features when defining the event selection.

5.3.2 Transverse mass, m_{T2} and variations

In an event with only one non-interacting particle such as a neutrino or neutralino, its transverse momentum is estimated directly as $p_T^{\mathrm{invisible}} = \vec{E}_{\mathrm{T}}^{\mathrm{miss}}$. For a leptonic W boson decay we can use this to compute the *transverse mass* m_{T} of the W boson. To motivate the m_{T} definition, we start from the W invariant mass and simplify the expression by

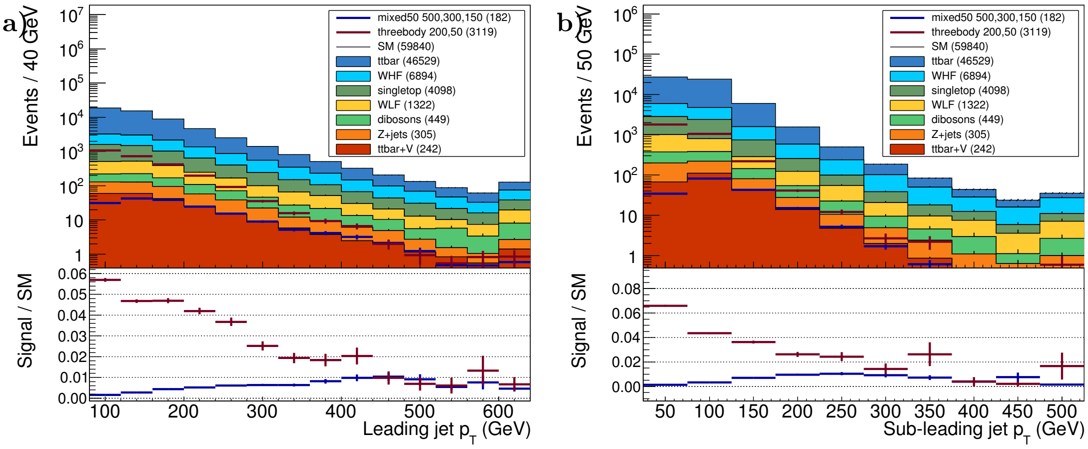

Figure 5.4: Transverse momentum distributions of the **a)** leading and **b)** sub-leading jet using a loosened 4 jet preselection ($p_{\mathrm{T}} > 60, 25, 25, 25$ GeV) with b-tag requirement.

neglecting the lepton and neutrino masses:

$$\begin{aligned} m_W^2 &= \left(\underline{p}_\ell + \underline{p}_\nu\right)^2 = (E_\ell + E_\nu)^2 - (\vec{p}_\ell + \vec{p}_\nu)^2 \\ &\approx (|\vec{p}_\ell| + |\vec{p}_\nu|)^2 - (\vec{p}_\ell + \vec{p}_\nu)^2 = 2\,|\vec{p}_\ell|\,|\vec{p}_\nu| - 2\,\vec{p}_\ell \cdot \vec{p}_\nu . \end{aligned}$$

We now replace the 3-momenta by transverse momenta to find the transverse mass

$$m_W^{\mathrm{T}} = \sqrt{2\,|\vec{p}_{\mathrm{T},\ell}|\,|\vec{p}_{\mathrm{T},\nu}| - 2\,\vec{p}_{\mathrm{T},\ell} \cdot \vec{p}_{\mathrm{T},\nu}} \tag{5.1}$$

$$\hat{=} \sqrt{2\,|\vec{p}_{\mathrm{T},\ell}|\,E_{\mathrm{T}}^{\mathrm{miss}}\left(1 - \cos\left(\Delta\phi(\vec{p}_{\mathrm{T},\ell}, \vec{E}_{\mathrm{T}}^{\mathrm{miss}})\right)\right)}, \tag{5.2}$$

In the second step, the scalar product is rewritten using the cosine of the azimuthal angle between lepton and neutrino, and replacing the neutrino's transverse momentum by $\vec{E}_{\mathrm{T}}^{\mathrm{miss}}$. Equation (5.2) is the commonly used expression for m_{T}; while it is aimed at events with one invisible particle, it is also meaningful in other cases.

Figure 5.5 shows the m_{T} distribution at preselection without b-tagging requirement. For accurately measured W+jets events, m_{T} is always smaller than or equal to m_W, and one sees a sharp decrease of the W+light jets contribution. This makes an $m_{\mathrm{T}} > m_W$ requirement an effective way to reject W+jets events and other SM backgrounds.

The fraction of signal events generally improves with increasing m_{T}. However, for three-body events, the distribution in figure 5.5a peaks near 100 GeV, and S/B reaches its maximum at around 140 GeV. This relative enhancement of signal events is less pronounced if the $E_{\mathrm{T}}^{\mathrm{miss}}$ requirement is not applied (figure 5.5b). The m_{T} distribution for mixed events is much broader, and its S/B does not show a local maximum (before run-

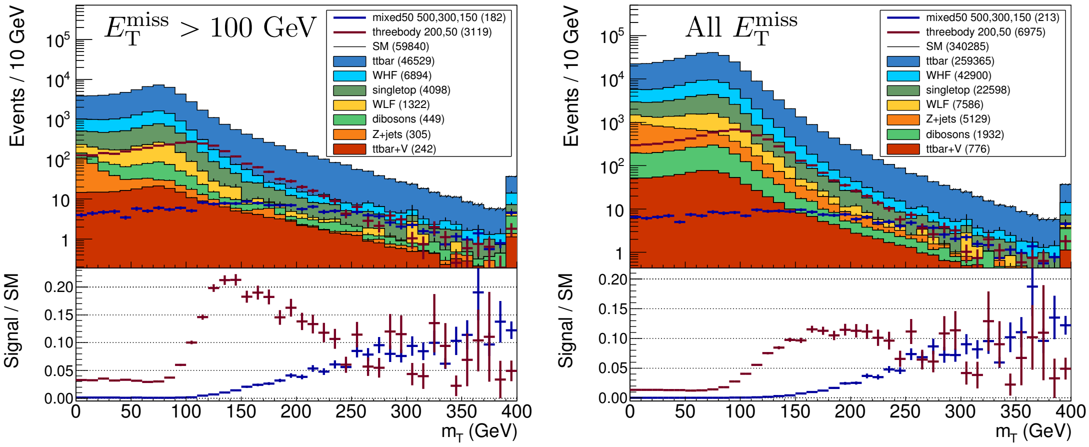

a) **b)**

Figure 5.5: Transverse mass distribution using the 4 jet preselection ($p_{\mathrm{T}} > 80, 25, 25, 25$ GeV) with b-tag requirement, shown **a)** with an $E_{\mathrm{T}}^{\mathrm{miss}} > 100$ GeV requirement and **b)** without $E_{\mathrm{T}}^{\mathrm{miss}}$ requirement. In both cases, most SM backgrounds have their largest contribution near $m_{\mathrm{T}} \approx m_W$, with the exception of the Z+jets component, which does not contain events with exactly one invisible particle.

ning into statistical limitations of the available simulated events). These characteristics are found over a wide range of stop masses and stop-neutralino mass differences.

While for the W transverse mass the lepton and neutrino masses can safely be neglected, it is useful to account for them in other cases. For a general two-body decay $A \to B + C$ one finds:

$$m_{\mathrm{T}}(B, C) = \sqrt{m_B^2 + m_C^2 + 2\left(E_{\mathrm{T},B}\ E_{\mathrm{T},C} - \vec{p}_{\mathrm{T},B} \cdot \vec{p}_{\mathrm{T},C}\right)} \leqslant m_A, \tag{5.3}$$

If C is an invisible particle, we may estimate its "transverse energy" E_T from the observed missing transverse momentum: $E_{\mathrm{T},C}^2 = \left(\vec{E}_{\mathrm{T}}^{\mathrm{miss}}\right)^2 + m_C^2$.

In events with two invisible particles, only the sum of their transverse momenta is measured, and assumptions need to be made to find the p_{T} of each particle. One possibility is to determine the invisible momenta assuming a specific decay topology. A very general class of topologies is targeted by the m_{T2} variable [176], designed for decays of two identical particles A, individually decaying as before, $A \to B + C$ (see sketch in figure 5.6). This variable is defined by the following minimisation prescription:

$$m_{\mathrm{T2}} = \min_{\vec{p}_{\mathrm{T,C_1}} + \vec{p}_{\mathrm{T,C_2}} = \vec{E}_{\mathrm{T}}^{\mathrm{miss}}} \left\{\max\left[m_T(\mathrm{B}_1, \mathrm{C}_1), m_T(\mathrm{B}_2, \mathrm{C}_2)\right]\right\} \leqslant m_A. \tag{5.4}$$

Each of the two m_{T} terms is smaller than m_A, the larger one is selected as it gives the stronger bound. The invisible transverse momenta $\vec{p}_{\mathrm{T},C_1}$ and $\vec{p}_{\mathrm{T},C_2}$ cannot be measured

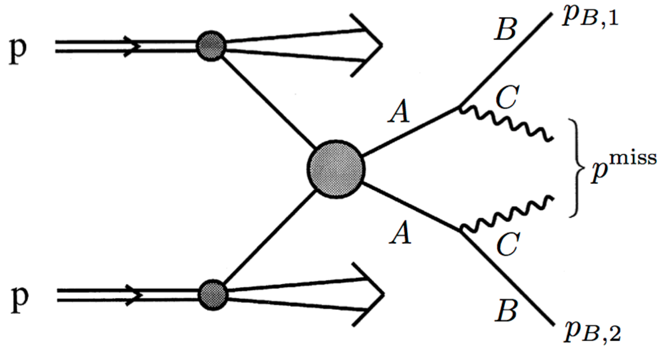

Figure 5.6: The m_{T2} variable assumes the production of a pair of A particles, each decaying into a reconstructed B particle and an invisible particle C. While the transverse momenta of the B particles are measured, for the C particles only the sum is known (adapted from [176]).

separately, and one instead evaluates all possible assignments using the observed $\vec{E}_{\mathrm{T}}^{\mathrm{miss}}$ as a constraint. Although the correct assignment is unknown, the minimum can safely be used as a lower bound on m_A. Because of this property, m_{T2} can either be used to constrain the masses of A and C, or to select signal events for given mass assumptions.

We use an m_{T2}-like variable to suppress incomplete dileptonic $t\bar{t}$ events. With the event topology shown in figure 5.7 in mind, we define an *asymmetric* m_{T2} variant, am$_{\mathrm{T2}}$, using the following assignments:

- visible object B$_1$: b-jet + lepton
- visible object B$_2$: other b-jet
- invisible mass $m_{C_1} = 0$ GeV (neutrino)
- invisible mass $m_{C_2} = m_W$ (missing lepton+other neutrino)
- reconstructed mass $m_{A_1} = m_{A_2} = m_t$

Not all events have two identified b-jets. Instead, the two jets with the highest MV1 weights are used. Both possible assignments are evaluated and the smaller am$_{\mathrm{T2}}$ result is kept. In the asymmetric case, the two m_{T} terms in (5.4) are evaluated using a different assumption about m_C. Since the larger of the two terms is chosen and $m_A > m_C$ by construction, am$_{\mathrm{T2}}$ has a lower bound of am$_{\mathrm{T2}} > m_W$. Using the same reasoning as for the symmetric case, and ignoring the detector resolution, one expects to find am$_{\mathrm{T2}} < m_t$ for *incomplete* dileptonic $t\bar{t}$ events (figure 5.8).

The top quarks in three-body stop decays are produced off-shell, and the upper bound becomes am$_{\mathrm{T2}} < \Delta m = m_{\tilde{t}_1} - m_{\tilde{\chi}_1^0}$. The upper bound is not strict: due to detector resolution it is often exceeded in reconstructed events, while the lower bound of m_W

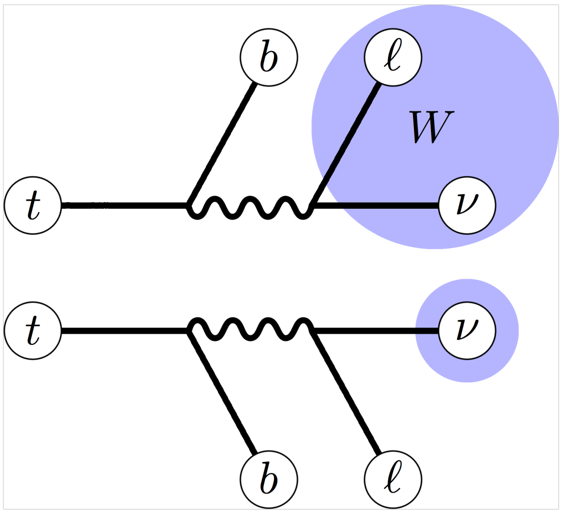

Figure 5.7: Topology of an incomplete dileptonic $t\bar{t}$ decay, targeted by the am$_{\mathrm{T2}}$ and topness variables. The non-reconstructed lepton renders the W boson it originated from invisible. This W boson and the neutrino from the other W boson decay contribute to the missing energy of the event.

holds by construction. This leads to an enrichment of three-body stop events at or near m_W.

5.3.3 Topness

The *topness* variable [177] was also designed to suppress incomplete dileptonic top-antitop events, with a particular emphasis on the discriminating power against asymmetric stop decay events.

The topness t of an event is defined as $t = \ln\left(\min(S)\right)$, where

$$\begin{aligned} &S(p_{W,x}, p_{W,y}, p_{W,z}, p_{\nu,z}) = \\ &\frac{\left(m_W^2 - (\overline{p}_\ell + \overline{p}_\nu)^2\right)^2}{a_W^4} + \frac{\left(m_t^2 - (\overline{p}_{\mathrm{b}_1} + \overline{p}_\ell + \overline{p}_\nu)^2\right)^2}{a_t^4} + \\ &\frac{\left(m_t^2 - (\overline{p}_{\mathrm{b}_2} + \overline{p}_{\mathrm{W}})^2\right)^2}{a_t^4} + \frac{\left(4\,m_t^2 - (\overline{p}_\ell + \overline{p}_\nu + \overline{p}_{\mathrm{b}_1} + \overline{p}_{\mathrm{b}_2} + \overline{p}_{\mathrm{W}})^2\right)^2}{a_{\mathrm{CM}}^4}. \end{aligned} \tag{5.5}$$

To motivate the topness definition we compare the individual terms of S to figure 5.7. Two four-momenta, $\overline{p}_{\mathrm{W}}$ and $\overline{p}_\nu$, are required to describe the not-reconstructed W boson and the neutrino, respectively. By assuming those particles to be on their mass shells ($\overline{p}_{\mathrm{W}}^2 = m_W^2$ and $\overline{p}_\nu^2 = 0$) and using the missing energy as an additional constraint ($p_{\mathrm{T}W} + p_{\mathrm{T}\nu} =$

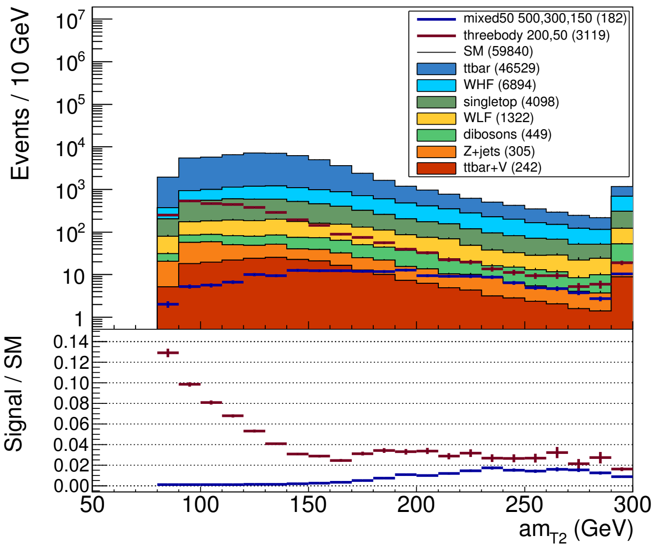

Figure 5.8: Distribution of $\mathrm{am}_{\mathrm{T2}}$ in signal and background, using the preselection with $\geqslant$1 b-tag requirement.

$\vec{E}_{\mathrm{T}}^{\mathrm{miss}}$), only four real parameters need to be determined in the minimisation (chosen as the W boson three-momentum and the longitudinal component of the neutrino).

The first term on the right-hand-side of equation (5.5) describes the observed W boson decay by relating the invariant mass of the presumed decay products to the W mass. Its relative impact is defined through the resolution term $a_W = 5$ GeV. Similarly, the second and third terms compare the invariant masses of the decay products of the reconstructed and non-reconstructed top decays, respectively, using $a_t = 15$ GeV. The last term captures the overall kinematics of the top-antitop pair and its decay products, using a centre-of-mass resolution term $a_{\mathrm{CM}} = 1$ TeV. The values of the resolution terms are the estimates suggested in ref. [177], describing “typical” resolutions for an individual event[1]. No improvement of the discrimination power was seen for modified resolution terms, so the suggested values were kept.

S is related to the centre-of-mass energy E_{CM} of the hard scattering. Since PDFs fall steeply as a function of E_{CM}, small values of S are more likely to correctly capture the event kinematics, thus motivating the minimisation. At the same time, S can be seen as a χ^2 variable describing the resemblance of the event kinematics to an incomplete dileptonic event, with a small value of S implying a good description.

An example of simulated topness distributions for $t\bar{t}$ background and an asymmetric stop signal benchmark point is shown in figure 5.9.

---

[1] The mass resolution in a dedicated ATLAS W boson or top mass measurement is significantly better, for example $m_t = (174.5 \pm 2.3)$ GeV was achieved in the one-lepton measurement using the 2011 dataset [129]

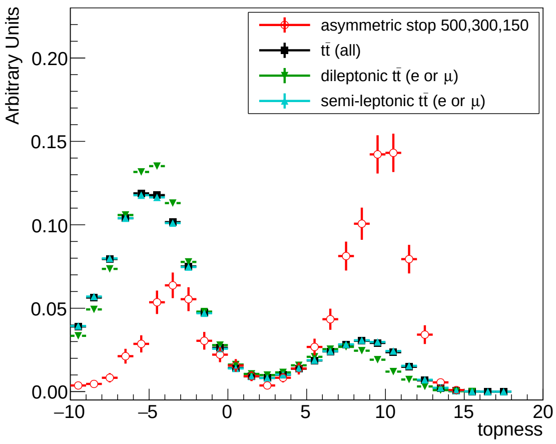

Figure 5.9: Topness distributions for $t\bar{t}$ events and fully asymmetric stop decays after preselection with a b-tag requirement, normalised to unit area. The processes targeted by the topness variable (partial dileptonic $t\bar{t}$ events, and asymmetric stop events) are separated very well. The $t\bar{t}$ sample does not contain fully hadronic events.

5.3.4 Hadronic top mass reconstruction

A top quark can in principle be identified through the invariant mass of its decay products. Selecting those decay products from all objects in an event is the main difficulty. Several of the variables introduced above make use of the missing transverse energy due to the neutrino originating from the leptonically decaying top quark; the m_{jjj} variable attempts to describe the invariant mass of three jets originating from the hadronic top decay. A variety of prescriptions for the jet selection have been tested, including a χ^2-based method analogous to the topness definition that fully evaluates the effect of the individual jet energy uncertainties on the resulting invariant mass.

However, for the signal regions developed in the following section 5.4, a much simpler approach produced the best results: using all selected jets, the invariant mass m_{jj} of all jet pairs is computed; of all pairs with $m_{\mathrm{jj}} > 60$ GeV, the jet pair with the smallest separation ΔR is retained. In a second iteration, all possible combinations of this pair with one of the remaining jets are evaluated. The three-jet invariant mass m_{jjj} is required to satisfy $m_{\mathrm{jjj}} > 130$ GeV, and the one with the smallest ΔR with respect to the combined two-jet four-momentum is kept. If no suitable jets are found, any selection requirement on m_{jjj} will lead to the rejection of the event. Figure 5.10a shows the simulated distributions; a slight enhancement in S/B of mixed stop events can be seen at least for intermediate m_{jjj} values.

This construction was developed for the 7 TeV stop search [169]. It was optimised to first find the two jets from the W boson and then combine them with the b-jet, together yielding the invariant mass of the top quark. It is problematic in the sense

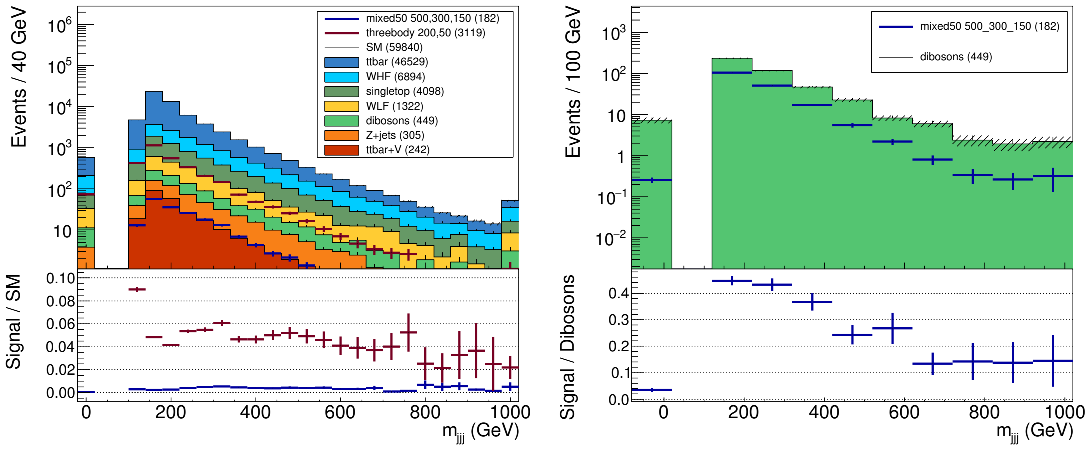

a)

b)

Figure 5.10: **a)** Distribution of the three-jet invariant mass m_{jjj}, using the jet selection method described in the text, after the preselection with b-tag requirement is applied; in **b)** only the diboson contribution and the mixed stop decay model are shown for a direct comparison; note the enhancement of signal events for lower m_{jjj}. The underflow bin contains events without three suitable jets.

that it only enforces minimal requirements on the combined invariant masses, and will find three suitable jets for the vast majority of SM events (~99% after preselection with b-tag, 99.6% for $t\bar{t}$ events), with m_{jjj} significantly larger than the top mass, resulting in a long tail in the distribution. Large values of m_{jjj} are seen especially for diboson events (figure 5.10b), for which the combined jets stem from two different objects. In consequence, during the SR optimisation discussed below, an upper limit on m_{jjj} is introduced to reduce the contribution of diboson events, although this is not what the variable was originally designed for.

5.3.5 Hadronic tau veto

Dileptonic $t\bar{t}$ decays involving a hadronically decaying τ lepton will frequently satisfy a semi-leptonic event selection. This background is also problematic because the τ neutrino created in the decay typically increases the $E_{\mathrm{T}}^{\mathrm{miss}}$ in the event (figure 5.11). To suppress such events, an explicit veto on an identified hadronic τ is employed, using the recommendation of the τ performance group [178]: the τ candidate is required to satisfy a transverse momentum $p_{\mathrm{T}}^{\tau} > 15$ GeV and to be contained within the ID acceptance ($|\eta| < 2.47$). At least one track needs to be associated to it – if the number of tracks is odd, it is assumed that all tracks originating from this τ decay have been reconstructed, and its charge is inferred from the tracks' curvatures. The summed track charge is required to be ±1 and to be opposite to the charge of the signal lepton. Tau candidates with two tracks are assumed to be incomplete 3-prong decays, and no charge requirement is applied in this case. Boosted decision trees (BDT) have been trained by the τ performance group that separate 1- or 3-prong τ jets from quark- or gluon-initiated jets; we use the tight BDT working points for τ identification. Lastly, the τ candidate is not considered if it is near a baseline lepton ($\Delta R < 0.2$).

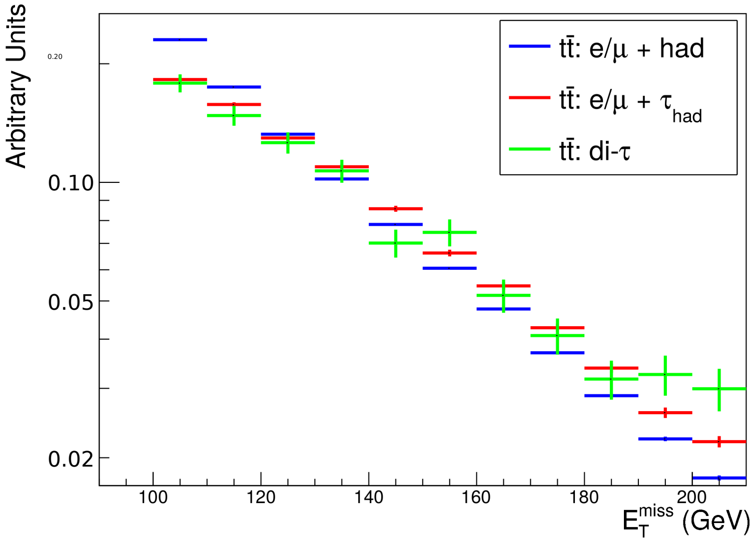

Figure 5.11: Normalised $E_{\mathrm{T}}^{\mathrm{miss}}$ distributions of different $t\bar{t}$ decay modes. The additional neutrinos in events with τ decays tend to increase the $E_{\mathrm{T}}^{\mathrm{miss}}$.

Any events with a τ candidate fulfilling the above identification requirements will be rejected. Because the tight BDT working point is used, the veto has a small effect overall. Once sufficiently high $E_{\mathrm{T}}^{\mathrm{miss}}$ and m_{T} requirements are imposed ($E_{\mathrm{T}}^{\mathrm{miss}} > 150$ GeV, $m_{\mathrm{T}} > 120$ GeV), the veto has little impact on stop signal events and primarily rejects the $t\bar{t}$ events it was designed for: 24% of dileptonic events with a 1- or 3-prong τ decay, and only 10% of semi-leptonic events. The veto rejects approximately 2% of the mixed benchmark events and approximately 6% of the three-body benchmark events.

5.4 Signal Region definition

Several important discriminating variables have been introduced above. We complete the list by briefly mentioning several other kinematic variables of potential interest:

- the transverse momentum of the selected lepton, $p_{\mathrm{T},\ell}$;
- various angular separations (ΔR or $\Delta\phi$) between the lepton, the jets, and the missing transverse momentum $E_{\mathrm{T}}^{\mathrm{miss}}$;

- the scalar sum of the leading four selected jets' transverse momenta, $H_{\mathrm{T}}^{4\,\mathrm{jets}} = \sum_{i=1}^{4} |\vec{p_{\mathrm{T}}}^{\mathrm{jet},i}|$;
- the $E_{\mathrm{T}}^{\mathrm{miss}}$ significance $E_{\mathrm{T}}^{\mathrm{miss}}/\sqrt{H_{\mathrm{T}}^{4\,\mathrm{jets}}}$; and
- the effective mass $m_{\mathrm{eff}}^{4\,\mathrm{jets}} = H_{\mathrm{T}}^{4\,\mathrm{jets}} + E_{\mathrm{T}}^{\mathrm{miss}} + p_{\mathrm{T}}^{\ell}$.

The two SRs targeting the mixed and three-body stop scenarios were defined in an iterative approach. The insights obtained from the study of individual variables as presented above was used as a starting point for the automated procedure defined in the following. The outcome of this procedure was in turn used as a starting point for further checks and adjustments before applying the automated procedure again; after a few iterations, the resulting SR definitions were adequate to proceed.

For each considered variable, a list of reasonable cut thresholds was defined, based on simulated distributions of the signal and background processes. The variables and their thresholds can be pictured on a grid as shown in figure 5.12. In this picture, a SR definition corresponds to the choice of up two points in each row, a lower and possibly an upper threshold: the preselection is shown with red markers as an example. Open line endings indicate that the corresponding cut is optional, a cross at a line ending indicates that introducing that cut is forbidden, e.g. while an upper limit on the lepton p_{T} might be reasonable for the soft kinematics of a three-body decay, this would have lead to an overlap with a concurrent analysis effort expressly focusing on leptons with low momentum. Similarly, requiring the τ veto to fail (by introducing a < 1 requirement) would have let to selections enriched in dileptonic events with a hadronically decaying τ.

Once the grid definition and a starting selection have been defined, the automated procedure performs the following steps:

1. *evaluate the current selection* on simulated signal and background samples to find expected yields S and B;
2. compute a *figure of merit* for the current selection:
    - For looser selections, a signal significance estimate is used, defined as $S/\sqrt{S + B + \Delta B^2}$, assuming a flat relative systematic uncertainty on the background;
    - Once S/B exceeds 0.2, or S drops below 15 events, the $\mathrm{CL_s}$ method [179, 180] is used[2] is used, with a flat relative systematic uncertainty on the expected yields, and without the data-driven background normalisation described later.
3. All *neighbouring selections* are found and their figures of merit are computed;

---

[2] This choice of goal function implies the SR will be optimised for its exclusion reach, not for discovery potential.

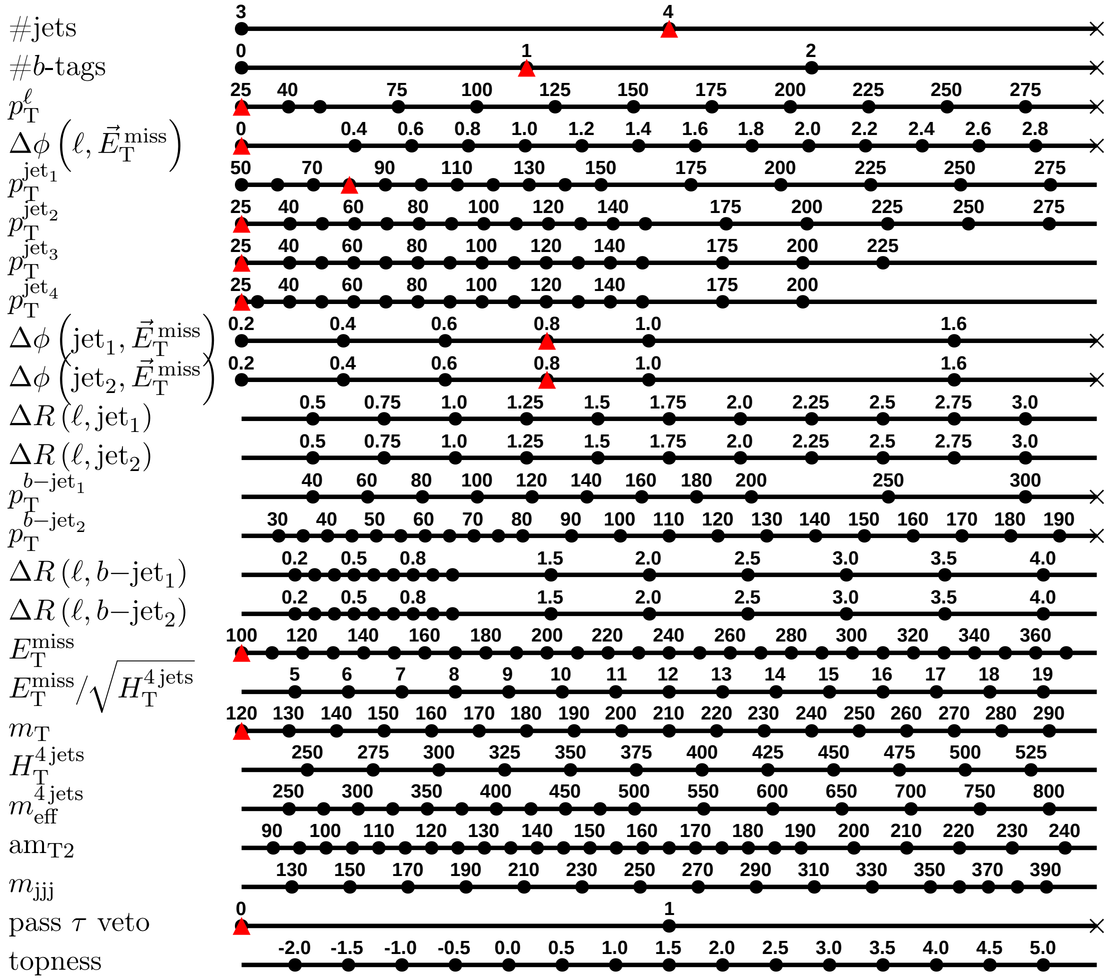

Figure 5.12: Illustration of the optimisation grid underlying the final stages of the signal region definition. The red markers show how the preselection is represented on this grid.

4. the *best performing* neighbouring selection is kept; and
5. the procedure terminates if no improvement is found, otherwise it is repeated from step 1.

Neighbouring selections are those for which only a single cut is tightened or loosened by one unit on the grid, or an optional cut is introduced (or possibly removed) at its loosest setting. In this manner, at most 4 neighbours per variable need to be evaluated; in practice this number is smaller, as not all possible lower or upper cuts are enabled.

Every five iterations and also after the final iteration, a summary plot is created, presenting the expected background composition and $\mathrm{CL_s}$ exclusion reach; the two summary plots for the final SR definitions are shown in figure 5.13. This type of summary plot has been used as a basis for adjustment to the grid, and eventually also for selecting the most suitable SR definitions.

While working with it, the technique has been refined in several ways:

- If a promising selection is found, it is tested for *stability*: iteratively, one cut at a time is removed, and the optimisation is rerun to test whether it converges to the same selection; this mitigates some cases of over-tuning the selection to statistical fluctuations of the simulated samples.
- If the optimisation cannot find any improvements, it randomly changes several cuts by a few steps, and resumes; this *mutation* sometimes helps to escape local minima.
- Optimisations were run alternately on signal models with different stop and neutralino mass assumptions; this helped finding selections that perform well across extended stretches of the mass-plane.
- To improve the available signal statistics, signal models corresponding to adjacent points on the mass-plane are simply evaluated as "combined models". Although this introduces a slight bias towards events from lower stop mass points (due to their higher production cross-section), the reduced statistical uncertainties result in an overall improvement.
- Attempts were made to reduce the bias towards very tight selections and the over-tuning this may cause: if S falls below 5, it is multiplied by a penalty term $\exp(S/5-1)$. Similarly, if B falls below 5, it is divided by $\exp(B/5-1)$.
- A significant speed-up was achieved by *caching* and *interpolating* $\mathrm{CL_s}$ values where possible, always computing them accurately if the estimate is near the current best.

The definition of the step-sizes on the grid is crucial: for this thesis, they were defined manually and were adjusted several times to balance the risks of over-tuning and missing interesting selections. If they are not well balanced between different variables,

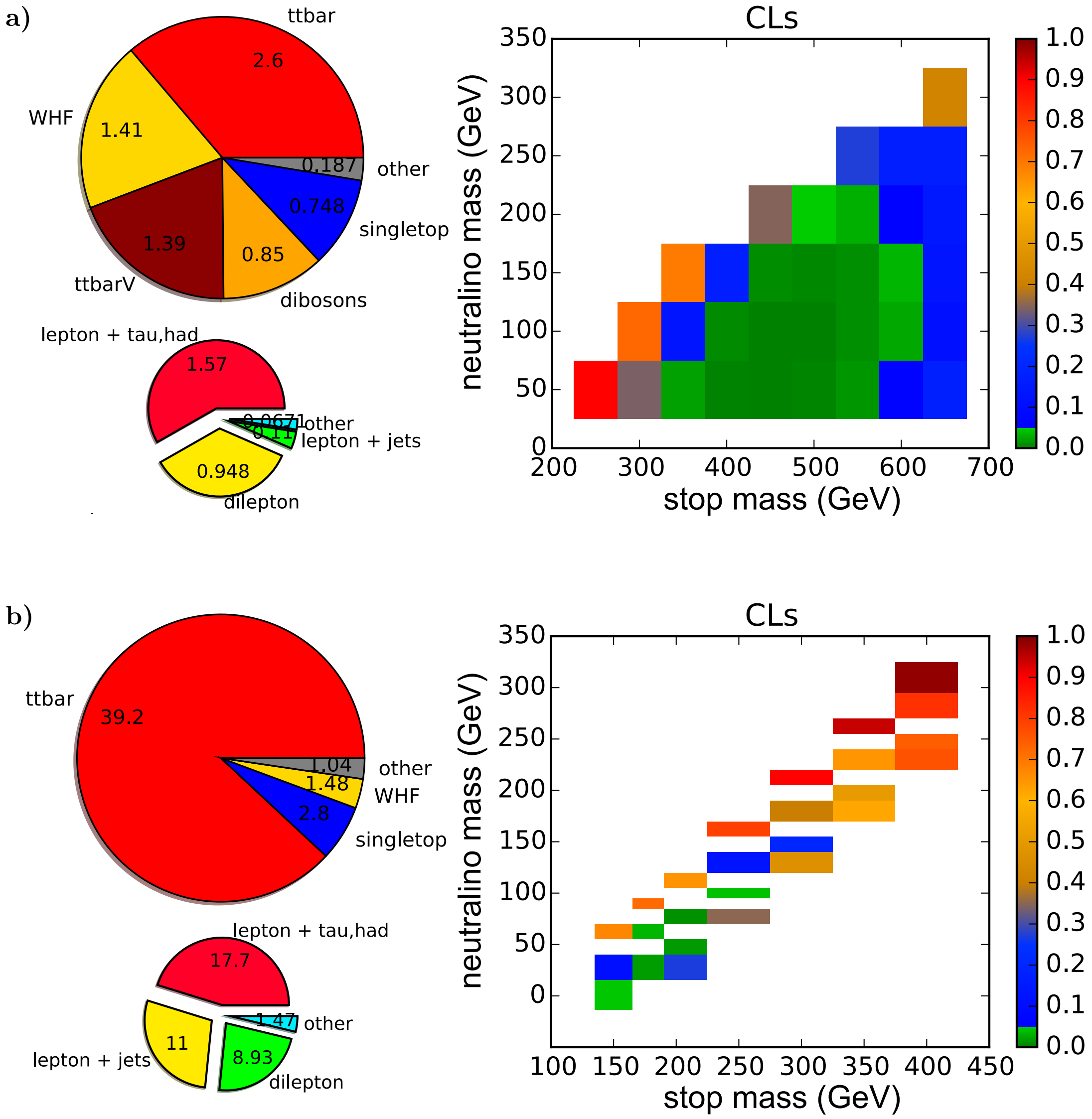

Figure 5.13: Visual representation of the SR performance for the definitions given in table 5.4. The upper pie chart shows the expected SM background yields, and the lower shows the dominant types of selected top-antitop events. The $\mathrm{CL_s}$ map shows an estimate of the expected exclusion reach, points with $\mathrm{CL_s} < 0.05$ are within reach and are shown in green. **a)** SR for mixed stop decays, **b)** SR for three-body stop decays. For the latter, the m_T and $\mathrm{am}_{\mathrm{T}2}$ cuts were loosened by 10 GeV each, as the SR is too tight to be used on its own; this will be discussed further in section 5.7.

some threshold changes may have relatively little impact and will be ignored by the optimisation, or picked up too late to guide the procedure in the best possible way. The grid definition was manually adapted whenever such an effect was observed, and the problem was mitigated to some extent by also considering "neighbouring" selections that are several steps away (e.g. exploring $E_{\mathrm{T}}^{\mathrm{miss}} > 120, 130, 140, \ldots$ GeV if the change from >100 to >110 resulted in an improvement). A possible improvement to be explored in the future is a dynamical definition of the step-sizes, based for example on quantiles of the current distributions.

The method has similarities to a simulated annealing optimisation: it should be explored if the convergence behaviour improves when not all neighbouring selections are evaluated, but instead a random neighbour is evaluated and selected with a probability that depends on its performance as well as the current "temperature" of the system. At high "temperature", a worse performing selection may also sometimes be selected. The system is then slowly "cooled" as the optimisation progresses. This strategy avoids local minima more elegantly than randomly loosening cuts if no improvement is possible.

After several iterations, suitable SR definitions for the three-body and mixed stop decay scenarios were found. In a final clean-up iteration, cuts with low impact or unclear physical interpretation were removed from the grid, to keep the definitions as simple as possible. Table 5.4 shows the final definitions, and the expected background composition is shown in table 5.5 (see also figure 5.13). For the most part, the SR definitions are intuitively understandable, while the interpretation is less clear for some cuts, for example the m_{jjj} requirement discussed above. The tight $\mathrm{am}_{\mathrm{T2}} < 90$ GeV requirement for the three-body SR is a consequence of the $\mathrm{am}_{\mathrm{T2}}$ definition (section 5.3.2): by construction we have $m_W \leqslant \mathrm{am}_{\mathrm{T2}} \lesssim m_t$; an off-shell top quark reduces the available range and leads to an enhanced S/B near the strict lower bound. The fact that only a small part at the edge of the $\mathrm{am}_{\mathrm{T2}}$ distribution is selected requires special attention (section 5.7).

5.5 Systematic uncertainties

The systematic uncertainties affecting the estimated SR yields can be divided into two main categories: theoretical uncertainties on the modelling of the particle physics processes that are studied, and uncertainties on the description of the experimental apparatus. The impact of all systematic uncertainties on the expected yields have been evaluated for all SM and SUSY processes to which they apply. All of the uncertainties are applied to simulated events; no unfolding of the data is needed for this search.

5.5.1 Modelling uncertainties

The following theoretical and modelling uncertainties have been evaluated:

	mixed SR	**three-body SR**
cleaning	ATLAS event and data quality cuts	
trigger	single lepton OR $E_{\mathrm{T}}^{\mathrm{miss}}$ trigger	
lepton	exactly one signal electron or muon, $p_{\mathrm{T}} > 25$ GeV	
jets	$p_{\mathrm{T}} > 80, 70, 50, 25$ GeV	$p_{\mathrm{T}} > 80, 25, 25, 25$ GeV
$\boldsymbol{b}$**-tagging**	$\geqslant$1 b-jet, $p_{\mathrm{T}} > 60$ GeV	$\geqslant$1 b-jet, $p_{\mathrm{T}} > 25$ GeV
$\boldsymbol{E_{\mathrm{T}}^{\mathrm{miss}}}$	>270 GeV	>150 GeV
$\boldsymbol{E_{\mathrm{T}}^{\mathrm{miss}}/\sqrt{H_T^{\mathrm{4\,jets}}}}$	>9 GeV$^{1/2}$	>5 GeV$^{1/2}$
$\boldsymbol{m_{\mathrm{T}}}$	>130 GeV	>120 GeV
am$_{\mathbf{T2}}$	>190 GeV	<90 GeV
$\boldsymbol{m_{\mathrm{jjj}}}$	<360 GeV	–
topness	>2	–
$\boldsymbol{\Delta\phi(\mathrm{jet}_{1,2}, \vec{E}_{\mathrm{T}}^{\mathrm{miss}})}$	>0.6	>0.2
$\boldsymbol{\Delta\phi(\ell, \vec{E}_{\mathrm{T}}^{\mathrm{miss}})}$	>0.6	>1.25
$\boldsymbol{\Delta R(\ell, \mathrm{jet}_1)}$	<2.75	>1.25
$\boldsymbol{\Delta R(\ell, \mathrm{jet}_2)}$	–	>2.0
$\boldsymbol{\Delta R(\ell, b\mathrm{-jet})}$	<3.0	–
$\boldsymbol{\tau}$**-veto**	yes	yes

Table 5.4: SR definitions optimised for the discovery of mixed and three-body stop decays. The jet p_{T} requirements are applied consecutively to the leading four selected jets, ordered by their p_{T}'s. B-jets are tagged using the MV1 algorithm at its 70% working point. The spatial separation between two objects is determined as $\Delta R = \sqrt{\Delta\phi^2 + \Delta\eta^2}$; for the separation with respect to $\vec{E}_{\mathrm{T}}^{\mathrm{miss}}$ only the azimuthal distance $\Delta\phi$ is used. See section 5.3 for the definition of the other discriminating variables.

process	**mixed SR**	**three-body SR**
$t\bar{t}$	2.60±0.30 (36%)	6.69±0.54 (90%)
W+jets	1.58±0.35 (22%)	0.14±0.10 (1.9%)
$t\bar{t}+Z$	1.08±0.07 (15%)	0.04±0.02 (0.5%)
$t\bar{t}+W/WW$	0.33±0.04 (4.6%)	0.05±0.02 (0.7%)
dibosons	0.85±0.31 (12%)	0.03±0.02 (0.4%)
single-top	0.75±0.14 (10%)	0.42±0.18 (5.7%)
SM	7.2± 0.6 (100%)	7.5± 0.6 (100%)
$m_{\tilde{t}_1}=400$ $m_{\tilde{\chi}_1^\pm}=200$ $m_{\tilde{\chi}_1^0}=100$	10.4± 0.9 (145%)	
$m_{\tilde{t}_1}=500$ $m_{\tilde{\chi}_1^\pm}=300$ $m_{\tilde{\chi}_1^0}=150$	12.1± 0.9 (169%)	
$m_{\tilde{t}_1}=600$ $m_{\tilde{\chi}_1^\pm}=400$ $m_{\tilde{\chi}_1^0}=200$	7.4± 0.4 (102%)	
$m_{\tilde{t}_1}=110$ $m_{\tilde{\chi}_1^0}=1$ $\Delta m=109$		5.1± 1.1 (69%)
$m_{\tilde{t}_1}=200$ $m_{\tilde{\chi}_1^0}=30$ $\Delta m=170$		3.0± 0.9 (41%)
$m_{\tilde{t}_1}=200$ $m_{\tilde{\chi}_1^0}=50$ $\Delta m=150$		6.8± 1.3 (91%)
$m_{\tilde{t}_1}=200$ $m_{\tilde{\chi}_1^0}=80$ $\Delta m=120$		11.3± 1.6 (151%)
$m_{\tilde{t}_1}=200$ $m_{\tilde{\chi}_1^0}=110$ $\Delta m=90$		1.5± 0.5 (20%)
$m_{\tilde{t}_1}=250$ $m_{\tilde{\chi}_1^0}=100$ $\Delta m=150$		9.6± 1.4 (129%)
$m_{\tilde{t}_1}=275$ $m_{\tilde{\chi}_1^0}=125$ $\Delta m=150$		4.5± 1.0 (61%)
$m_{\tilde{t}_1}=300$ $m_{\tilde{\chi}_1^0}=150$ $\Delta m=150$		5.4± 0.9 (72%)
$m_{\tilde{t}_1}=325$ $m_{\tilde{\chi}_1^0}=175$ $\Delta m=150$		2.6± 0.5 (35%)

Table 5.5: The expected yield and the relative contribution of each SM background process in the mixed and three-body SRs. Values for several stop benchmark points are shown. All sparticle masses are given in GeV, a branching ratio of 50% is assumed for the three mixed models.

- *Theoretical cross-section* uncertainties for the smaller SM backgrounds are obtained directly from the publications used for the nominal theoretical cross-section: 22% for the $t\bar{t}+W/Z$ process [164, 165], 5%–7% for the diboson processes [158, 159], and 7% for the single-top processes [160–162].

- Theoretical uncertainties on the total cross-section are irrelevant for $t\bar{t}$ and W+jets processes as they are later normalised on data.

- For the *scales* uncertainty, simulated samples with factorisation and renormalisation scale variations (scales changed up or down by a factor of 2) have been used. For the single-top uncertainty, the full difference between PowHeg and MC@NLO is considered instead (listed as the *generator* uncertainty).

- The *initial and final state radiation* (ISR and FSR) uncertainties for $t\bar{t}$ and single-top processes are obtained using dedicated AcerMC samples with different parton shower settings.
- The *PDF uncertainties* are obtained by varying the choice of PDF between CT10 NLO [105], MSTW2008 NNLO [181] and NNPDF21_100 [182], following the PDF4LHC recommendations [183].
- The *$t\bar{t}$ parton shower* uncertainty was evaluated in a comparison between PowHeg+Pythia6 and PowHeg+Herwig+Jimmy.
- The W+jets finite parton uncertainty accounts for the fact that only samples with up to 5 additional partons were produced.
- Due to the b-veto requirement of the WCR, the fraction of $W + b$ jet events cannot be estimated well, and the uncertainty on the normalisation coefficient μ_W does not account for this. Instead, we use the uncertainty of 24% on the measured $W + b$ cross-section with 2 additional jets [184][3]. A study using W+jets events with simulated Alpgen+Herwigfound an additional uncertainty of 15% for the extrapolation from 2 to 4 additional jets, to be added in quadrature. The resulting systematic uncertainty of 28% is applied to the $W + b$ yields in all regions with a b-tagging requirement.
- The uncertainty related to the interference between LO $t\bar{t}$ and NLO single-top production in the Wt-channel is evaluated by comparing the sum of the nominal $t\bar{t}$ and Wt samples treated with the diagram removal scheme to an inclusive AcerMC $WWbb$ sample.
- The contribution from Z+jets events is negligible for both SRs. Its theoretical/modelling uncertainty was conservatively estimated to be ±50%.

The effect of these systematic uncertainties on the expected SR yields is shown in table 5.6.

The uncertainty on the stop production cross-section varies between about 15% at $m(\tilde{t}_1) = 200$ GeV and 18% at $m(\tilde{t}_1) = 700$ GeV [185]. This is accounted for in the results by computing two additional exclusion contours using the $\pm 1\sigma$ cross-section variations.

5.5.2 Experimental uncertainties

The experimental uncertainties are evaluated either by using a modified set of scale factors (SFs; see section 4.4.2) or by running a modified object reconstruction.

The following experimental effects are described by modified SFs corresponding to $\pm 1\sigma$ variations:

---

[3] The final publication suggests a slightly larger uncertainty of 26%, while at the time of discussion the estimate was 24%.

process	**variation**	**mixed SR**	**three-body SR**
$t\bar{t}$	ISR/FSR	±7%	±2%
	scales	±1%	±2%
	parton shower	±1%	±7%
	PDFs	±1%	±4%
W+jets	finite partons	±6%	±2%
	scales	±5%	±23%
	PDFs	±2%	±5%
$t\bar{t}+V$	cross-section	±22%	±22%
	scales	±17%	±18%
	PDFs	±5%	±5%
WW,WZ,ZZ	scales	±30%	±26%
	cross-section	±7%	±7%
	PDFs	±6%	±6%
single-top	interference	±27%	±27%
	generator	±11%	±11%
	cross-section	±7%	±7%
	PDFs	±5%	±5%
	ISR/FSR	±1%	±1%
	hadronisation	±1%	±1%

Table 5.6: Relative size of each applicable generator systematic uncertainty for all SM background processes, shown separately for both SR definitions. The meaning of the different contributions is explained in the text.

- For electrons and muons, SF variations exist that model higher or lower lepton reconstruction and ID efficiencies.
- The uncertainty on the lepton trigger response was evaluated and is negligible.
- Three sets of $\pm 1\sigma$ b-tagging SF variations are used to model the effect of a higher or lower probability to assign a b-tag to a jet initiated by a b-quark, a c-quark, or by a light quark or gluon.
- An estimated pile-up distribution is used to generate the simulated samples, and then re-weighted to reflect the distribution found in data. Also for this weight, $\pm 1\sigma$ variations are computed. This is done by shifting the simulated number of interactions per bunch-crossing by $\pm 15\%$.

For the physics objects used in the event selection (electrons, muons, jets and $E_{\mathrm{T}}^{\mathrm{miss}}$), *scale* and *resolution* uncertainties are evaluated. Scale uncertainties are modelled by multiplying an object's energy or p_{T} by a factor (usually p_{T}- and η-dependent) that models the $+1\sigma$ or -1σ accuracy to which the underlying calibration is known ("up" or "down" variation, respectively). The resolution terms on the other hand are evaluated by randomly "smearing" an object's energy or p_{T}, using a multiplicative factor drawn from a normal distribution $\mathcal{N}(1, \sigma)$, where again the standard deviation σ is matched to the underlying resolution. While possible in principle, it is not always practical to have "up" and "down" variations for the resolution uncertainties. Since $E_{\mathrm{T}}^{\mathrm{miss}}$ is composed of the reconstructed physics objects, its uncertainty is mostly found by propagating the changes from the objects. Only the contribution from calorimeter clusters not assigned to a physics objects (*soft-term*) is subjected to scale variation and resolution smearing.

Table 5.7 shows the effect of the experimental systematic uncertainties on the event yields in the mixed SR. The normalisation of the dominant backgrounds discussed in the following section has not yet been applied to this table. The expected contribution from Z+jets processes is below 0.02 events and is not shown. The jet energy resolution (JER) and $E_{\mathrm{T}}^{\mathrm{miss}}$ soft-term resolution are one-sided by design; for the remaining uncertainties both variations are shown if they differ in magnitude, and summarised as $\pm x\%$ otherwise.

The dominant experimental uncertainties affecting the estimated signal and background yields arise from imperfect knowledge of the jet energy scale (JES) and jet energy resolution (JER) as well as from the modelling of the flavour tagging efficiencies. Generally the $+1\sigma$ uncertainties increase the selection efficiency, as they result in increased object momenta, $E_{\mathrm{T}}^{\mathrm{miss}}$ in the event, or number of b-tagged jets in the event; therefore, the selection requirements tend to be fulfilled more often. The reverse is also correct in general, but the effect may be pronounced when the relevant kinematic distributions have negative slopes.

The JES uncertainty is derived using a combination of data and simulated samples [93, 95]. It is applied to each jet as a function of the jet p_{T}, η, flavour (b, c or light/gluon

	SM	$t\bar{t}$	W**+jets**	$t\bar{t}+V$	VV	t	$\tilde{t}_1$ **400** $\tilde{\chi}_1^0$ **100**	$\tilde{t}_1$ **500** $\tilde{\chi}_1^0$ **150**	$\tilde{t}_1$ **600** $\tilde{\chi}_1^0$ **200**
Nominal	7.2	2.60	1.58	1.41	0.85	0.75	10.4	12.1	7.4
JES (1 parameter)	20%	19%	34%	12%	17%	11%	16%	20%	8%
	−9%	−11%	−9%	−8%	−2%	−16%	−19%	−12%	−7%
JES (17 parameters)	22%	31%	35%	9%	36%	12%	15%	16%	7%
	−15%	−19%	−26%	−8%	−33%	−18%	−17%	−16%	−5%
nuisance parameter 2	14%	15%	26%	6%	15%	1%	6%	9%	4%
	1%	1%	−1%	−4%	21%	−8%	−11%	−5%	−2%
η-intercalibration	13%	12%	26%	2%	20%	6%	3%	6%	3%
	0%	−2%	3%	−1%	−2%	0%	−5%	−7%	0%
flavour composition	12%	13%	22%	4%	15%	2%	7%	7%	2%
	0%	−1%	0%	−2%	21%	−14%	−9%	−4%	−2%
flavour response	8%	11%	5%	3%	17%	0%	2%	4%	2%
	1%	0%	0%	−2%	21%	−4%	−4%	−3%	−1%
JER	+5%	+7%	+16%	-2%	-8%	+3%	0%	+10%	+2%
flavour tagging (combined)	±4%	±3%	±5%	±4%	±8%	±6%	±7%	±4%	±4%
b-tagging	±3%	±2%	±2%	±4%	±2%	±6%	±3%	±5%	±4%
mistagging, c-jets	±3%	±2%	±3%	±1%	±8%	±1%	0%	0%	±1%
mistagging, light jets	±2%	±1%	±4%	0%	±3%	0%	±1%	0%	0%
$E_{\mathrm{T}}^{\mathrm{miss}}$ soft-term	+5%	+4%	0%	+1%	+22%	+2%	+2%	−3%	0%
	+2%	+3%	+5%	+1%	0%	0%	−2%	+1%	+1%
$E_{\mathrm{T}}^{\mathrm{miss}}$ soft-term resolution	+2%	+5%	0%	0%	0%	0%	-1%	-1%	0%
lepton (combined)	±2%	±3%	±4%	±1%	±1%	0%	±2%	±1%	±1%
pile-up model	±2%	±3%	±2%	0%	0%	±3%	±1%	0%	0%

Table 5.7: The expected number of events in the mixed SR and the relative size of experimental systematic uncertainties. Three benchmark signal models mixed at 50% BR are shown for comparison (sparticle masses in GeV). Only the largest of the 17 JES components are shown. "Up"-type and "Down"-type uncertainties have been combined where appropriate. Jet energy resolution (JER) and the $E_{\mathrm{T}}^{\mathrm{miss}}$ soft-term resolution are one-sided; assuming a deteriorated resolution typically results in an increased event acceptance. The systematic uncertainties related to lepton reconstruction and identification efficiencies, energy scale and resolution, and triggers, are all small and have been combined for this table (summation in quadrature).

jet) and the amount of pile-up; especially the changed jet momenta significantly affect the estimated rate of accepted events. There are two prescriptions to compute the JES uncertainty: either using a simplified description with a single uncertainty term, or decomposed into 17 components. The former does not capture all of the experimental aspects modelled by the individual components. The following contributions are accounted for in the detailed JES model: the uncertainty for an individual high momentum jet, and uncertainties due to the calibration method, related to pile-up correction, or related to the flavour composition and flavour response. The JER uncertainty is determined with in situ measurements of the jet response balance in di-jet events [99]. The b-tagging uncertainty is estimated by varying the b-tagging efficiency and mistag rate SFs, that have been measured in $t\bar{t}$ and di-jet events [186–189].

A large uncertainty for events with diboson production (VV) stems from the $E_{\mathrm{T}}^{\mathrm{miss}}$ soft-term. These decays often involve several neutrinos, making them sensitive to an $E_{\mathrm{T}}^{\mathrm{miss}}$ mismeasurement; further, the large fraction of c-jets ($\mathcal{BR}(W \to c + X) = 0.333 \pm 0.026$, [2]) in these events results in an increased c-mistagging uncertainty, as well as a large sensitivity to changes in the assumed jet energy scale or jet energy resolution. Single-top events with t-channel production have only one b-jet at tree-level, increasing the dependence on b-tagging.

The combined effect of all lepton related uncertainties (electron and muon ID and reconstruction efficiencies; electron and muon energy scale uncertainties; electron energy resolution; and electron trigger efficiency) on the expected yields is $\leqslant 4\%$ in all cases. The systematic uncertainty related to the average number of pp interactions per bunch crossing does not exceed 3%.

5.6 Control regions

Uncertainties can be reduced in a number of ways when designing a SR. It is important to rely as much as possible on variables that are well modelled in simulation and by using data-driven methods where possible. A major improvement of this kind is achieved by estimating the normalisation of the dominant backgrounds, $t\bar{t}$ and W+jets in dedicated *control regions* (CRs) that are enriched in SM background events and have only a small contribution from hypothetical signal events. The CRs neither overlap with the SR nor with each other. Instead of directly estimating the contribution from background processes to the SR using simulation, only the ratio between SR and CR yields is estimated in this way. The systematic uncertainties of these ratios are much smaller than the corresponding uncertainties of the simulated $t\bar{t}$ and W+jets yields in the SR.

The background normalisations are determined separately for the mixed and three-body SRs; we start with the mixed SR, as the situation is less complicated in this case.

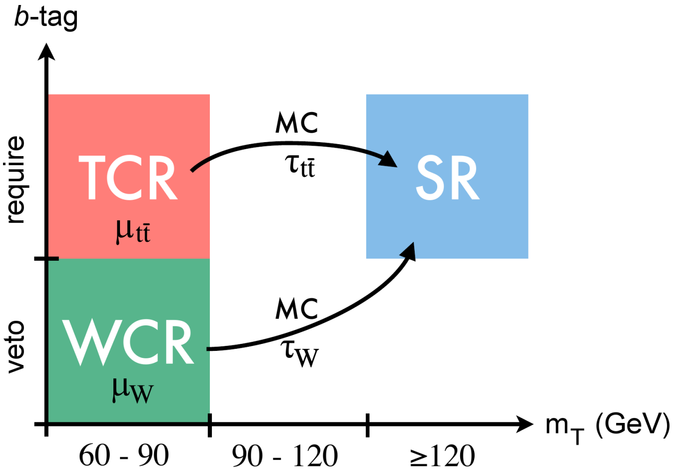

Figure 5.14: Illustration of the CR-based normalisation of the $t\bar{t}$ and W+jets backgrounds used for the mixed region. The normalisation coefficients μ are found using data, while the transfer factors τ used in the extrapolation are determined using simulated events.

As shown schematically in figure 5.14, two corresponding CRs are defined, one for each data-driven background normalisation.

- The TCR differs from the SR by a 60 GeV$< m_{\mathrm{T}} <$ 90 GeV requirement, in order to select $t\bar{t}$ and other events with leptonically decaying W bosons enriched in the Jacobian peak in the m_{T} distribution.
- The W control region (WCR) also requires 60 GeV$< m_{\mathrm{T}} <$ 90 GeV, and replaces the $\geqslant$1 b-tag requirement by a b-tag veto. This suppresses $t\bar{t}$ events and increases the number of selected W+jets events.
- To enhance statistics in the CRs, several other requirements are loosened:
  - am$_{\mathrm{T2}}$ needs to satisfy >120 GeV (instead of >190 GeV);
  - $E_{\mathrm{T}}^{\mathrm{miss}}$ needs to satisfy >170 GeV (instead of >270 GeV); and
  - $E_{\mathrm{T}}^{\mathrm{miss}}/\sqrt{H_{\mathrm{T}}^{4\,\mathrm{jets}}}$ needs to satisfy >5 GeV$^{1/2}$ (instead of >9 GeV$^{1/2}$).

The relevant distributions and their agreement with data are shown in figure 5.15. Each changed requirement leads to an uncertainty on the extrapolation factor. Special attention is needed for events with a W boson and a heavy flavour jet (originating from a b or c quark): the normalisation coefficient μ_W is applied to all W boson events, but it is determined in the WCR which has a b-veto. An additional systematic uncertainty for the fraction of $W+b$ events will be added to reflect this.

To better understand the idea behind the CR-based normalisation for $t\bar{t}$ and W+jets events, we think of the expected number of SM background events in the SR, $b_{\mathrm{SR}}^{\mathrm{SM}}$, as

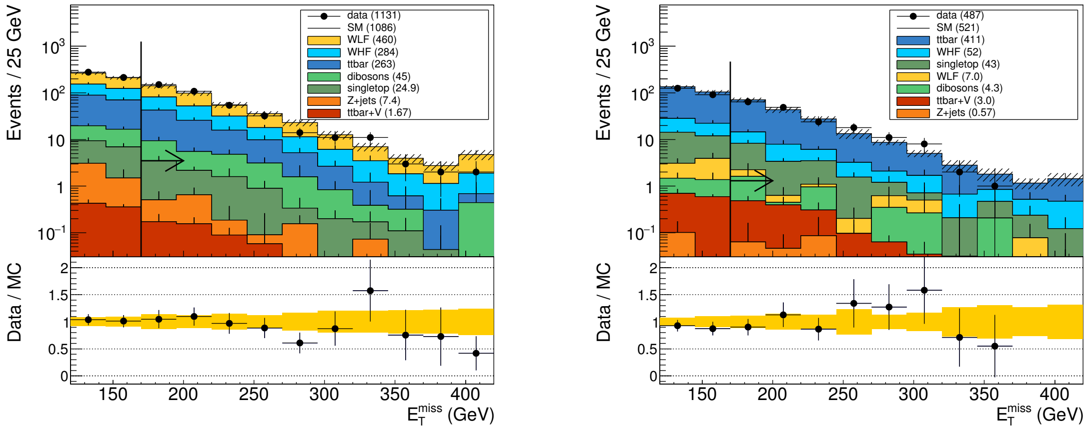

a) mixed WCR, distribution of $E_{\mathrm{T}}^{\mathrm{miss}}$ **b)** mixed TCR, distribution of $E_{\mathrm{T}}^{\mathrm{miss}}$

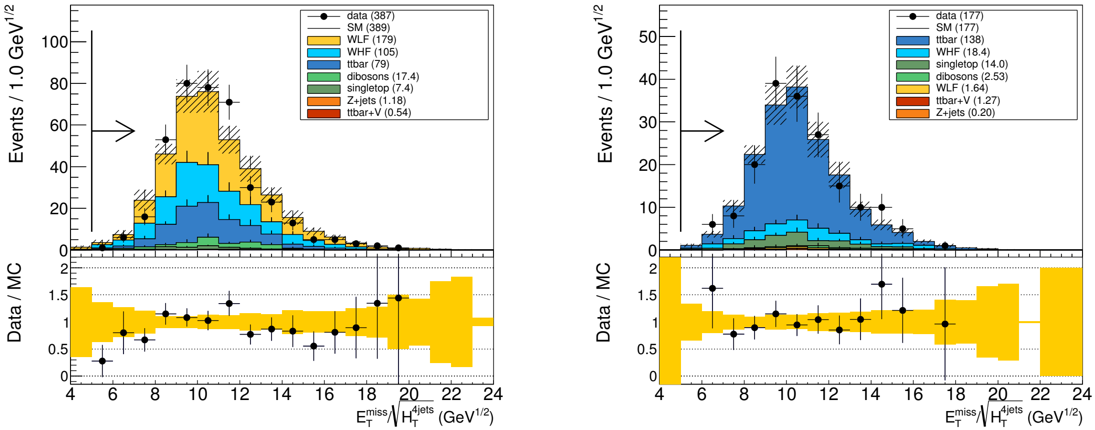

c) mixed WCR: $E_{\mathrm{T}}^{\mathrm{miss}}/\sqrt{H_{\mathrm{T}}^{4\,\mathrm{jets}}}$ **d)** mixed TCR: $E_{\mathrm{T}}^{\mathrm{miss}}/\sqrt{H_{\mathrm{T}}^{4\,\mathrm{jets}}}$

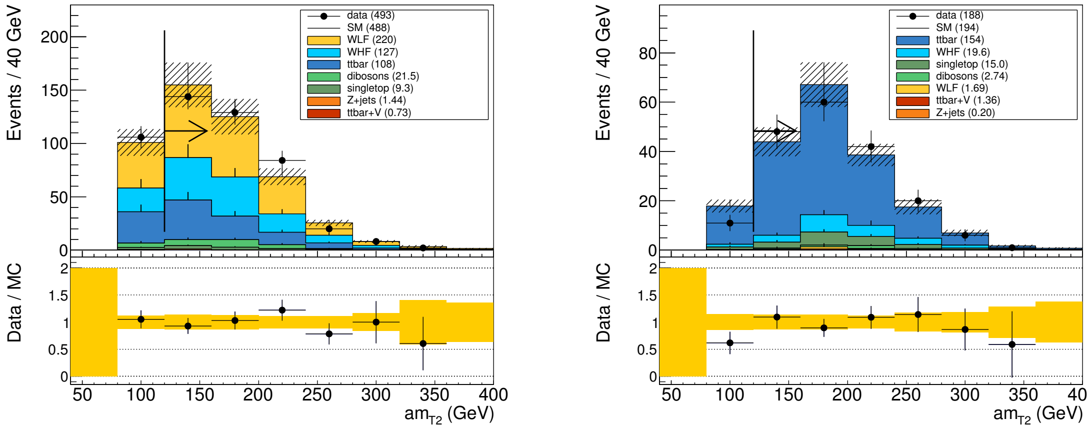

e) mixed WCR, distribution of am$_{\mathrm{T2}}$ **f)** mixed TCR, distribution of am$_{\mathrm{T2}}$

Figure 5.15: Control plots for the mixed TCR and WCR definitions, showing the three variables for which less stringent requirements are applied in the CRs than in the SR. The systematic uncertainties on the simulated distributions are represented by yellow bands. In each plot, the CR requirement on the presented variable is not applied, but instead indicated by an arrow. The background normalisation coefficients $\mu_{t\bar{t}} = 1.11$ and $\mu_W = 0.81$ obtained in the background-only fit have been applied.

separated into three components:

$$b_{\mathrm{SR}}^{\mathrm{SM}} = b_{\mathrm{SR}}^{t\bar{t}} + b_{\mathrm{SR}}^{W+\mathrm{jets}} + b_{\mathrm{SR}}^{\mathrm{other}}. \tag{5.6}$$

Only the sum is measured directly[4]. Instead of directly estimating the components using simulated samples, we introduce the *transfer factors* $\tau_{t\bar{t}}$ and τ_W:

$$b_{\mathrm{SR}}^{t\bar{t},\mathrm{data}} = b_{\mathrm{TCR}}^{t\bar{t},\mathrm{data}} \cdot \underbrace{\frac{b_{\mathrm{SR}}^{t\bar{t},\mathrm{MC}}}{b_{\mathrm{TCR}}^{t\bar{t},\mathrm{MC}}}}_{\tau_{t\bar{t}}}, \qquad b_{\mathrm{SR}}^{W,\mathrm{data}} = b_{\mathrm{WCR}}^{W,\mathrm{data}} \cdot \underbrace{\frac{b_{\mathrm{SR}}^{W,\mathrm{MC}}}{b_{\mathrm{WCR}}^{W,\mathrm{MC}}}}_{\tau_W}. \tag{5.7}$$

Although these are evaluated using simulation, they have much smaller systematic uncertainties than the estimated SR- and CR-yields, as many experimental effects affect the SR- and CR-yields in a similar manner, which reduces their impact on $\tau_{t\bar{t}}$ and τ_W. Now, $b_{\mathrm{TCR}}^{t\bar{t},\mathrm{data}}$ and $b_{\mathrm{WCR}}^{W,\mathrm{data}}$ are also not measured directly, but can be constrained much better than the corresponding SR yields. We introduce the normalisation coefficients $\mu_{t\bar{t}}$ and μ_W for the background estimates from simulation:

$$\mu_{t\bar{t}} = b_{\mathrm{TCR}}^{t\bar{t},\mathrm{data}} / b_{\mathrm{TCR}}^{t\bar{t},\mathrm{MC}}, \qquad \mu_W = b_{\mathrm{WCR}}^{t\bar{t},\mathrm{data}} / b_{\mathrm{WCR}}^{t\bar{t},\mathrm{MC}}, \tag{5.8}$$

and rewrite (5.6) as:

$$b_{\mathrm{SR}}^{\mathrm{SM}} = \mu_{t\bar{t}}\, \tau_{t\bar{t}} \cdot b_{\mathrm{TCR}}^{t\bar{t},\mathrm{MC}} + \mu_W\, \tau_W \cdot b_{\mathrm{WCR}}^{W,\mathrm{MC}} + b_{\mathrm{SR}}^{\mathrm{other},\mathrm{MC}}, \tag{5.9}$$

with similar definitions for the expected CR yields, $b_{\mathrm{TCR}}^{\mathrm{SM}}$ and $b_{\mathrm{WCR}}^{\mathrm{SM}}$, but with only one transfer factor TCR↔WCR. The background normalisation coefficients $\mu_{t\bar{t}}$ and μ_W are obtained using a simultaneous fit of the CR yields.

The expected background yields are affected by the systematic uncertainties described in section 5.5. These need to be accounted for in the fit, but their actual values are of little interest; the corresponding model parameters $\vec{\theta}$ are thus referred to as *nuisance parameters*. For a SM background process j, the estimated yield under nominal conditions is b_j^{nom}, and b_j^k when the systematic variation k is assumed. We define the difference between the two yields as $\Delta_{j,k} = b_j^{\mathrm{nom}} - b_j^k$, which allows us to interpolate between the two conditions by varying the corresponding nuisance parameter θ_k, resulting in the background estimate

$$b_j = b_j^{\mathrm{nom}} \left(1 + \theta_k \Delta_{j,k}\right). \tag{5.10}$$

---

[4] We are only concerned with expectation values at this point, statistical uncertainties are accounted for in the fitting procedure described below.

This can directly be expanded to the case of multiple systematic variations considered simultaneously:

$$b_j = b_j^{\text{nom}} \times \prod_{\text{systematics}}^{k} \left(1 + \theta_k \Delta_{j,k}\right). \tag{5.11}$$

The total estimate of the number of selected signal and background events in a region is $\lambda = \mu_{\text{sig}} \cdot s + \sum_j b_j$, where we have introduced the *signal strength* parameter μ_{sig}, which allows to perform the fit under varying assumptions: the expected yield λ is identical to the background yield for $\mu_{\text{sig}} = 0$, and corresponds to the signal + background yield of a given signal model for $\mu_{\text{sig}} = 1$. Further, μ_{sig} can be used as a free fit parameter to determine the amount of signal events which best describes the data. Lastly, μ_{sig} can be scanned to determine the maximum amount of signal compatible with a given observation.

For the initial determination of the background normalisation, one sets $\mu_{\text{sig}} = 0$ and does not include the SR in the fit, in order to obtain estimates independent of the observation in the SR, where signal may be present; this setup is referred to as *background-only fit.*

The likelihood function is

$$\mathcal{L}(\mu_{\text{sig}}, \mu_{t\bar{t}}, \mu_W \,\Big|\, \vec{n}, \vec{\theta}) = \prod_{\text{systematics}}^{k} \underbrace{\prod_{\text{TCR,WCR,(SR)}}^{r} \frac{\lambda_i^{n_i} e^{-\lambda_i}}{n_i!}}_{\text{Poisson constraints}} \times \underbrace{\frac{1}{\sqrt{2\pi}} e^{-\theta_k^2/2}}_{\text{nuisance parameters}} \quad , \tag{5.12}$$

where λ_i is the expected yield in region i and n_i is the corresponding yield in data (either experimentally observed data or simulation-based pseudo-data). The likelihood is maximised to obtain estimates of the background normalisations $\mu_{t\bar{t}}$ and μ_W and optionally the signal strength μ_{sig}.

The Poisson terms result in a high value of the likelihood function when observed and expected yields are in good agreement, while the Gaussian constraint terms try to reduce the nuisance parameters. It is technically possible that the fit constrains the nuisance parameters to an interval smaller than $[-1, 1]$, which means the corresponding systematic uncertainty is constrained more strongly than initially estimated. This is referred to as *profiling*, and would be seen as an indication of a problem in the fit setup, because a search should not be able to reduce the systematic uncertainties below the level determined in dedicated studies in the detector performance groups. No significant profiling was observed in the fits presented in this thesis.

The normalisation method works best if the CR contents are pure: the TCR should only contain $t\bar{t}$ events, while the WCR should only contain W+jets events. In practice, a certain contribution from other SM processes cannot be avoided (see table 5.8). While it is preferable to have no signal contamination in the CRs, a small amount is tolerable and leads to a conservative estimate of the discovery probability, as the SM background in the SR will be overestimated in this case (as $\mu = 0$ is used in this fit). The opposite is true if one wants to make statements about the exclusion of a hypothetical signal. In this case, the fit needs to be redone accounting for signal contamination in the CRs, as the resulting estimate would be to aggressive otherwise.

process	**TCR**	**WCR**	**SR**
$t\bar{t}$ (theory)	124.7± 2.5 (74.5%)	70.8± 2.0 (15.9%)	2.60±0.30 (36%)
W+jets (theory)	24.8± 1.4 (14.8%)	349.5± 8.4 (78.2%)	1.58±0.35 (22%)
dibosons	2.5± 0.7 (1.5%)	17.4± 1.8 (3.9%)	0.85±0.31 (12%)
single-top	14.0± 0.7 (8.4%)	7.3± 0.7 (1.6%)	0.75±0.14 (10%)
$t\bar{t} + W/Z$	1.3± 0.1 (0.76%)	0.5± 0.1 (0.12%)	1.41±0.08 (20%)
Z+jets	0.2± 0.1 (0.12%)	1.2± 0.3 (0.27%)	0.01±0.01 (0%)
SM (theory)	167.5± 3.0 (100%)	446± 9 (100%)	7.2± 0.6 (100%)
data	177	387	10
$t\bar{t}$ (data-driven)	138.9 (78.5%)	78.9 (20.4%)	2.9 (40%)
W+jets (data-driven)	20.0 (11.3%)	281.8 (72.8%)	1.3 (18%)
SM (data-driven)	176.9 (100%)	387.1 (100%)	7.2 (100%)
$m_{\tilde{t}_1}$=400 $m_{\tilde{\chi}_1^\pm}$=200 $m_{\tilde{\chi}_1^0}$=100	4.9± 0.7 (2.9%)	0.52±0.17 (0.12%)	10.4± 0.9 (145%)
$m_{\tilde{t}_1}$=500 $m_{\tilde{\chi}_1^\pm}$=300 $m_{\tilde{\chi}_1^0}$=150	1.06±0.23 (0.63%)	0.39±0.17 (0.09%)	12.1± 0.9 (169%)
$m_{\tilde{t}_1}$=600 $m_{\tilde{\chi}_1^\pm}$=400 $m_{\tilde{\chi}_1^0}$=200	0.23±0.05 (0.14%)	0.07±0.04 (0.02%)	7.4± 0.4 (102%)

Table 5.8: Expected yields and relative contribution of different SM processes in the mixed CRs, the expected SR yields from table 5.5 are repeated for completeness, together with the yield observed in data. The results for three mixed stop benchmark points are shown (50% branching ratio, masses in GeV); a small amount of signal contamination is present, especially in the TCR. The expected yields from $t\bar{t}$ and W+jets are shown with two different normalisations: using the theoretical cross-sections, and using the coefficients found in the background-only fit.

5.6.1 Reduced systematic uncertainties

After the background-only fit, the modelling uncertainties for $t\bar{t}$ and W+jets affect only the extrapolation from the CRs into the signal regions (and between TCR and WCR), instead of affecting SR and CR yields separately. This allows for the cancellation of systematic uncertainties that affect the SR and CRs in a similar way. As is shown in table 5.9, this approach strongly reduces the effect of the systematic uncertainties on the expected background yield.

In the table, the uncertainties are ordered loosely by the magnitude of their effect on the mixed SR estimate. This order is clearly different from what was shown in table 5.7.

While the JER and JES uncertainties still contribute significantly, they are surpassed by the b-tagging efficiency uncertainty. The largest contribution comes from the uncertainty of the $t\bar{t} + V$ cross-section. Thus a possible future improvement might be a data-driven estimate of the $t\bar{t} + V$ normalisation. However, due to the similar kinematics of stop pair production with $\tilde{t}_1 \to t + \tilde{\chi}_1^0$ and $t\bar{t} + Z$ production with $Z \to \nu\nu$ there are limits to this approach. For the high stop mass SRs `tN_high` and `tN_boost` in the published analysis [121], the $t\bar{t} + Z$ background estimate is therefore validated indirectly, using comparisons of the related process $t\bar{t} + \gamma$ between data and simulation .

Due to the data-driven normalisation of the TCR and WCR yields, the effective systematic uncertainty is largely defined by the statistical uncertainty of the observed signal: if for example the $t\bar{t}$ estimate is increased in the evaluation of the $t\bar{t}$ parton shower uncertainty, the fit will try to compensate this by adjusting $\tau_{t\bar{t}}$ to keep the expected TCR yield close to the observed one. The likelihood balances the Poisson constraint (for the CR yields) against the Gaussian constraint (for the parton shower strength), effectively coupling the statistical and systematic uncertainties. Since the WCR also contains $t\bar{t}$ events, it is also necessary to adjust $\tau_{W+\text{jets}}$, and anticorrelations between the transfer factors may result.

The systematic uncertainty on the SR yield is smaller than the statistical uncertainty achieved with the 20.3 fb^{-1} ATLAS dataset recorded at $\sqrt{s} = 8$ TeV. This suggests that the SR definition was designed to be tighter than would have been optimal. This may in part be due to the incomplete setup used in the optimisation, which uses simplified systematic uncertainty estimates and no data-driven background estimate. The analysis would thus benefit from additional recorded events; however, at the planned centre-of-mass energy of $\sqrt{s} = 13$ TeV, the event kinematics will change and the SR definition will need to be reoptimised.

5.6.2 Comparison of measurement and simulation

Besides their role for the background normalisation, the CRs also can be used to check if important kinematic distributions agree well between recorded data and simulated events; however, the CR yields have already been used to estimate the normalisation of the dominant backgrounds. The check cannot be performed in the SRs because a discrepancy there might also be the result of new physics. As a compromise, the comparison is performed on *validation regions* (VRs) in the intermediate region 90 GeV$< m_\text{T} <$ 120 GeV, with all other requirements unchanged from the CR definitions, resulting in a top validation region (TVR) and a W+jets validation region (WVR). Figure 5.16 shows a selection of control plots, comparing kinematic distributions in data and simulation in the mixed validation regions. After the agreement in CRs and VRs had been confirmed and the SR definition was final, comparison plots for data and simulation were prepared for the SR itself (figure 5.17).

	mixed TCR	**mixed WCR**	**mixed SR**
Total background expectation	176.92	387.12	7.18
Total statistical ($\sqrt{N_{\mathrm{exp}}}$)	±13.30 (7.5%)	±19.68 (5.1%)	±2.68 (37.3%)
Total background systematic	±13.29 (7.5%)	±19.67 (5.1%)	±1.00 (13.9%)
$\boldsymbol{t\bar{t}+V}$			
cross-section	±0.28 (0.2%)	±0.12 (0.0%)	±0.31 (4.3%)
scale variation	±0.21 (0.1%)	±0.09 (0.0%)	±0.24 (3.3%)
PDFs	±0.06 (0.0%)	±0.03 (0.0%)	±0.07 (1.0%)
detector: jets			
b-tagging efficiency	±8.86 (5.0%)	±9.38 (2.4%)	±0.30 (4.2%)
mistagging, c efficiency	±3.05 (1.7%)	±3.14 (0.8%)	±0.15 (2.1%)
mistagging, LF efficiency	±1.32 (0.7%)	±1.46 (0.4%)	±0.09 (1.3%)
JER	±0.45 (0.3%)	±0.99 (0.3%)	±0.27 (3.8%)
JES	±1.09 (0.6%)	±6.01 (1.6%)	±0.24 (3.3%)
diboson			
scale variation	±0.76 (0.4%)	±5.18 (1.3%)	±0.25 (3.5%)
cross-section	±0.18 (0.1%)	±1.21 (0.3%)	±0.06 (0.8%)
PDFs	±0.14 (0.1%)	±0.95 (0.2%)	±0.05 (0.7%)
detector: $\boldsymbol{E_{\mathrm{T}}^{\mathrm{miss}}}$ cell-out			
scale	±0.63 (0.4%)	±0.79 (0.2%)	±0.23 (3.2%)
resolution	±0.45 (0.3%)	±1.35 (0.3%)	±0.17 (2.4%)
$\boldsymbol{W}$**+jets**			
heavy flavour content	±2.05 (1.2%)	±2.20 (0.6%)	±0.15 (2.1%)
finite partons	±0.01 (0.0%)	±0.07 (0.0%)	±0.08 (1.1%)
scale variation	±0.00 (0.0%)	±0.06 (0.0%)	±0.07 (1.0%)
PDFs	±0.15 (0.1%)	±0.17 (0.0%)	±0.02 (0.3%)
$\boldsymbol{t\bar{t}}$			
parton shower	±5.59 (3.2%)	±5.42 (1.4%)	±0.16 (2.2%)
ISR/FSR	±5.19 (2.9%)	±5.10 (1.3%)	±0.09 (1.3%)
scale variation	±0.02 (0.0%)	±0.01 (0.0%)	±0.03 (0.4%)
PDFs	±0.35 (0.2%)	±0.35 (0.1%)	±0.01 (0.1%)
single-top			
interference	±3.79 (2.1%)	±1.96 (0.5%)	±0.20 (2.8%)
generator	±1.55 (0.9%)	±0.80 (0.2%)	±0.08 (1.1%)
cross-section	±0.96 (0.5%)	±0.49 (0.1%)	±0.05 (0.7%)
ISR/FSR	±0.14 (0.1%)	±0.07 (0.0%)	±0.01 (0.1%)
parton shower	±0.14 (0.1%)	±0.07 (0.0%)	±0.01 (0.1%)
PDFs	±0.70 (0.4%)	±0.36 (0.1%)	±0.04 (0.6%)
pile-up model	±0.21 (0.1%)	±0.46 (0.1%)	±0.14 (1.9%)
luminosity	±0.51 (0.3%)	±0.74 (0.2%)	±0.08 (1.1%)
Z+jets cross-section	±0.10 (0.1%)	±0.59 (0.2%)	±0.01 (0.1%)

Table 5.9: Breakdown of the systematic uncertainties for the mixed SR background estimates after applying the background-only fit. The percentages show the size of the uncertainty relative to the total expected background. Because the CR yields are used to determine data-driven $t\bar{t}$ and W+jets normalisations in the background-only fit, the expected CR yields closely match the values observed in data (TCR: 177, WCR: 387). For the SR, 10 events were observed in data, exceeding the expectation by one standard deviation. The SRs exclusion power is limited by its statistical uncertainty, indicating that a looser definition may have been preferable.

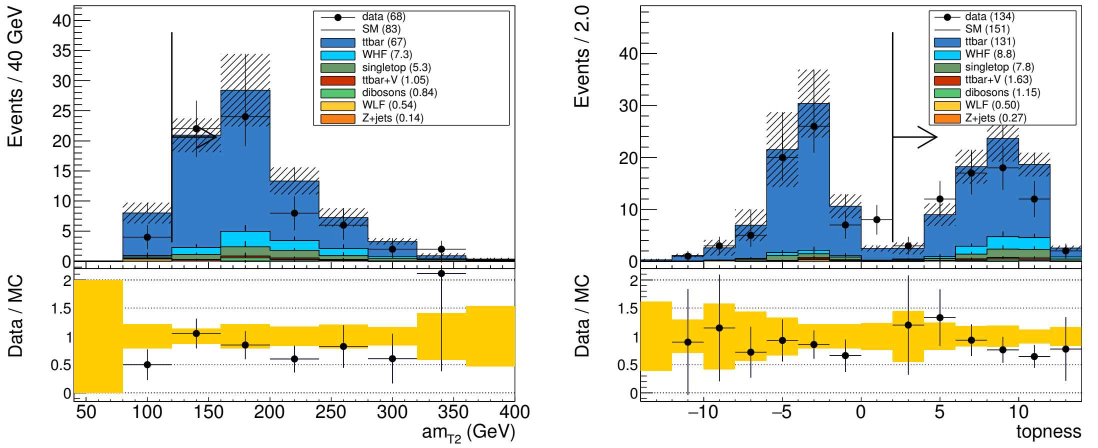

a) mixed TVR, distribution of am$_{\mathrm{T2}}$ **b)** mixed TVR, distribution of *topness*

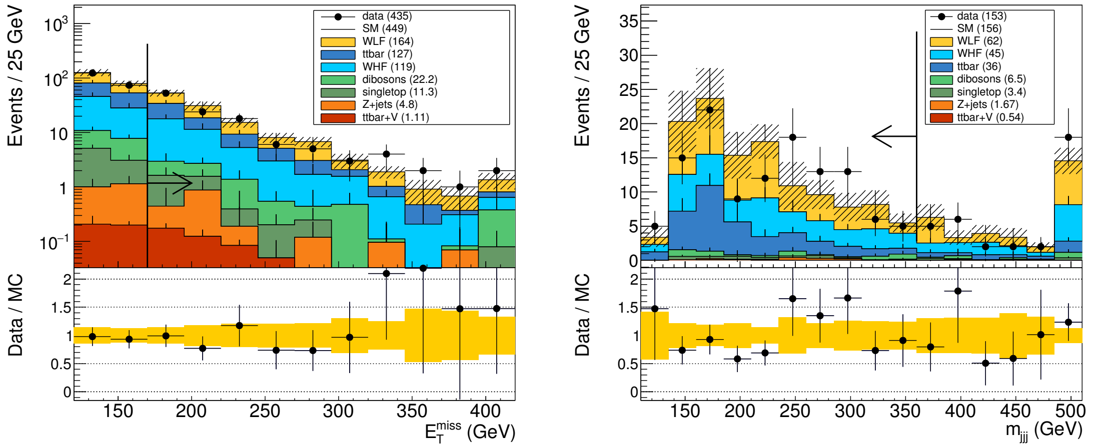

c) mixed WVR, distribution of $E_{\mathrm{T}}^{\mathrm{miss}}$ **d)** mixed WVR, distribution of m_{jjj}

Figure 5.16: Kinematic distributions of variables underlying the mixed SR definition, evaluated in the associated $t\bar{t}$ and W+jets VRs. The systematic uncertainties on the simulated distributions are represented by yellow bands.

Figure 5.18 shows an overview of the expected yields for all mixed regions (CRs, VRs, SR). The dashed line uses the theoretical SM cross-sections (i.e. before-fit normalisation), while the solid line uses the normalisation coefficients determined by the fit, $\mu_{t\bar{t}} = 1.11$ and $\mu_W = 0.81$, with negligible uncertainties.

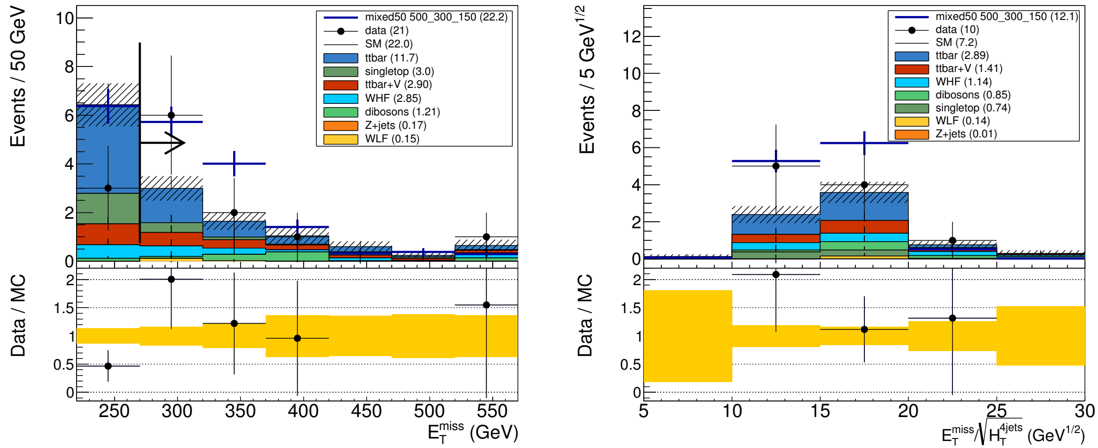

a) distribution of $E_{\mathrm{T}}^{\mathrm{miss}}$ **b)** distribution of $E_{\mathrm{T}}^{\mathrm{miss}}/\sqrt{H_{\mathrm{T}}^{4\,\mathrm{jets}}}$

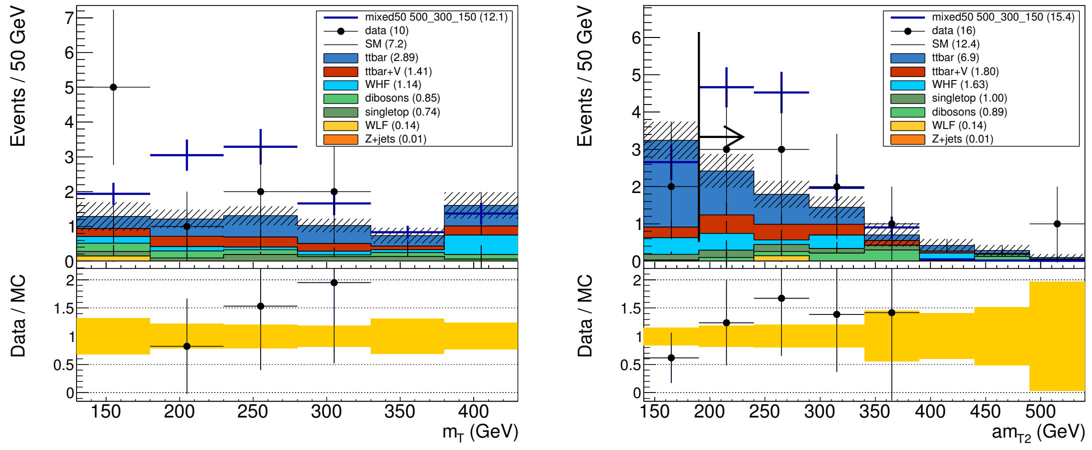

c) distribution of m_{T} **d)** distribution of am$_{\mathrm{T2}}$

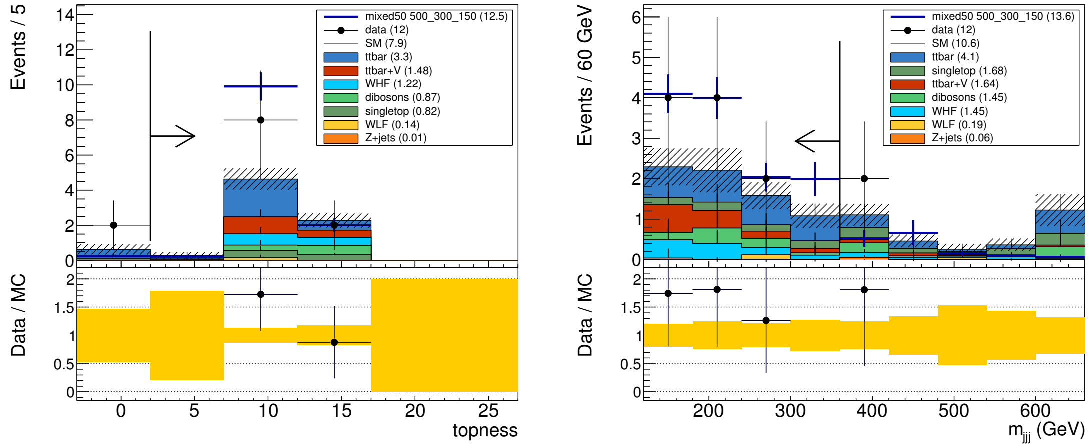

e) distribution of *topness* **f)** distribution of m_{jjj}

Figure 5.17: Kinematic distributions of variables underlying the mixed SR definition, evaluated in the SR itself after validating the agreement of data and simulation in the associated VRs. The systematic uncertainties on the simulated distributions are represented by yellow bands. The distributions predicted using the mixed benchmark model are included for comparison.

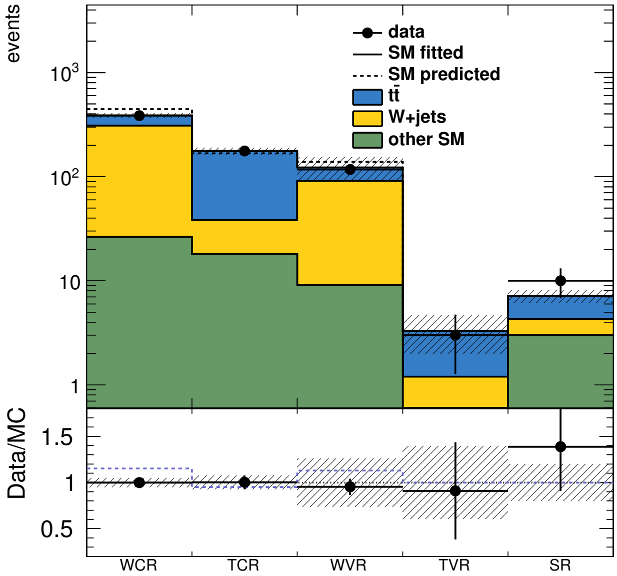

Figure 5.18: Overview of the agreement of data and simulation for the mixed signal region and the corresponding control and validation regions. The dashed line shows the SM estimates using theoretical cross-sections for the $t\bar{t}$ and W+jets processes, while the solid line uses the fitted normalisation coefficients. Good agreement between data and simulation is observed in all control and validation regions.

5.7 Shape-fit for three-body decays

Two CRs for the three-body SR were defined in a similar fashion as for the mixed SR. The expected exclusion reach of this approach was not entirely satisfactory, as it barely improved on existing limits [175]. The exclusion reach is limited because the SR definition is tight, resulting in large statistical uncertainties, and because the expected S/B drops quickly for increasing $m_{\tilde{t}_1}$ and near the kinematic boundaries of the three-body decay scenario ($\Delta m = m_{\tilde{t}_1} - m_{\tilde{\chi}_1^0} \approx m_W$ or $\Delta m \approx m_t$), see also table 5.8.

To improve the available statistics and to reduce the reliance on the edge of the am$_{\mathrm{T2}}$ distribution, the background normalisation setup was extended into a *shape-fit*: the single signal region was replaced by 12 regions that differ in their m_{T} and am$_{\mathrm{T2}}$ requirements, and augmented by WCR-like bins that require 60 GeV$< m_{\mathrm{T}} <$ 90 GeV and 0 b-tags. The shape-fit setup is illustrated in figure 5.19. The $t\bar{t}$ and W+jets background normalisation is obtained in a fit that uses observed event yields for the 8 WCR- and TCR-like bins, and simulated event yields in all 16 bins. The fit uses the full JES uncertainty description with 17 components.

Figure 5.20 shows control plots for the region with highest signal-to-background ratio; to have sufficiently many events in the selection, the requirements on m_T and am$_\mathrm{T2}$ are relaxed to $m_\mathrm{T} > 110$ GeV and am$_\mathrm{T2} < 100$ GeV in these plots. There is good overall agreement, especially in the two variables defining the shape-fit binning.

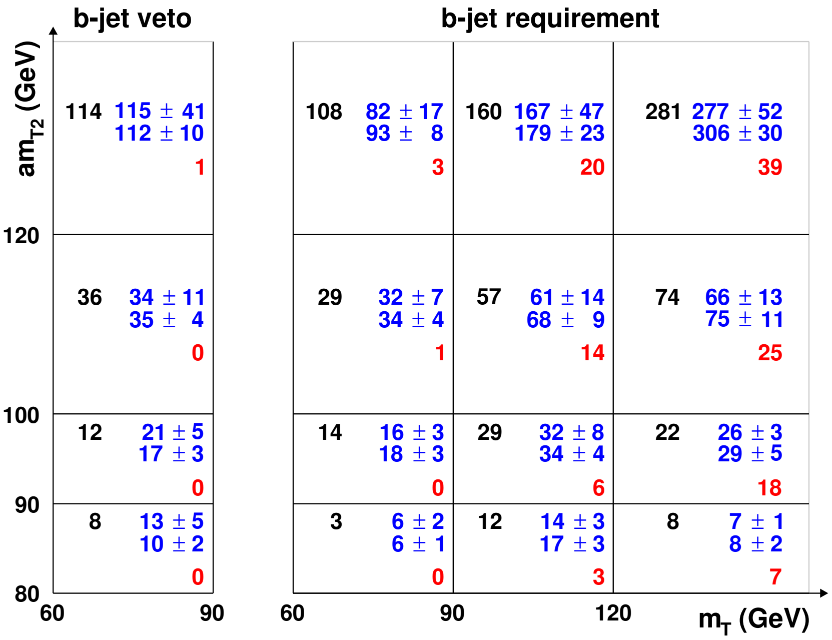

Figure 5.19: Layout of the three-body shape-fit performed in bins of m_T and am$_\mathrm{T2}$. The expected and observed yields are evaluated for each bin. Yields observed in data are shown in black. The background estimates before and after the fit are shown in blue (upper and lower numbers, respectively), illustrating the improvement reached by the data-driven background normalisation. The numbers in red are the expected signal yields for a benchmark model with $m(\tilde{t}_1) = 200$ GeV and $m(\tilde{\chi}^0_1) = 50$ GeV. The lower right bin corresponds to the SR definition obtained earlier; the highest S/B is found here. The highest significance ($S/\sqrt{S+B+\Delta B^2}$) is found in the adjacent 90 GeV<am$_\mathrm{T2}$<100 GeV bin.

This concludes the discussion of the analysis method. In the following chapter, the observed and expected signal and background yields are run through a statistical analysis to extract statements about discovery and exclusion of the stop.

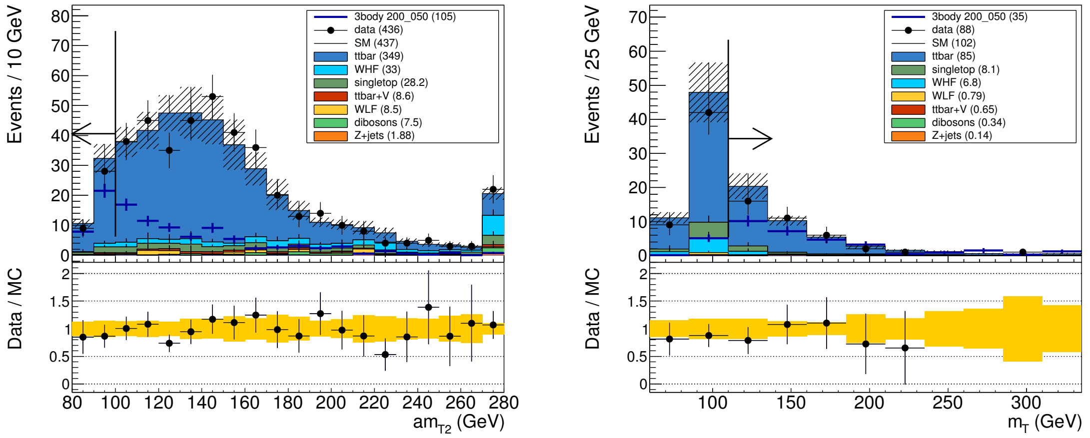

a) distribution of $\mathrm{am}_{\mathrm{T2}}$ **b)** distribution of m_{T}

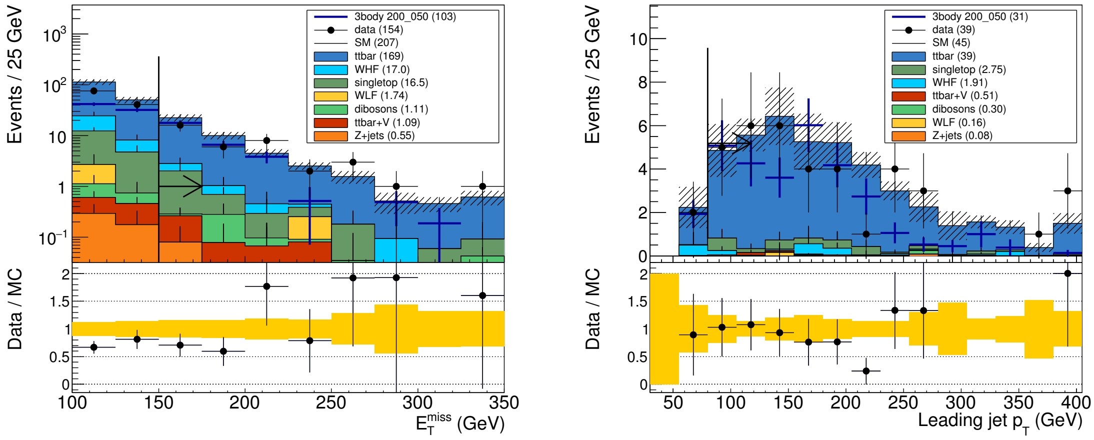

c) distribution of $E_{\mathrm{T}}^{\mathrm{miss}}$ **d)** distribution of $p_{\mathrm{T}}^{\mathrm{jet}\,1}$

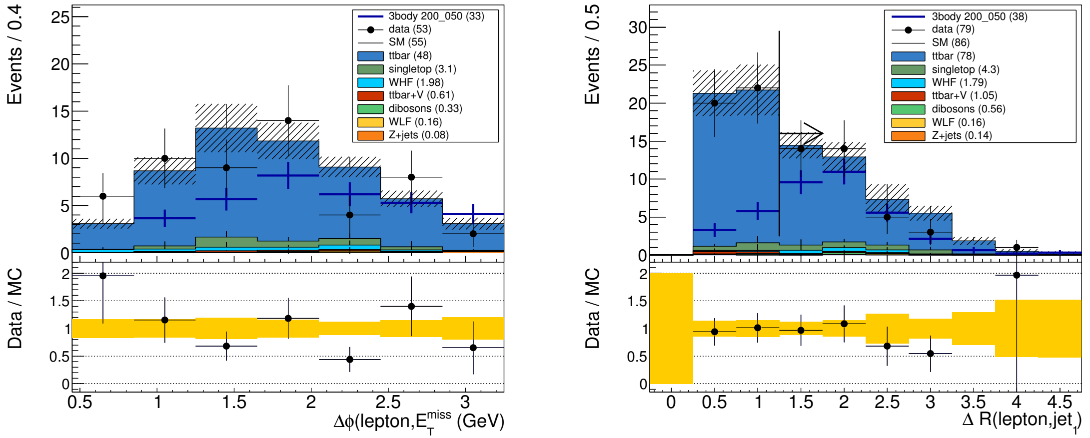

e) distribution of $\Delta\phi\left(\vec{p_{\mathrm{T}}}^{\ell}, \vec{E_{\mathrm{T}}^{\mathrm{miss}}}\right)$ **f)** distribution of $\Delta R\left(\vec{p_{\mathrm{T}}}^{\ell}, \vec{p_{\mathrm{T}}}^{\mathrm{jet}\,1}\right)$

Figure 5.20: Kinematic distributions of variables underlying the three-body shape-fit definition, evaluated in the region where $mT > 110$ GeV and $\mathrm{am}_{\mathrm{T2}} < 100$ GeV. In each plot, the region requirement on the presented variable is not applied, but instead indicated by an arrow. The distributions predicted using the three-body benchmark model are included for comparison.

6 | Results

> Experiments within the next five to ten years will enable us to decide whether supersymmetry as a solution of the naturalness problem of the weak interactions scale is a myth or a reality.
>
> *H.P. Nilles, Supersymmetry, supergravity and particle physics (1984)*

> If SUSY exists at the weak scale, M∼1 TeV, then discovering evidence for SUSY particles at the LHC seems to be straightforward.
>
> *ATLAS Technical Design Report Vol. II (25 May 1999), p. 811*

6.1 Statistical method

We introduce the statistical methods before applying them to the two signal region definitions developed in the previous chapter. We first check for deviations from the SM prediction, which may be a hint of signal. The null-hypothesis is that only SM processes were observed: if the corresponding probability p_0 is below 0.05, a significant deviation from the SM prediction was observed. This might be due to the supersymmetric processes targeted by the signal region design, but the p_0-value alone is insufficient to make such a claim: no signal model is used in the computation of p_0, and further studies would be needed to understand the nature of any deviation.

For a counting experiment, the p_0-value is the probability of observing n_{obs} events if n_{SM} background events are expected and in the absence of signal (see for example [190]):

$$p_0 = \sum_{n=n_{\mathrm{obs}}}^{\infty} f(n|\lambda = b_{\mathrm{SM}}) = 1 - \sum_{n=0}^{n_{\mathrm{obs}}-1} \frac{\lambda^n}{n!} e^{-\lambda}, \tag{6.1}$$

where the probability density function f has been replaced by a Poisson distribution in the second step. If $p_0 < 1 - \mathrm{CL}$, the SM-only hypothesis is rejected at the *confidence level* CL. A commonly used choice is CL = 95%.

If however $p_0 > 0.05$, there is no sufficiently large deviation to possibly claim an observation of physics beyond the SM. One then proceeds to the second part of the statistical analysis: excluding sparticle mass hypotheses of models that should have been observed if they were realised in nature.

The exclusion analysis uses the $\mathrm{CL_s}$ method [179, 180]. $\mathrm{CL_s}$ is defined as a ratio of the likelihood of the signal + background hypothesis ($\mu = 1$, see equation (5.12)) and the likelihood of the background-only hypothesis ($\mu = 0$):

$$\mathrm{CL_s} = \mathrm{CL_{s+b}}/\mathrm{CL_b}. \tag{6.2}$$

It approaches $\mathrm{CL_{s+b}}$ when a sufficient number of signal events is expected, or if a sufficient number of events is observed in data [179]. However, while $\mathrm{CL_{s+b}}$ approaches by construction a false exclusion rate of 5% (corresponding to a 95% confidence level) even for models for which the experiment has little or no sensitivity, $\mathrm{CL_s}$ slowly approaches zero in these cases.

Since the $\mathrm{CL_s}$ computation depends on the expected number of signal events, it is performed for each studied decay mode and each sparticle mass hypothesis. Signal contamination in the CRs is accounted for by re-running an adjusted background-normalisation fit beforehand. Signal models with $\mathrm{CL_s} < 0.05$ are excluded.

It is common to reverse this exclusion approach and determine the minimal amount of signal events in the SR that a model would have to predict in order to be excluded at $\mathrm{CL_s} = 0.05$. This is done by scanning the signal strength parameter μ to find the value at which the exclusion threshold is reached. In this way, a *model-independent* statement about the exclusion power of a SR can be made[1]. This allows to estimate the exclusion reach for arbitrary signal models with relatively little effort; in particular, it will allow theorists to test models not invented yet.

6.2 Mixed and three-body stop decays

Table 6.1 compares the expected SM yields and the yields observed in data for the mixed SR and for the most signal sensitive bins of the three-body shape-fit. From those, the p_0 values are computed, confirming that no BSM physics was observed. While there is an excess of events in the mixed SR, all sensitive bins of the three-body shape-fit have at most as many events as expected. In the latter case, the p_0 computation is skipped. The signal model independent upper limits are evaluated separately for the most signal-sensitive bins, one at a time.

---

[1] There is a remaining model dependence through the signal contamination in the CRs.

region / bin	**SM expected**	**data obs.**	p_0	$n^{\mathrm{max}}_{\mathrm{non-SM}}$	
				exp.	**obs.**
mixed SR	7.2 ± 1.0	10	0.13	7.0	9.7
threebody shape-fit:					
$\mathrm{am_{T2}} \in [80, 90]$ GeV, $m_{\mathrm{T}} \in [90, 120]$ GeV	16.9 ± 2.8	12	$\geqslant 0.5$	9.9	7.3
$\mathrm{am_{T2}} \in [80, 90]$ GeV, $m_{\mathrm{T}} > 120$ GeV	8.4 ± 2.2	8	$\geqslant 0.5$	7.8	7.9
$\mathrm{am_{T2}} \in [90, 100]$ GeV, $m_{\mathrm{T}} \in [90, 120]$ GeV	35 ± 4	29	$\geqslant 0.5$	14.7	11.7
$\mathrm{am_{T2}} \in [90, 100]$ GeV, $m_{\mathrm{T}} > 120$ GeV	29 ± 5	22	$\geqslant 0.5$	47.8	55.4

Table 6.1: Expected and observed event yields for the mixed and three-body regions (most signal-sensitive bins), with systematic uncertainties for the expected yields. The p_0 values indicate no significant deviation from the SM. The rightmost columns show the expected and observed upper limits placed on the number of non-SM events present in these regions, which can be used to constrain arbitrary models of BSM physics.

Figure 6.1 shows the observed exclusion probabilities computed with the $\mathrm{CL_s}$ method for the mixed region, using a 50% branching ratio for each decay mode ($\tilde{t}_1 \to t + \tilde{\chi}^0_1$ and $\tilde{t}_1 \to b + \tilde{\chi}^\pm_1$). The corresponding contour of the region excluded at 95% is shown in figure 6.2, also for branching ratios of 25% and 75%. The central part of the mass plane is expected to be excluded, although the observed reach is smaller than expected due to the slight observed excess.

Table 6.2 shows a summary of the additional 13 SRs defined in the full analysis [121]. The `tN` regions have been optimised for $\tilde{t}_1 \to t + \tilde{\chi}^0_1$ decays, targeting different parts of the $m_{\tilde{t}_1}$–$m_{\tilde{\chi}^0_1}$ mass-plane: `tN_diag` for the region near the “diagonal” (kinematic boundary); `tN_med` and `tN_high` for medium and high stop masses, respectively; and `tN_boost` for the highest stop masses and *boosted* topologies, where individual jets cannot always be fully resolved and may instead merge into one larger jet (reconstructed with the anti-k_t algorithm with a size parameter of $R = 1.0$). The `bC` regions have been optimised for the selection of $\tilde{t}_1 \to b + \tilde{\chi}^\pm_1$ decays, assuming various mass differences between $\tilde{t}_1$, $\tilde{\chi}^\pm_1$, and $\tilde{\chi}^0_1$. Due to the additional sparticle in these decays, the parameter space to be covered is larger, and more regions have been defined. For the mixed models with $m_{\tilde{\chi}^\pm_1} = 2 \times m_{\tilde{\chi}^0_1}$, mostly the `bCc` and `bCd` regions with are of interest, as the `bCa` and `bCb` regions primarily target *compressed* spectra with small mass differences.

The exclusion reach is augmented towards lower stop masses and towards the kinematic boundary when these SRs are also taken into consideration. This is done by evaluating the performance of each SR at each mass point, always choosing the one with the lowest expected $\mathrm{CL_s}$ value. The resulting exclusion reach is shown in figure 6.3, for several $\tilde{t}_1 \to t + \tilde{\chi}^0_1$ branching ratios from 0% ($\tilde{t}_1 \to b + \tilde{\chi}^\pm_1$ only) to 100% ($\tilde{t}_1 \to t + \tilde{\chi}^0_1$ only). For neutralino masses up to ∼160 GeV, stop masses from the kinematic boundary up to about 500 GeV are excluded independently of the assumed branching ratio.

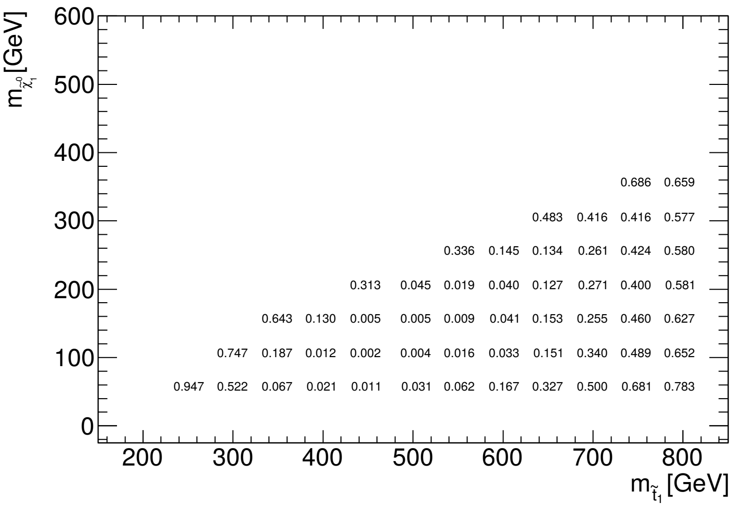

a) Expected $\mathrm{CL_s}$ values

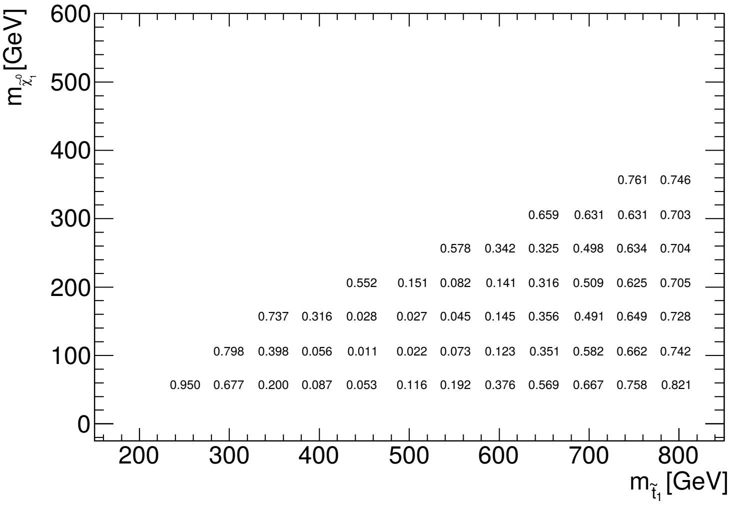

b) Observed $\mathrm{CL_s}$ values

Figure 6.1: **a)** Expected and **b)** observed $\mathrm{CL_s}$ values for the mixed region, using stop pair production models with 50% branching ratio for either $\tilde{t}_1 \rightarrow t + \tilde{\chi}_1^0$ or $\tilde{t}_1 \rightarrow b + \tilde{\chi}_1^{\pm}$. The chargino mass is chosen as $m(\tilde{\chi}_1^{\pm}) = 2 \times m(\tilde{\chi}_1^0)$, and all charginos decay into $W + \tilde{\chi}_1^0$.

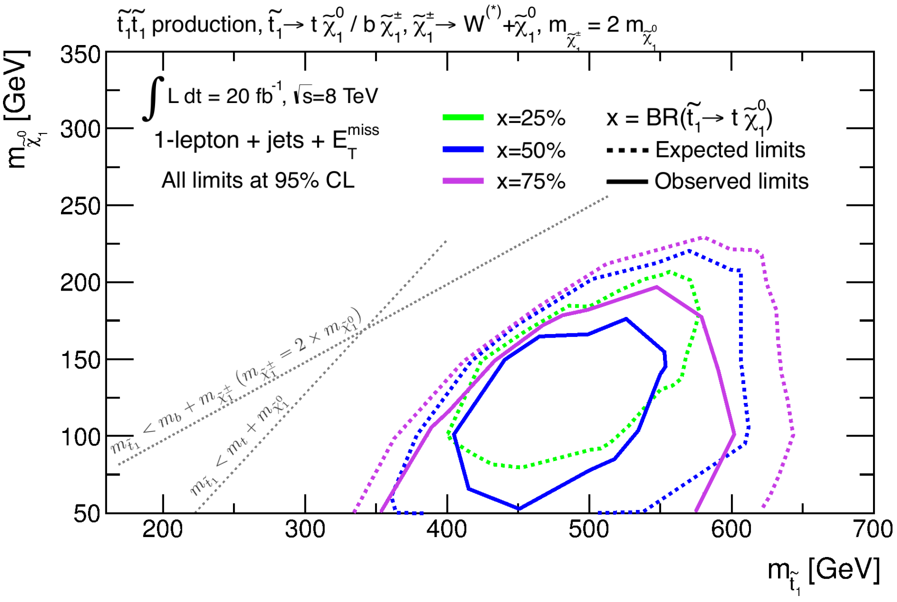

Figure 6.2: Mixed stop pair-production models excluded by the mixed SR developed in this thesis. The exclusion contour is shown for different branching ratios of $\tilde{t}_1 \to t + \tilde{\chi}_1^0$ and $\tilde{t}_1 \to b + \tilde{\chi}_1^\pm$ decays. In each case, the observed (expected) exclusion contour is shown as a solid (dashed) line. Since no other stop decay modes are considered in the models, the two branching ratios always sum up to 1. At a $\tilde{t}_1 \to t + \tilde{\chi}_1^0$ branching ratio of 25%, no signal models were observed to be excluded, and only the expected exclusion contour is shown.

region	**Signal scenario**	**Exclusion technique**
`tN_diag`	$\tilde{t}_1 \to t + \tilde{\chi}_1^0$, $m_{\tilde{t}_1} \gtrsim m_t + m_{\tilde{\chi}_1^0}$	shape-fit ($E_{\mathrm{T}}^{\mathrm{miss}}$ and m_{T})
`tN_med`	$\tilde{t}_1 \to t + \tilde{\chi}_1^0$, $m_{\tilde{t}_1} \sim 550$ GeV, $m_{\tilde{\chi}_1^0} \lesssim 225$ GeV	cut-and-count
`tN_high`	$\tilde{t}_1 \to t + \tilde{\chi}_1^0$, $m_{\tilde{t}_1} \gtrsim 600$ GeV	cut-and-count
`tN_boost`	$\tilde{t}_1 \to t + \tilde{\chi}_1^0$, $m_{\tilde{t}_1} \gtrsim 600$ GeV, with a $R = 1.0$ jet	cut-and-count
`bCa_low`	$\tilde{t}_1 \to b + \tilde{\chi}_1^{\pm}$, $\Delta M \lesssim 50$ GeV	shape-fit (lepton p_{T})
	$\tilde{t}_1 \to bff'\tilde{\chi}_1^0$	
`bCa_med`	$\tilde{t}_1 \to b + \tilde{\chi}_1^{\pm}$, 50 GeV $\lesssim \Delta M \lesssim$ 80 GeV	shape-fit (lepton p_{T})
	$\tilde{t}_1 \to bff'\tilde{\chi}_1^0$	
`bCb_med1`	$\tilde{t}_1 \to b + \tilde{\chi}_1^{\pm}$, $\Delta m \lesssim 25$ GeV, $m_{\tilde{t}_1} \lesssim 500$ GeV	shape-fit (am$_{\mathrm{T2}}$)
`bCb_high`	$\tilde{t}_1 \to b + \tilde{\chi}_1^{\pm}$, $\Delta m \lesssim 25$ GeV, $m_{\tilde{t}_1} \gtrsim 500$ GeV	shape-fit (am$_{\mathrm{T2}}$)
`bCb_med2`	$\tilde{t}_1 \to b + \tilde{\chi}_1^{\pm}$, $\Delta m \lesssim 80$ GeV, $m_{\tilde{t}_1} \lesssim 500$ GeV	shape-fit (am$_{\mathrm{T2}}$ and m_{T})
`bCc_diag`	$\tilde{t}_1 \to b + \tilde{\chi}_1^{\pm}$, $m_{\tilde{t}_1} \gtrsim m_{\tilde{\chi}_1^{\pm}}$	cut-and-count
`bCd_bulk`	$\tilde{t}_1 \to b + \tilde{\chi}_1^{\pm}$, $\Delta M, \Delta m \gtrsim 100$ GeV, $m_{\tilde{t}_1} \lesssim 500$ GeV	shape-fit (am$_{\mathrm{T2}}$ and m_{T})
`bCd_high1`	$\tilde{t}_1 \to b + \tilde{\chi}_1^{\pm}$, $\Delta M, \Delta m \gtrsim 100$ GeV, $m_{\tilde{t}_1} \gtrsim 500$ GeV	cut-and-count
`bCd_high2`	$\tilde{t}_1 \to b + \tilde{\chi}_1^{\pm}$, $\Delta M \gtrsim 250$ GeV, $m_{\tilde{t}_1} \gtrsim 500$ GeV	cut-and-count

Table 6.2: Summary of additional SRs in the published analysis [121], the targeted signal scenarios, and the analysis technique used for model-dependent exclusions For the $\tilde{t}_1 \to b + \tilde{\chi}_1^{\pm}$ decay scenarios, the mass splittings $\Delta M = m(\tilde{t}_1) - m(\tilde{\chi}_1^0)$ and $\Delta m = m(\tilde{\chi}_1^{\pm}) - m(\tilde{\chi}_1^0)$ are used to characterise the mass hierarchies. The regions `tN_med`, `tN_high`, `tN_boost`, `bCc_diag`, `bCd_high1`, and `bCd_high2` use a CR-based normalisation as is done for the mixed SR. This technique is referred to as *cut-and-count*, while the remaining regions use a shape-fit technique with bins defined in one or two variables, similar to the three-body region.

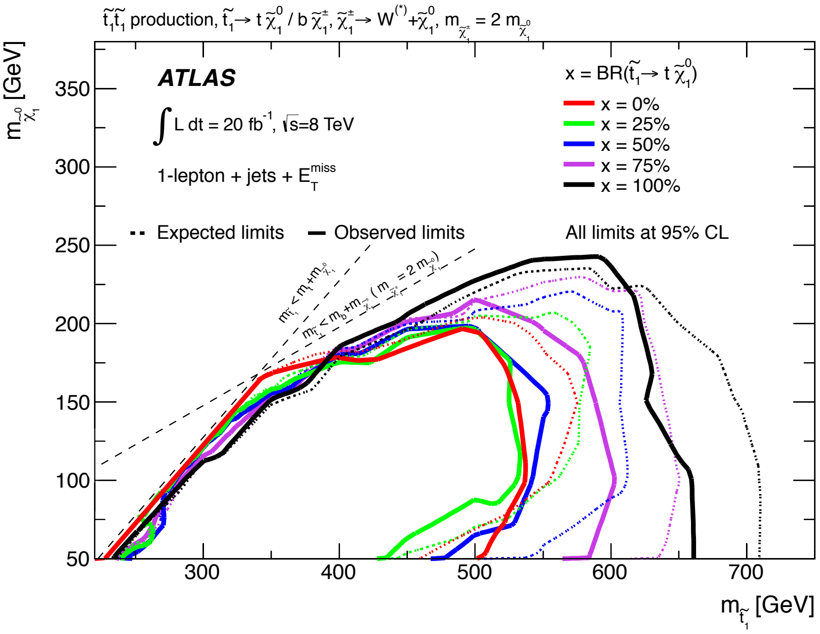

Figure 6.3: Excluded stop pair-production models using the SR from the full stop 1-lepton analysis with the lowest expected $\mathrm{CL_s}$ at each point.

The expected and observed $\mathrm{CL_s}$ values for the three-body region are shown in figure 6.4. Here, no combination with other regions is needed. Figure 6.5 shows the resulting exclusion contour, along with the exclusion contours for on-shell $\tilde{t}_1 \to t + \tilde{\chi}_1^0$ decays and four-body stop decays ($\tilde{t}_1 \to b\ell^+\ell^-\tilde{\chi}_1^0$ or $bq\bar{q}\tilde{\chi}_1^0$) from the published analysis. For intermediate Δm, stop masses up to 300 GeV are excluded using the three-body shape-fit.

We conclude this section by revisiting the topic of systematic uncertainties. Up to this point, they were accounted for as uncertainties on the expected yields, and the likelihood fit made small adjustments to their magnitude in order to find the overall best description of the observed data. At the end of the day, however, we're interested in the estimated signal strength μ_{sig}, or the $\mathrm{CL_s}$ for a given signal model. Table 6.3 shows how these statistical measures change if only a limited number of systematic uncertainties are accounted for in the fit model. Removing degrees of freedom from a fit can lead to problems in the convergence; in some cases this effect was mitigated by constraining the normalisation coefficients $\mu_{t\bar{t}}$ and μ_W to the confidence interval found in the background-only fit. The change to the best-fit value of μ_{sig} is typically small compared to the change of its uncertainty $\Delta\mu_{\mathrm{sig}}$. As long as this is the case, studying the change of $\Delta\mu_{\mathrm{sig}}$ is equivalent to studying the effect on $\mathrm{CL_s}$. Table 6.4 shows this decomposition of the signal strength uncertainty for three additional benchmark points.

Large contributions stem from the jet energy scale and resolution uncertainties, for the non-excluded models, the sensitivity to b-tagging and $t\bar{t}$ modelling uncertainties becomes

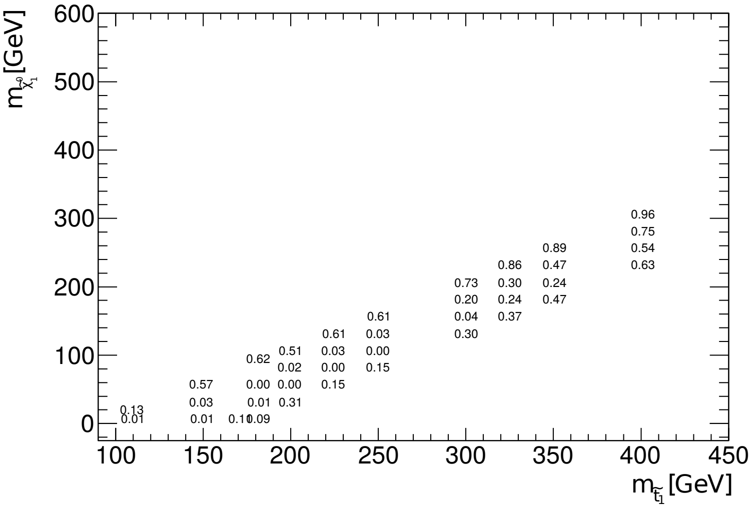

a) Expected $\mathrm{CL_s}$ values

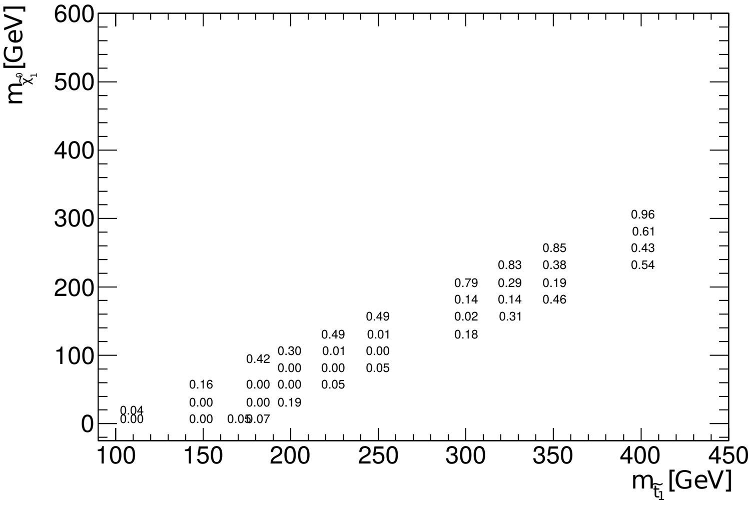

b) Observed $\mathrm{CL_s}$ values

Figure 6.4: **a)** Expected and **b)** observed $\mathrm{CL_s}$ values for the three-body region, using stop pair production models with off-shell top quarks ($m_W < \Delta m = m_{\tilde{t}_1} - m_{\tilde{\chi}_1^0} < m_t$).

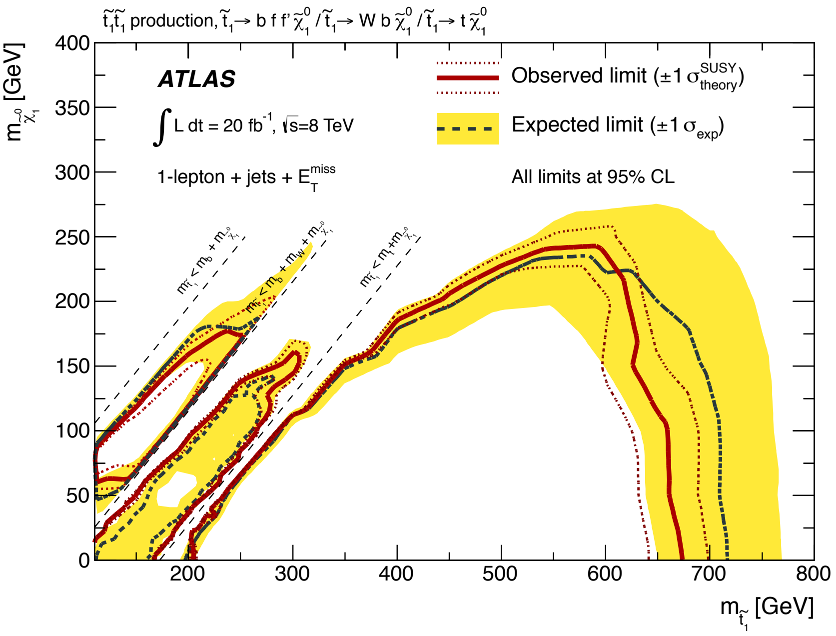

Figure 6.5: Excluded stop pair-production models, assuming 100% $\tilde{t}_1 \to t + \tilde{\chi}_1^0$ decays. From left to right, the different areas correspond to four-body, three-body and two-body decays. The shown three-body stop exclusion is obtained using only the three-body shape-fit presented in this thesis; the other stop decay modes are excluded by other SRs from the full stop 1-lepton analysis. The expected exclusion contour is shown in black, with the experimental $\pm 1\sigma$ uncertainty band in yellow; the observed contour is shown in red, with the $\pm 1\sigma$ theory uncertainty as dashed lines.

larger. While the observed $\mathrm{CL_s}$ values for the non-excluded mixed and three-body models are similar, the uncertainties on the signal strength is very different; this is related to the data excess in the mixed SR, which results in a non-zero best-fit result for μ_{sig}, making it more difficult to exclude the mixed scenario even when the uncertainty on μ_{sig} is smaller. As the expected signal contamination in the CRs is low, the fit parameters found in the background-only fit will also describe the signal+background CR yields well; the fit will accommodate any excess in the SR by increasing the μ_{sig} parameter. This does not allow any conclusion on the nature of the observed excess –it may be due to a SUSY signal, but could equally well be an underestimated SM process, or merely a statistical fluctuation– but it will be worthwhile to check whether a similar excess can be observed also in the larger data sample to be recorded during LHC run 2.

omitted uncertainty	$\boldsymbol{\mu_{\mathrm{sig}}}$	**change**	$\mathbf{CL_s}$
none	0.2345±0.2645		0.0268
JER	0.2306±0.2390	0.1133	0.0208
JES	0.2352±0.2417	0.1074	0.0213
b-tagging	0.2320±0.2435	0.1033	0.0249
other SM backgrounds	0.2318±0.2435	0.1032	0.0256
$t\bar{t}$ model	0.2306±0.2445	0.1008	0.0260
$E_{\mathrm{T}}^{\mathrm{miss}}$ soft-term	0.2311±0.2455	0.0983	0.0261
W+jets model	0.2313±0.2455	0.0983	0.0262
pile-up model	0.2312±0.2456	0.0982	0.0262

Table 6.3: Effect of different systematic uncertainties on μ_{sig} and $\mathrm{CL_s}$ for the mixed SR using an excluded signal model ($\tilde{t}_1$ 500 GeV, $\tilde{\chi}_1^{\pm}$ 300 GeV, $\tilde{\chi}_1^0$ 150 GeV, 50% BR), using the event yields observed in data. The result obtained by the complete fit model is shown in the first line. The contributions of systematic uncertainties are estimated by removing fit parameters related to one source of systematic uncertainty at a time. The shifts of the central value for μ_{sig} is small compared to the change of the corresponding uncertainty $\Delta\mu_{\mathrm{sig}}$. The quoted change to $\Delta\mu_{\mathrm{sig}}$ is the squared difference with respect to the complete fit; due to correlations, the individual contributions to do not add up to the full uncertainty.

region / model	**mixed SR**		**three-body SR**	
$m(\tilde{t}_1), m(\tilde{\chi}_1^0)$ (GeV)	500,150	600,200	200,50	300,180
JES	0.1074	0.1550	0.2016	0.2745
JER	0.1133	0.0577	0.0357	0.4183
b-tagging	0.0983	0.1857	0.1271	0.4273
$E_{\mathrm{T}}^{\mathrm{miss}}$ soft-term	0.0982	0.1060	0.0462	0.2181
pile-up model	0.1033	0.0262	0.0486	0.0647
$t\bar{t}$ model	0.1008	0.1519	0.1086	0.2553
W+jets model	0.0983	0.0251	0.0513	0.2275
other SM backgrounds	0.1032	0.0361	0.0276	0.2026
total uncertainty	0.2645	0.4343	0.1410	0.6732
observed $\mathrm{CL_s}$	0.0268	0.1407	6.7×10^{-5}	0.1769

Table 6.4: Contribution of different systematic uncertainties to the uncertainty on the signal strength, $\Delta\mu_{\mathrm{sig}}$, determined with the same method as used for table 6.3. The results from table 6.3 are repeated for comparison with a non-excluded benchmark point for the mixed signal regions, as well as two benchmark points (excluded and non-excluded) for the three-body signal region.

6.3 LHC run 1 limits on SUSY

Supersymmetric particles have not yet been experimentally observed, and limits on sparticle masses and other model parameters have been inferred. Several SUSY (breaking) models have also been made less probable by the Higgs boson discovery at $m_h = 125$ GeV (see section 2.5).

The searches performed at the LHC during run 1 cover a large variety of final states, ranging from events without any leptons or with only one energetic jet [191] to signatures with many leptons (e.g. $4\ell + E_{\mathrm{T}}^{\mathrm{miss}}$ [192]), $\geqslant$3 b-jets [193] or even $\geqslant$7 jets [194]. A requirement of large $E_{\mathrm{T}}^{\mathrm{miss}}$ resulting from escaping sparticles is an important ingredient in all R-parity conserving analyses.

Searches for the direct pair production of top squarks in different final states have been made by the ATLAS and CMS experiments. The excluded stop and neutralino mass hypotheses for $\tilde{t}_1 \to t + \tilde{\chi}_1^0$ models are shown in figure 6.6 for ATLAS, and a similar exclusion reach is achieved by the CMS collaboration. The areas excluded by the stop search in one lepton final states, part of which is described in this thesis, is shown in yellow (on-shell top), bright purple (three-body decays with off-shell top quark), and dark grey (four-body decays, off-shell W boson). A statistical combination of the 0- and 1-lepton ATLAS results has been performed, slightly extending the exclusion reach. The plot further presents the $\tilde{t}_1 \to t + \tilde{\chi}_1^0$ exclusion limits obtained in analyses with 0 or 2 leptons in the final states [174, 175], as well as results for four-body and $\tilde{t}_1 \rightarrow c + \tilde{\chi}_1^0$ decays [191]. A wide range of stop and neutralino masses has been excluded, and future searches are expected to improve the coverage towards higher sparticle masses, and may close the allowed gaps between the on-shell and off-shell decay modes.

Searches for pair produced stop quarks in models with $\tilde{t}_1 \rightarrow b + \tilde{\chi}_1^\pm$ decays have also been studied by ATLAS and CMS, an overview of the ATLAS results is shown in figure 6.7. Care has to been taken with the interpretation, as different assumptions on the $\tilde{\chi}_1^\pm$ mass are presented in this figure, including compressed models with a small assumed mass difference between $\tilde{\chi}_1^\pm$ and $\tilde{\chi}_1^0$ (upper left sub-figure) or between $\tilde{t}_1$ and $\tilde{\chi}_1^\pm$ (lower right), as well as models with a fixed assumption on $\tilde{\chi}_1^\pm$ (upper right) or a constant ratio between the gaugino masses, $m_{\tilde{\chi}_1^\pm} = 2 \times m_{\tilde{\chi}_1^0}$, as is used for the mixed signal models in this thesis (lower left sub-figure).

Stops with a mass near the top mass have been searched for indirectly by measurements of the $t\bar{t}$ production cross-section [118] and spin correlation of top-antitop pairs [119], and have been excluded in the mass range from m_t up to 177 GeV and up 191 GeV, respectively, assuming stop pair production and $\tilde{t}_1 \rightarrow t + \tilde{\chi}_1^0$ decays with a light neutralino.

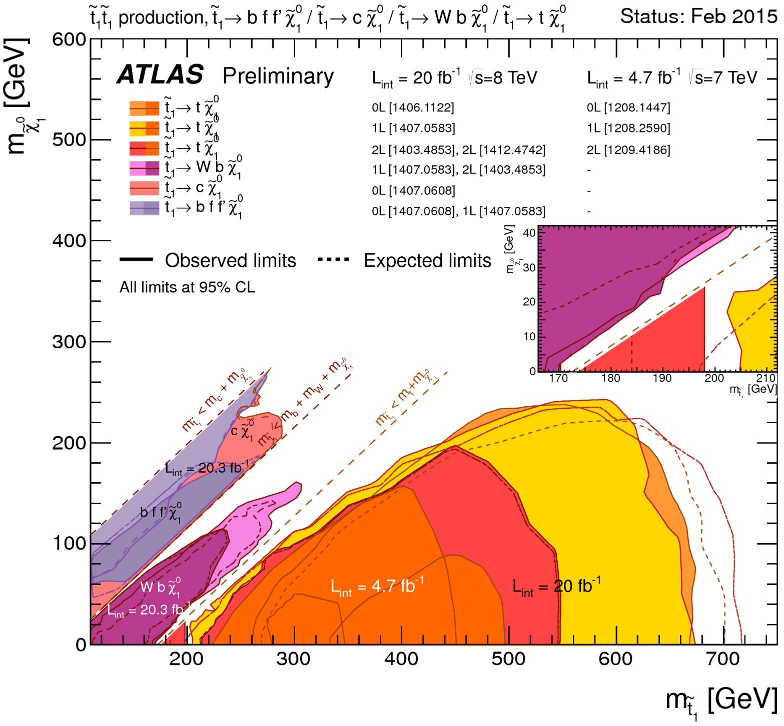

Figure 6.6: Summary plot of ATLAS direct stop searches assuming $\tilde{t}_1 \rightarrow t + \tilde{\chi}_1^0$ decays, from [195].

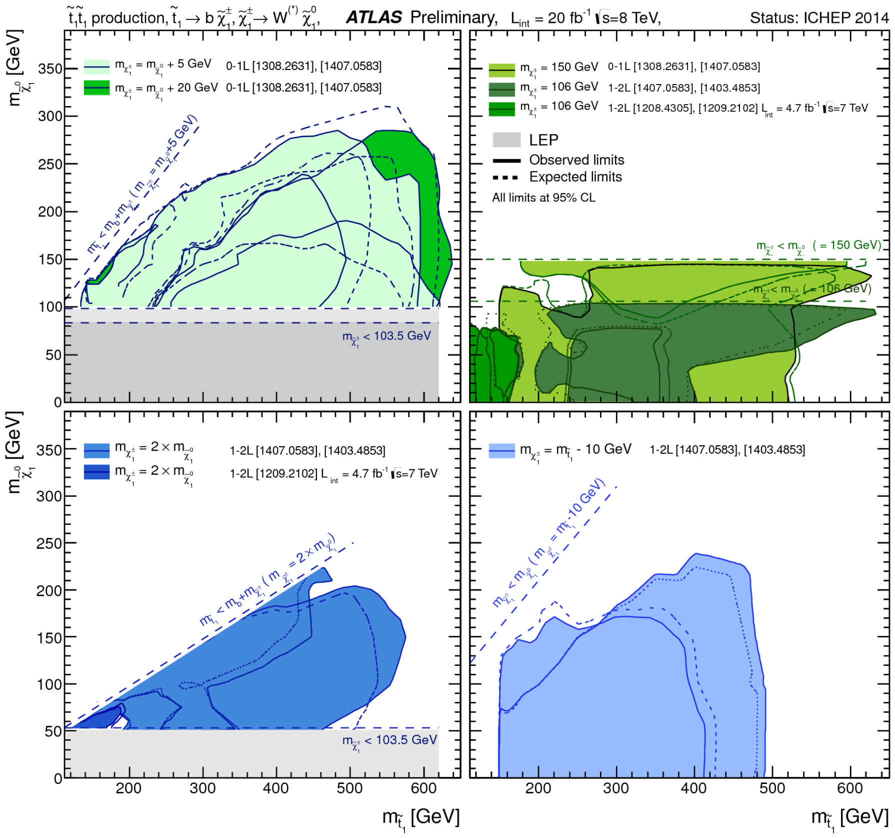

Figure 6.7: Summary plot of ATLAS direct stop searches assuming $\tilde{t}_1 \rightarrow b + \tilde{\chi}_1^{\pm}$ decays, from [195].

The ATLAS experiment excludes gluino masses for a variety of SUSY models: $m_{\tilde{g}} < 1.7$ TeV for an mSUGRA search assuming degenerate squark and gluino masses, $m_{\tilde{q}} = m_{\tilde{g}}$ [196]; $m_{\tilde{g}} < 1.24$ TeV over a large range of $\tan\beta$ [197, 198]. Gluinos decaying via third generation squarks are excluded for $m_{\tilde{g}} < 1.34$ TeV provided that $m_{\tilde{\chi}_1^0} < 400$ GeV [193]. The direct production of charginos is not observed, and is excluded for $m_{\tilde{\chi}_1^\pm} < 465$ GeV for a massless neutralino [199] ($m_{\tilde{\chi}_1^\pm} < 700$ GeV if in addition $\tilde{\chi}_1^\pm$ and $\tilde{\chi}_2^0$ are mass degenerate [200]). There are a variety of limits on R-parity violating SUSY models and long-lived sparticles, as well as specific signatures, such as a photon from a displaced vertex [201] or disappearing tracks [202].

As an example of limits placed on model parameters, figure 6.8 shows a summary of excluded m_0 and $m_{1/2}$ values for mSUGRA models with $\tan(\beta) = 30$, $A_0 = -2m_0$, $\mu > 0$.

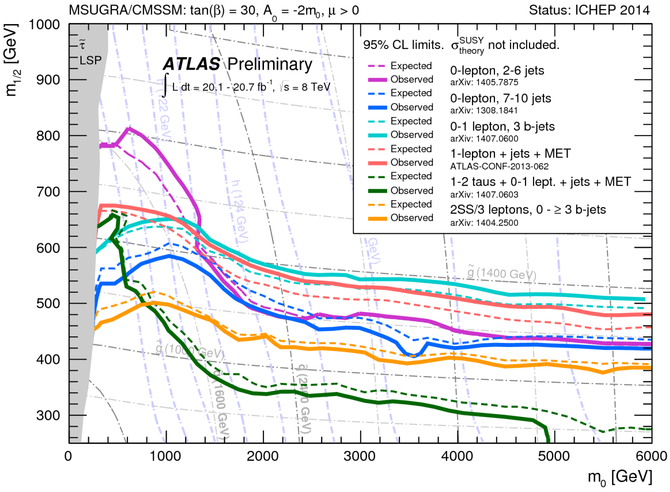

Figure 6.8: Summary of ATLAS exclusion limits from 8 TeV analyses in the m_0–$m_{1/2}$ plane for mSUGRA models with the remaining parameters set to $\tan(\beta) = 30$, $A_0 = -2m_0$, $\mu > 0$. The purple dashed-dotted lines indicate the mass of the lightest neutral Higgs boson in the models. Theoretical signal cross-section uncertainties are not included, all limits are at 95% CL (from [195]).

Searches for supersymmetry are conducted also by the CMS collaboration. The production of squarks decaying as $\tilde{q} \to q + \tilde{\chi}_1^0$ is excluded for $m(\tilde{q}) < 890$ GeV [203]. Searches for gluino production in several final states exclude gluino masses up to $m_{\tilde{g}} \approx 1.3$ TeV [204, 205]. Direct chargino production searches yield $m_{\tilde{\chi}_1^\pm} \gtrapprox 700$ GeV for different neutralino mass assumptions, and the pair production of heavier neutralinos is not observed up to $m_{\tilde{\chi}_2^0} \approx 400$ GeV [206, 207].

7 | Summary and Outlook

> All the signs are good for a great run 2... In the grand scheme of things, a few weeks delay in humankind's quest to understand our universe is little more than the blink of an eye.
>
> *Rolf-Dieter Heuer, CERN Director General, 2015*

In this thesis, a search for a supersymmetric partner of the top quark was presented, performed in one lepton final states using $\mathcal{L} = 20.3\ \text{fb}^{-1}$ recorded with the ATLAS detector in 2012. Particular attention was given to stop decays with non-zero branching ratios for both $\tilde{t}_1 \rightarrow t + \tilde{\chi}_1^0$ and $\tilde{t}_1 \rightarrow b + \tilde{\chi}_1^{\pm}$ decays, as well as models with small Δm, leading to off-shell top quark production. This effort was part of a larger analysis, recently published in ref. [121]. No significant deviations from SM expectations were observed; limits on sparticle masses were placed instead. For neutralino masses up to ∼160 GeV, stop masses from the kinematic boundary up to about 500 GeV are excluded independently of the assumed branching ratio. For models with an off-shell top, stop masses up to 300 GeV are excluded.

In 2015, the LHC will resume its operation at an increased centre-of-mass energy of 13 TeV, and the estimated integrated luminosity for 2015 is 10 fb^{-1}. The increased energy has an effect on the PDFs describing the quark and gluon content of the colliding protons (see figure 7.1), leading to increased theoretical stop pair-production cross-sections, and to an extended mass reach. The strongest benefit is expected at high stop masses: for $m_{\tilde{t}_1} = 700$ GeV, the stop pair production cross-section would increase by a factor of ∼8, while the $t\bar{t}$ production cross-section is increased only by a factor of ∼3. Table 7.1 shows the effects on the estimated yields in the mixed and three-body regions one obtains when one applies a PDF-based weight to each event, using the ratio of the appropriate PDFs (CT10 NLO or CTEQ6.1) at 13 TeV and 8 TeV, and taking into account the types of the interacting partons and their momentum fractions x. Not all parts of the x distribution relevant for pp collisions at 13 TeV are sampled well in simulated 8 TeV samples (or even kinematically accessible; i.e. $\sqrt{x_1 x_2} > 8/13$), therefore this approach has a large uncertainty that cannot be fully quantified. For both types of stop decays, the exclusion reach will be extended; as expected, the improvement is stronger for the mixed benchmark models, but already around $m_{\tilde{t}_1} \approx 300$ GeV the signal-to-background ratio benefits from the increased centre-of-mass energy. The strongest gain in production cross-section is estimated to occur for $t\bar{t} + V$ events, while single-top production occurs at a lower rate.

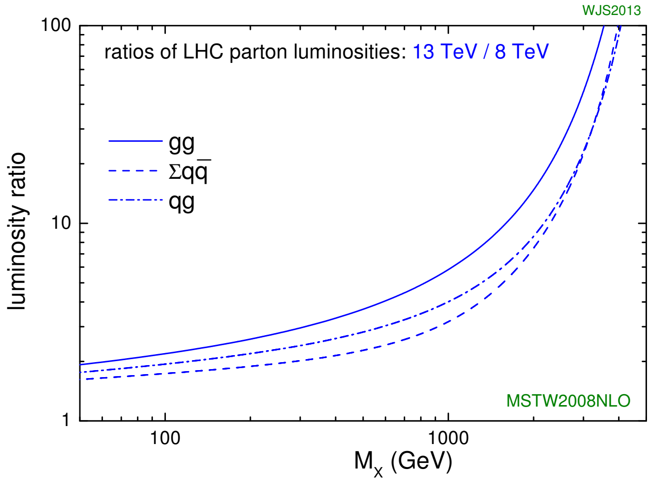

Figure 7.1: The change of the LHC centre-of-mass energy from 8 TeV to 13 TeV will increase the rate of many processes. This is shown separately for different types of interacting partons (gluon-gluon, quark-antiquark, or quark-gluon), as a function of the mass of the produced particle (from [208]).

Although the estimated run 2 performance of the existing region definitions already promises an extended search reach, it will be reasonable to refine them to account for the changes in event kinematics and background composition resulting from the increased centre-of-mass energy. To this end, several improvements to the local-gradient based optimisation detailed in section 5.4 may prove to be useful, in particular a dynamic selection of step-sizes, and the implementation of simulated annealing. The bias towards tight selections should be reduced further, for example by dividing the simulated samples into training and testing sets as is done in multivariate analyses. As the contribution from $t\bar{t} + Z$ processes will become more relevant for searches at higher stop mass, improved data-driven methods for estimating this background have to be defined.

To summarise: although no evidence for supersymmetric particles has been observed yet, significant progress has been made in constraining models of stop quark production and decay, and stop searches in one lepton final states promise exciting results also in the near future.

	shape-fit, signal bins			shape-fit, $t\bar{t}$-control bins			shape-fit, W-control bins		
process	**ratio**	$\boldsymbol{N^{2012}_{\text{expected}}}$	$\boldsymbol{N^{2015}_{\text{expected}}}$	**ratio**	$\boldsymbol{N^{2012}_{\text{expected}}}$	$\boldsymbol{N^{2015}_{\text{expected}}}$	**ratio**	$\boldsymbol{N^{2012}_{\text{expected}}}$	$\boldsymbol{N^{2015}_{\text{expected}}}$
SM	3.2±0.1	79.5± 2.2	125.4±3.9	3.2±0.1	137.2±3.2	218.0±5.5	2.8±0.2	182.7±7.4	249.8±10.7
$t\bar{t}$	3.4±0.1	66.7± 1.7	110.4±3.1	3.4±0.1	107.6±2.3	180.3±4.1	3.5±0.2	27.2±1.2	47.2± 2.3
W+jets	2.5±0.7	5.8± 1.1	7.3±1.4	3.1±0.5	19.9±2.0	30.0±3.4	2.7±0.2	145.3±7.1	190.2±10.2
t	1.4±0.3	6.0± 0.7	4.0±0.8	1.3±0.3	7.6±0.8	4.9±1.1	1.0±0.3	2.6±0.4	1.2± 0.4
$t\bar{t}+V$	10.3±6.0	0.6± 0.1	3.0±1.8	3.9±0.8	0.3±0.0	0.7±0.1	3.9±1.1	0.2±0.0	0.3± 0.1
VV	3.9±2.3	0.3± 0.1	0.7±0.3	2.7±1.7	1.0±0.4	1.3±0.6	2.7±0.7	5.7±1.0	7.5± 1.5
$m_{\tilde{t}_1}$, $m_{\tilde{\chi}^0_1}$ (GeV)									
110, 1	3.7±0.6	29.1± 3.0	53.6±5.8	3.4±0.6	24.1±2.7	39.8±4.9	3.4±0.6	19.8±2.6	32.8± 4.4
200, 50	3.9±0.5	33.9± 2.9	64.9±6.1	4.0±1.3	4.5±1.0	8.8±2.1	4.9±2.7	1.7±0.6	4.1± 1.6
300, 180	4.8±0.7	12.7± 1.3	30.0±3.4	5.4±3.2	0.8±0.4	2.2±0.9	4.4±2.7	0.6±0.3	1.3± 0.5
350, 200	5.0±0.8	10.2± 1.1	25.4±2.9	5.0±4.5	0.3±0.2	0.8±0.5	3.3±3.0	0.3±0.2	0.4± 0.3

	mixed SR			mixed TCR			mixed WCR		
process	**ratio**	$\boldsymbol{N^{2012}_{\text{expected}}}$	$\boldsymbol{N^{2015}_{\text{expected}}}$	**ratio**	$\boldsymbol{N^{2012}_{\text{expected}}}$	$\boldsymbol{N^{2015}_{\text{expected}}}$	**ratio**	$\boldsymbol{N^{2012}_{\text{expected}}}$	$\boldsymbol{N^{2015}_{\text{expected}}}$
SM	4.0±0.5	7.2± 0.6	14.3±1.3	3.4±0.1	167.5±3.0	280.7±6.2	3.3±0.1	445.7±8.8	726.1±18.1
$t\bar{t}$	4.0±0.7	2.6± 0.3	5.1±0.6	3.7±0.1	124.7±2.5	228.2±4.9	3.6±0.1	70.8±2.0	127.0± 3.8
W+jets	3.8±1.3	1.6± 0.4	3.0±0.7	3.5±0.4	24.8±1.4	43.1±3.6	3.2±0.1	348.5±8.4	553.0±15.7
$t\bar{t}+V$	6.5±0.9	1.4± 0.1	4.5±0.6	3.7±0.4	1.3±0.1	2.3±0.2	3.9±0.6	0.5±0.1	1.0± 0.1
VV	3.9±2.0	0.8± 0.3	1.6±0.6	3.3±1.4	2.5±0.7	4.1±1.2	4.6±1.1	17.4±1.8	39.1± 8.2
t	0.1±0.0	0.7± 0.1	0.0±0.0	0.4±0.1	14.0±0.7	2.5±0.6	0.8±0.2	7.3±0.7	3.0± 0.8
$m_{\tilde{t}_1}$, $m_{\tilde{\chi}^\pm_1}$, $m_{\tilde{\chi}^0_1}$ (GeV)									
400, 200, 100	5.6±0.7	10.4± 0.9	28.8±2.7	5.7±1.2	4.9±0.7	13.8±2.1	7.6±3.7	0.5±0.2	1.9± 0.7
500, 300, 150	7.4±0.9	12.1± 0.9	44.0±4.0	5.9±1.6	1.1±0.2	3.1±0.5	4.8±2.9	0.4±0.2	0.9± 0.4
600, 400, 200	8.2±0.7	7.4± 0.4	29.6±1.9	7.3±2.2	0.2±0.0	0.8±0.2	6.8±5.2	0.1±0.0	0.2± 0.1
700, 500, 250	10.3±0.8	3.7± 0.2	18.6±1.2	10.2±4.8	0.1±0.0	0.5±0.2	7.8±6.1	0.0±0.0	0.1± 0.0

Table 7.1: Change in production cross-section and estimated yields in the mixed and three-body regions for 2012 ($\sqrt{s} = 8$ TeV, $\mathcal{L}_{\text{int}} = 20.3$ fb^{-1}) compared to 2015 ($\sqrt{s} = 13$ TeV, $\mathcal{L}_{\text{int}} = 10$ fb^{-1}). The *ratio* columns show the estimated change in the production cross-section, not accounting for the difference in integrated luminosity between 2012 and 2015. The limitations of the PDF reweighting approach are explained in the text. For the three-body shape-fit, the four most signal-sensitive bins have been summed and are labelled as *signal bins*, while $t\bar{t}$- and W-*control bins* are defined using the 60 GeV$<m_{\text{T}} < 90$ GeV window and a b-tag requirement/veto. The uncertainties do not account for systematic effects, and background normalisation coefficients are not applied here.

A | Long term study of SCT optical units

The modules in the Pixel and SCT detectors receive their timing, trigger and control (TTC) information as digital optical signals using biphase mark (BPM) encoding. The recorded data is also transmitted in this way. The optical signals are generated with vertical cavity surface emitting lasers (VCSELs). The VCSEL units for TTC are on the transmitting (Tx) end of the connection, and are frequently referred to as TX units, the on-detector readout links are referred to as RX units.

One TX unit contains 12 VCSELs in a commercial array, also referred to as *channels*. All 12 channels are used in case of the SCT TX units, while in the Pixel TX units only the central 8 channels are used. For both detectors a total of 664 units are used. Each VCSEL is responsible for sending TTC to one detector module (4088 modules in the SCT, 1744 modules in the Pixel detector).

Beginning in March 2010, some VCSELs permanently stopped working, and soon it became apparent that the rate at which additional units failed was increasing over time. By the end of June 2010, there were 39 TX units with at least one broken VCSEL (see figure A.1). With only 220 spare units, it seemed to be not possible to keep the inner detector operational until the end of 2011 even with an optimistic extrapolation of the failure rate[1].

The control and readout scheme for the SCT allows data to flow through an adjacent module in case of problems, meaning that usually no or very little data is lost. However, the Pixel detector does not have this redundancy and if there is a communication problem for any module, this immediately results in incomplete recorded data. There were two main obstacles to simply producing replacement TX units: the problem was not understood, and there were no spare BPM-12 chips available (custom chips).

The reasons for the failures were unclear. Earlier failures in 2008 were shown to be a result of electrostatic discharge (ESD) during VCSEL production, after which a complete replacement of all units took place in May and July 2009; it thus seemed unlikely that ESD was a possible cause for the failures in 2010. Several approaches to understand

---

[1] The decision to run the LHC also in 2012 had not been taken at that time.

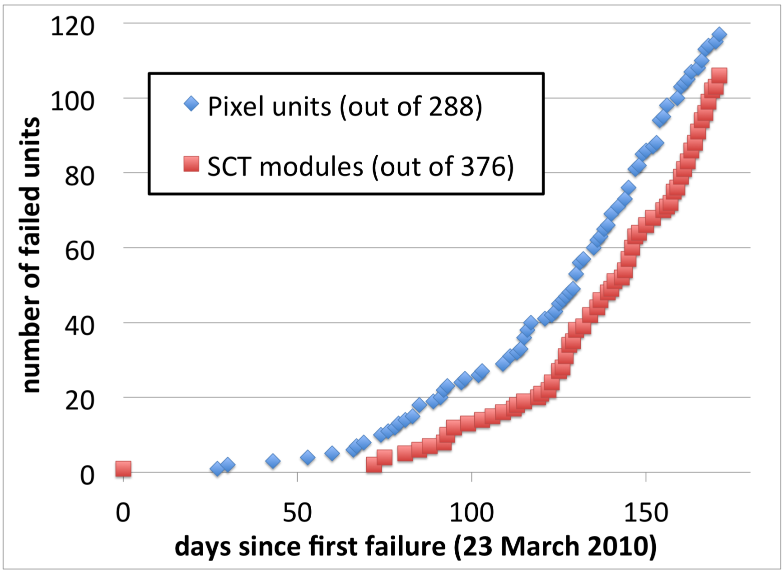

Figure A.1: Occurrence of failures of the VCSELs used in SCT and Pixel detector TTC. Ignoring the isolated failure on 23 March 2010 and accounting for the different amount of units in each sub-detector, the development of the failure rate is similar between them.

the VCSEL failures were followed concurrently, the following describes a study of the influence of humidity.

As a first step, three sets of VCSEL arrays in different conditions were studied with an optical spectrum analyser (OSA), which records the VCSEL output power as a function of wavelength. One set consisted of unused (or *fresh*) units, the two other sets were used units from the SCT or Pixel detector which had been removed after one of their 12 channels had stopped working. Figure A.2 shows examples of the recorded spectra.

Early findings indicated that lasers that have been in operation for some time (a few days up to a few months) tend to have a more narrow spectral distribution. To quantify this, the spectral width of a distribution was defined as its full width at peak level -30 dB. Figure A.3 summarises the results per array (averaged over functional channels). For the used Pixel units, there was a clear difference in the widths for the 8 central and the 4 outer channels of each array (figure A.4). Only the 8 central channels are used for Pixel TTC, in line with the hypothesis of spectral narrowing through usage. However, at this stage it was still an open question whether the narrowing would saturate or lead to a VCSEL failure eventually.

For this reason, a long term study of the effect of humidity on the VCSEL spectra was started. For a period of two years, the spectra of all channels of four fresh units were recorded, and four used units with a broken channel were added a few months into the measurements. Half of the units were kept in normal air (relative humidity (RH) around 50%), the other half were kept in N_2 (dry-air, $\sim 1\%$ RH). The units were

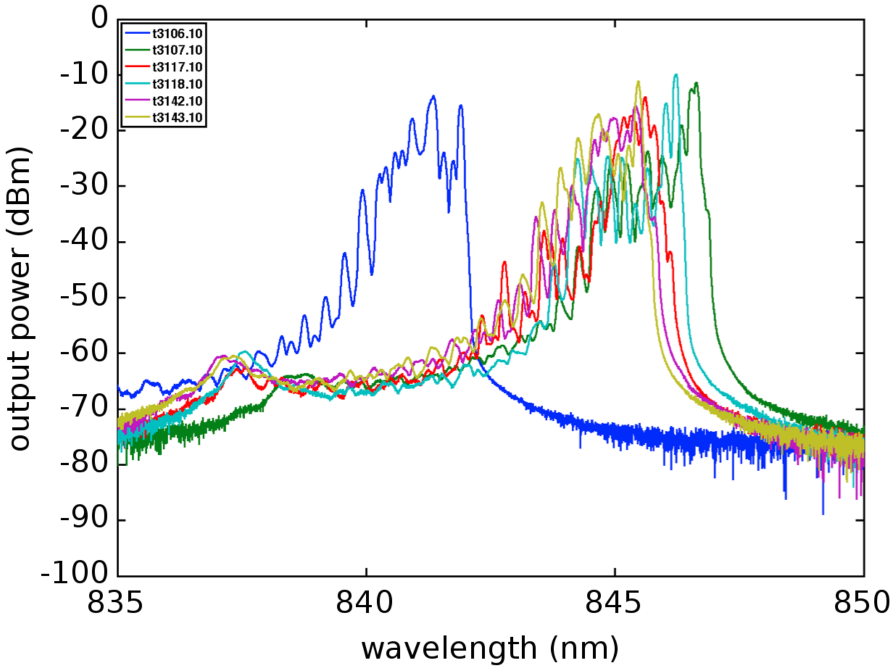

Figure A.2: Examples of output power spectra for a random selection of functional VCSELs, all of them located at the same position within their respective array. The spectra have been recorded with an OSA (Agilent 86140B). Similar shapes are observed, with typical peak positions between 840 nm and 850 nm. The spread of peak positions within one array is not larger than $1 - 2$ nm.

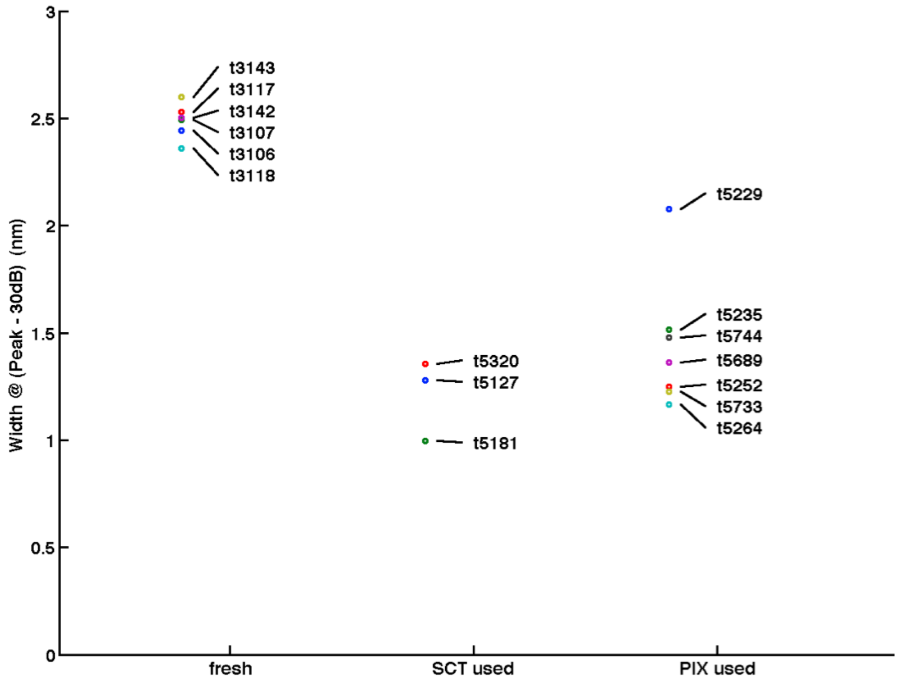

Figure A.3: Comparison of widths for the three VCSEL sets studied initially.

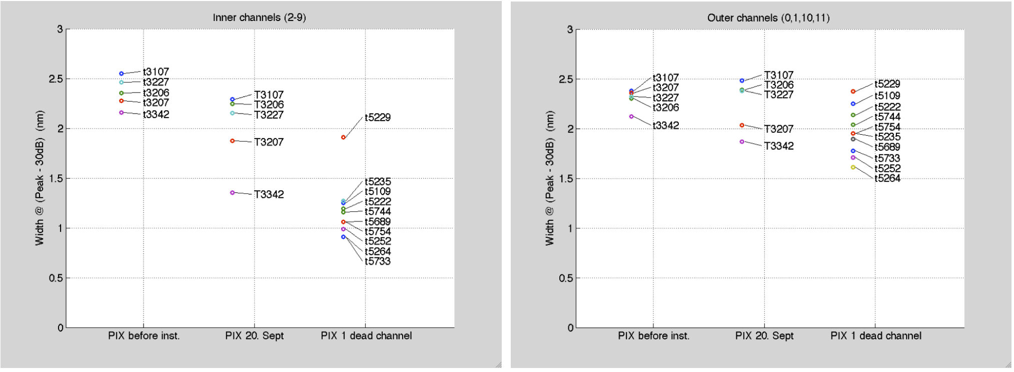

Figure A.4: Comparison of widths for the VCSEL arrays of used Pixel units. The plots show separately the average widths of the 8 central channels (left) or the 4 outer channels (right) of each unit.

flashed continuously at high rate (CLOCK/2). Several properties of the spectra were monitored: the peak power and wavelength, the integrated power, the width of the distribution containing 90% of the integrated power, as well as the width at peak level −30 dB mentioned above. Of these, only the widths (both definitions) showed a clear systematic change over time. This is shown in figure A.5, together with a simple linear slope + constant plateau fit for each unit. The comparison between units in normal air and dry air clearly shows that humidity is responsible for the spectral narrowing, and was concluded to be the main cause for the premature VCSEL failures. However, no VCSEL failure was observed over the full period, while a few were expected based on the failure rate observed in USA15; this discrepancy is not understood. Meanwhile, VCSEL arrays from a different vendor were obtained and were found to be much more reliable (about 10 failures since early 2012).

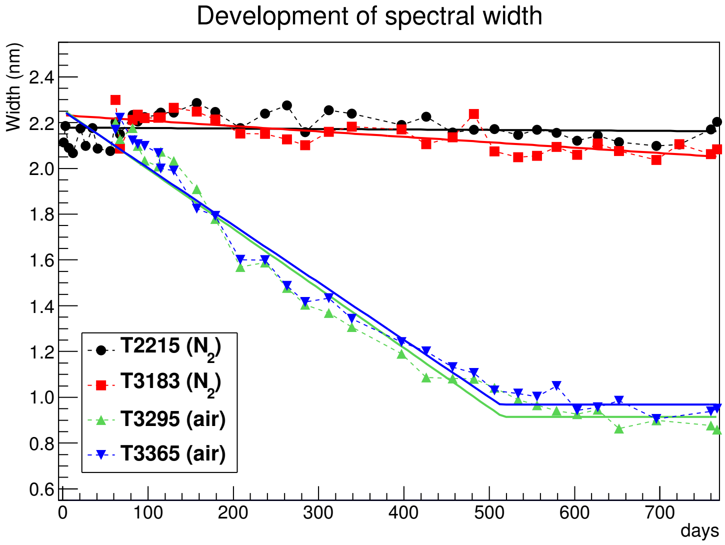

Figure A.5: Long-term study of spectral narrowing for modules kept in air and in nitrogen. The widths for each unit are averaged over its 12 channels. The trend lines were obtained by a χ^2-fit with 3 parameters: linear slope, linear offset, and starting day of the plateau. For the units kept in nitrogen, the fit moved the last parameter all the way to the right, effectively removing the plateau.

About 300 TX VCSELs had failed in 2010, compared to only 3 RX VCSELs, so the latter were no major concern, and still aren't at the time of writing. Since failures of on-detector VCSELs would cause significant problems, the RX VCSELs were produced as single VCSELs instead of arrays using a slower, but better understood technology (proton implant instead of ion implant). Additionally, accelerated ageing tests had been performed on these VCSELs [209]. Despite of this, the optical output spectra of all 8000 on-detector VCSELs were recorded in January 2011, to facilitate diagnostics in case of any future problem. The measurement setup was improved for this large-scale acquisition: an additional OSA was obtained (Yokogawa AQ6370B), optical switches were employed (fibres from the detector arrive in ribbons of twelve; the switches significantly reduced the amount of effort and risk of faulty optical connections), and a dedicated acquisition software with integrated heuristics to detect problematic measurements was developed. The full set of optical spectra was recorded by a small team in less than one week, it has been archived and has fortunately not been needed since.

B | Data-driven QCD multi-jet estimate

This appendix describes a study done from late 2011 to mid 2012. The goal was an improvement of the existing "anti-electron method".

The accurate simulation of QCD multi-jet events is challenging because such events tend to have a relatively low momentum transfer Q^2, resulting in a higher value of the strong coupling α_S and thus a less reliable QCD perturbation series expansion. Only a small fraction of QCD multi-jet events will release any of the triggers commonly used for physics analysis, and the vast majority of those will be rejected by typical selection cuts, making it also computationally expensive to estimate this background from simulation alone. Whenever QCD multi-jet events are expected to be an important background component, it is therefore common to rely less on simulation and more on data-driven methods. Very often the main concerns are misidentified leptons from semi-leptonic b-jet decays, long-lived weakly decaying states such as $\pi^{\pm}$ or K mesons, the reconstruction of a π^0 shower as an electron, or the reconstruction of electrons from photon conversions or direct photons [210].

This section presents the anti-electron method, which was originally studied in the context of semi-leptonic $t\bar{t}$ analyses Events with $t\bar{t}$ production are an important background in the search for pair-produced top squarks ($\tilde{t}_1$), especially when $\tilde{t}_1 \rightarrow t + \tilde{\chi}_1^0$ decays with a neutralino LSP are considered. In these decays, the neutralino escapes the detector without interaction, and their decay signature differs from $t\bar{t}$ events only in the missing transverse momentum distribution.

For a given nominal event selection, the anti-electron method selects a sample of data events containing jets that have failed electron identification requirements only by a small margin and could under similar circumstances have passed the nominal event selection. This selected event sample is then used to derive template distributions of kinematic quantities of interest.

The nominal semi-leptonic $t\bar{t}$ selection in the electron channel comprises the following object requirements:

- exactly one electron fulfilling the requirements discussed below,
- an electron trigger condition was satisfied and the selected electron matches the object that initiated the trigger,
- no muon with $p_{\mathrm{T}} > 20$ GeV,
- 4 or more jets reconstructed using the anti-k_t algorithm [94] (radius parameter $R = 0.4$) with $p_{\mathrm{T}} > 25$ GeV, $|\eta| < 2.5$ and 75% of the tracks inside this jet originate from the primary vertex (*jet vertex fraction*> 0.75),
- object-based $E_{\mathrm{T}}^{\mathrm{miss}} > 30$ GeV,
- transverse W mass $m_{\mathrm{T}} >35$ GeV.

Only data events in runs and luminosity blocks on the recommended good run list [1] were considered. Additionally, there are some requirements on the overall event to suppress backgrounds from in-time or out-of-time pile-up and various other sources (beam-gas interactions, cosmic-ray induced showers, or hardware problems).

While the QCD multi-jet estimate is derived from data, contributions from other processes were estimated from the simulated samples listed in table B.1.

process	**generator**	**decay mode**	**simulation dataset IDs**
$t\bar{t}$	Alpgen+ Jimmy	semi-leptonic, Np 0–5	105890–2, 117887–9
		dileptonic, Np 0–5	105894–6, 117897–9
W	Alpgen+ Jimmy	leptonic, Np 0–5	107680–705
$W + c$	Alpgen	Np 0–4	117293–7
$W + c\bar{c}$	Alpgen	Np 0–3	117284–7
$W + b\bar{b}$	Alpgen+ Jimmy	Np 0–3	107280–3
Z	Alpgen+ Jimmy	leptonic, Np 0–5	107650–75
$Z + b\bar{b}$	Alpgen+ Jimmy	leptonic, Np 0–3	109300–13
single-top	AcerMC	s-channel	117363–5
		t-channel	117360–2
diboson	Herwig		105985–7

Table B.1: Simulated samples used to estimate $t\bar{t}$ and the non-QCD backgrounds. Np: number of additional partons in the samples (resulting in additional jets).

B.1 Anti-electron selection

The most important ingredient for the anti-electron method is a modified electron object definition. We start by discussing the nominal definition: electron candidates are selected

---

[1] data11_7TeV.periodAllYear_DetStatus-v36-pro10_CoolRunQuery-00-04-08_Top_allchannels.xml

using recommendations from the ATLAS electron/photon performance group, which are regularly updated as the understanding of the detector improves. The following describes the situation in early 2012. Electron identification is made in several steps (see for example [84], section 10.2.5), starting with hit cluster identification in the silicon detectors, followed by track reconstruction (allowing for bremsstrahlung losses), and vertex finding. Using information from the TRT, most importantly the number of high-threshold hits, it is possible to identify pions and photons that convert to electron-positron pairs. For each electron candidate, the most important features found by the identification algorithms are stored as a list of flags, which are then used to define several electron categories from *loose++* to *tight++* (table B.2). All of the input variables underlying the flag definitions are described in ref. [88]. The bits selected for the anti-electron method (as explained below) rely on the following variables, all of which use properties of the track associated to the electron candidate:

- `TrackBlayer` – the track has a hit in the innermost silicon layer (*B-layer*).
- `TrackMatchEoverP` – ratio of cluster energy and track momentum
- `TrackTRThits` – number of TRT hits
- `TrackTRTratio` – fraction of highly energetic TRT hits

The tighter selections have a lower selection efficiency but also a higher purity, i.e. a lower probability of incorrectly identifying objects as electrons. The nominal electron definition in the semi-leptonic $t\bar{t}$ analysis requires the tight++ bits to pass. There are further requirements on the electron transverse momentum and pseudo-rapidity ($E_{\mathrm{T}} > 25$ GeV, $|\eta| < 2.47$, excluding the transition region $1.37 < |\eta| < 1.52$ between the barrel and end-cap cryostats), and on the electron isolation (both track-based and calorimeter-based).

To obtain a data-driven QCD estimate, the electron definition is now replaced by an "anti-electron" definition, in which some of the tight bits are required to fail. The choice of suitable bits is an important part of this study. To make the modified selection orthogonal to the nominal one, events with a selected standard electron are rejected. The missing transverse energy $E_{\mathrm{T}}^{\mathrm{miss}}$ is adjusted such that the anti-electron contributes with the correct calibration (electromagnetic scale instead of jet energy scale). Lastly, the set of accepted triggers needs to be changed: the nominal selection uses a trigger optimised for medium electrons, but due to the bit-reversal the anti-electrons can fall outside the trigger acceptance. The choice of anti-electron triggers presented a challenge because the trigger menu changed several times over the course of 2011.

An earlier version of the anti-electron method relied solely on the reversal of the `ClusterHadronicLeakage` bit, which is not part of even the loosest available electron definition. The loose single electron triggers impose a requirement on the leakage variable, making the anti-electron definition sensitive to hardware features outside the control of

bit	**name**	**loose++**	**medium++**	**tight++**
0	ClusterEtaRange	×	×	×
1	ConversionMatch			×
2	ClusterHadronicLeakage	×	×	×
3	ClusterMiddleEnergy	×	×	×
4	ClusterMiddleEratio37	×	×	×
5	ClusterMiddleEratio33			
6	ClusterMiddleWidth	×	×	×
		...		
15	ClusterStripsDEmaxs1	×	×	×
16	**TrackBlayer**		×	×
17	TrackPixel	×	×	×
18	TrackSi	×	×	×
19	TrackA0		×	×
20	TrackMatchEta	×	×	×
21	TrackMatchPhi			×
22	**TrackMatchEoverP**			×
23	—			
24	**TrackTRThits**			×
25	**TrackTRTratio**		×	×
		...		

Table B.2: Electron property bits and their use in different electron definitions. Not all bits are defined, and several bits are defined but not used. The table reflects the situation in early 2012 [88]. As detailed in the text, only the four bits in bold print are relevant for the anti-electron definition.

the analyser and without any physical meaning. A trigger match was not required in the earlier version, as this condition removed a significant fraction of the anti-electron candidates. This introduces a bias in the event selection, since events with an anti-electron candidate (with a failed `ClusterHadronicLeakage` bit, not very likely to initiate a trigger) can be selected if another electron is present in the event. An important technical difficulty resulting from this earlier anti-electron definition is that none of the $E_{\mathrm{T}}^{\mathrm{miss}}$ terms in the available datasets account for electrons that do not fulfil the loose++ electron definition, making it impossible to correct the $E_{\mathrm{T}}^{\mathrm{miss}}$ in the manner described above.

To improve on this, only electron property bits that are required for tight++ but not for loose++ electrons have been considered for reversal. Within these requirements, it is found that most of the `ClusterStrips` bits never fail, and only the following bits remained to be studied: `ConversionMatch`, `TrackBlayer`, `TrackA0`, `TrackMatchPhi`, `TrackMatchEoverP`, `TrackTRThits` and `TrackTRTratio`. The `TrackA0` bit has been dropped because it fails very rarely, and the following bits were removed because of correlations: `ConversionMatch` (correlated with `TrackBLayer`), and `TrackMatchPhi` (correlated with `TrackMatchEoverP`). Four bits remain, each of them apriori suitable for building an anti-electron model: `TrackBlayer`, `TrackMatchEoverP`, `TrackTRThits`, `TrackTRTratio`.

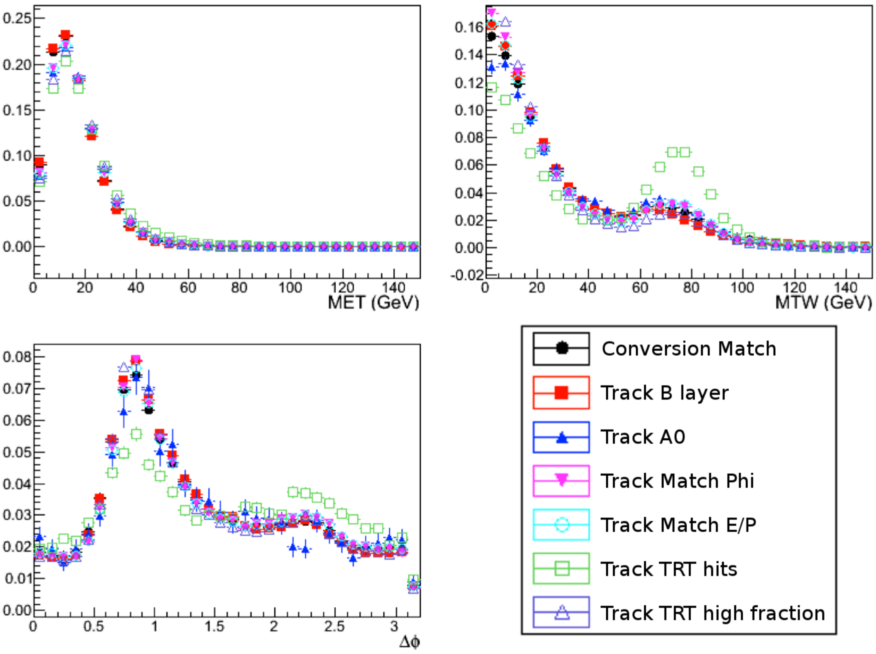

Figure B.1: Distributions of $E_{\mathrm{T}}^{\mathrm{miss}}$, m_{T} and $\Delta\phi(\ell, \vec{E}_{\mathrm{T}}^{\mathrm{miss}})$ for anti-electron QCD multi-jet models based on the reversal of different electron property bits. Only one bit is reversed for each model.

To decide if the anti-electron definition based on a given bit, or set of bits, results in a reasonable QCD model, several kinematic distributions are built. As seen in figure B.1, most models behave similarly to each other, with the exception of the model obtained by reverting the `TrackTRThits`. For practical reasons, it was decided not to use this bit, and group the remaining bits. From here on, QCD models are only distinguished by the minimum number of failed bits used in the anti-electron definition[2]. While the QCD model built from events with one or more failed bits has the largest statistics, it also has the largest estimated contamination from real electrons. At least for the looser jet bins, it is preferable to require two or more failed bits.

B.2 QCD multi-jet model evaluation

The candidate QCD distributions are judged for their agreement between data and simulated events: for each variable under consideration, the resulting QCD distribution (found with the anti-electron selection) is combined with the stack of simulated events for the remaining SM processes (found using the nominal semi-leptonic $t\bar{t}$ selection). The stacked distribution is compared to the one found in nominally selected data events. As the selection efficiency for QCD multi-jet events of the anti-electron method is unknown, the overall normalisation of the QCD distributions is initially undetermined and is derived in a sideband fit. This normalisation fit is performed for events with a missing momentum below 30 GeV, inverting the nominal selection cut which otherwise strongly suppresses QCD multi-jet events.

In practice, it is also necessary to adjust the normalisation of the simulated samples; especially the contribution of W boson events with additional jet production is overestimated in the recommended Alpgen+Jimmy samples. To this end, a refined fit procedure was established:

1. Set all simulated samples to their expected normalisation. Do not fit minor background normalisations (single-top and dibosons).
2. Float $t\bar{t}$ and Z+jets by 10%, W+jets by 30%. The QCD normalisation can float arbitrarily.
3. Fit the full $E_{\mathrm{T}}^{\mathrm{miss}}$ distribution obtained after the $m_{\mathrm{T}} > 35$ GeV cut,
4. Fit W+jets and $t\bar{t}$ to the m_{T} peak (60–90 GeV) after the $E_{\mathrm{T}}^{\mathrm{miss}} > 30$ GeV cut.
5. Lastly, determine the QCD normalisation while keeping all other components fixed, by fitting to the low MET range (5–30 GeV).

A smoothing (averaging over 3 adjacent bins) is applied before fitting if a distribution appears to have features that are likely to be statistical fluctuations. This is decided by a

---

[2] By mistake, also the `ClusterStripsDEmaxs1` bit was included in the count.

periods	runs	nominal trigger	anti-electron trigger
B–J	178044–186755	`e20_medium`	`e20_loose`
K	186873–187815	`e22_medium`	`e22_loose`
L–M	188921–191933	`e22vh_medium1` (+ `e45_medium1`)	`e22vh_loose` + `e22vh_loose_4j15_a4tc_EFFS`

Table B.3: Choice of nominal and anti-electron triggers in 2011. `e45_medium1` is used in only some of the top physics analyses.

simple heuristic counting the number of sign-changes in the derivative of the distribution (i.e. the difference between neighbouring bins).

This fit procedure has been chosen for stability across different jet bins, but does not perform well in all cases. Not all distributions in the control plots are well-described using this approach. Bad fit results are observed most often in low jet multiplicity bins.

Figures B.2 to B.5 show overviews of the QCD models built with one or more failed electron property bit (figs. B.2 & B.3) and two or more failed bits (figs. B.4 & B.5), obtained from the full 2011 dataset, in different jet bins. The normalisation coefficients given in the legend are relative to the usual sample normalisation determined from the recorded luminosity, simulated sample sizes and theoretical process cross-sections. The fit errors are not meaningful as the fits are strongly constrained and the fitted parameters are often at one of their boundaries. There are two main weights applied to the events constituting the QCD models: the trigger prescales described below, and the normalisation extracted from the fit, on the order of 0.01–0.10.

The figures show that the QCD model does not describe the 3 jet, no b-tag bin very well. There are several parts of phase space that appear to be too challenging for this simple approach, for example m_{T} at energies below the W peak, or the angular separation between the lepton and the missing momentum. However, in the 4 jet, b-tag bin, where QCD plays a smaller role, the modelling is sufficient.

B.3 Triggers for the anti-electron model

An important technical issue, but secondary to understanding the ideas of the method, is the choice of triggers in the event selection. The medium electron triggers used in the nominal analysis selection have a low efficiency for anti-electrons, and a set of corresponding triggers with looser electron requirements needed to be found. The trigger menu evolved over the course of 2011, and so did the choice of nominal and anti-electron triggers. Table B.3 summarises the different nominal and anti-electron triggers that were used.

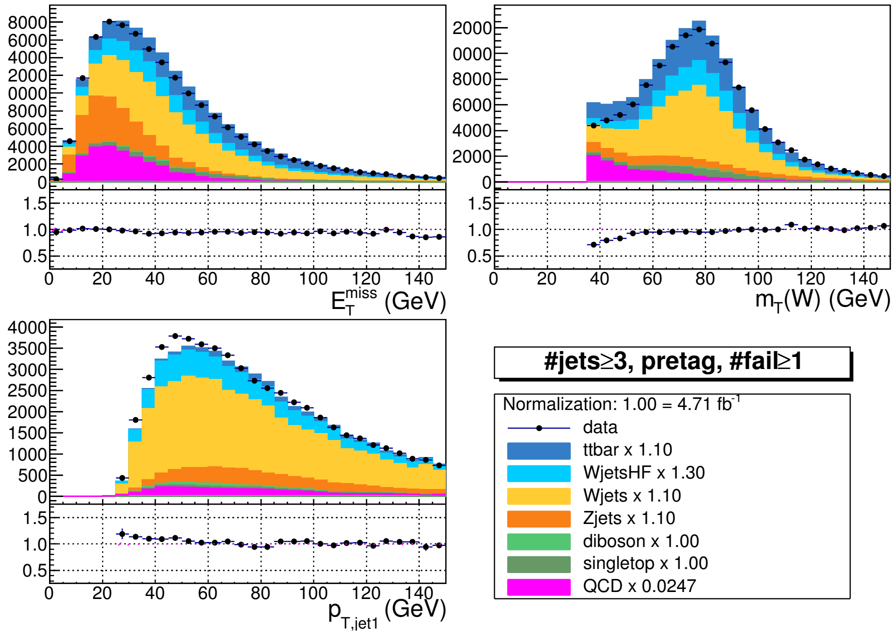

Figure B.2: Distributions of missing transverse energy $E_{\mathrm{T}}^{\mathrm{miss}}$, transverse W-boson momentum m_{T}, and leading jet momentum for an anti-electron model requiring at least one failed bit. A $\geqslant$3 jets requirement has been applied.

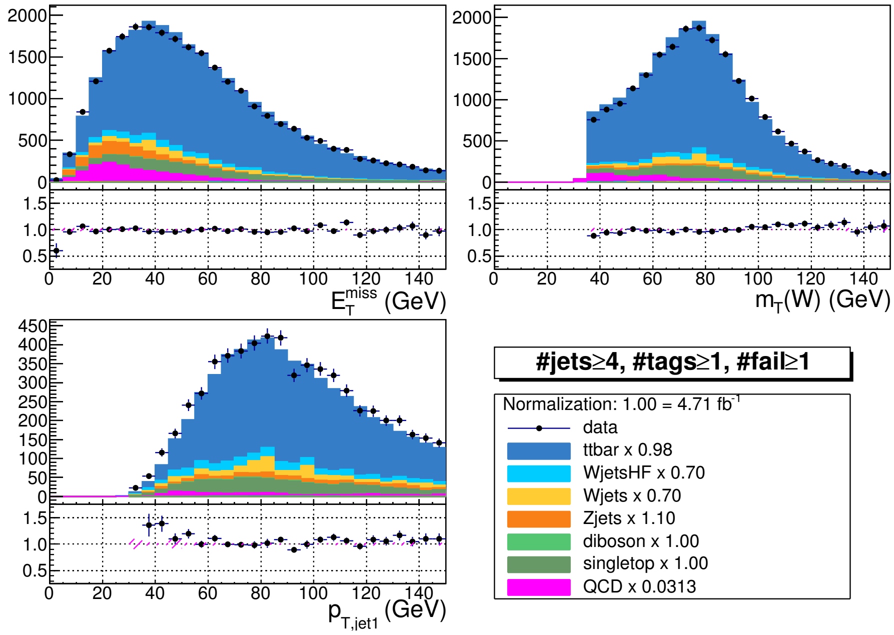

Figure B.3: Anti-electron model requiring at least one failed bit, shown for events with at least 4 jets and one or more b-tags.

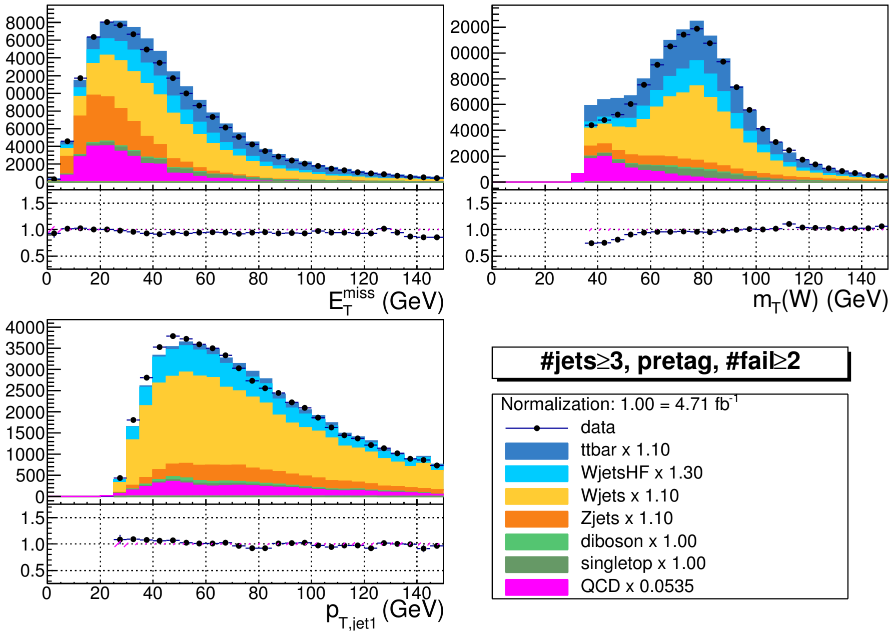

Figure B.4: Anti-electron model requiring two or more failed bits ($\geqslant$ 3 jets, no b-tag requirement).

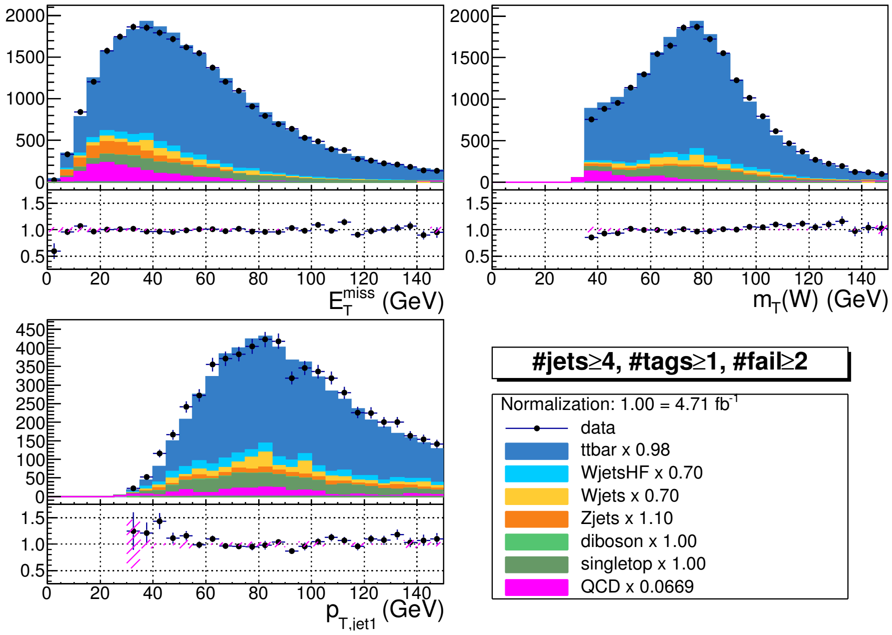

Figure B.5: Anti-electron model requiring two or more failed bits ($\geqslant$ 4 jets, $\geqslant$ 1 b-tag).

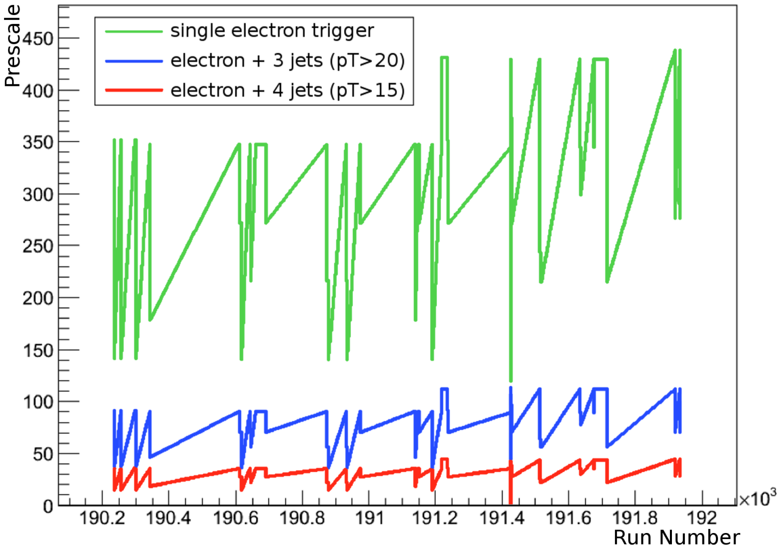

Figure B.6: Prescale values for the triggers used in periods L+M of the 2011 data-taking period. The prescales decrease in each run, but are returned to a higher value at the beginning of the following run. The large prescale value for the single electron trigger `ev22vh_loose` results in too few recorded events for this trigger to build a usable anti-electron model. For this reason lepton+jets triggers were taken into consideration.

Unfortunately, the looser triggers are often "prescaled", which means that only a certain fraction of the triggering events will also be recorded. The prescale values used for each of the anti-electron triggers changes between periods, and also change within a run to balance the decreasing instantaneous luminosity (figure B.6).

To have a sample of anti-electron events that is representing all parts of the data-taking at a comparable level, the events in the anti-electron model are weighted with their corresponding trigger prescale.

For periods L and M, a multi-object trigger responding to the presence of a loose electron and 4 jets ($p_{\mathrm{T}} > 15$ GeV) in the event is included to improve the statistics of the model. The turn-on of this trigger is sufficiently steep to not have to correct for the inefficiency for low momentum jets (the nominal analysis requires 4 jets with $p_{\mathrm{T}} > 25$ GeV). This additional trigger leads to a slight over-representation of periods L+M. Although the trigger requires 4 jets with $p_{\mathrm{T}} > 15$ GeV, this is also clearly seen in the 3 jet ($p_{\mathrm{T}} > 25$ GeV) bins, see for example the bottom middle plot in figure B.2.

B.4 Extraction of QCD multi-jet fraction

Table B.4 summarises the observed counts and fractions of the QCD models for 1–3 failed bits. The last column shows the estimated QCD multi-jet fractions. Table B.5 shows the fraction of real electron events picked up in the model building, estimated by applying the anti-electron method to simulated samples. The QCD multi-jet fractions corrected for this contribution is also shown. The real electron estimates are not affected by trigger prescales, but the per-process normalisation derived in the fit still needs to be applied.

Each model and each jet bin leads to a different prediction of the QCD fraction, but the correction brings the estimates of the different QCD models closer to each other. The uncertainties in the table are based on the statistical uncertainties of the yields and the uncertainty of the fitted QCD normalisation. They are clearly optimistic in many cases. The nominal analysis requires four or more jets, and optionally one or more b-tags. Averaging over the three estimates available per jet bin, and increasing the uncertainty to also cover most of the estimated fractions of neighbouring jet bins, the following anti-electron QCD fractions are found:

- $\geqslant 4$ jets, no b-tag requirement: $(7 \pm 2)\%$
- $\geqslant 4$ jets, and b-tag requirement: $(3.1 \pm 1.4)\%$

For comparison we quote the results of the *matrix method* (MM; see e.g. [190], chapter 10.3), commonly used for QCD multi-jet estimates. At the time of the Moriond conference 2011, the following estimates were found for the electron channel of the semi-leptonic $t\bar{t}$ analysis using the MM:

- $\geqslant 4$ jets, no b-tag requirement: $(5.5 \pm 2.0)\%$
- $\geqslant 4$ jets, and b-tag requirement: $(5.4 \pm 5.9)\%$

The results are compatible. The anti-electron estimates have smaller uncertainties, and the effect of the b-tag requirement is more visible there.

jet bin	**data 2011**	**QCD model**					**uncorrected QCD fraction**
		bits	**raw**	**⟨PS⟩**	**fit norm.**	**weighted**	
$\geqslant$ 1j, 0b	1669412	$\geqslant$ 1	29489	110.0	0.0409±0.0001	132590	7.94%± 0.05%
$\geqslant$ 1j, 0b	1669412	$\geqslant$ 2	14343	109.5	0.0882±0.0003	138531	8.30%± 0.07%
$\geqslant$ 1j, 0b	1669412	$\geqslant$ 3	3792	108.1	0.3414±0.0010	139908	8.38%± 0.14%
$\geqslant$ 1j, 1b	121012	$\geqslant$ 1	2441	92.8	0.0470±0.0005	10652	8.80%± 0.20%
$\geqslant$ 1j, 1b	121012	$\geqslant$ 2	1147	94.8	0.1025±0.0011	11151	9.21%± 0.29%
$\geqslant$ 1j, 1b	121012	$\geqslant$ 3	295	89.4	0.3982±0.0041	10504	8.68%± 0.51%
$\geqslant$ 2j, 0b	430108	$\geqslant$ 1	14934	85.7	0.0333±0.0002	42581	9.90%± 0.11%
$\geqslant$ 2j, 0b	430108	$\geqslant$ 2	7435	85.4	0.0725±0.0005	46038	10.70%± 0.14%
$\geqslant$ 2j, 0b	430108	$\geqslant$ 3	1979	83.4	0.2753±0.0019	45435	10.56%± 0.25%
$\geqslant$ 2j, 1b	73931	$\geqslant$ 1	1846	78.9	0.0417±0.0008	6075	8.22%± 0.24%
$\geqslant$ 2j, 1b	73931	$\geqslant$ 2	846	79.3	0.0906±0.0016	6079	8.22%± 0.32%
$\geqslant$ 2j, 1b	73931	$\geqslant$ 3	219	74.2	0.3201±0.0058	5202	7.04%± 0.49%
$\geqslant$ 2j, 2b	18502	$\geqslant$ 1	232	67.2	0.0375±0.0033	585	3.16%± 0.35%
$\geqslant$ 2j, 2b	18502	$\geqslant$ 2	90	61.3	0.0712±0.0063	393	2.12%± 0.29%
$\geqslant$ 2j, 2b	18502	$\geqslant$ 3	25	73.9	0.3686±0.0347	682	3.68%± 0.81%
$\geqslant$ 3j, 0b	122577	$\geqslant$ 1	6341	67.5	0.0247±0.0004	10565	8.62%± 0.19%
$\geqslant$ 3j, 0b	122577	$\geqslant$ 2	3122	65.8	0.0535±0.0009	10997	8.97%± 0.22%
$\geqslant$ 3j, 0b	122577	$\geqslant$ 3	806	65.9	0.1909±0.0033	10141	8.27%± 0.33%
$\geqslant$ 3j, 1b	42208	$\geqslant$ 1	1027	64.5	0.0351±0.0014	2324	5.50%± 0.27%
$\geqslant$ 3j, 1b	42208	$\geqslant$ 2	458	61.5	0.0793±0.0031	2233	5.29%± 0.32%
$\geqslant$ 3j, 1b	42208	$\geqslant$ 3	117	61.8	0.2660±0.0103	1925	4.56%± 0.46%
$\geqslant$ 3j, 2b	15533	$\geqslant$ 1	183	64.0	0.0334±0.0050	392	2.52%± 0.42%
$\geqslant$ 3j, 2b	15533	$\geqslant$ 2	67	54.0	0.0741±0.0105	269	1.73%± 0.32%
$\geqslant$ 3j, 2b	15533	$\geqslant$ 3	14	61.1	0.3059±0.0475	262	1.69%± 0.52%
$\geqslant$ 4j, 0b	40021	$\geqslant$ 1	1885	66.5	0.0217±0.0009	2724	6.81%± 0.33%
$\geqslant$ 4j, 0b	40021	$\geqslant$ 2	942	64.7	0.0478±0.0021	2912	7.28%± 0.39%
$\geqslant$ 4j, 0b	40021	$\geqslant$ 3	229	72.7	0.1609±0.0070	2679	6.69%± 0.53%
$\geqslant$ 4j, 1b	21299	$\geqslant$ 1	405	64.1	0.0303±0.0028	787	3.69%± 0.38%
$\geqslant$ 4j, 1b	21299	$\geqslant$ 2	181	63.2	0.0647±0.0060	740	3.47%± 0.41%
$\geqslant$ 4j, 1b	21299	$\geqslant$ 3	47	69.2	0.1874±0.0176	610	2.86%± 0.50%
$\geqslant$ 4j, 2b	9661	$\geqslant$ 1	100	65.3	0.0322±0.0081	211	2.17%± 0.59%
$\geqslant$ 4j, 2b	9661	$\geqslant$ 2	39	57.0	0.0559±0.0157	125	1.28%± 0.42%
$\geqslant$ 4j, 2b	9661	$\geqslant$ 3	7	56.7	0.1294±0.0657	52	0.53%± 0.34%
$\geqslant$ 5j, 0b	12753	$\geqslant$ 1	490	65.3	0.0258±0.0023	826	6.48%± 0.66%
$\geqslant$ 5j, 0b	12753	$\geqslant$ 2	240	59.3	0.0563±0.0051	802	6.28%± 0.71%
$\geqslant$ 5j, 0b	12753	$\geqslant$ 3	61	73.1	0.1310±0.0126	585	4.58%± 0.73%
$\geqslant$ 5j, 1b	8372	$\geqslant$ 1	127	61.3	0.0301±0.0053	235	2.80%± 0.55%
$\geqslant$ 5j, 1b	8372	$\geqslant$ 2	52	49.7	0.0619±0.0111	160	1.91%± 0.43%
$\geqslant$ 5j, 1b	8372	$\geqslant$ 3	12	42.5	0.0857±0.0223	44	0.52%± 0.20%
$\geqslant$ 5j, 2b	4236	$\geqslant$ 1	36	56.4	0.0262±0.0216	54	1.25%± 1.06%
$\geqslant$ 5j, 2b	4236	$\geqslant$ 2	15	29.7	0.0960±0.0774	43	1.01%± 0.85%
$\geqslant$ 5j, 2b	4236	$\geqslant$ 3	3	41.6	0.0941±0.2427	12	0.28%± 0.73%

Table B.4: Observed events in 2011 data using the nominal selection, QCD yields and applied scales, and the QCD fraction without the correction for the real electron contribution.

jet bin	data 2011	QCD model		real electrons		corrected QCD fraction
		bits	weighted	raw	weighted	
⩾ 1j, 0b	1669412	⩾ 1	132590	409825	10417.2±31.9	7.32%± 0.06%
⩾ 1j, 0b	1669412	⩾ 2	138531	76079	4021.4±20.8	8.06%± 0.08%
⩾ 1j, 0b	1669412	⩾ 3	139908	8363	1352.2±19.5	8.30%± 0.14%
⩾ 1j, 1b	121012	⩾ 1	10652	109390	842.0± 6.7	8.11%± 0.21%
⩾ 1j, 1b	121012	⩾ 2	11151	19384	340.2± 5.2	8.93%± 0.29%
⩾ 1j, 1b	121012	⩾ 3	10504	2534	148.2± 5.4	8.56%± 0.51%
⩾ 2j, 0b	430108	⩾ 1	42581	230791	2214.6±12.2	9.39%± 0.11%
⩾ 2j, 0b	430108	⩾ 2	46038	43832	956.0± 7.6	10.48%± 0.15%
⩾ 2j, 0b	430108	⩾ 3	45435	5125	343.8± 6.5	10.48%± 0.25%
⩾ 2j, 1b	73931	⩾ 1	6075	92883	477.6± 5.5	7.57%± 0.25%
⩾ 2j, 1b	73931	⩾ 2	6079	16753	198.5± 3.3	7.95%± 0.32%
⩾ 2j, 1b	73931	⩾ 3	5202	2237	79.0± 2.3	6.93%± 0.49%
⩾ 2j, 2b	18502	⩾ 1	585	32499	99.7± 6.8	2.62%± 0.38%
⩾ 2j, 2b	18502	⩾ 2	393	5745	33.2± 2.3	1.94%± 0.30%
⩾ 2j, 2b	18502	⩾ 3	682	824	24.8± 2.1	3.55%± 0.82%
⩾ 3j, 0b	122577	⩾ 1	10565	104179	492.6± 5.2	8.22%± 0.19%
⩾ 3j, 0b	122577	⩾ 2	10997	19932	208.5± 2.9	8.80%± 0.23%
⩾ 3j, 0b	122577	⩾ 3	10141	2636	87.1± 2.6	8.20%± 0.33%
⩾ 3j, 1b	42208	⩾ 1	2324	64308	227.0± 6.6	4.97%± 0.29%
⩾ 3j, 1b	42208	⩾ 2	2233	11868	93.6± 2.9	5.07%± 0.32%
⩾ 3j, 1b	42208	⩾ 3	1925	1680	42.7± 1.8	4.46%± 0.46%
⩾ 3j, 2b	15533	⩾ 1	392	27352	75.4± 9.6	2.04%± 0.45%
⩾ 3j, 2b	15533	⩾ 2	269	4884	29.7± 3.7	1.54%± 0.33%
⩾ 3j, 2b	15533	⩾ 3	262	723	18.3± 2.7	1.57%± 0.52%
⩾ 4j, 0b	40021	⩾ 1	2724	50321	138.5± 3.7	6.46%± 0.34%
⩾ 4j, 0b	40021	⩾ 2	2912	9687	57.2± 1.7	7.13%± 0.39%
⩾ 4j, 0b	40021	⩾ 3	2679	1420	25.7± 1.2	6.63%± 0.53%
⩾ 4j, 1b	21299	⩾ 1	787	38434	98.9± 7.5	3.23%± 0.41%
⩾ 4j, 1b	21299	⩾ 2	740	7251	38.5± 3.1	3.29%± 0.42%
⩾ 4j, 1b	21299	⩾ 3	610	1107	16.7± 1.5	2.79%± 0.50%
⩾ 4j, 2b	9661	⩾ 1	211	18626	45.4±10.4	1.70%± 0.63%
⩾ 4j, 2b	9661	⩾ 2	125	3464	14.7± 3.8	1.13%± 0.42%
⩾ 4j, 2b	9661	⩾ 3	52	542	5.4± 2.6	0.48%± 0.34%
⩾ 5j, 0b	12753	⩾ 1	826	22098	52.6± 3.6	6.06%± 0.67%
⩾ 5j, 0b	12753	⩾ 2	802	4296	22.0± 1.6	6.11%± 0.71%
⩾ 5j, 0b	12753	⩾ 3	585	673	7.5± 0.7	4.52%± 0.73%
⩾ 5j, 1b	8372	⩾ 1	235	18491	38.7± 6.0	2.34%± 0.58%
⩾ 5j, 1b	8372	⩾ 2	160	3551	15.1± 2.4	1.73%± 0.44%
⩾ 5j, 1b	8372	⩾ 3	44	576	3.3± 0.8	0.48%± 0.20%
⩾ 5j, 2b	4236	⩾ 1	54	9789	16.6±12.8	0.86%± 1.11%
⩾ 5j, 2b	4236	⩾ 2	43	1847	11.6± 8.7	0.74%± 0.89%
⩾ 5j, 2b	4236	⩾ 3	12	311	2.0± 4.8	0.23%± 0.74%

Table B.5: Estimates of the real electron fraction in the QCD models, and corrected QCD fractions per jet bin and model.

Bibliography

[1] M. Breidenbach et al. *Observed Behavior of Highly Inelastic Electron-Proton Scattering* Phys. Rev. Lett. 23(16) (1969) 935. DOI: `10.1103/PhysRevLett.23.935`.

[2] J. Beringer et al. *Particle Data Group* Phys. Rev. D86, 010001. 2012.

[3] V. Ezhela, S. Lugovsky, and O. Zenin. *Hadronic part of the muon* $g-2$ *estimated on the* $\sigma_{\text{tot}}^{2003}(e^+e^- \rightarrow \text{hadrons})$ *evaluated data compilation* (2003). arXiv: `hep-ph/0312114 [hep-ph]`.

[4] C. Cowan et al. *Detection of the free neutrino: A Confirmation* Science 124 (1956) 103. DOI: `10.1126/science.124.3212.103`.

[5] F. Reines and C. L. Cowan. *The neutrino* Nature 178 (1956) 446. DOI: `10.1038/178446a0`.

[6] K. Nakamura. *Physics of Neutrinos* J. Phys. Soc. Japan 76(11) (2007) 111008. DOI: `10.1143/JPSJ.76.111008`.

[7] S. Schael et al. *Precision electroweak measurements on the Z resonance* Phys. Rept. 427 (2006) 257. DOI: `10.1016/j.physrep.2005.12.006`.

[8] ATLAS Collaboration. *Search for pair production of heavy top-like quarks decaying to a high-*p_T *W boson and a b quark in the lepton plus jets final state at* $\sqrt{s} = 7$ *TeV with the ATLAS detector* Phys. Lett. B 718 (2012) 1284. DOI: `10.1016/j.physletb.2012.11.071`.

[9] ATLAS Collaboration. *Measurement of the Higgs boson mass from the* $H \rightarrow \gamma\gamma$ *and* $H \rightarrow ZZ^* \rightarrow 4\ell$ *channels with the ATLAS detector using 25 fb*$^{-1}$ *of pp collision data* Phys. Rev. D 90(5) (2014) 052004. DOI: `10.1103/PhysRevD.90.052004`.

[10] CMS Collaboration. *Precise determination of the mass of the Higgs boson and studies of the compatibility of its couplings with the standard model.* CMS-PAS-HIG-14-009. 2014.

[11] D. Griffiths. *Introduction to Elementary Particles, Second Edition* Wiley-VCH, 2008.

[12] W. N. Cottingham and D. A. Greenwood. *An Introduction to the Standard Model of Particle Physics* 2nd ed. Cambridge Univ. Press, 2007. URL: `http://www.einstein-schrodinger.com/Standard_Model.pdf`.

[13] F. Englert and R. Brout. *Broken Symmetry and the Mass of Gauge Vector Mesons* Phys. Rev. Lett. 13(9) (1964) 321. DOI: `10.1103/PhysRevLett.13.321`.

[14] P. W. Higgs. *Broken Symmetries and the Masses of Gauge Bosons* Phys. Rev. Lett. 13(16) (1964) 508. DOI: `10.1103/PhysRevLett.13.508`.

[15] G. S. Guralnik, C. R. Hagen, and T. W. B. Kibble. *Global Conservation Laws and Massless Particles* Phys. Rev. Lett. 13(20) (1964) 585. DOI: `10.1103/PhysRevLett.13.585`.

[16] J. Goldstone. *Field theories with "Superconductor" solutions* Nuovo Cimento 19(1) (1961) 154. DOI: `10.1007/BF02812722`.

[17] M. E. Peskin and D. V. Schroeder. *An Introduction to Quantum Field Theory* Addison-Wesley, 1995.

[18] F. J. Hasert et al. *Observation of Neutrino Like Interactions Without Muon Or Electron in the Gargamelle Neutrino Experiment* Phys. Lett. B 46 (1973) 138. DOI: `10.1016/0370-2693(73)90499-1`.

[19] G. Arnison et al. *Experimental observation of isolated large transverse energy electrons with associated missing energy at* $\sqrt{s} = 540\ GeV$ Phys. Lett. B 122(1) (1983) 103. DOI: `10.1016/0370-2693(83)91177-2`.

[20] M. Banner et al. *Observation of single isolated electrons of high transverse momentum in events with missing transverse energy at the CERN pp collider* Phys. Lett. B 122(5-6) (1983) 476. DOI: `10.1016/0370-2693(83)91605-2`.

[21] G. Arnison et al. *Experimental observation of lepton pairs of invariant mass around 95* GeV/c^2 *at the CERN SPS collider* Phys. Lett. B 126(5) (1983) 398. DOI: `10.1016/0370-2693(83)90188-0`.

[22] P. Bagnaia et al. *Evidence for* $Z^0 \to e^+e^-$ *at the CERN pp collider* Phys. Lett. B 129(1-2) (1983) 130. DOI: `10.1016/0370-2693(83)90744-X`.

[23] ATLAS Collaboration. *A particle consistent with the Higgs Boson observed with the ATLAS Detector at the Large Hadron Collider* Science 338 (2012) 1576. DOI: `10.1126/science.1232005`.

[24] CMS Collaboration. *Observation of a new boson at a mass of 125 GeV with the CMS experiment at the LHC* Phys. Lett. B 716 (2012) 30. arXiv: `1207.7235`.

[25] ATLAS Collaboration. *Evidence for the spin-0 nature of the Higgs boson using ATLAS data* Phys. Lett. B 726 (2013) 120. arXiv: `1307.1432`.

[26] CMS Collaboration. *Study of the Mass and Spin-Parity of the Higgs Boson Candidate via Its Decays to Z Boson Pairs. On the mass and spin-parity of the Higgs boson candidate via its decays to Z boson pairs* Phys. Rev. Lett. 110 (2012) 081803. arXiv: `1212.6639`.

[27] ATLAS Collaboration. *Observation of a new particle in the search for the Standard Model Higgs boson with the ATLAS detector at the LHC* Phys. Lett. B 716 (2012) 1. DOI: `10.1016/j.physletb.2012.08.020`.

[28] S. Dittmaier et al. *Handbook of LHC Higgs Cross Sections: 2. Differential Distributions* (2012). DOI: `10.5170/CERN-2012-002`.

[29] F. Zwicky. *On the Masses of Nebulae and of Clusters of Nebulae* Astrophys. J. 86 (1937) 217. DOI: `10.1086/143864`.

[30] R. N. Cahn. *The eighteen arbitrary parameters of the standard model in your everyday life* Rev. Mod. Phys. 68(3) (1996) 951. DOI: `10.1103/RevModPhys.68.951`.

[31] S. P. Martin. *A Supersymmetry primer* Adv. Ser. Direct. High Energy Phys. 21 (2010) 1. DOI: `10.1142/9789814307505_0001`.

[32] H. W. Baer and X. Tata. *Weak scale supersymmetry: from superfields to scattering events* Cambridge Univ. Press, 2006.

[33] M. Drees, R. Godbole, and P. Roy. *Theory and phenomenology of Sparticles: an account of four-dimensional N=1 supersymmetry in high-energy physics* World Scientific, 2004.

[34] U. Amaldi, W. de Boer, and H. Fürstenau. *Comparison of grand unified theories with electroweak and strong coupling constants measured at LEP* Phys. Lett. B 260 (1991) 447.

[35] CMS Collaboration. *Search for leptonic decays of W' bosons in pp collisions at $\sqrt{s} = 7$ TeV* J. High Energy Phys. 1208 (2012) 023. DOI: `10.1007/JHEP08(2012)023`.

[36] ATLAS Collaboration. *ATLAS search for a heavy gauge boson decaying to a charged lepton and a neutrino in pp collisions at $\sqrt{s} = 7$ TeV* Eur. Phys. J. C 72 (2012) 2241. DOI: `10.1140/epjc/s10052-012-2241-5`.

[37] CMS Collaboration. *Search for narrow resonances in dilepton mass spectra in pp collisions at $\sqrt{s} = 7$ TeV* Phys. Lett. B 714 (2012) 158. DOI: `10.1016/j.physletb.2012.06.051`.

[38] ATLAS Collaboration. *Search for high-mass resonances decaying to dilepton final states in pp collisions at $\sqrt{s} = 7$ TeV with the ATLAS detector* J. High Energy Phys. 1211 (2012) 138. DOI: `10.1007/JHEP11(2012)138`.

[39] S. Dodelson and L. M. Widrow. *Sterile-neutrinos as dark matter* Phys. Rev. Lett. 72 (1994) 17. DOI: `10.1103/PhysRevLett.72.17`.

[40] E. Bulbul et al. *Detection of An Unidentified Emission Line in the Stacked X-ray spectrum of Galaxy Clusters* Astrophys. J. 789 (2014) 13. DOI: `10.1088/0004-637X/789/1/13`.

[41] A. Boyarsky et al. *An unidentified line in X-ray spectra of the Andromeda galaxy and Perseus galaxy cluster* (2014). arXiv: `1402.4119 [astro-ph.CO]`.

[42] L. Susskind. *Dynamics of spontaneous symmetry breaking in the Weinberg-Salam theory* Phys. Rev. D 20(10) (1979) 2619. DOI: `10.1103/PhysRevD.20.2619`.

[43] L. Randall and R. Sundrum. *Large Mass Hierarchy from a Small Extra Dimension* Phys. Rev. Lett. 83(17) (1999) 3370. DOI: `10.1103/PhysRevLett.83.3370`.

[44] H. P. Nilles. *Supersymmetry, Supergravity and Particle Physics* Phys. Rept. 110 (1984) 1. DOI: `10.1016/0370-1573(84)90008-5`.

[45] I. Aitchison. *Supersymmetry in Particle Physics: An Elementary Introduction* Cambridge Univ. Press, 2007.

[46] M. E. Peskin. *Supersymmetry in Elementary Particle Physics* (2008) 609. arXiv: `0801.1928 [hep-ph]`.

[47] J. Wess and B. Zumino. *A Lagrangian Model Invariant Under Supergauge Transformations* Phys. Lett. B 49 (1974) 52. DOI: `10.1016/0370-2693(74)90578-4`.

[48] S. R. Coleman and J. Mandula. *All Possible Symmetries of the S Matrix* Phys. Rev. 159 (1967) 1251. DOI: `10.1103/PhysRev.159.1251`.

[49] R. Haag, J. T. Lopuszanski, and M. Sohnius. *All Possible Generators of Supersymmetries of the S-Matrix* Nucl. Phys. B 88 (1975) 257.

[50] P. Binétruy. *Supersymmetry: Theory, Experiment, and Cosmology* Oxford Graduate Texts. Oxford Univ. Press, 2006.

[51] S. Ferrara, L. Girardello, and F. Palumbo. *A General Mass Formula in Broken Supersymmetry* Phys. Rev. D 20 (1979) 403. DOI: `10.1103/PhysRevD.20.403`.

[52] G. R. Farrar and S. Weinberg. *Supersymmetry at Ordinary Energies. 2. R Invariance, Goldstone Bosons, and Gauge Fermion Masses* Phys. Rev. D 27 (1983) 2732. DOI: `10.1103/PhysRevD.27.2732`.

[53] D. J. Gross, R. W. Jackiw, and S. B. Treiman. *Lectures on Current Algebra and its Applications.* Princeton Univ. Press, 1972.

[54] S. Dimopoulos and L. J. Hall. *Lepton and Baryon Number Violating Collider Signatures from Supersymmetry* Phys. Lett. B 207 (1988) 210. DOI: `10.1016/0370-2693(88)91418-9`.

[55] D. Chung et al. *The Soft supersymmetry breaking Lagrangian: Theory and applications* Phys. Rept. 407 (2005) 1. DOI: `10.1016/j.physrep.2004.08.032`.

[56] R. Mahbubani et al. *Light Nondegenerate Squarks at the LHC* Phys. Rev. Lett. 110 15 (2013) 151804. DOI: `10.1103/PhysRevLett.110.151804`. URL: `http://link.aps.org/doi/10.1103/PhysRevLett.110.151804`.

[57] R. Barbieri and G. F. Giudice. *Upper bounds on supersymmetric particle masses* Nucl. Phys. B 306 (1987) 63.

[58] M. Papucci, J. T. Ruderman, and A. Weiler. *Natural SUSY Endures* J. High Energy Phys. 1209 (2012) 035. DOI: `10.1007/JHEP09(2012)035`.

[59] A. Djouadi, J.-L. Kneur, and G. Moultaka. *SuSpect: A Fortran code for the supersymmetric and Higgs particle spectrum in the MSSM* Comput. Phys. Commun. 176 (2007) 426. DOI: `10.1016/j.cpc.2006.11.009`.

[60] C. F. Berger et al. *Supersymmetry Without Prejudice* J. High Energy Phys. 0902 (2009) 023. DOI: `10.1088/1126-6708/2009/02/023`.

[61] G. D'Ambrosio et al. *Minimal flavor violation: An Effective field theory approach* Nucl. Phys. B 645 (2002) 155. DOI: `10.1016/S0550-3213(02)00836-2`.

[62] M. Perelstein and A. Weiler. *Polarized Tops from Stop Decays at the LHC* J. High Energy Phys. 0903 (2009) 141. DOI: `10.1088/1126-6708/2009/03/141`.

[63] H. E. Haber and R. Hempfling. *Can the mass of the lightest Higgs boson of the minimal supersymmetric model be larger than $m(Z)$?* Phys. Rev. Lett. 66 (1991) 1815. DOI: `10.1103/PhysRevLett.66.1815`.

[64] M. Yamaguchi. *Prospects of Physics Beyond the Standard Model: Supersymmetry* J. Phys. Soc. Japan 76(11) (2007) 111012. DOI: `10.1143/JPSJ.76.111012`.

[65] M. S. Carena and H. E. Haber. *Higgs boson theory and phenomenology* Prog. Part. Nucl. Phys. 50 (2003) 63. DOI: `10.1016/S0146-6410(02)00177-1`.

[66] H. Baer et al. *Radiative natural SUSY with a 125 GeV Higgs boson* Phys. Rev. Lett. 109 (2012) 161802. DOI: `10.1103/PhysRevLett.109.161802`.

[67] A. Arbey et al. *Implications of a 125 GeV Higgs for supersymmetric models* Phys. Lett. B 708 (2012) 162. DOI: `10.1016/j.physletb.2012.01.053`.

[68] N. Zhou et al. *Bounds on Invisible Higgs boson Decays from $t\bar{t}H$ Production* (2014). arXiv: `1408.0011 [hep-ph]`.

[69] LEPSUSYWG, ALEPH, DELPHI, L3 and OPAL experiments. *Notes LEPSUSYWG/01-03.1 and 02-04.1* URL: `http://lepsusy.web.cern.ch/lepsusy`.

[70] M. Jaffre. *SUSY searches at the Tevatron* Eur. Phys. J.Web Conf. 28 (2012) 09006. DOI: `10.1051/epjconf/20122809006`.

[71] OPAL Collaboration. *Search for a scalar top quark using the OPAL detector* Phys. Lett. B 337 (1994) 207. DOI: `10.1016/0370-2693(94)91470-2`.

[72] D0 Collaboration. *Search for Light Top Squarks in $p\overline{p}$ Collisions at $\sqrt{s} = 1.8$ TeV* Phys. Rev. Lett. 76(13) (1996) 2222. DOI: `10.1103/PhysRevLett.76.2222`.

[73] OPAL Collaboration. *Search for scalar top and scalar bottom quarks at LEP* Phys. Lett. B 545 (2002) 272. DOI: `10.1016/S0370-2693(02)02593-5`.

[74] CDF Collaboration. *Note 9834, Search for scalar top decaying into $c + \tilde{\chi}^0$ in the MET+jets sample.* 2009.

[75] CDF Collaboration. *Note 8701, Search for charged, massive stable particles.* 2007.

[76] D0 Collaboration. *Search for pair production of the scalar top quark in the electron+muon final state* Phys. Lett. B 696 (2011) 321. DOI: `10.1016/j.physletb.2010.12.052`.

[77] L. Evans and P. Bryant. *LHC Machine* J. Instrum. 3(08) (2008) 08001. URL: `http://stacks.iop.org/1748-0221/3/i=08/a=S08001`.

[78] ATLAS Collaboration. *Public Website.* 2014. URL: `https://twiki.cern.ch/twiki/bin/view/AtlasPublic/StandardModelPublicResults`.

[79] LHCb Collaboration. *Implications of LHCb measurements and future prospects* Eur. Phys. J. C 73(4), 2373 (2013) 1. DOI: `10.1140/epjc/s10052-013-2373-2`.

[80] LHCb Collaboration. *Observation of the $B_s^0 \to J/\psi K_s^0 K^{\pm}\pi^{\mp}$ decay* J. High Energy Phys. 1407 (2014) 140. DOI: `10.1007/JHEP07(2014)140`.

[81] LHCb Collaboration. *Observation of two new Ξ_b^- baryon resonances* Phys. Rev. Lett. 114(6) (2014) 062004. DOI: `10.1103/PhysRevLett.114.062004`.

[82] ALICE Collaboration. *Suppression of Charged Particle Production at Large Transverse Momentum in Central Pb–Pb Collisions at $\sqrt{s_{NN}} = 2.76$ TeV* Phys. Lett. B 696 (2011) 30. DOI: `10.1016/j.physletb.2010.12.020`.

[83] ATLAS Collaboration. *Public Website.* URL: `https://twiki.cern.ch/twiki/bin/view/AtlasPublic/LuminosityPublicResults`.

[84] ATLAS Collaboration. *The ATLAS Experiment at the CERN Large Hadron Collider* J. Instrum. 3(08) (2008) 08003. URL: `http://stacks.iop.org/1748-0221/3/i=08/a=S08003`.

[85] ATLAS Collaboration. *Luminosity determination in pp collisions at $\sqrt{s} = 7$ TeV using the ATLAS detector at the LHC* Eur. Phys. J. C 71(4), 1630 (2011) 1. DOI: `10.1140/epjc/s10052-011-1630-5`.

[86] ATLAS Collaboration. *Improved electron reconstruction in ATLAS using the Gaussian Sum Filter-based model for bremsstrahlung.* ATLAS-CONF-2012-047.

[87] ATLAS Collaboration. *Performance of the ATLAS Inner Detector Track and Vertex Reconstruction in the High Pile-Up LHC Environment.* ATLAS-CONF-2012-042.

[88] ATLAS Collaboration. *Electron reconstruction and identification efficiency measurements with the ATLAS detector using the 2011 LHC proton-proton collision data* Eur. Phys. J. C 74(7) (2014) 2941. DOI: `10.1140/epjc/s10052-014-2941-0`.

[89] ATLAS Collaboration. *Electron efficiency measurements with the ATLAS detector using the 2012 LHC proton-proton collision data.* ATLAS-CONF-2014-032.

[90] ATLAS Collaboration. *Alignment of the ATLAS Inner Detector and its Performance in 2012.* ATLAS-CONF-2014-047.

[91] ATLAS Collaboration. *Electron and photon energy calibration with the ATLAS detector using LHC Run 1 data* Eur. Phys. J. C 74(10) (2014) 3071. DOI: `10.1140/epjc/s10052-014-3071-4`.

[92] ATLAS Collaboration. *Measurement of the muon reconstruction performance of the ATLAS detector using 2011 and 2012 LHC proton-proton collision data.* CERN-PH-EP-2014-151. arXiv: `1407.3935`.

[93] ATLAS Collaboration. *Jet energy measurement with the ATLAS detector in proton-proton collisions at $\sqrt{s} = 7$ TeV* Eur. Phys. J. C 73(3), 2304 (2013) 1. DOI: `10.1140/epjc/s10052-013-2304-2`.

[94] M. Cacciari, G. P. Salam, and G. Soyez. *The Anti-k(t) jet clustering algorithm* J. High Energy Phys. 0804 (2008) 063. DOI: `10.1088/1126-6708/2008/04/063`.

[95] ATLAS Collaboration. *Jet energy measurement and its systematic uncertainty in proton-proton collisions at $\sqrt{s} = 7$ TeV with the ATLAS detector* (2014). arXiv: `1406.0076 [hep-ex]`.

[96] ATLAS Collaboration. *Characterisation and mitigation of beam-induced backgrounds observed in the ATLAS detector during the 2011 proton-proton run* J. Instrum. 8(07) (2013) 07004.

[97] ATLAS Collaboration. *Public Website.* URL: `https://twiki.cern.ch/twiki/bin/view/AtlasPublic/JetEtmissApproved2013JESUncertainty`.

[98] ATLAS Collaboration. *Public Website.* URL: `https://twiki.cern.ch/twiki/bin/view/AtlasPublic/JetEtmissApproved2013Jer2011`.

[99] ATLAS Collaboration. *Jet energy resolution in proton-proton collisions at* $\sqrt{s} = 7$ *TeV recorded in 2010 with the ATLAS detector* Eur. Phys. J. C 73 (2013) 2306. DOI: `10.1140/epjc/s10052-013-2306-0`.

[100] ATLAS Collaboration. *Commissioning of the ATLAS high-performance b-tagging algorithms in the 7 TeV collision data.* ATLAS-CONF-2011-102.

[101] ATLAS Collaboration. *Calibration of the performance of b-tagging for c and light-flavour jets in the 2012 ATLAS data.* ATLAS-CONF-2014-046.

[102] ATLAS Collaboration. *Performance of Missing Transverse Momentum Reconstruction in ATLAS studied in Proton-Proton Collisions recorded in 2012 at 8 TeV.* ATLAS-CONF-2013-082.

[103] ATLAS Collaboration. *Performance of the ATLAS Trigger System in 2010* Eur. Phys. J. C 72 (2011) 1849. arXiv: `1110.1530`.

[104] ATLAS Collaboration. *Charged-particle multiplicities in pp interactions measured with the ATLAS detector at the LHC* New J. Phys. 13(5) (2011) 053033. DOI: `10.1088/1367-2630/13/5/053033`.

[105] H.-L. Lai et al. *New parton distributions for collider physics* Phys. Rev. D 82 (2010) 074024. DOI: `10.1103/PhysRevD.82.074024`.

[106] J. Pumplin et al. *New generation of parton distributions with uncertainties from global QCD analysis* J. High Energy Phys. 0207 (2002) 012. DOI: `10.1088/1126-6708/2002/07/012`.

[107] V. D. Barger and R. Phillips. *Collider physics; 2nd ed.* Frontiers in Physics. Westview Press, 1997.

[108] M. L. Mangano et al. *ALPGEN, a generator for hard multiparton processes in hadronic collisions* J. High Energy Phys. 0307 (2003) 001. DOI: `10.1088/1126-6708/2003/07/001`.

[109] T. Gleisberg et al. *Event generation with SHERPA 1.1* J. High Energy Phys. 0902 (2009) 007. DOI: `10.1088/1126-6708/2009/02/007`.

[110] M. L. Mangano. *QCD and the physics of hadronic collisions* Physics-Uspekhi 53(2) (2010) 109. URL: `http://stacks.iop.org/1063-7869/53/i=2/a=R01`.

[111] B. R. Webber. *Fragmentation and Hadronization* (2000).

[112] J. Alwall et al. *Comparative study of various algorithms for the merging of parton showers and matrix elements in hadronic collisions* Eur. Phys. J. C 53 (2008) 473. DOI: `10.1140/epjc/s10052-007-0490-5`.

[113] ATLAS Collaboration. *Measurement of the underlying event in jet events from 7 TeV proton-proton collisions with the ATLAS detector* Eur. Phys. J. C 74(8), 2965 (2014). DOI: `10.1140/epjc/s10052-014-2965-5`.

[114] S. Agostinelli et al. *Geant4–a simulation toolkit* NIM A 506(3) (2003) 250. DOI: `10.1016/S0168-9002(03)01368-8`.

[115] Z. Marshall. *Simulation of Pile-up in the ATLAS Experiment.* ATL-SOFT-PROC-2013-030.

[116] J. Boudreau and V. Tsulaia. *The GeoModel toolkit for detector description.* 2005. URL: `http://doc.cern.ch/yellowrep/2005/2005-002/p353.pdf`.

[117] ATLAS Collaboration. *Performance of the Fast ATLAS Tracking Simulation (FATRAS) and the ATLAS Fast Calorimeter Simulation (FastCaloSim) with single particles.* ATL-SOFT-PUB-2014-001.

[118] ATLAS Collaboration. *Measurement of the* $t\bar{t}$ *production cross-section using* $e\mu$ *events with b -tagged jets in pp collisions at* $\sqrt{s} = 7$ *and 8 TeV with the ATLAS detector* Eur. Phys. J. C 74(10) (2014) 3109. DOI: `10.1140/epjc/s10052-014-3109-7`.

[119] ATLAS Collaboration. *Measurement of Spin Correlation in Top-Antitop Quark Events and Search for Top Squark Pair Production in pp Collisions at* $\sqrt{s} =$ *8 TeV Using the ATLAS Detector* Phys. Rev. Lett. 114 14 (2015). DOI: `10.1103/PhysRevLett.114.142001`.

[120] B. Altunkaynak et al. *Studying Gaugino Mass Unification at the LHC* J. High Energy Phys. 04 (2009) 114. DOI: `10.1088/1126-6708/2009/04/114`.

[121] ATLAS Collaboration. *Search for top squark pair production in final states with one isolated lepton, jets, and missing transverse momentum in* $\sqrt{s} = 8$ *TeV pp collisions with the ATLAS detector* J. High Energy Phys. 11 (2014) 118. DOI: `10.1007/JHEP11(2014)118`.

[122] ATLAS Collaboration. *Measurement of the production cross section for W-bosons in association with jets in pp collisions using 33 pb-1 at* $\sqrt{s} = 7$ *TeV with the ATLAS detector.* ATLAS-CONF-2011-060.

[123] ATLAS Collaboration. *Study of jets produced in association with a W boson in pp collisions at* $\sqrt{s} = 7$ *TeV with the ATLAS detector* Phys. Rev. D 85 (2012) 092002. DOI: `10.1103/PhysRevD.85.092002`.

[124] ATLAS Collaboration. *Top Quark Pair Production Cross-section Measurements in ATLAS in the Single Lepton+Jets Channel without b-tagging.* ATLAS-CONF-2011-023.

[125] ATLAS Collaboration. *A combined measurement of the top quark pair production cross-section using dilepton and single-lepton final states.* ATLAS-CONF-2011-040.

[126] ATLAS Collaboration. *Measurement of the* $t\bar{t}$ *production cross section in the all-hadronic channel in ATLAS with* $\sqrt{s} = 7$ *TeV data.* ATLAS-CONF-2012-031.

[127] ATLAS Collaboration. *Measurement of the $t\bar{t}$ production cross-section as a function of jet multiplicity and jet transverse momentum in 7 TeV proton-proton collisions with the ATLAS detector* J. High Energy Phys. 1501 (2015) 020. DOI: `10.1007/JHEP01(2015)020`.

[128] ATLAS Collaboration. *Measurements of normalized differential cross sections for $t\bar{t}$ production in pp collisions at $\sqrt{s} = 7$ TeV using the ATLAS detector* Phys. Rev. D 90(7) (2014) 072004. DOI: `10.1103/PhysRevD.90.072004`.

[129] ATLAS Collaboration. *Measurement of the top quark mass with the template method in the $t\bar{t}$ -> lepton + jets channel using ATLAS data* Eur. Phys. J. C 72 (2012) 2046. DOI: `10.1140/epjc/s10052-012-2046-6`.

[130] ATLAS, CDF, CMS, and D0 Collaborations. *First combination of Tevatron and LHC measurements of the top-quark mass* (2014). arXiv: `1403.4427 [hep-ex]`.

[131] ATLAS Collaboration. *Measurement of the $WW + WZ$ cross section and limits on anomalous triple gauge couplings using final states with one lepton, missing transverse momentum, and two jets with the ATLAS detector at $\sqrt{\mathrm{s}} = 7$ TeV* J. High Energy Phys. 01 (2014) 049. arXiv: `1410.7238`.

[132] ATLAS Collaboration. *Comprehensive measurements of t-channel single top-quark production cross sections at $\sqrt{s} = 7$ TeV with the ATLAS detector* Phys. Rev. D 90 (2014) 112006. arXiv: `1406.7844`.

[133] ATLAS Collaboration. *Measurement of the production cross section for Z/γ^* in association with jets in pp collisions at $\sqrt{s} = 7$ TeV with the ATLAS Detector.* ATLAS-CONF-2011-042.

[134] ATLAS Collaboration. *Evidence for the associated production of a vector boson (W, Z) and top quark pair in the dilepton and trilepton channels in pp collision data at $\sqrt{s} = 8$ TeV collected by the ATLAS detector at the LHC.* ATLAS-CONF-2014-038.

[135] ATLAS Collaboration. *Search for $t\bar{t}Z$ production in the three lepton final state with* 4.7 fb^{-1} *of $\sqrt{s} = 7$ TeV pp collision data collected by the ATLAS detector.* ATLAS-CONF-2012-126.

[136] CMS Collaboration. *Measurement of the Associated Production of Vector Bosons with Top-Antitop Pairs at 7 TeV.* CMS-PAS-TOP-12-014. 2012.

[137] S. Dittmaier et al. *Handbook of LHC Higgs Cross Sections: 1. Inclusive Observables* (2011). DOI: `10.5170/CERN-2011-002`.

[138] M. Bahr et al. *Herwig++ Physics and Manual* Eur. Phys. J. C 58 (2008) 639. DOI: `10.1140/epjc/s10052-008-0798-9`.

[139] J. Alwall et al. *MadGraph 5 : Going Beyond* J. High Energy Phys. 1106 (2011) 128. DOI: `10.1007/JHEP06(2011)128`.

[140] S. Frixione, P. Nason, and C. Oleari. *Matching NLO QCD computations with Parton Shower simulations: the POWHEG method* J. High Energy Phys. 0711 (2007) 070. DOI: `10.1088/1126-6708/2007/11/070`.

[141] B. P. Kersevan and E. Richter-Was. *The Monte Carlo event generator AcerMC versions 2.0 to 3.8 with interfaces to PYTHIA 6.4, HERWIG 6.5 and ARIADNE 4.1* Comput. Phys. Commun. 184 (2013) 919. DOI: `10.1016/j.cpc.2012.10.032`.

[142] *New ATLAS event generator tunes to 2010 data.* ATL-PHYS-PUB-2011-008.

[143] P. Z. Skands. *Tuning Monte Carlo Generators: The Perugia Tunes* Phys. Rev. D 82 (2010) 074018. DOI: `10.1103/PhysRevD.82.074018`.

[144] S. Gieseke, C. Rohr, and A. Siodmok. *Colour reconnections in Herwig++* Eur. Phys. J. C 72 (2012) 2225. DOI: `10.1140/epjc/s10052-012-2225-5`.

[145] T. Sjostrand, S. Mrenna, and P. Z. Skands. *PYTHIA 6.4 Physics and Manual* J. High Energy Phys. 0605 (2006) 026. DOI: `10.1088/1126-6708/2006/05/026`.

[146] T. Sjostrand, S. Mrenna, and P. Z. Skands. *A Brief Introduction to PYTHIA 8.1* Comput. Phys. Commun. 178 (2008) 852. DOI: `10.1016/j.cpc.2008.01.036`.

[147] M. L. Mangano et al. *Matching matrix elements and shower evolution for top-quark production in hadronic collisions* J. High Energy Phys. 0701 (2007) 013. DOI: `10.1088/1126-6708/2007/01/013`.

[148] S. Catani et al. *QCD matrix elements + parton showers* J. High Energy Phys. 0111 (2001) 063. DOI: `10.1088/1126-6708/2001/11/063`.

[149] ATLAS Collaboration. *Performance of the ATLAS Electron and Photon Trigger in pp Collisions at* $\sqrt{s} = 7$ *TeV in 2011.* ATLAS-CONF-2012-048.

[150] ATLAS Collaboration. *Performance of the ATLAS muon trigger in 2011.* ATLAS-CONF-2012-099.

[151] M. Cacciari et al. *Top-pair production at hadron colliders with next-to-next-to-leading logarithmic soft-gluon resummation* Phys. Lett. B 710 (2012) 612. DOI: `10.1016/j.physletb.2012.03.013`.

[152] P. Bärnreuther, M. Czakon, and A. Mitov. *Percent Level Precision Physics at the Tevatron: First Genuine NNLO QCD Corrections to* $q\bar{q} \to t\bar{t} + X$ Phys. Rev. Lett. 109 (2012) 132001. DOI: `10.1103/PhysRevLett.109.132001`.

[153] M. Czakon and A. Mitov. *NNLO corrections to top-pair production at hadron colliders: the all-fermionic scattering channels* J. High Energy Phys. 1212 (2012) 054. DOI: `10.1007/JHEP12(2012)054`.

[154] M. Czakon and A. Mitov. *NNLO corrections to top pair production at hadron colliders: the quark-gluon reaction* J. High Energy Phys. 1301 (2013) 080. DOI: `10.1007/JHEP01(2013)080`.

[155] M. Czakon, P. Fiedler, and A. Mitov. *Total Top-Quark Pair-Production Cross Section at Hadron Colliders Through* $O(\alpha_S^4)$ Phys. Rev. Lett. 110 (2013) 252004. DOI: `10.1103/PhysRevLett.110.252004`.

[156] M. Czakon and A. Mitov. *Top++: A Program for the Calculation of the Top-Pair Cross-Section at Hadron Colliders* Comput. Phys. Commun. 185 (2014) 2930. DOI: `10.1016/j.cpc.2014.06.021`.

[157] S. Catani et al. *Vector boson production at hadron colliders: a fully exclusive QCD calculation at NNLO* Phys. Rev. Lett. 103 (2009) 082001. DOI: `10.1103/PhysRevLett.103.082001`.

[158] J. M. Campbell and R. K. Ellis. *An Update on vector boson pair production at hadron colliders* Phys. Rev. D 60 (1999) 113006. DOI: `10.1103/PhysRevD.60.113006`.

[159] J. M. Campbell, R. K. Ellis, and C. Williams. *Vector boson pair production at the LHC* J. High Energy Phys. 07 (2011) 018. DOI: `10.1007/JHEP07(2011)018`.

[160] N. Kidonakis. *Next-to-next-to-leading-order collinear and soft gluon corrections for t-channel single top quark production* Phys. Rev. D 83 (2011) 091503. DOI: `10.1103/PhysRevD.83.091503`.

[161] N. Kidonakis. *Two-loop soft anomalous dimensions for single top quark associated production with a W- or H-* Phys. Rev. D 82 (2010) 054018. DOI: `10.1103/PhysRevD.82.054018`.

[162] N. Kidonakis. *NNLL resummation for s-channel single top quark production* Phys. Rev. D 81 (2010) 054028. DOI: `10.1103/PhysRevD.81.054028`.

[163] J. Campbell, R. K. Ellis, and R. Röntsch. *Single top production in association with a Z boson at the LHC* Phys. Rev. D 87 (2013) 114006. DOI: `10.1103/PhysRevD.87.114006`.

[164] J. M. Campbell and R. K. Ellis. *$t\bar{t}W^{+-}$ production and decay at NLO* J. High Energy Phys. 1207 (2012) 052. DOI: `10.1007/JHEP07(2012)052`.

[165] M. Garzelli et al. *$t\,\bar{t}\,W^{\pm}$ and $t\,\bar{t}\,Z$ Hadroproduction at NLO accuracy in QCD with Parton Shower and Hadronization effects* J. High Energy Phys. 11 (2012) 056. DOI: `10.1007/JHEP11(2012)056`.

[166] W. Beenakker et al. *Stop Production at Hadron Colliders* Nucl. Phys. B 515 (1997) 3.

[167] A. Kulesza and L. Motyka. *Threshold Resummation for Squark-Antisquark and Gluino-Pair Production at the LHC* Phys. Rev. Lett. 102(11) (2009) 111802. DOI: `10.1103/PhysRevLett.102.111802`.

[168] ATLAS collaboration. *Comparison of Monte Carlo generator predictions for gap fraction and jet multiplicity observables in top-antitop events.* ATL-PHYS-PUB-2014-005. URL: `https://cds.cern.ch/record/1703034`.

[169] ATLAS Collaboration. *Search for direct top squark pair production in final states with one isolated lepton, jets, and missing transverse momentum in $\sqrt{s} = 7$ TeV pp collisions using 4.7 fb^{-1} of ATLAS data* Phys. Rev. Lett. 109 (2012) 211803. arXiv: `1208.2590`.

[170] ATLAS Collaboration. *Search for direct top squark pair production in final states with one isolated lepton, jets, and missing transverse momentum in $\sqrt{s} = 8$ TeV pp collisions using 13.0 fb^{-1} of ATLAS data.* ATLAS-CONF-2012-166.

[171] ATLAS Collaboration. *Search for direct top squark pair production in final states with one isolated lepton, jets, and missing transverse momentum in $\sqrt{s} = 8$ TeV pp collisions using 21 fb^{-1} of ATLAS data.* ATLAS-CONF-2013-037.

[172] ATLAS Collaboration. *Combined search for the Standard Model Higgs boson in pp collisions at $\sqrt{s} = 7$ TeV with the ATLAS detector* Phys. Rev. D 86 (2012) 032003. DOI: `10.1103/PhysRevD.86.032003`.

[173] CMS Collaboration. *Combined results of searches for the standard model Higgs boson in pp collisions at $\sqrt{s} = 7$ TeV* Phys. Lett. B 710 (2012) 26. DOI: `10.1016/j.physletb.2012.02.064`.

[174] ATLAS Collaboration. *Search for direct pair production of the top squark in all-hadronic final states in proton-proton collisions at $\sqrt{s} = 8$ TeV with the ATLAS detector* J. High Energy Phys. 2014(9), 15 (2014). DOI: `10.1007/JHEP09(2014)015`.

[175] ATLAS Collaboration. *Search for direct top-squark pair production in final states with two leptons in pp collisions at $\sqrt{s} = 8$ TeV with the ATLAS detector* J. High Energy Phys. 2014(6), 124 (2014). DOI: `10.1007/JHEP06(2014)124`.

[176] C. Lester and D. Summers. *Measuring masses of semi-invisibly decaying particle pairs produced at hadron colliders* Phys. Lett. B 463 (1999) 99. DOI: `10.1016/S0370-2693(99)00945-4`.

[177] M. L. Graesser and J. Shelton. *Hunting Asymmetric Stops* Phys. Rev. Lett. 111 (2013) 121802. DOI: `10.1103/PhysRevLett.111.121802`.

[178] ATLAS Collaboration. *Performance of the Reconstruction and Identification of Hadronic Tau Decays in ATLAS with 2011 Data.* ATLAS-CONF-2012-142.

[179] A. L. Read. *Modified frequentist analysis of search results (the CL_s method).* CERN-OPEN-2000-205.

[180] A. Read. *Presentation of search results: the CL(s) technique* J. Phys. G 28 (2002) 2693.

[181] A. Martin et al. *Parton distributions for the LHC* Eur. Phys. J. C 63 (2009) 189. DOI: `10.1140/epjc/s10052-009-1072-5`.

[182] R. D. Ball et al. *Parton distributions with LHC data* Nucl. Phys. B 867 (2013) 244. DOI: `10.1016/j.nuclphysb.2012.10.003`.

[183] M. Botje et al. *The PDF4LHC Working Group Interim Recommendations* (2011). arXiv: `1101.0538 [hep-ph]`.

[184] ATLAS Collaboration. *Measurement of the cross-section for W boson production in association with b-jets in pp-collisions at $\sqrt{s} = 7$ TeV with the ATLAS detector* J. High Energy Phys. 06 (2013) 084. DOI: `10.1007/JHEP06(2013)084`.

[185] M. Kramer et al. *Supersymmetry production cross sections in pp collisions at $\sqrt{s} = 7$ TeV* (2012). arXiv: `1206.2892 [hep-ph]`.

[186] ATLAS Collaboration. *Calibration of b-tagging using dileptonic top pair events in a combinatorial likelihood appoach with the ATLAS experiment.* ATLAS-CONF-2014-004.

[187] ATLAS Collaboration. *Measurement of the b-tag Efficiency in a Sample of Jets Containing Muons with* $5\,fb^{-1}$ *of Data from the ATLAS Detector*. ATLAS-CONF-2012-043.

[188] ATLAS Collaboration. *b-jet tagging calibration on c-jets containing* $D^{\star+}$ *mesons.* ATLAS-CONF-2012-039.

[189] ATLAS Collaboration. *Measurement of the Mistag Rate with 5* fb^{-1} *of Data Collected by the ATLAS Detector*. ATLAS-CONF-2012-040.

[190] O. Behnke et al. *Data analysis in high energy physics: a practical guide to statistical methods* Wiley-VCH, 2013.

[191] ATLAS Collaboration. *Search for pair-produced third-generation squarks decaying via charm quarks or in compressed supersymmetric scenarios in pp collisions at* $\sqrt{s} = 8$ *TeV with the ATLAS detector* Phys. Rev. D 90 (2014) 052008. DOI: `10.1103/PhysRevD.90.052008`.

[192] ATLAS Collaboration. *Search for supersymmetry in events with four or more leptons in* $\sqrt{s} = 8$ *TeV pp collisions with the ATLAS detector* Phys. Rev. D 90 (2014) 052001. DOI: `10.1103/PhysRevD.90.052001`.

[193] ATLAS Collaboration. *Search for strong production of supersymmetric particles in final states with missing transverse momentum and at least three b-jets at* $\sqrt{s} =$ *8 TeV proton-proton collisions with the ATLAS detector* J. High Energy Phys. 1410 (2014) 24. DOI: `10.1007/JHEP10(2014)024`.

[194] ATLAS Collaboration. *Search for new phenomena in final states with large jet multiplicities and missing transverse momentum at* $\sqrt{s} = 8$ *TeV proton-proton collisions using the ATLAS experiment* J. High Energy Phys. 1310 (2013) 130. DOI: `10.1007/JHEP10(2013)130,10.1007/JHEP01(2014)109`.

[195] ATLAS Collaboration. *Public Website.* URL: `https://twiki.cern.ch/twiki/bin/view/AtlasPublic/SupersymmetryPublicResults`.

[196] ATLAS Collaboration. *Search for squarks and gluinos with the ATLAS detector in final states with jets and missing transverse momentum using* $\sqrt{s} = 8$ *TeV proton–proton collision data* J. High Energy Phys. 1409 (2014) 176. DOI: `10.1007/JHEP09(2014)176`.

[197] ATLAS Collaboration. *Further search for supersymmetry at* $\sqrt{s} = 7$ *TeV in final states with jets, missing transverse momentum and isolated leptons with the ATLAS detector* Phys. Rev. D 86 (2012) 092002. DOI: `10.1103/PhysRevD.86.092002`.

[198] ATLAS Collaboration. *Search for supersymmetry in events with large missing transverse momentum, jets, and at least one tau lepton in 20* fb^{-1} *of* $\sqrt{s} = 8$ *TeV proton-proton collision data with the ATLAS detector* J. High Energy Phys. 1409 (2014) 103. DOI: `10.1007/JHEP09(2014)103`.

[199] ATLAS Collaboration. *Search for direct production of charginos, neutralinos and sleptons in final states with two leptons and missing transverse momentum in pp collisions at* $\sqrt{s} = 8$ *TeV with the ATLAS detector* J. High Energy Phys. 1405 (2014) 071. DOI: `10.1007/JHEP05(2014)071`.

[200] ATLAS Collaboration. *Search for direct production of charginos and neutralinos in events with three leptons and missing transverse momentum in* $\sqrt{s} = 8$ *TeV pp collisions with the ATLAS detector* J. High Energy Phys. 1404 (2014) 169. DOI: `10.1007/JHEP04(2014)169`.

[201] ATLAS Collaboration. *Search for non-pointing and delayed photons in the diphoton and missing transverse momentum final state in 8 TeV pp collisions at the LHC using the ATLAS detector* Phys. Rev. D 90 (2014) 112005. DOI: `10.1103/PhysRevD.90.112005`.

[202] ATLAS Collaboration. *Search for charginos nearly mass degenerate with the lightest neutralino based on a disappearing-track signature in pp collisions at* $\sqrt{s} = 8$ *TeV with the ATLAS detector* Phys. Rev. D 88 (2013) 112006. DOI: `10.1103/PhysRevD.88.112006`.

[203] CMS Collaboration. *Search for supersymmetry in hadronic final states using MT2 with the CMS detector at* $\sqrt{s} = 8$ *TeV*. CMS-PAS-SUS-13-019. 2014.

[204] CMS Collaboration. *Exclusion limits on gluino and top-squark pair production in natural SUSY scenarios with inclusive razor and exclusive single-lepton searches at 8 TeV*. CMS-PAS-SUS-14-011. 2014.

[205] CMS Collaboration. *Search for new physics in events with same-sign dileptons and jets in pp collisions at* $\sqrt{s} = 8$ *TeV* J. High Energy Phys. 01 (2013) 163. arXiv: `1311.6736`.

[206] CMS Collaboration. *Searches for electroweak production of charginos, neutralinos, and sleptons decaying to leptons and W, Z, and Higgs bosons in pp collisions at 8 TeV* Eur. Phys. J. C 74 (2014) 3036. arXiv: `1405.7570`.

[207] CMS Collaboration. *Searches for electroweak neutralino and chargino production in channels with Higgs, Z, and W bosons in pp collisions at 8 TeV*. 2014. arXiv: `1409.3168`.

[208] W. Stirling. URL: `http://www.hep.ph.ic.ac.uk/~wstirlin/plots/plots.html`.

[209] P. Teng et al. *Radiation hardness and lifetime studies of the VCSELs for the ATLAS SemiConductor Tracker* NIM A 497(2-3) (2003) 294. DOI: `10.1016/S0168-9002(02)01922-8`.

[210] ATLAS Collaboration. *Measurement of the charge asymmetry in dileptonic decay of top quark pairs in pp collisions at* $\sqrt{s} = 7$ *TeV using the ATLAS detector*. ATLAS-CONF-2012-057.

List of Figures

1.1 R-ratio: experimental proof of 3 colours. 4
1.2 Elementary QED vertex and processes. 9
1.3 Illustration of the Higgs field potential $V(\phi)$. 11
1.4 Higgs observation probability. 13
1.5 Expected branching ratios for different Higgs boson mass assumptions. . . 13
1.6 Feynman diagrams of top-loop contributions to m_H^2. 14
1.7 Near miss of gauge coupling unification in SM. 16

2.1 Feynman diagrams of cancelling top and stop-loop contributions. 20
2.2 Gauge coupling unification in the MSSM. 30
2.3 Kaon mixing diagrams in the SM. 31
2.4 Kaon mixing diagrams in the MSSM. 32
2.5 Natural SUSY mass spectrum example. 33
2.6 Upper limits on light Higgs mass for different SUSY models. 36
2.7 Exclusion in $m(\tilde{t}_1)$-$m(\tilde{\nu})$ plane by D0. 37

3.1 Overview of SM cross-section results from ATLAS. 40
3.2 Integrated luminosity recorded with the ATLAS detector in 2012. 41
3.3 ATLAS detector layout. 43
3.4 Layout of the inner detector. 45
3.5 Schematic view of an electromagnetic barrel module. 46
3.6 Coverage and material of ATLAS calorimeters. 47
3.7 Layout of the muon spectrometer. 48
3.8 Interactions per bunch crossing in 2012 ATLAS *pp* events. 50
3.9 Vertex reconstruction efficiency in a minimum bias sample. 51
3.10 Electron reconstruction and identification efficiency in 2012 data. 52
3.11 Electron performance in 2012 53
3.12 Muon reconstruction efficiency in 2012 data. 54
3.13 Jet energy scale uncertainty and resolution. 56
3.14 Performance of the MV1 *b*-tagging algorithm. 57
3.15 Comparison between data and simulation of the MV1 *b*-tagging algorithm. 58
3.16 Illustration of trigger decision. 60

4.1 CT10 NLO parton distribution functions example. 64

4.2 Sketch of pp collision, hard process and underlying event. 66
4.3 Feynman diagrams of $\tilde{t}_1 \rightarrow t + \tilde{\chi}_1^0$ and $\tilde{t}_1 \rightarrow b + \tilde{\chi}_1^\pm$ decays. 68
4.4 Tree-level Feynman diagrams of targeted stop decay modes. 69
4.5 Impact of stop mixing assumption on the exclusion reach. 70
4.6 Feynman diagrams contributing to diboson production. 72
4.7 Feynman diagrams contributing to single-top production. 73
4.8 Signal comparison between Herwig++ and MadGraph+Pythia6. 76
4.9 Grid of stop and neutralino masses used in study. 77
4.10 Theoretical sparticle production cross-sections at NLO+NLL. 78
4.11 Effect of $t\bar{t}$ reweighting on $E_{\mathrm{T}}^{\mathrm{miss}}$ distribution. 81

5.1 Excluded stop and LSP masses using 2011 ATLAS data. 85
5.2 Distribution of b-tagging SFs. 91
5.3 Distribution of #jets in signal and background events. 94
5.4 Distribution of m_{T} in signal and background events. 95
5.5 Distribution of m_{T} with and without $E_{\mathrm{T}}^{\mathrm{miss}}$ requirement. 96
5.6 Illustration of m_{T2} definition. 97
5.7 Topology of an incomplete dileptonic $t\bar{t}$ decay. 98
5.8 Distribution of am$_{\mathrm{T2}}$ in preselection. 99
5.9 Topness distributions for $t\bar{t}$ and asymmetric $\tilde{t}_1$ decays. 100
5.10 Distribution of m_{jjj} in signal and background events. 101
5.11 Distribution of $E_{\mathrm{T}}^{\mathrm{miss}}$ for different $t\bar{t}$ decay modes. 102
5.12 Grid of variables used in optimisation. 104
5.13 Visual representation of the SR performance. 106
5.14 Illustration of CR-based normalisation. 115
5.15 Control plots for the mixed CRs. 116
5.16 Control plots for the mixed VRs. 122
5.17 Control plots for the mixed SR. 123
5.18 Data/simulation validation for the mixed regions. 124
5.19 The binning used in the three-body shape-fit. 125
5.20 Control plots for three-body shape-fit. 126

6.1 CL$_{\mathrm{s}}$ maps for the mixed SR. 130
6.2 Exclusion contours for mixed models using the mixed SR only. 131
6.3 Exclusion contours for mixed models using the best expected SR. 133
6.4 CL$_{\mathrm{s}}$ maps for three-body shape-fit. 134
6.5 Excluded $\tilde{t}_1 \rightarrow t + \tilde{\chi}_1^0$ models using 2012 ATLAS data. 135
6.6 Summary plots of run 1 ATLAS $\tilde{t}_1 \rightarrow t + \tilde{\chi}_1^0$ searches. 138
6.7 Summary plots of run 1 ATLAS $\tilde{t}_1 \rightarrow b + \tilde{\chi}_1^\pm$ searches. 139
6.8 Exclusion limits on mSUGRA models. 140

7.1 Increase in LHC production rates due to increased $\sqrt{s}$. 142

A.1 Timeline of VCSEL failures in the ATLAS silicon detectors. 146
A.2 Examples of VCSEL output power spectra. 147

A.3 Comparison of widths for the three VCSEL sets studied initially. 148
A.4 Spectral widths for Pixel VCSEL arrays. 148
A.5 Long-term study of spectral narrowing for modules in air and in nitrogen. 149

B.1 Kinematic distributions of anti-electron QCD models. 155
B.2 Anti-electron model requiring one failed bit ($\geqslant$3 jets, no b-tag requirement). 158
B.3 Anti-electron model (1 failed bit, $\geqslant$4 jets, $\geqslant$1 b-tag). 158
B.4 Anti-electron model (2 failed bits, $\geqslant$4 jets, $\geqslant$1). 159
B.5 Anti-electron model (2 failed bits, $\geqslant$4 jets, $\geqslant$1 b-tag). 159
B.6 Prescale values for the triggers used in periods L+M of the 2011 data-taking. 160

List of Tables

1.1 An overview of SM particles. 8

2.1 Particle content of the MSSM. 28

3.1 Performance goal specification for the ATLAS detector. 49
3.2 Summary of object definitions used in the stop analysis. 59

4.1 Software and settings used in production of background samples. 74
4.2 Software and settings used in production of signal samples. 75
4.3 Summary of SM sample sizes and theoretical cross-sections. 79
4.4 Weights applied to simulated $t\bar{t}$ events. 80

5.1 Preselection cutflow for $t\bar{t}$ and W+jets events. 88
5.2 Preselection cutflow for signal benchmark models. 89
5.3 Effect of individual preselection requirements ($n-1$). 92
5.4 SR definitions for mixed and three-body stop decays. 108
5.5 SR composition. 109
5.6 Relative size of generator systematics for both SRs. 111
5.7 Systematic uncertainties (before fit) for the mixed SR. 113
5.8 Background composition of mixed CRs. 119
5.9 Breakdown of uncertainty on background estimates for the mixed SR. . . 121

6.1 Discovery probabilities and signal-independent upper limits. 129
6.2 Summary of additional signal regions in the published analysis. 132
6.3 Effect of different systematic uncertainties on μ_{sig} and CL_s. 136
6.4 Systematic uncertainty of the signal strength for additional models. 137

7.1 Comparison of estimated run 1 and run 2 production rates and yields. . . 143

B.1 Simulated samples used in anti-electron study. 152
B.2 Electron property bits and their use in different electron definitions. . . . 154
B.3 Choice of nominal and anti-electron triggers in 2011. 157
B.4 QCD fraction estimates for 2011 data, before correction. 162
B.5 QCD fraction estimates for 2011 data, corrected for real electrons. 163

Acknowledgements

> I say it was nothing... obviously, it was something.
> I was just trying to say that it's not worth making too much of a fuss about...
> saving everybody's lives...
>
> *Arthur Dent (after saving everybody's lives)*

Many people contributed to the success of the journey culminating in this thesis.

I am indebted to professor Allan Clark for giving me the opportunity to pursue a PhD in particle physics at the University of Geneva, and for his guidance and invaluable advice on countless occasions during this time. I am grateful also to professor Giuseppe Iacobucci for his continued support, and also to the other members of the thesis committee, Monica D'Onofrio and Xin Wu who significantly improved the quality of the thesis with their questions and suggestions.

Big thanks go to the past and present students and post-docs of the ATLAS group at the University of Geneva, for showing me the ropes, for being nice office mates, for many interesting lunch discussions, for listening to my complaints about ROOT and other causes of evil in the world, and generally for making my time in Geneva fun and interesting: Akshay, Alison, Alix, Andrée, Andrew, Anthony, Antonio, Attilio, Caterina, Chris, Daniel, Ece, Eleonora, Elina, Francesca, Francesco, Gabi, Gaetano, Gauthier, Ian, Javier, Johanna, Jose, Katalin, Lucian, Marc, Moritz, Noemi, Paul, Philippe, Reina, Sergio, Snezana, Sofia, Spyros, Szymon, Valerio, and Will. Thanks go to Yann Meunier for keeping the computers running, and Alessandro Bravar for organising the lab courses so smoothly all these years. Nothing in the physics department would function without Catherine Blanchard, and she has saved my life repeatedly.

Being at CERN for nearly five years means meeting more interesting people than I can possibly list here. My thanks go to the entire stop 1-lepton team, especially to Till, Sophio, Priscilla, Anna, Xiaoxiao, and Ben; it was an amazing experience! I am also very grateful to have met and have worked with Steve McMahon, Illona Kostyukhina and Dave Robinson on the SCT VCSELs.

I want to say "thank you" to my friends in Alfter, Amsterdam, Austin, Basel, Bonn, Cambridge, Ditzingen, Dormagen, Düsseldorf, East Lansing, Eichwalde, Freiburg, Hamburg, Jülich, Köln, Landsberg am Lech, Meyrin, München, Nijmegen, and Saint Genis Pouilly: you did not see me much in the past years, but you stayed in touch nonetheless. I could not have done this without you! (And I hope I have your correct addresses.)

Heartfelt thanks go to my entire family for their unwavering support, and for resisting the temptation to ask me about the remaining duration of my thesis work as much as humanly possible. Last but not least, although words cannot express the full scale of it: Lisa, I thank you for being there and giving meaning to it all.